

https://dspace.org/

Investigation of corrosion behaviour of aluminium alloy 7075 processed by laser shock peening without coating

Shonhai, Natsai

2024

University of the Witwatersrand, Johannesburg

https://hdl.handle.net/10539/45389

Shonhai, Natsai . (2024). Investigation of corrosion behaviour of aluminium alloy 7075 processed by laser shock peening without coating [Masters dissertation, University of the Witwatersrand, Johannesburg]. WIReDSpace. https://hdl.handle.net/10539/45389

Downloaded from a DSpace repository. https://dspace.org/



Investigation of Corrosion Behaviour of Aluminium Alloy 7075 Processed by Laser Shock Peening without Coating

Natsai Shonhai

A dissertation submitted to the Faculty of Engineering and the Built Environment, University of the Witwatersrand, in fulfilment of the requirements for the degree of Master of Science in Engineering (Metallurgy and Materials)

Supervisors: Prof. L.A. Cornish

Prof. C. Polese

Johannesburg, September 2024

DECLARATION

I, Natsai Shonhai, hereby declare that, unless otherwise acknowledged, this dissertation is my unaided work and has not been submitted previously at this, or any other institution of learning for any degree or examination.



11 September 2024

Signature Date

ABSTRACT

Laser shock peening (LSP) is a surface treatment to induce beneficial compressive residual stresses in metallic structures, thus improving their fatigue resistance. This technology has the potential to improve aeronautical component performance during application and maintenance. Aluminium alloys are used in the aviation industry due to their high strength-to-weight ratios and ease of design and manufacturing. However, they are susceptible to localised corrosion in some aggressive environments.

This study investigated the corrosion behaviour of AA7075-T651 after LSP without a protective coating (LSPwC). Variations in power intensity (PI) of 1-6 GW/cm^2, coverage (N_p) of 2.5-67 spots/mm^2 and spot size (SS) of 0.5-1.5 mm were explored. Surface modifications were evaluated using stereo microscopy, scanning electron microscopy (SEM), contact profilometry and Vickers microhardness tests. Three types of corrosion tests were conducted in 3.5 wt% NaCl solution on the peened and unpeened samples: potentiodynamic polarisation tests, 30-day immersion tests and stress corrosion cracking by three-point bending for 40 days.

Microscopic examination revealed rough surfaces with areas of melting and solidification in LSPwC samples. Surface roughness increased in all samples post-LSPwC due to induced plastic deformation and surface ablation. Increasing PI and N_p led to increased surface roughness. All peened samples had increased microhardness with a positive correlation with N_p. Potentiodynamic polarisation revealed higher corrosion rates for most LSPwC samples, likely due to increased surface roughness which reduced corrosion resistance. Corrosion rate had a positive linear correlation with PI and N_p with aluminium oxide formation and pitting as the dominant corrosion mechanisms. Improved corrosion resistance after LSPwC was observed in some samples with specific parameters. Notably, one sample had a corrosion rate four times lower than the unpeened one. The three-point bending induced tensile stresses on the peened surfaces, which led to the formation of multiple tangled cracks on the top surface of all specimens. The LSPwC samples were less susceptible to SCC and the best resistance was observed for Sample P3-SS1-N_p50.38 which had no visible cracks in the sample cross-section.

DEDICATION

I dedicate my dissertation work to God almighty, who gave me life, sustained me, and equipped me with all the knowledge and understanding to accomplish this work and to my dearest loving husband, Taona Malvin and my beautiful mother, Luccinah, the greatest woman in my world, with so much love that overflows throughout my life and to my father, Vitalis. I also dedicate it to my brother, Tapiwanashe, and the rest of my family and friends. Your love, support and prayers got me where I am today, I am eternally grateful to have all of you in my life; you are the reflection of God's love for me.

ACKNOWLEDGEMENTS

My supervisors, Prof. L.A. Cornish and Prof. C. Polese, for their support, motivation and constant guidance.

I would like to acknowledge the following institutions for their generous financial and administrative support:

- African Laser Centre (ALC) Programme, ALC Projects No: HLHA22X Task ALC-R007, HLHA23X Task ALC-R018, HLHA24X Task ALC-R023
- African Laser Centre (ALC) Scholarship Program, for support in 2021-2023, ALC Project No.: HLHA21X Task ALC S100, HLHA22X Task ALC S100, HLHA23X Task ALC S100
- CSIR Photonics Centre Rental Pool Programme (RPP), Contracts No: NLC-LRERA20-CON001, NLC-LRESA20-CON001 (2022), NLC-LRETA21-CON001
- DSI-NRF Centre of Excellence in Strong Materials (CoE-SM)
- DSI Collaborative Programme in Additive Manufacturing (CPAM)
- School of Chemical and Metallurgical Engineering at the University of the Witwatersrand, for providing facilities and equipment.

Mr. Shaun Riekert and the School of Mechanical, Industrial and Aeronautical Engineering Workshop staff at Wits, for their invaluable machining expertise, insightful advice and enjoyable camaraderie.

TABLE OF CONTENTS

DECLARATION i
ABSTRACT ii
DEDICATION iii
ACKNOWLEDGEMENTS iv
TABLE OF CONTENTS v
LIST OF FIGURES x
LIST OF TABLES xvii
NOMENCLATURE xviii
CHAPTER 1: INTRODUCTION 20
1.1 Background 20
1.2 Problem Statement 21
1.3 Research Objectives 21
1.3.1 Aim 21
1.3.2 Objectives 21
1.4 Dissertation Outline 21
CHAPTER 2: LITERATURE REVIEW 22
2.1 Introduction 22
2.2 Aluminium Alloys 22
2.2.1 Designation of alloys and tempers 23
2.2.2 The 7xxx series 24
2.2.3 Aluminium Alloy 7075-T651 25
2.3 Corrosion 27
2.3.1 Corrosion of aluminium alloys 28
2.3.1.1 Pitting corrosion 29
2.3.1.2 Stress corrosion cracking (SCC) 31
2.3.2 Corrosion testing and evaluation 33
2.3.2.1 Immersion tests 33
2.3.2.2 Electrochemical corrosion tests 34

2.3.2.3 Stress corrosion cracking (SCC) tests 35
2.3.2.3.1 Tests on statically loaded smooth samples 36
2.3.2.3.2 Tests on statically loaded pre-cracked samples 37
2.3.2.3.3 Slow Strain Rate Testing 38
2.4 Laser Shock Peening 38
2.4.1 LSP process description 38
2.4.2 Comparison of LSP with and without coatings 39
2.4.3 LSP parameters 40
2.4.3.1 Laser system parameters 40
2.4.3.2 Control parameters 41
2.4.3.3 Interaction Parameters 42
2.4.4 Effect of LSP on residual stress 42
2.4.5 Effect of LSP on surface roughness 43
2.4.6 Effect of LSP on microstructure 47
2.4.7 Effect of LSP on microhardness 48
2.4.8 Effect of LSP on corrosion 49
2.5 Rationale of the project 52
CHAPTER 3: EXPERIMENTAL PROCEDURE 53
3.1 Introduction 53
3.2 Sample Preparation 53
3.3 Laser Shock Peening 54
3.3.1 LSP process 54
3.3.2 Sample identification 55
3.4 Metallographic Sample Preparation 56
3.4.1 Sample sectioning 56
3.4.2 Mounting 58
3.4.2.1 Cold Mounting 58
3.4.2.2 Hot mounting 58
3.4.3 Grinding and polishing 58
3.4.4 Etching 59
3.5 Microscopy 59

3.5.1 Optical and stereo microscopy 59
3.5.2 Scanning electron microscopy 59
3.6 Surface Roughness 59
3.7 Microhardness Tests 61
3.8 Corrosion Testing 63
3.8.1 Potentiodynamic polarisation tests 63
3.8.2 Full immersion corrosion tests 66
3.8.3 Stress corrosion cracking tests 66
CHAPTER 4: RESULTS 69
4.1 Introduction 69
4.2 Analysis of AA7075-T651 as the Control Sample 69
4.3 Surface Morphology After LSPwC 72
4.3.1 Varying N_p at constant PI and SS 74
4.3.2 Varying PI at constant SS and N_p 76
4.3.3 Varying SS at constant PI and N_p 78
4.4 Cross-sections after LSPwC 80
4.4.1 Cross-section of P3-SS0.8-N_p10 80
4.4.2 Cross-section of P3-SS1.5-N_p10 81
4.5 Surface Roughness 83
4.6 Microhardness 85
4.7 Electrochemical Corrosion 88
4.7.1 Open circuit potential (OCP) 88
4.7.2 Potentiodynamic polarisation 89
4.7.3 Corrosion products after potentiodynamic polarisation tests 94
4.7.3.1 Sample 0 94
4.7.3.2 P1-SS0.8-N_p40 95
4.7.3.3 P3-SS0.8-N_p2.5 97
4.7.3.4 P3-SS0.8-N_p5 98
4.7.3.5 P3-SS0.8-N_p10 100
4.7.3.6 P3-SS0.8-N_p20 101
4.7.3.7 P3-SS0.8-N_p40 103

4.7.3.8 P5-SS0.8-N_p40 105
4.7.3.9 P3-SS1.5-N_p2.5 106
4.7.3.10 P3-SS1.5-N_p5 108
4.7.3.11 P3-SS1.5-N_p10 109
4.7.4 Corroded surface morphology after cleaning 112
4.8 Full Immersion Corrosion Tests - Weight loss for Sample 0 and P3-SS1.5-N_p5 117
4.9 Stress Corrosion Cracking (SCC) 125
4.9.1 Sample 0 125
4.9.2 P3-SS0.5-N_p45 127
4.9.3 P3-SS1-N_p50.38 128
4.9.4 P3-SS0.5-N_p67.1 130
4.9.5 P3-SS1.5-N_p21.88 131
CHAPTER 5: DISCUSSION 132
5.1 Effect of LSPwC on surface morphology 132
5.1.1 Surface features when varying coverage (N_p) 132
5.1.2 Surface features when varying power intensity (PI) 133
5.1.3 Surface features when varying spot size (SS) 133
5.1.4 Oxide formation 133
5.2 Effect of LSPwC on surface roughness 133
5.2.1 Effect of varying power intensity on surface roughness 134
5.2.2 Effect of varying coverage on surface roughness 137
5.2.3 Effect of varying spot size (SS) on surface roughness 143
5.3 Effect of LSPwC on microhardness 146
5.4 Potentiodynamic polarisation behaviour after LSPwC 148
5.4.1 Open circuit potential (OCP) 148
5.4.2 Potentiodynamic polarisation curves 148
5.4.3 Effect of LSP parameters on corrosion parameters 149
5.4.3.1 Varying power intensity (PI) 149
5.4.3.2 Varying coverage (N_p) 150
5.4.3.3 Varying spot size 154
5.4.4 Surface analysis after potentiodynamic polarisation 156

5.5 Immersion weight loss tests 156
5.6 Stress corrosion cracking (SCC) 158
5.7 Summary 159
CHAPTER 6: CONCLUSIONS AND RECOMMENDATIONS 161
6.1 Conclusions 161
6.1.1 Effect of LSPwC on surface roughness 161
6.1.2 Effect of LSPwC on hardness 162
6.1.3 Effect of LSPwC on corrosion 162
6.1.3.1 Potentiodynamic polarisation 162
6.1.3.2 Immersion weight loss tests 163
6.1.3.3 Stress corrosion cracking (SCC) 163
6.1.4 Overall Findings 163
6.2 Recommendations For Future Work 164
REFERENCES 165
APPENDICES 176
Appendix 1: AA7075-T651 Data Sheet 176
Appendix 2: Salt concentrations in selected oceans and seas 177
Appendix 3: SCC Sample Holder Specifications 178
Appendix 4: Potentiodynamic Polarisation Curves for the Second Test 179
Appendix 5: Contributions From This Study 182

LIST OF FIGURES

Figure 2.1. Optical micrograph showing the microstructure of AA7075 (Chan et al., 2003). 27
Figure 2.2. Common forms of corrosion (Davis, 2000). 28
Figure 2.3. Mechanism of pitting corrosion in aluminium alloys (Vargel, 2004). 30
Figure 2.4. Polarisation curves: a) An example of a Tafel diagram with theoretical Tafel lines extrapolated (PalmSens, 2023), b) The AA7075 alloy's potentiodynamic polarisation curve in a 3.0 wt% NaCl solution (AlHazaa and Sherif, 2015). 35
Figure 2.5. Schematic diagram of a typical time to failure vs initially applied stress for smooth sample SCC tests (Jones, 2003). 36
Figure 2.6. Schematic diagram of crack propagation rate as a function of crack tip stress-intensity behaviour (Jones, 2003). 37
Figure 2.7. The process of LSP: shock waves cause plastic deformation, inducing a compressive residual stress field on and below the surface (Stiekema, 2021). 39
Figure 2.8. Different LSP techniques: a) LSP with black paint coating and b) LSPwC (Sano et al, 2006). 40
Figure 2.9. Laser shock peening patterns (Correa et al., 2015; Salimianrizi et al., 2016). 42
Figure 2.10. Typical Residual Stress Profile through the thickness and describing its characteristics (Busse, 2017). 43
Figure 2.11. Definitions for surface profile (Tseng et al., 2016). 44
Figure 2.12. Roughness value R_a measurement (Mitutoyo America Corporation, 2016). 44
Figure 2.13. Measurement profile for R_t and R_z (Mitutoyo America Corporation, 2016). 45
Figure 2.14. SEM-SE images of AA6056-T4 surfaces after a) LPwC and b) SP (Glaser et al., 2022). 46
Figure 2.15. Optical micrographs of a cross-section of AZ31B Mg alloy showing grain refinement after different LSP impacts (Zhang et al., 2010). 48
Figure 2.16. Surface morphology of AA7075 specimens' surface after corrosion test: (a) and (b) untreated; and (c) and (d) LSP treated once with 7.17 GW/cm^2 (Wang, 2017). 50
Figure 2.17. Optical images showing SUS304 a) with and b) without peening (Sano et al., 2006). 51
Figure 3.1. Geometry of milled AA7075-T651 samples: a) 14 mm thickness plates and b) 1.6 mm and 10 mm thickness plates. 53
Figure 3.2. Schematic diagram of the experimental LSP configuration (van Staden, 2018). 54
Figure 3.3. Dimensions for a typical AA7075 sample processed by LSPwC with thickness of a) 14 mm and b) 1.6 mm and 10 mm. 55
Figure 3.4. Convention for naming samples processed by LSPwC. 55
Figure 3.5. Photographs showing: a) sample placement, b) EDM cutting and c) segments obtained from the cutting. 57

Figure 3.6. Method for surface roughness measurements: a) Peened area showing directions in which surface roughness profile was taken and b) pattern followed to obtain five measurements in each direction..... 60
Figure 3.7. Vickers hardness measurements: a) micrograph of typical indentation b) minimum recommended spacing for Vickers indentations (ASTM E384, 2022) and b) indentation pattern adopted for the sample cross-section..... 62
Figure 3.8. Corrosion cell a) photograph b) cross-section. 64
Figure 3.9. Sample holder for SCC: a) design specifications, b) schematic diagram of typical test sample under three-point bending and c) photograph of loaded samples..... 68
Figure 4.1. SEM images of the unpeened Sample 0: a) SEM-SE showing topography and b) SEM-BSE showing composition with red arrows indicating particles on the surface. 70
Figure 4.2. a) SEM-BSE image of Sample 0 cross-section showing light precipitates and b) EDX spectrum of the precipitates. 71
Figure 4.3. Optical images showing the microstructure of AA7075-T651 at different orientations: a) top surface in the transverse direction (to original rolling), b) cross-section in the longitudinal direction at lower and c) higher magnification. 72
Figure 4.4. Stereo microscope image of the surface of P3-SS1.5-N_p20 after LSPwC..... 73
Figure 4.5. SEM-BSE image of the surface of P1.5-SS1-N_p11.25 showing the peened-unpeened interface after LSPwC, with some solidified droplets..... 73
Figure 4.6. SEM-SE images of P3-SS0.8-N_p2.5 surface at different magnifications, showing laser spots (dotted red circle and arrows), solidified ablated particles (red arrows) and pores (orange arrows). 74
Figure 4.7. SEM-SE images of P3-SS0.8-N_p20 surface at increasing magnifications a) – d), showing peening paths (red lines), ablated products and few pores. 75
Figure 4.8. SEM-SE images of peened surfaces showing topographic differences at varying PI (GW/cm^2): a) PI=1 b) PI=3 c) PI=5 and constant SS=0.8 mm and N_p=40 spots/mm^2 (white particles in a) and b) are corrosion products)..... 76
Figure 4.9. SEM-BSE images of PI of a) 1.5 b) 3 c) 4.5 d) 6 GW/cm^2 surfaces showing surface irregularities at varying PI. 77
Figure 4.10. SEM-SE images of P3-SS0.8-N_p2.5 surface at: a) lower and b) higher magnification showing pores (red arrows). 78
Figure 4.11. SEM-SE images of P3-SS1.5-N_p2.5 surface at: a) lower and b) higher magnification, showing pores (red arrows). 78
Figure 4.12. SEM-SE micrographs of P3-SS0.8-N_p10 surface at: a) lower and b) higher magnification showing "mounts" and flatter areas from LSPwC. 79
Figure 4.13. SEM-SE micrographs of P3-SS1.5-N_p10 surface at: a) lower and b) higher magnification showing solidified droplets from LSPwC. 79
Figure 4.14. SEM-BSE images of P3-SS0.8-N_p10 cross-section at: a) lower and b) higher magnification, showing depressions (red arrows), pores (blue arrow and circle) and cracks (yellow arrows). 80

Figure 4.15. SEM-BSE image of P3-SS1.5-N_p10 cross-section, showing hollows and mounts from LSPwC..... 82
Figure 4.16. Surface roughness a) R_a (mean vertical deviation) b) R_z (distance between the averages of the five highest peaks and lowest valleys) for unpeened and peened samples in the scanning and stepping directions..... 83
Figure 4.17. Surface roughness a) R_q (square root of the mean of the square of vertical deviation), b) R_t (distance between the highest peak and lowest valley) for unpeened and peened samples in the scanning and stepping directions..... 84
Figure 4.18. Optical microscope image showing Vickers indentation with a) barrelling and b) a combination of barrelling and pin cushioning..... 85
Figure 4.19. Microhardness results of samples at different depths from the peened surface. 86
Figure 4.20. Variation of microhardness with laser power intensity. 86
Figure 4.21. Variation of microhardness with spot coverage (N_p) at PI = 3 GW/cm^2, SS = 0.8 mm. 87
Figure 4.22. Variation of microhardness with spot coverage (N_p) at PI = 3 GW/cm^2, SS = 1.5 mm. 88
Figure 4.23. Variation of OCP measurements with time in 3.5 wt% NaCl. 89
Figure 4.24. Potentiodynamic polarisation curves of a) P1-SS0.8-N_p40 and b) P3-SS0.8-N_p2.5 compared to Sample 0..... 90
Figure 4.25. Potentiodynamic polarisation curves of a) P3-SS0.8-N_p5 and b) P3-SS0.8-N_p10 compared to Sample 0..... 91
Figure 4.26. Potentiodynamic polarisation curves of a) P3-SS0.8-N_p20 and b) P3-SS0.8-N_p40 compared to Sample 0..... 91
Figure 4.27. Potentiodynamic polarisation curves of a) P5-SS0.8-N_p40 and b) P3-SS1.5-N_p2.5 compared to Sample 0..... 91
Figure 4.28. Potentiodynamic polarisation curves of a) P3-SS1.5-N_p5 and b) P3-SS1.5-N_p10 compared to Sample 0..... 92
Figure 4.29. Corrosion rates of specimens after potentiodynamic polarisation tests in 3.5 wt% NaCl. 93
Figure 4.30. SEM-BSE images of Sample 0 surface after potentiodynamic polarisation corrosion test showing corrosion products at: a) lower and b) higher magnification with lighter parts circled. 94
Figure 4.31. SEM-BSE images of P1-SS0.8-N_p40 surface after potentiodynamic polarisation corrosion showing corrosion products at: a) lower and b) higher magnification. 96
Figure 4.32. SEM-BSE images of P3-SS0.8-N_p2.5 surface after potentiodynamic polarisation corrosion showing corrosion products at: a) lower and b) higher magnification. 97
Figure 4.33. SEM-BSE images of P3-SS0.8-N_p5 surface after potentiodynamic polarisation corrosion showing corrosion products at: a) lower and b) higher magnification. 99
Figure 4.34. SEM-BSE images of P3-SS0.8-N_p10 surface after potentiodynamic polarisation corrosion showing corrosion products at: a) lower and b) higher magnification. 100

Figure 4.35. SEM-BSE images of P3-SS0.8-N_p20 surface after potentiodynamic polarisation corrosion showing corrosion products at: a) lower and b) higher magnification. 102
Figure 4.36. SEM-BSE images of P3-SS0.8-N_p40 surface after potentiodynamic polarisation corrosion showing corrosion products at: a) lower and b) higher magnification. 104
Figure 4.37. SEM-BSE images of P5-SS0.8-N_p40 surface after potentiodynamic polarisation corrosion at: a) lower and b) higher magnification showing corrosion products and light contrast feature (circled). 105
Figure 4.38. SEM-BSE images of P3-SS1.5-N_p2.5 surface after potentiodynamic polarisation corrosion showing corrosion products at: a) lower and b) higher magnification. 107
Figure 4.39. SEM-BSE images of P3-SS1.5-N_p5 surface after potentiodynamic polarisation corrosion test showing corrosion products at: a) lower and b) higher magnification..... 108
Figure 4.40. SEM-BSE images of P3-SS1.5-N_p10 surface after potentiodynamic polarisation corrosion at: a) lower and b) higher magnification showing corrosion products, including lighter particles (circles). 110
Figure 4.41. SEM-SE images of Sample 0 surface after potentiodynamic polarisation corrosion at: a) lower and b) higher magnification showing pits and cracks. 112
Figure 4.42. SEM-BSE images of P1-SS0.8-N_p40 surface after potentiodynamic polarisation corrosion at: a) lower and b) higher magnification showing pits, larger hole (orange arrow), cracks (red arrows) and lighter particles. 113
Figure 4.43. SEM-SE images of P3-SS0.8-N_p2.5 surface after potentiodynamic polarisation corrosion at: a) lower magnification showing pits and light features and b) higher magnification showing square pits..... 113
Figure 4.44. SEM-SE images of P3-SS0.8-N_p5 surface after potentiodynamic polarisation corrosion at: a) lower and b) higher magnification showing some square pits. 114
Figure 4.45. SEM-SE images of P3-SS0.8-N_p10 surface after potentiodynamic polarisation corrosion at: a) lower and b) higher magnification showing pits. 114
Figure 4.46. SEM-SE images of P3-SS0.8-N_p20 surface after potentiodynamic polarisation corrosion at: a) lower and b) higher magnification showing many square pits. 115
Figure 4.47. SEM-SE images of P3-SS0.8-N_p40 surface after potentiodynamic polarisation corrosion at: a) lower and b) higher magnification showing square pits and light particles.... 115
Figure 4.48. SEM-SE images of P5-SS0.8-N_p40 surface after potentiodynamic polarisation corrosion test at: a) lower and b) higher magnification showing irregular pits. 116
Figure 4.49. SEM-SE images of P3-SS1.5-N_p2.5 surface after potentiodynamic polarisation corrosion test at: a) lower and b) higher magnification showing few pits and unaffected area with light particles. 116
Figure 4.50. SEM-BSE images of P3-SS1.5-N_p5 surface after potentiodynamic polarisation corrosion test at: a) lower and b) higher magnification showing few pits. 117
Figure 4.51. SEM-SE images of P3-SS1.5-N_p10 surface after potentiodynamic polarisation corrosion test at: a) lower and b) higher magnification showing many square pits. 117

Figure 4.52. SEM-BSE images of Sample 0 surface after 30-day immersion at: a) lower and b) higher magnification, showing areas with less corrosion product (red ovals) and cracks on the corrosion product (red arrows). *118*
Figure 4.53. SEM-BSE images of the corroded surface of P3-SS1.5-N_p5 after 30-day immersion at: a) lower and b) higher magnification, showing corrosion products and light particles. *119*
Figure 4.54. Variation of weight loss as a function of immersion time for Sample 0 and P3-SS1.5-N_p5 immersed in 3.5 wt% NaCl solution (standard deviations for the LSPwC samples were too small to show). *120*
Figure 4.55. Variation of the corrosion rate as a function of immersion time for Sample 0 and P3-SS1.5-N_p5 immersed in 3.5 wt% NaCl solution. *120*
Figure 4.56. SEM-BSE images of Sample 0 surface after 3-day immersion at: (a) lower and (b) higher magnification showing corrosion pits (red arrows) and rolling lines. *121*
Figure 4.57. SEM-BSE images of P3-SS1.5-N_p5 surface at: (a) lower and (b) higher magnification showing corrosion pits (red arrows) after 3-day immersion. *121*
Figure 4.58. SEM-BSE images of Sample 0 surface at: (a) lower and (b) higher magnification showing hemispherical corrosion pits with white particles after 7-day immersion. *122*
Figure 4.59. SEM-BSE images of P3-SS1.5-N_p5 surface at: (a) lower and (b) higher magnification showing hemispherical corrosion pits with white particles after 7-day immersion. *122*
Figure 4.60. SEM-BSE images of Sample 0 surface at: (a) lower and (b) higher magnification showing hemispherical corrosion pits merging after 14-day immersion. *123*
Figure 4.61. SEM-BSE images of P3-SS1.5-N_p5 surface at: (a) lower and (b) higher magnification showing hemispherical corrosion pits merging after 14-day immersion. *123*
Figure 4.62. SEM-BSE images of P3-SS1.5-N_p5 surface at: (a) lower and (b) higher magnification showing hemispherical corrosion pits after 21-day immersion. *124*
Figure 4.63. SEM-BSE images of Sample 0 surface at: (a) lower and (b) higher magnification showing corrosion pits after 30-day immersion. *124*
Figure 4.64. SEM-BSE images of P3-SS1.5-N_p5 surface at: (a) lower and (b) higher magnification showing hemispherical corrosion pits after 30-day immersion. *125*
Figure 4.65. SEM-BSE images of Sample 0 after 40 days of SCC, showing surface cracks indicated by red arrows, pits circled in red and corrosion products inside the crack (orange arrows). ... *126*
Figure 4.66. SEM-BSE image of a cross-section of Sample 0 showing cracks after SCC. *127*
Figure 4.67. SEM-BSE images of P3-SS0.5-N_p45 surface after 40 days of SCC, at: a) lower and b) higher magnifications, showing arrows pointing to cracks and crack clusters circled in red. *127*
Figure 4.68. SEM-BSE image of a cross-section of P3-SS0.5-N_p45 showing the depth of the major crack caused by SCC and orange arrows indicating the shallow one. *128*
Figure 4.69. SEM-BSE images of P3-SS1-N_p50.38 surface after SCC, at: a) lower and b) higher magnification, showing major cracks (red arrows), minor cracks circled in red, corrosion product (orange arrow) and pits (blue arrows). *129*
Figure 4.70. SEM-BSE image of a cross-section of P3-SS1-N_p50.38 showing shallow pits (red arrows) and horizontal cracks (orange arrows). *129*

Figure 4.71. SEM-BSE images of P3-SS0.5-N_p67.1 surface after 40 days of SCC at: a) lower and b) higher magnifications, showing major (red arrows) and minor cracks (orange arrows). 130
Figure 4.72. SEM-BSE image of a cross-section of P3-SS0.5-N_p67.1 after SCC showing pits indicated by red arrows and a crack (orange arrow)..... 130
Figure 4.73. SEM-BSE images of P3-SS1.5-N_p21.88 surface after 40 days of SCC at: a) lower and b) higher magnifications showing red arrows pointing to the major crack. 131
Figure 4.74. SEM-BSE image of a cross-section of P3-SS1.5-N_p21.88 showing the depth of cracks caused by SCC with orange arrows pointing to pits. 131
Figure 5.1. Relationship of power intensity (PI) and surface roughness: a) R_a (mean vertical deviation), b) R_q (square root of the mean of the square of vertical deviation). 135
Figure 5.2. Relationship of power intensity (PI) and surface roughness: a) R_z (distance between the averages of the five highest peaks and lowest valleys), b) R_t (distance between the highest peak and lowest valley). 136
Figure 5.3. Comparison of surface roughness metrics at varying power intensity. 137
Figure 5.4. Surface roughness: a) R_a (mean vertical deviation), b) R_z (distance between the averages of the five highest peaks and lowest valleys relationship with coverage at PI = 3 GW/cm^2, SS = 0.8 mm. 138
Figure 5.5. Surface roughness: a) R_q (square root of the mean of the square of vertical deviation), b) R_t (distance between the highest peak and lowest valley) relationship with coverage at PI = 3 GW/cm^2, SS = 0.8 mm. 139
Figure 5.6. Surface roughness: a) R_a (mean vertical deviation), b) R_z (distance between the averages of the five highest peaks and lowest valleys) relationship with coverage at PI = 3 GW/cm^2, SS = 1.5 mm. 140
Figure 5.7. Surface roughness: a) R_q (square root of the mean of the square of vertical deviation), b) R_t (distance between the highest peak and lowest valley) relationship with coverage at PI = 3 GW/cm^2, SS = 1.5 mm. 141
Figure 5.8. Comparison of surface roughness metrics varying coverage at PI = 3 GW/cm^2, SS = 0.8 mm. 142
Figure 5.9. Comparison of surface roughness metrics varying coverage at PI = 3 GW/cm^2, SS = 1.5 mm. 142
Figure 5.10. Comparison of surface roughness metrics at SS = 0.8 mm & SS = 1.5 mm..... 143
Figure 5.11. Surface roughness: a) R_a (mean vertical deviation), b) R_q (square root of the mean of the square of vertical deviation) comparison at SS = 0.8 mm & SS = 1.5 mm. 144
Figure 5.12. Surface roughness: a) R_z (distance between the averages of the five highest peaks and lowest valleys), b) R_t (distance between the highest peak and lowest valley) comparison at SS = 0.8 mm & SS = 1.5 mm. 145
Figure 5.13. Relationship of the peak hardness for: a) N_p at constant P3-SS0.8 (blue), P3-SS1.5 (orange) and b) PI at constant SS0.8-N_p40 with Sample 0 in red. 147
Figure 5.14. Relationships between laser power intensity for: OCP and E_{corr}. 149
Figure 5.15. Relationships between laser power intensity for: a) i_{corr} and b) corrosion rate.... 150

Figure 5.16. Relationship of spot coverage with: a) E_{corr}, OCP and b) i_{corr} at PI = 3 GW/cm^2, SS = 0.8 mm. 151
Figure 5.17. Relationship of spot coverage with corrosion rate at PI = 3 GW/cm^2, SS = 0.8 mm. 152
Figure 5.18. Relationship of spot coverage with E_{corr} and OCP at PI = 3 GW/cm^2, SS = 0.8 mm. 152
Figure 5.19. Relationship of spot coverage with: a) i_{corr} and b) corrosion rate at PI = 3 GW/cm^2, SS = 0.8 mm. 153
Figure 5.20. Effect of varying spot size on: a) E_{corr}, b) OCP. 154
Figure 5.21. Effect of varying spot size on: a) i_{corr}, b) corrosion rate. 155
Figure 5.22. Difference of: a) weight loss and b) corrosion rate between Sample 0 and P3-SS1.5-N_p5 over time immersed in NaCl. 157
Figure 5.23. Maximum crack depth of specimens after SCC tests. 159
Figure A4.0.1. Potentiodynamic polarisation curves of a) Sample 0 and b) P1-SS0.8-N_p40 after duplicate tests. 179
Figure A4.0.2. Potentiodynamic polarisation curves of a) P3-SS0.8-N_p2.5 and b) P3-SS0.8-N_p5 after duplicate tests. 179
Figure A4.0.3. Potentiodynamic polarisation curves of a) P3-SS0.8-N_p10 and b) P3-SS0.8-N_p20 after duplicate tests. 180
Figure A4.0.4. Potentiodynamic polarisation curves of a) P3-SS0.8-N_p40 and b) P5-SS0.8-N_p40 after duplicate tests. 180
Figure A4.0.5. Potentiodynamic polarisation curves of a) P3-SS1.5-N_p2.5 and b) P3-SS1.5-N_p5 after duplicate tests. 181
Figure A4.0.6. Potentiodynamic polarisation curves of a) P3-SS1.5-N_p10 after duplicate tests. 181

LIST OF TABLES

Table 2.1. Alloy designation according to IADS and the associated applications (*Ghali, 2010; Polmear et al., 2017).* 23
Table 2.2. IADS Aluminium alloy temper designation (Ghali, 2010; Polmear et al., 2017)...... 24
Table 2.3. Chemical composition of AA7075 (wt%) (The Aluminium Association, 2018)...... 26
Table 2.4. Material properties of AA7075-T651 (ASM Aerospace Specification Metals INC, 2023) 26
Table 2.5. Aircraft failures that occurred due to pitting corrosion (Hoeppner et al., 2000). 31
Table 2.6. Surface roughness (R_a) in μm of Shot Peening and Laser Shock Peening (Becker, 2017). 46
Table 3.1. Sample information: 14x14 mm LSPwC area...... 56
Table 3.2. Variables of the SRT-6210 surface roughness tester...... 60
Table 3.3. Samples used for SCC testing. 67
Table 4.1. EDX results of the unpeened Sample 0. 70
Table 4.2. EDX results of P3-SS0.8-N_p10...... 81
Table 4.3. EDX results of P3-SS1.5-N_p10 cross-section...... 82
Table 4.4. Corrosion parameters were obtained for each pair of samples. 93
Table 4.5. EDX results of corrosion products on Sample 0...... 95
Table 4.6. EDX results of corrosion products on P1-SS0.8-N_p40. 96
Table 4.7. EDX results of corrosion products on P3-SS0.8-N_p2.5. 98
Table 4.8. EDX results of corrosion products on P3-SS0.8-N_p5. 99
Table 4.9 EDX results of corrosion products on P3-SS0.8-N_p10. 101
Table 4.10. EDX results of corrosion products on P3-SS0.8-N_p20. 103
Table 4.11. EDX results of corrosion products on P3-SS0.8-N_p40. 104
Table 4.12. EDX results of corrosion products on P5-SS0.8-N_p40. 106
Table 4.13. EDX results of corrosion products on P3-SS1.5-N_p2.5. 107
Table 4.14. EDX results of corrosion products on P3-SS1.5-N_p5. 109
Table 4.15. EDX results of corrosion products on P3-SS1.5-N_p10. 111
Table 4.16. EDX results of corroded Sample 0 after 30 days in 3.5 wt% NaCl solution...... 118
Table 4.17. EDX results of corroded P3-SS1.5-N_p5 after 30 days in 3.5 wt% NaCl solution.... 119
Table A2.1. Salt concentrations in selected oceans and seas (Arriscorreta and Hoeppner, 2012). 177

NOMENCLATURE

ALC	African Laser Centre
ASM	American Society for Metals
ASTM	American Society for Testing and Materials
BSE	Back-scattered electron
CNC	Computerised Numerical Control
CSIR	Council for Scientific and Industrial Research
E_{corr}	Corrosion Potential
EDM	Electrical Discharge Machining
EDX	Electron Dispersive X-ray spectroscopy
gf	Gram-force
HV	Vickers Hardness (numerical suffix indicates kgf)
i_{corr}	Corrosion Current
kgf	Kilogram-force
LSP	Laser Shock Peening
LSPwC	Laser Shock Peening without Coating
Nd: YAG	Neodymium-doped Yttrium Aluminium Garnet
NLC	National Laser Centre
N_p	Pulse Density/coverage
OCP	Open Circuit Potential
PI	Power Intensity (or Density)

NOMENCLATURE

R_a	Surface Roughness- *mean vertical deviation*
R_q	Surface Roughness- *square root of the mean of the square of vertical deviation*
R_t	Surface Roughness- *distance between the highest peak and lowest valley*
R_z	Surface Roughness- *distance between the averages of the five highest peaks and lowest valleys*
SE	Secondary electron
SEM	Scanning Electron Microscopy
SS	Spot Size

CHAPTER 1: INTRODUCTION

1.1 Background

The manufacturing industry is constantly facing challenges related to the quality of the final products and ways to improve their resistance to failure. In all sectors that use metal components, the components will eventually need to be replaced because of material deterioration from fatigue, corrosion or wear (Davis, 2000). The effects of corrosion are both direct because they affect the useful service life of the material and indirect, in that manufacturers incur corrosion costs, which they pass on to consumers (Davis, 2000). Demand has increased to reduce life cycle costs and improve safety by extending material components' fatigue life (Adachi *et al.*, 2008). Technologies that increase resistance to these degradation processes are beneficial to the industry for extending the service life and reducing maintenance costs (Hombergsmeier *et al*., 2014).

An emerging surface treatment technology is Laser Shock Peening (LSP), which can be used as an alternative to conventional Shot Peening (SP) to introduce residual compressive stresses to a metallic structure (Rankin *et al.*, 2003; Sano *et al.*, 2006; Adachi *et al.*, 2008). This aims to improve the fatigue performance of metallic components (Ding and Ye, 2006). This research was aimed at the application of Laser Shock Peening without Coating (LSPwC) to aluminium alloy 7075-T651, which contains zinc as the primary alloying element. The 7xxx series is widely used in transportation applications such as aerospace, aviation, marine and automobile because of their good mechanical properties, low density and high strength-to-weight ratios (Imran and Khan, 2019). The high strength makes these alloys valuable in high-stress situations so that highly stressed parts, such as gears, fuselage and the upper outer wing panels are often made from AA7075 (Starke and Staley, 1996; Pedersen, *et al.*, 2011; Pantelakis and Tserpes, 2020; Khalid *et al.*, 2023). The copper content of 1.2-2.0 wt% (The Aluminium Association, 2018) in AA7075 unfortunately increases its susceptibility to corrosion (Singleton, 2003), so it is essential to develop and utilise superior surface treatment methods to counteract this.

LSP is used in many current aerospace, automotive, power generation, marine and biomedical applications (Wu *et al*., 2020). However, despite the great potential that LSP technology may offer, there are still few LSP commercial service providers globally. Therefore, it is essential to invest further in research and process development to expand the knowledge to make the process more understandable.

1.2 Problem Statement

All industries use metal components which can inevitably require replacement due to fatigue, corrosion or wear. LSP is a novel surface enhancement technology used to improve the fatigue performance of metal components. Despite the great potential that LSP technology offers, there is limited knowledge of its applicability for corrosion control in aluminium alloys. Thus, it is essential to investigate LSPwC to determine whether it can improve the corrosion resistance of aluminium alloys, specifically AA7075-T651, or at least not reduce the corrosion resistance.

1.3 Research Objectives

1.3.1 Aim

To investigate the corrosion behaviour of Aluminium Alloy 7075-T651 that has been processed by Laser Shock Peening without Coating.

1.3.2 Objectives

- To analyse surface modifications induced on AA7075-T651 by LSPwC.
- To assess the resistance of LSPwC-treated components to corrosion.

1.4 Dissertation Outline

This chapter introduces the project. Chapter Two contains the literature review on aluminium alloy 7075, LSP and corrosion. Chapter Three contains the experimental procedure. Chapter Four gives the results and analyses. Chapter Five discusses and compares the findings and Chapter Six gives the conclusions and recommendations for future work.

CHAPTER 2: LITERATURE REVIEW

2.1 Introduction

This chapter aims to lay the theoretical foundation for the fundamental aspects of this project. The microstructural characteristics of materials have a crucial effect on their susceptibility to corrosion. Thus, a comprehensive study of the 7xxx series of aluminium alloys used in this study is important. This includes understanding the base material behaviour to evaluate modifications resulting from LSP. The LSP technology is described to understand how it works and its effects on aluminium alloys.

2.2 Aluminium Alloys

Aluminium alloys are classified according to their mode of manufacture and can be separated into wrought or cast alloys (Vargel, 2004; Ghali, 2010; Polmear *et al.*, 2017). Cast aluminium alloys have been melted, poured into a mould and allowed to cool. In contrast, wrought aluminium alloys are heated and then worked to shape them (Vargel, 2004; Ghali, 2010; Polmear *et al.*, 2017;). About 75–80% of aluminium alloys are used as wrought products (Polmear *et al.*, 2017). The scope of this MSc project is limited to wrought alloys, which can be either strain- or age-hardened.

i. Strain-hardened alloys are also known as non-heat treatable alloys. All metals can be strain-hardened to some degree, although this term is reserved for alloys in the 1xxx, 3xxx, 5xxx and 8xxx series which cannot be age-hardened (Vargel, 2004). The processing method involves a sequence of hot-forming and cold-forming steps with intermediate or final annealing (Vargel, 2004).
ii. Age-hardened alloys, also known as heat treatable alloys, belong to the 2xxx, 6xxx and 7xxx series and can achieve maximum mechanical properties through a three-step process (Vargel, 2004; Ghali, 2010). In the first step, the alloy is heated to a high temperature (which varies depending on the specific alloy) to dissolve the alloying element(s) in the aluminium solid solution (Vargel, 2004). The second step is rapid cooling to maintain the alloying elements in the supersaturated solid solution of the aluminium matrix (Vargel, 2004). Finally, the alloy undergoes natural ageing at ~20°C, or artificial ageing at elevated temperatures (100-200°C), leading to the formation of

hardening precipitates from the supersaturated solid solution (Vargel, 2004; Ghali, 2010). The nature, size and volume fractions of these precipitates determine the resulting mechanical properties (Vargel, 2004).

2.2.1 Designation of alloys and tempers

There are several alloys within the wrought category which necessitates precise designation for identification of each alloy by their composition, manufacturing method and properties. The International Alloy Designation System (IADS) for wrought products gives each alloy a four-digit number of which the first digit is assigned based on the significant alloying elements (Polmear *et al*., 2017; The Aluminium Association, 2018). The third and fourth digits are significant in the 1xxx series where they denote the minimum purity of the aluminium. In other series, the third and fourth digits serve only to identify the different aluminium alloys in the series (Polmear *et al*., 2017). The details of each alloy series are listed in Table 2.1.

Table 2.1. Alloy designation according to IADS and the associated applications (*Ghali, 2010; Polmear et al., 2017).*

Aluminium Alloy Series	**Major Alloying Element**	**Application**
1xxx	Unalloyed aluminium (> 99%)	Electrical and chemical industries
2xxx	Copper	Aircraft industry
3xxx	Manganese	Architectural applications
4xxx	Silicon	Welding rods and brazing sheet
5xxx	Magnesium	Boat hulls, gangplanks and other products are exposed to marine environments
6xxx	Magnesium and silicon	Architectural extrusions
7xxx	Zinc and magnesium	Aircraft structural components and other high-strength applications
8xxx	Miscellaneous alloys not covered by other groups	Aerospace and electrical industry

The nomenclature is applied differently to heat- and non-heat treated alloys. Heat-treatable alloy tempers are denoted by the letter O or T, followed by numbers that match the heat treatment method used to make the alloy. This is listed in Table 2.2.

Table 2.2. IADS Aluminium alloy temper designation (Ghali, 2010; Polmear et al., 2017).

Suffix letter	**Condition**
F	As fabricated, no thermal treatments or strain-hardening methods are used to shape the product
O	Annealed, wrought alloys are annealed to obtain the softest temper and cast alloys are annealed to improve ductility and dimensional stability
H	Cold-worked (strain-hardened) to increase strength
T	Heat treatment applies to products that have increased strength because of thermal treatments, with or without supplementary strain-hardening

2.2.2 The 7xxx series

In the 7xxx series aluminium alloys, T6 heat treatment ensures superior strength and hardness (Kalyon and Özyürek, 2017). They can be divided into alloys with or without copper. The highest mechanical strength aluminium alloys in the T6 temper are created by adding copper to the Al-Zn-Mg system. (ASM International, 1990). The process of duplex ageing, specifically tempers T73 and T76, can generate products that possess the ability to withstand corrosion in aggressive environments (Vargel, 2004). Such products exhibit resistance to stress corrosion in the short-transverse direction. However, the duplex ageing process results in a reduction of approximately 20% in mechanical strength (Vargel, 2004). These alloys are available in various forms (sheet, plate, extruded sections) and are used extensively in the aerospace industry (ASM International, 1990).

High resistance to general corrosion is common in heat treatable alloys from the 7xxx series that do not contain copper. Compared to the 2xxx series alloys, the 7xxx series alloys have greater resistance to general corrosion (ASM International, 1990; Vargel, 2004; Ghali, 2010). However, they are susceptible to pitting, stress corrosion cracking and exfoliation corrosion, as explained in Section 2.3. High copper containing 7xxx series alloys can be aged at higher ageing temperatures without excessive loss of strength (Ghali, 2010). The properties of 7xxx

series alloys, including their resistance to fatigue and corrosion, are determined by the microstructure that results from the manufacturing process (Rometsch *et al.*, 2014). Since these alloys are precipitation-hardened, careful attention to the manufacturing steps is crucial to ensure desirable microstructural characteristics and optimal performance (Rometsch *et al.*, 2014).

2.2.3 Aluminium Alloy 7075-T651

The code AA7075-T651 refers to an aluminium alloy (7075) that has undergone solution heat treatment and artificial ageing (Ghali, 2010; Polmear *et al*., 2017). The temper condition is specified by the "651" following the "-T." This means that the aluminium alloy has undergone a solution heat treatment (T6 temper) and then has been artificially aged (T-51 temper). The "51" in T651 means that the aging has been conducted at a lower temperature than the standard T6 temper (Ghali, 2010). This is done to improve stress corrosion cracking resistance while maintaining a high level of strength.

In the aerospace industry, the high-strength aluminium alloy AA7075 is frequently utilised for structural components. (ASM International, 1990; Kaylon and Özyürek, 2017; Polmear *et al.*, 2017). Its high strength-to-weight ratio is obtained by precipitation hardening. The alloying elements and impurities interact to produce the intermetallic strengthening precipitates. (Aliyah and Anawati, 2019). This alloy is composed of alloying elements Zn, Mg and Cu. The Cu- and Fe-rich phases of the alloy, such as Al_7Cu_2Fe and $(Al,Cu)_6(Fe,Cu)$, are the primary precipitates and their sizes range between 1–20 µm. The $MgZn_2$ phase, which emerges as tiny particles a few nanometres across the nanograin boundaries, is the alloy's strengthening precipitate. (Aliyah and Anawati, 2019). The other precipitates, such as Al_2CuMg and Mg_2Si, are present in small quantities. (Aliyah and Anawati, 2019). The recommended chemical composition for AA7075 is given in Table 2.3 and the material properties of the alloy are shown in Table 2.4.

Table 2.3. Chemical composition of AA7075 (wt%) (The Aluminium Association, 2018).

Reference	**Si**	**Fe**	**Cu**	**Mn**	**Mg**	**Zn**	**Ti**	**Cr**	**Other**	**Al**
Aluminium Association	Max. 0.4	Max. 0.5	1.2 - 2	Max. 0.3	2.1 - 2.9	5.1 - 6.1	Max. 0.2	0.18 - 0.28	Max. 0.15	Balance
NK cutting	0.08	0.27	1.5	0.06	2.4	5.7	0.05	0.22	0.15	Balance

Table 2.4. Material properties of AA7075-T651 (ASM Aerospace Specification Metals INC, 2023)

Material Property	**Value**
Modulus of Elasticity	71.7 GPa
Vicker's Hardness	175 HV
Tensile Yield Strength	503 MPa
Bulk Poisson's Ratio	0.33
Elongation at Break	11 %

The microstructure of AA7075 (Figure 2.1) (Chan *et al*., 2003)), has a deformed, fibrous grain structure due to rolling deformation, with coarse recrystallised grains. These recrystallised grains have irregular, elongated shapes and are flattened in the rolling direction (Pedersen *et al.*, 2011; Jin *et al.*, 2015). During homogenisation, dispersoids (small, finely distributed particles within a material matrix) develop in the alloy, inhibiting recrystallisation and are evenly distributed throughout the grains. Additionally, a high density of the hardening phase is found in the interior of the grain, as well as with grain boundary precipitates (Pedersen *et al.*, 2011; Jin *et al.*, 2015). Precipitation-free zones, which are softer than the matrix and more prone to strain localisation during deformation, form close to the grain and sub-grain borders. (Gao *et al.*, 1998; Pedersen *et al.*, 2011; Kalyon and Özyürek, 2017; Aliyah and Anawati, 2019).

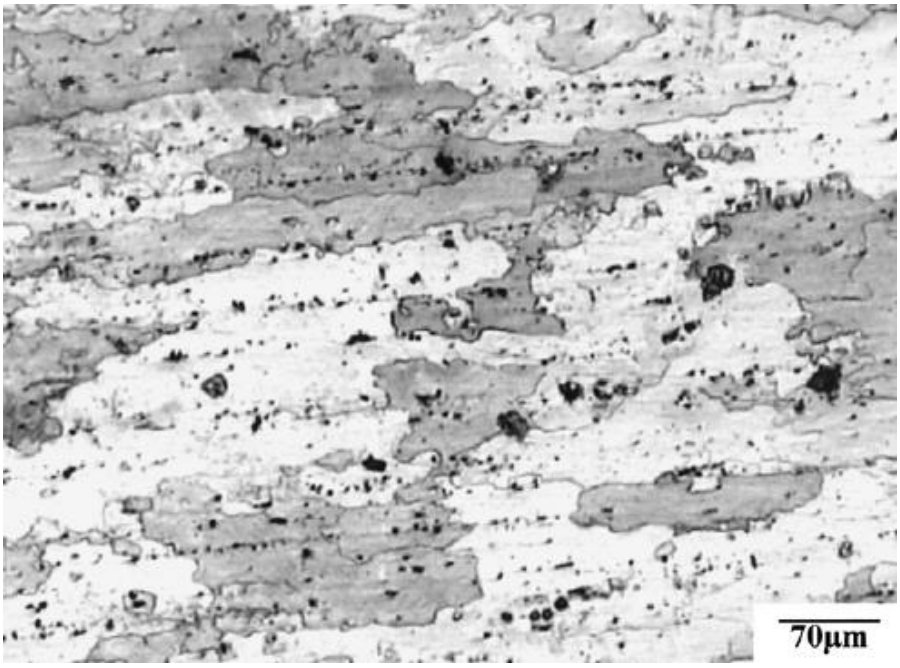


Figure 2.1. Optical micrograph showing the microstructure of AA7075 (Chan et al., 2003).

2.3 Corrosion

Corrosion is the deterioration of metal by chemical or electrochemical reaction(s) with the environment (Fontana, 1986; Davis, 2000; Callister, 2007). Corrosion occurs in several forms and classification can be based on the following (Davis, 2000; Callister, 2007):

- *Nature of the corrodent*: depending on the presence of moisture, corrosion can be categorised as wet or dry.
- *Mechanism of corrosion*: Chemical or electrochemical reactions are involved and thus differentiate the forms of corrosion.
- *Corroded metal's appearance*: Corrosion can be localised, affecting only a small region, or uniform, affecting the metal throughout its surface at the same rate.

According to Davis (2000), the morphology of attack differentiates the various forms of corrosion and failure analysis is carried out by using one's own eyes to visually observe or at higher magnification. Figure 2.2 shows some common forms of corrosion and their visual differences.

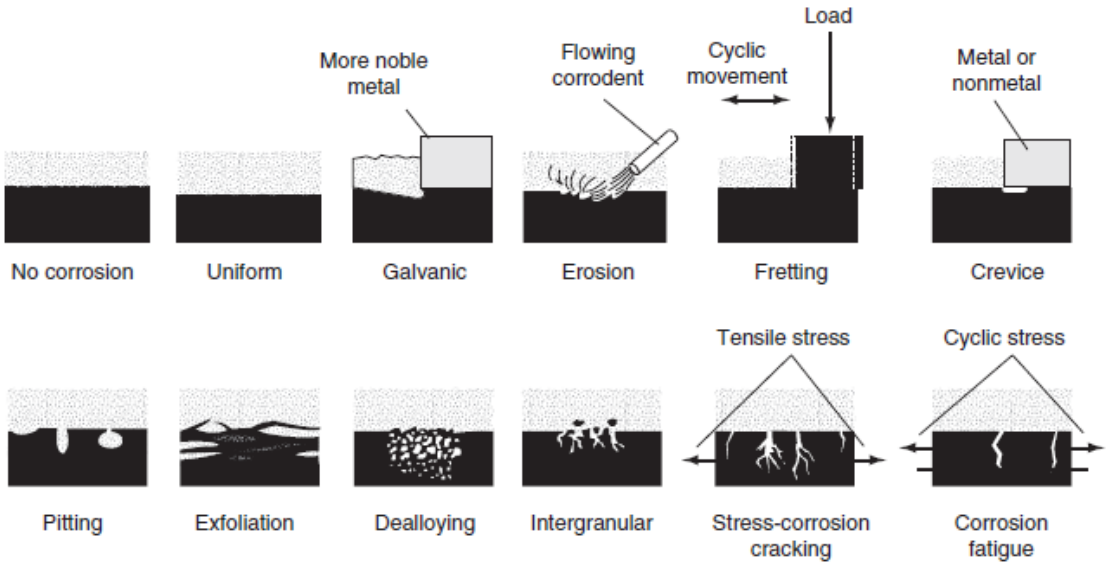


Figure 2.2. Common forms of corrosion (Davis, 2000).

A further distinction can be made between macroscopic and microscopic localised corrosion (Davis, 2000). In the latter case, observation can only be achieved at higher magnification as the metal damage is insignificant. A significant amount of damage can occur before the attack is visibly noted. Macroscopic forms of corrosion which affect greater areas can be seen with the aid of a low-power magnifying lens or the naked eye (Davis, 2000).

2.3.1 Corrosion of aluminium alloys

Aluminium alloys are very reactive and form an oxide film (alumina) when exposed to the atmosphere. This film prevents further oxidation thus protecting the surface and quickly regenerates if damaged (ASM International, 2005). While stable in pH 4.5-8.5 aqueous solutions, the oxide layer dissolves in strong acids/alkalis, leading to corrosion. The initial thin oxide film thickens over time, influenced by temperature and humidity (Fontana, 1986). In aqueous solutions, aluminium hydroxide transforms into hydrated aluminium oxide, offering less protection than the air-formed film.

Alloys in the T6 temper condition exhibit heightened susceptibility to pitting, stress corrosion cracking and exfoliation (Birbilis and Hinton, 2011). The susceptibility of the material to corrosion is closely linked to the type, amount and arrangement of intermetallic compounds. These particles have different reactivities than the matrix, which can cause galvanic coupling.

The main intermetallic compounds in AA7075-T6 are Al_7Cu_2Fe and $(Al,Cu)_6(Fe,Cu)$ (Gao *et al.*, 1998; Andreatta *et al.*, 2004), which are electrochemically less active than the matrix and can lead to the dissolution of surrounding areas. Strengthening particles primarily comprise $MgZn_2$ and are electrochemically more active than the matrix, thus contributing to the intergranular corrosion of AA7075-T6 (Gao *et al.*, 1998; Andreatta *et al.*, 2004).

2.3.1.1 Pitting corrosion

Precipitates of alloying elements in 7xxx aluminium alloys initiate pitting, with severity influenced by copper content (ASM International, 2005; Birbilis and Hinton, 2011). Alloys containing lower copper exhibit reduced susceptibility to pitting corrosion. The protective oxide film (alumina) inhibits corrosion by resisting dissolution and acting as a good insulator. Pitting in aluminium occurs in the passive range and manifests as random pits (ASM International, 2005; Birbilis and Hinton, 2011). The breakdown of the oxide layer releases electrons from the exposed metal with ease, and the reaction creates small pits with localised chemistry that facilitate a swift attack. (ASM International, 2005; Birbilis and Hinton, 2011). This attack results in pit propagation (Figure 2.3) beyond the cavity where water (Equation 2.1) and H^+ (Equation 2.2) reduction occurs (Vargel, 2004; Ghali, 2010), locally producing an alkaline pH (basic environment).

$$\frac{2}{3}O_2 + 3H_2O + 6e^- \rightarrow 6OH^- \qquad \textit{Equation 2.1}$$

$$6H^+ + 6e^- \rightarrow 6OH^- \qquad \textit{Equation 2.2}$$

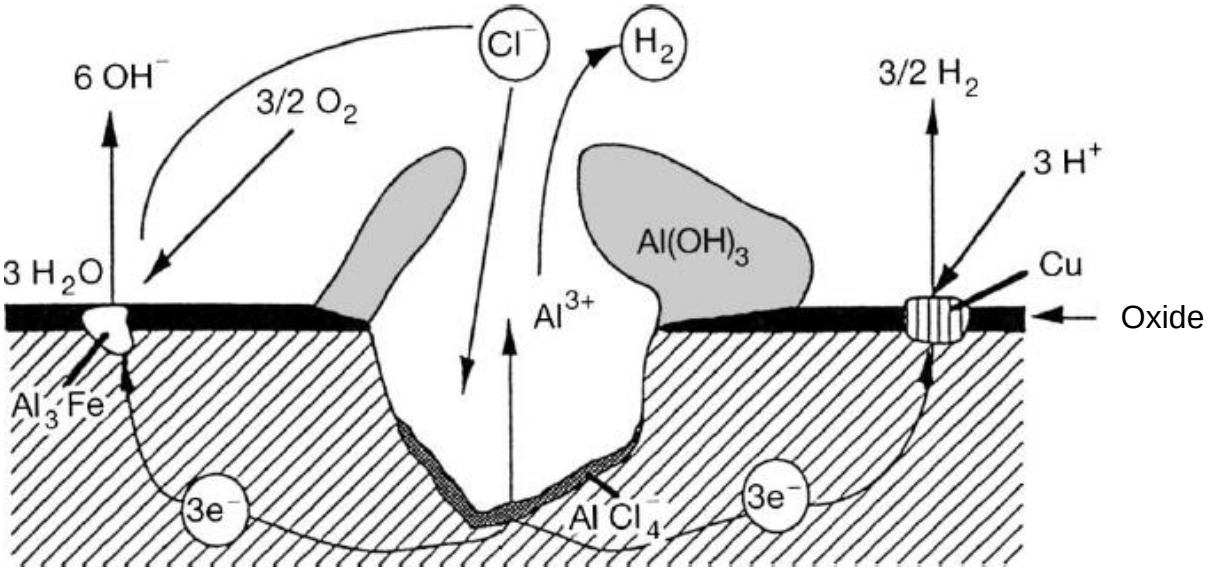


Figure 2.3. Mechanism of pitting corrosion in aluminium alloys (Vargel, 2004).

At the pit's bottom, aluminium oxidation occurs (Equation 2.3) (Vargel, 2004) creating an electrical field that causes Cl^- ions to be shifted towards the pit bottom forming aluminium chlorides.

$$Al \rightarrow Al^{3+} + 3e^- \qquad \textit{Equation 2.3}$$

The aluminium chlorides then suffer hydrolysis (Equation 2.4) (Vargel, 2004) forming aluminium hydroxides ($Al(OH)_3$) plus an excess of H^+ and Cl^- ions.

$$Al_{(s)} + 3OH^- \rightarrow Al(OH)_3 + 3e^- \qquad \textit{Equation 2.4}$$

As a result, the pit's bottom becomes more acidic, causing pit propagation. Since pitting is an autocatalytic process, once it starts, it modifies the surrounding environment to boost further pit growth. The $Al(OH)_3$ precipitates as white deposits. The potential in a given solution above which pits will originate and spread, and below which they may form, is known as the pitting potential (Ghali, 2010). It is commonly referred to as the oxide film's breakdown potential. This type of corrosion will occur in the pH range where the metal is passive. The corrosive attack becomes more uniform if the acidity or alkalinity rises above the passive range (Vargel, 2004; Ghali, 2010). Pitting corrosion is a major problem affecting the structural integrity of aircraft. Examples of degradation originating from pitting corrosion are listed in Table 2.5 (Hoeppner *et al.*, 2000).

Table 2.5. Aircraft failures that occurred due to pitting corrosion (Hoeppner et al., 2000).

Aircraft	**Location of failure**	**Severity**	**Place**	**Year**
Bell Helicopter	Fuselage, longeron	Serious	AR, USA	1997
DC-6	Engine, master connecting rod	Fatal	AK, USA	1996
Piper PA-23	Engine, Cylinder	Fatal	AL, USA	1996
Boeing 75	Rubber control	Substantial damage to the plane	WI, USA	1996
Embraer 120	Propeller Blade	Fatal and serious, loss of plane	GA, USA	1995
Gulfstream GA-681	Hydraulic Line	Loss of plane, no injuries	AZ, USA	1994
L-1011	Engine, compressor assembly disk	Loss of plane, no injuries	AK, USA	1994
Embraer 120	Propeller blade	Damage to the plane, no injuries	Canada	1994
Embraer 120	Propeller blade	Damage to the plane, no injuries	Brazil	1994
F/A-18	Trailing edge Flap (TEF) Outboard Hinge Lug	Loss of TEF	Australia	1993
Mooney Mooney 20	Engine, interior	Minor injuries	TX, USA	1993
Aero Commander 680	Lower Spar Cap	Fatal	Sweden	1990

2.3.1.2 Stress Corrosion Cracking (SCC)

Stress corrosion cracking occurs by slow environmentally induced crack propagation (Davis, 2000; Cramer *et al.*, 2003; Jones, 2003). For SCC to prevail, three conditions should occur: a crack-promoting environment, stress and material susceptibility to SCC (Davis, 2000). Small tensile stresses that are lower than the macroscopic yield stress have the potential to cause SCC (Jones, 2003). They can be either residual or externally applied and cause crack opening, which gives the corrodent access to the crack tip (Dollah and Robinson, 2011). This can be prevented by inducing compressive residual stresses in the material (Jones, 2003). Stress corrosion

cracking mainly results from static loading, while corrosion fatigue occurs due to cyclic loading (Jones, 2003).

Environments conducive to SCC are often aqueous, and sometimes condensed layers of moisture (Jones, 2003). Usually, the SCC of an alloy occurs due to the existence of particular chemical components within the environment. Altering factors such as temperature, degree of aeration and concentration of ionic species can transform an initially harmless environment into one that triggers SCC failure (Jones, 2003). The sequence of events involved in SCC is usually divided into three stages:

i. Crack initiation,
ii. Steady-state crack propagation,
iii. Crack propagation and final failure.

However, the difference between these stages is difficult to detect because of continuous transition and the division is therefore arbitrary (Jones, 2003).

Pre-existing defects like porosity and hot tears (cracks formed in a hot metal during cooling) can lead to SCC (Raja and Shoji, 2011). Machining can introduce discontinuities and microstructural changes, triggering SCC. Oxide films are less protective near metallurgical inhomogeneities including grain boundaries and inclusions hence, pits are more prevalent in those areas. Other factors that can initiate SCC include crevice corrosion, de-alloying and intergranular corrosion (Raja and Shoji, 2011). Because oxide layers are not as protective in corrosion pits as they are in nearby places, corrosion pits are frequently linked to metallurgical inhomogeneities such as inclusions and grain boundaries. According to Raja and Shoji (2011), intergranular corrosion, de-alloying and crevice corrosion are additional variables that might cause SCC.

Crack propagation can be transgranular or intergranular. While transgranular cracking does not prefer borders and spreads over low-index crystal planes, intergranular cracking, which is more prevalent, occurs along grain boundaries (Popov, 2015). The major cause of SCC in the 2xxx and 7xxx alloys is believed to be anodic dissolution that occurs along the grain boundaries because of the presence of precipitates (Cartner *et al.,* 2008). When anodic particles are adjacent to a cathodic matrix, galvanic corrosion takes place, leading to the dissolution of anodic particles. The absorption of hydrogen into the aluminium alloy triggers hydrogen embrittlement, which can cause localised corrosion sites and cracks, leading to crack

propagation (Cartner *et al*., 2008; Al-Haidary *et al.*, 2020). The stresses induced in the corroded parts come from different sources applied: residual, thermal or welding.

Products of corrosion may act as a wedge, creating tensile strains laterally (Rao *et al*., 2016; Al-Haidary *et al*., 2020). The direction of the tensile stress in relation to the direction of rolling and grain flow plays a significant role in the SCC behaviour of heat-treated aluminium alloys. The three main directions of stress corrosion resistance for specimens are longitudinal, long transverse and short transverse. These directions are determined by the shape and morphology of the grains, which are influenced by composition and fabrication history (Rao *et al*., 2016; Al-Haidary *et al*., 2020).

2.3.2 Corrosion testing and evaluation

2.3.2.1 Immersion tests

Immersion tests are governed by environmental conditions that must be simulated (Roberge, 2000) and the degree of acceleration required. This is achieved by:

- Increasing exposure to the critical conditions that cause corrosion damage,
- Intensifying conditions such as salt concentration, temperature, or pressure to increase corrosion rates.

Immersion tests can be divided into two categories (Roberge, 2000):

- Simple immersion tests expose specimens to the corrosive environment for a known time and the weight loss of the material is measured.
- Cyclic alternative immersion tests in which specimens are repeatedly immersed in a corrosive solution and dried for a prescribed duration.

2.3.2.2 Electrochemical corrosion tests

Electrochemical polarisation tests are used to evaluate a material's resistance to corrosion as well as the effect of changes in the corrosive environment (Ghali, 2010). The DC electrochemical techniques include potentiostatic, potentiodynamic, cyclic voltammetric and galvanostatic practices (Ghali, 2010). Polarisation methods used in corrosion testing involve controlling potential or current changes on the specimen under investigation whilst monitoring the resultant response in current or potential (Roberge, 2008). The experimental set-up includes:

i. A potentiostat to maintain the working electrode's potential close to a preset value,
ii. A current measuring device to monitor the current produced by the applied potential,
iii. Polarisation cells with various configurations tailored to testing requirements. Features include:
    - The working electrode (test sample) with an auxiliary or counter electrode,
    - The reference electrode which is separated from the solution by a solution bridge or a capillary Luggin probe,
    - A temperature monitoring device,
    - The test cell is made from a corrosion resistant material, ensuring no contamination of the test solution (Roberge, 2008).

Anodic polarisation accelerates electrode processes by shifting the potential positively, making the working electrode the anode and withdrawing electrons (Roberge, 2008). Cathodic polarisation accelerates processes by shifting the potential negatively, adding electrons and potentially causing electrodeposition. Potentiodynamic polarisation involves varying the electrode potential over a large range at a selected rate using current (Roberge, 2008). The corrosion potential (E_{corr}) is where anodic and cathodic rates are equal. The potential-time curve or polarisation resistance technique determines E_{corr} and corrosion rate. The E_{corr} increases with time for passive samples and decreases with the onset of localised corrosion.

However, interpreting E_{corr} alone can lead to misinterpretation (ASM International, 1990). Polarisation tests, when used alongside other methods, establish criteria for anodic or cathodic protection and susceptibility to various corrosion forms, aiding in characterising aluminium alloys (Ghali, 2010). Potentiodynamic polarisation curves are a useful way to compare electrochemical behaviour between different materials and/or surface states. Figure 2.4a)

shows how to obtain corrosion potential and current using the Tafel method. Figure 2.4b) shows how the cathodic branch current drops with increasing potential until it achieves the corrosion current density. In near-neutral solutions, the cathodic process for aluminium is mainly the reduction of oxygen, which is followed by its adsorption in Equation 2.1 (AlHazaa and Sherif, 2015). Just after the corrosion potential, the current increases quickly as the applied potential in the anodic branch increases (AlHazaa and Sherif, 2015). This is because of the dissolution of aluminium (Al^0) into aluminium cations (Al^{3+}) according to Equation 2.1. The current then stays almost unchanged, with a large increase in the applied potential in the passive region. This is due to the formation of aluminium hydroxide, $Al(OH)_3$, according to Equation 2.4, which may arise early stages of the anodic reaction and then transform into aluminium oxide, $Al_2O_3{\cdot}3H_2O$, as per Equation 2.5 (AlHazaa and Sherif, 2015).

$$2Al(OH)_3 \rightarrow Al_2O_3.3H_2O \qquad \textit{Equation 2.5}$$

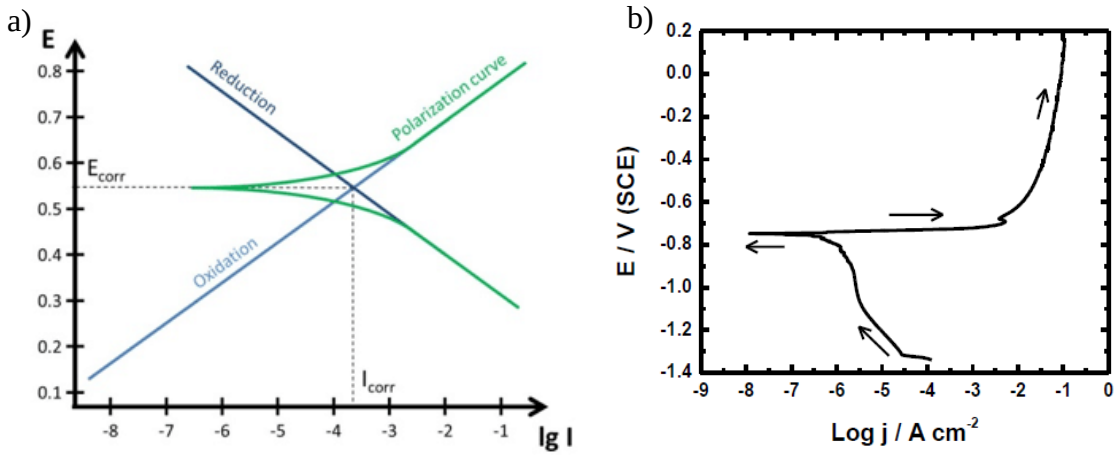


Figure 2.4. Polarisation curves: a) An example of a Tafel diagram with theoretical Tafel lines extrapolated (PalmSens, 2023), b) The AA7075 alloy's potentiodynamic polarisation curve in a 3.0 wt% NaCl solution (AlHazaa and Sherif, 2015).

2.3.2.3 Stress corrosion cracking tests

The stress corrosion cracking (SCC) test methods follow two philosophies which underlie structural design (Dietzel *et al*., 2011): safe life approach and damage tolerance strategy. The safe life approach is an older philosophy which designs material for a limited-service life during which there is no significant damage or critical cracking. The damage tolerance approach evolved later and was designed for an adequate service life without significant

damage, whilst also allowing for operation beyond the actual life at which damage starts to occur. The damage is detected by routine inspection before it propagates to the extent that there is a decrease in the residual strength of the material below a safe level (Dietzel *et al*., 2011). SCC experiments can be carried out on statically loaded smooth samples or pre-cracked samples and samples under slowly straining conditions (Jones, 2003):

2.3.2.3.1 Tests on statically loaded smooth samples

These tests are conducted at various fixed stress levels and the time to failure of the sample in the environment is measured (Jones, 2003). Typically, the applied stress, $\sigma_{applied,}$ is plotted against the logarithm of the measured time to failure, t_f. When the failure time approaches infinity, a threshold stress, σ_{th}, is determined. The time needed for crack formation, known as initiation time, $t_{in,}$ and the time of crack propagation, $t_{cp,}$ add up to the overall time to failure at a given stress. A typical plot is shown in Figure 2.5 (Jones, 2003).

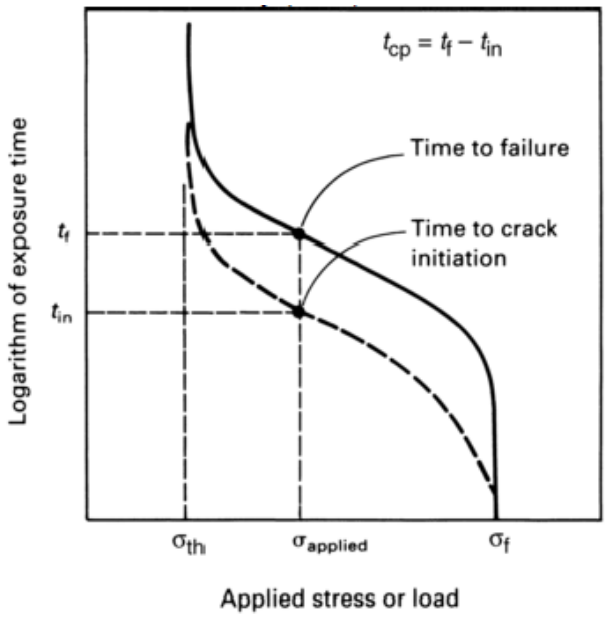


Figure 2.5. Schematic diagram of a typical time to failure vs initially applied stress for smooth sample SCC tests (Jones, 2003).

Experiments on statically loaded smooth specimens have the following aims (Jones, 2003):

- determining the highest stress that can be applied to avoid SCC failure,
- establishing frequency of inspection to verify the absence of SCC crack propagation,
- evaluating the impact of metallurgical and environmental conditions on SCC.

2.3.2.3.2 Tests on statically loaded pre-cracked samples

Tests on statically loaded pre-cracked samples are carried out with either a fixed crack opening displacement or a constant applied load (Jones, 2003). For a given crack and loading geometry, the stress intensity factor, K_I, quantifies the amplitude of the stress distribution at the crack tip and measures the rate of crack propagation.

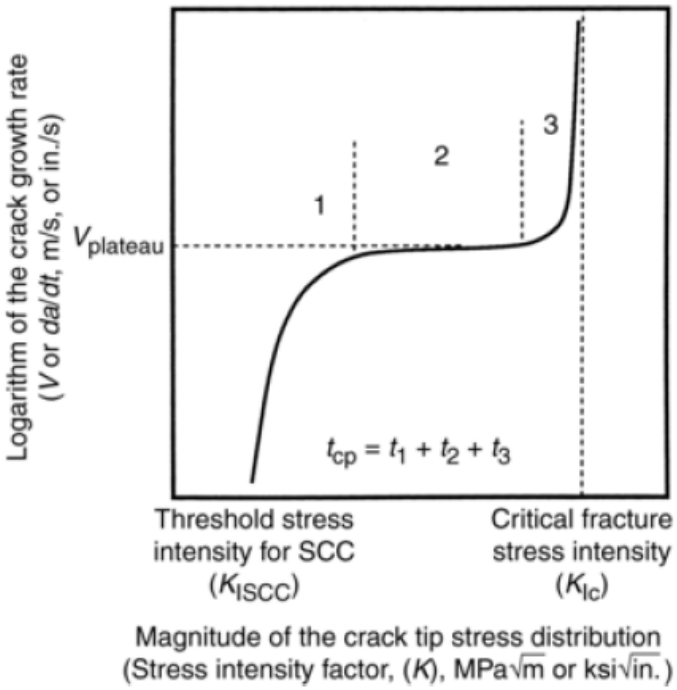


Figure 2.6. Schematic diagram of crack propagation rate as a function of crack tip stress-intensity behaviour (Jones, 2003).

Figure 2.6 shows three regions of crack propagation (Stages 1, 2, and 3) identifiable by stress-intensity factor increase. No crack growth is observed below the threshold stress-intensity level, K_{ISCC}, which is the lowest stress level necessary for synergistic interaction with the environment. The fracture propagation rate grows quickly with the stress-intensity component

at low stress-intensity levels (Stage 1). The crack propagation rate approaches a constant velocity at intermediate stress-intensity levels (Stage 2), irrespective of the mechanical driving force. This plateau velocity ($V_{plateau}$) is the result of rate-limiting environmental activity such as the mass transport of environmental species up the crack to the crack tip. In Stage 3, the crack growth rate surpasses $V_{plateau}$ as the stress-intensity level approaches the critical stress for mechanical fracture in inert conditions, K_{IC} (Jones, 2003).

2.3.2.3.3 Slow strain rate testing

Material may be resistant to SCC under static loading, but highly susceptible under continuous slow plastic straining (Dietzel *et al*., 2011), thus testing SCC whilst slowly increasing the load is essential. These tests can be done on smooth or pre-cracked samples. Experiments can be done in a tensile machine, pulling a sample at a low crosshead speed, 10^{-5} to 10^{-9} m/s, that is exposed to a corrosive environment (Jones, 2003). The strain rate can be plotted against strain-failure in a corrosive and an inert environment. Alternatively, these ratios can be plotted for ductility. The ratio of other tensile property measurements, such as reduction in area and ultimate tensile strength, could also be plotted. These tests are known as straining electrode tests, constant extension rates tests and slow strain rate tests (Jones, 2003; Dietzel *et al.*, 2011).

2.4 Laser Shock Peening

Laser Shock Peening (LSP) is an innovative surface enhancement technology capable of imparting compressive surface residual stress, thereby improving the resistance of components to fatigue failure (Rankin *et al.*, 2003; Sano *et al.*, 2006; Adachi *et al.*, 2008). Even though LSP and Shot Peening (SP) create residual stresses of similar magnitude, the compressive stresses extend far deeper from the surface for LSP, thereby offering improved resistance to the growth of near-surface, macroscopic cracks (Rankin *et al.*, 2003).

2.4.1 LSP process description

Laser pulses are irradiated on the metal component and interact with the surface, generating ablation plasma (Ivetic *et al*., 2011; Sano *et al*., 2012). A transparent overlay (usually water) covers the metal surface confining the plasma and increasing the pressure to GPa ranges (Ding and Ye, 2006; Sano *et al.*, 2006; Adachi *et al*., 2008; Sano *et al*., 2012). The plasma absorbs

subsequent laser energy and creates a heat-sustained shock wave, which intrudes into the material with a high intensity that exceeds the material's yield strength (Sano *et al.*, 2006). The surface is plastically strained to form compressive residual stress (Sano *et al.*, 2006; Adachi *et al.*, 2008). A schematic diagram of the LSP process is shown in Figure 2.7.

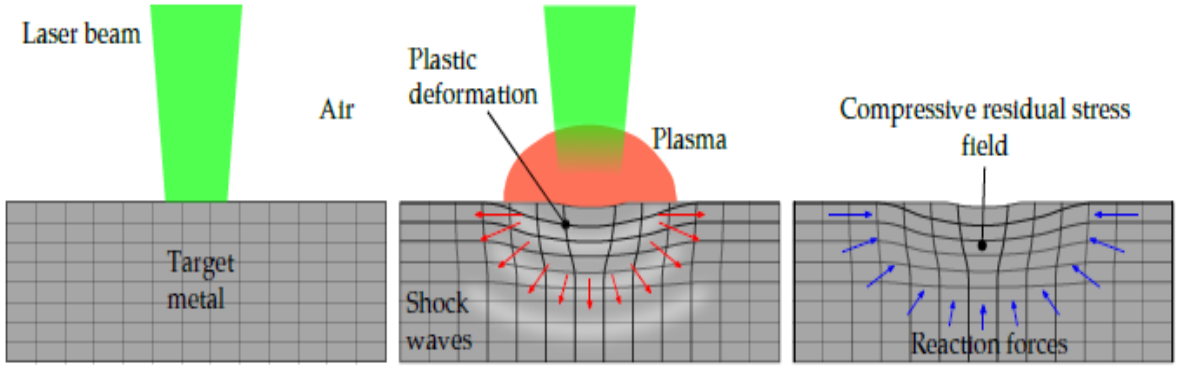


Figure 2.7. The process of LSP: shock waves cause plastic deformation, inducing a compressive residual stress field on and below the surface (Stiekema, 2021).

LSP will change the material on and below the surface. Rankin *et al.* (2003) observed varying residual stress, surface roughness and hardening after LSP treatment. In aluminium and its alloys, LSP may enhance the surface properties (Rankin *et al.*, 2003), reducing the occurrence of surface lapping, folds and other undesirable features that occur with SP. The improved surface condition should cause improved resistance to crack initiation. Surface treatments like LSP are often applied to a component's specific, highly stressed locations (Rankin *et al.*, 2003).

2.4.2 Comparison of LSP with and without coatings

Conventional LSP utilises a coating (sacrificial overlay) on the metal surface (Figure 2.8a) and an Nd:YAG laser (Sano *et al.*, 2006). The coating enhances laser absorption (Sano *et al.*, 2006) and prevents surface damage (Ivetic *et al.*, 2011). This sacrificial overlay can be aluminium foil, copper, lead, vinyl tape, zinc or black paint (Gujba and Medraj, 2014). Black paint is usually used as a coating before laser irradiation and the remaining paint is removed after the treatment. Figure 2.8b shows the newer process, Laser shock peening without coating – LSPwC, does not utilise a coating and employs a Q-switched Nd:YAG laser (Sano *et al.*, 2006). To avoid surface damage in this set-up, a lower power laser with a small impact size is used

(Ivetic *et al*., 2011). In LSPwC, the surface residual stress becomes compressive by increasing the density of irradiating laser pulses (Sano *et al.*, 2006).

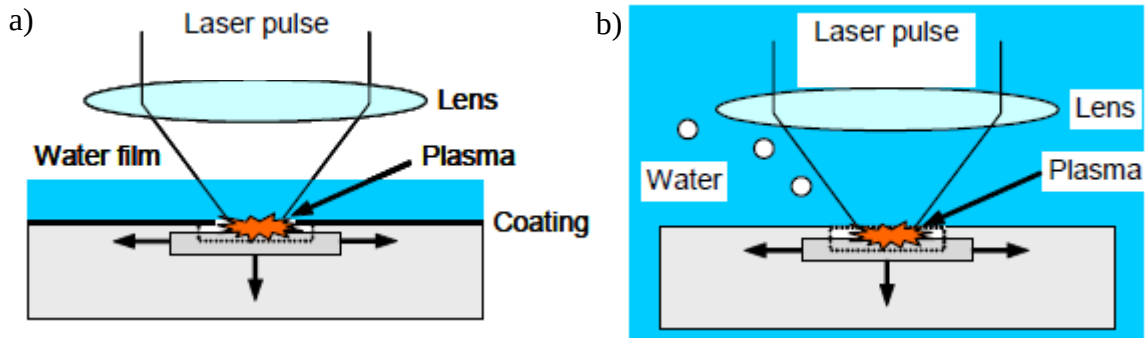


Figure 2.8. Different LSP techniques: a) LSP with black paint coating and b) LSPwC (Sano et al, 2006).

2.4.3 LSP parameters

Controlling LSP can be achieved by adjusting various parameters that affect the properties of the induced shock wave, its penetration depth and the performance of the resulting peened material. These parameters fall into three categories: laser system, control and interaction (Ding and Ye, 2006; Sano *et al*, 2006).

2.4.3.1 Laser system parameters

These parameters, determined by the laser system that is used to perform the LSP, are:

i. **Laser type**, which can be classified according to the type of material used for light amplification. The most used are Nd:YAG and Nd:glass, but Diode-Pumped Solid-State Lasers (DPSSL), CO_2 and Potassium Dihydrogen Phosphate (KDP) are also used (Ding and Ye, 2006; Gujba and Medraj, 2014).
ii. **Spot geometry**, circular, square, elliptical and rectangular have been studied (Cao *et al.*, 2011; Kim *et al.*, 2012).
iii. **Pulse length,** or duration, is the time between the start and end of a pulse measured in nanoseconds (ns).
iv. **Pulse frequency** is the number of laser pulses emitted per second. It is usually in the 10-100 Hz range for Q-switched lasers.
v. **Laser wavelength** is measured in micrometres (µm) and significantly influences the absorption of laser energy by the material's surface (Ding and Ye, 2006). Different laser

wavelengths of 1054 nm (infra-red), 532 nm (green) and 355 nm (ultraviolet) are used (Gujba and Medraj, 2014). Different wavelengths result in varied plasma generation, affecting the peak pressures developed during the process. Shorter wavelengths are absorbed more superficially, leading to more intense and localised plasma generation, potentially resulting in higher peak pressures. The choice of laser wavelength is crucial for optimising the LSP process, as it affects the depth of energy penetration, plasma formation and ultimately the characteristics of the shockwaves that induce compressive residual stresses in the material.

2.4.3.2 Control parameters

These are the parameters that can be changed to control the LSP process:

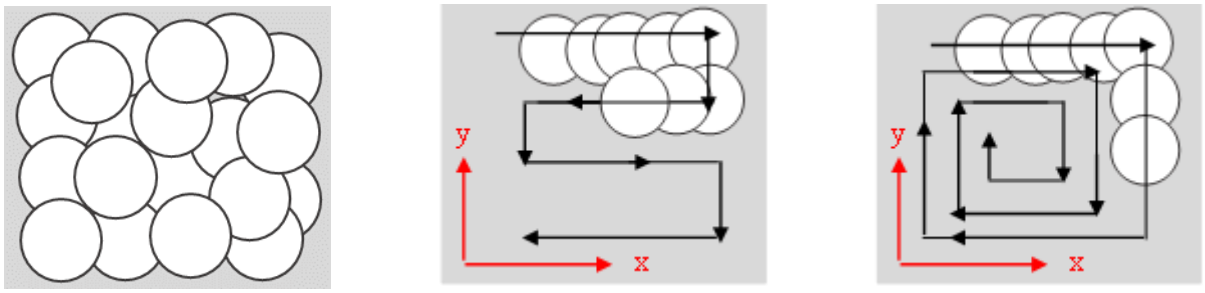
i. **Laser energy**: This is the energy output of the laser that can be varied by using an attenuator. The output laser energy is measured in Joules (J).

ii. **Spot size (SS)**: Refers to the diameter or width of the laser spot on the treated surface, measured in millimetres (mm). It can be varied by either changing the focal distance of the laser beam from the sample or by moving the sample along the laser beam path.

iii. **Pulse density (N_p)**: This is the number of spots in a unit area, measured in spots per square millimetre (spots/mm^2). For a pulsed laser, it can be varied by changing the speed at which the laser scans over the sample, as well as the step dimension. From an industrial processing perspective, N_p, also referred to as equivalent overlapping density is directly proportional to processing time (Glaser *et al*., 2014).

iv. **Ablative medium**: This is an external coating applied to protect the surface from thermal damage.

v. **Peening pattern**: This refers to the pattern in which the peening spots are applied, as shown in Figure 2.9. These could be a raster pattern, a helix pattern or applied randomly. It is typically controlled using CNC.



a) random pattern *b) raster pattern* *c) helix pattern*

Figure 2.9. Laser shock peening patterns (*Correa et al., 2015; Salimianrizi et al., 2016).*

2.4.3.3 Interaction Parameters

The interaction parameters are a result of interactions of the control parameters.

i. **Power intensity (PI)** indicates the intensity of the laser on the surface of the sample, measured in GW/cm^2. It is also referred to as power density or irradiance and is calculated according to Equation 2.6.

$$Power\ intensity = \frac{Laser\ energy}{Pulse\ duration\ x\ Irradiated\ spot\ area} \qquad \textit{Equation 2.6}$$

ii. **Coverage (C_v)** indicates how much of the treated area is covered by spots. It is obtained utilising Equation 2.7 and is measured in 'spots'.

$$C_v = N_p\ x\ \frac{\pi}{4} SS^2 \qquad \textit{Equation 2.7}$$

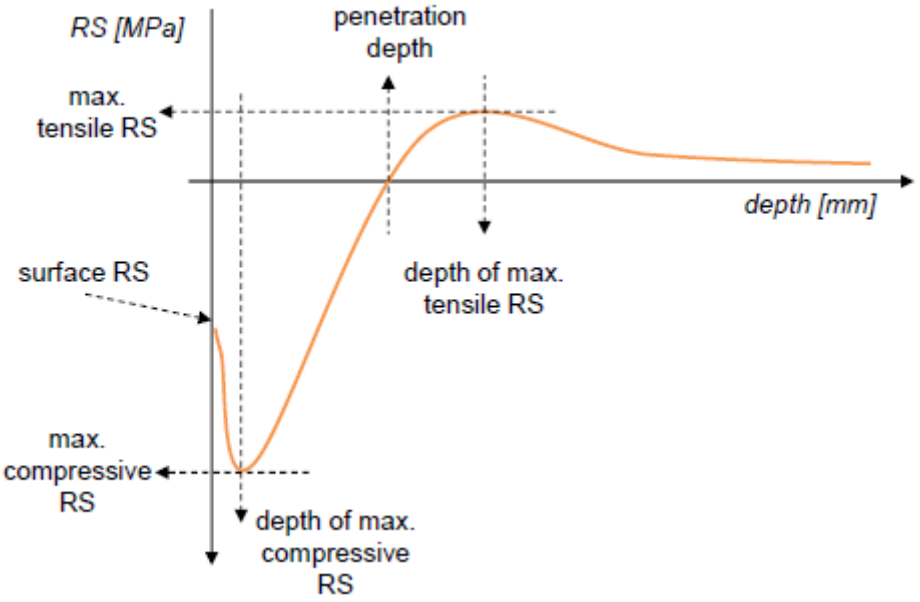
where N_p = laser pulse density (spots/mm^2) and SS = spot size (mm) (Glaser *et al*., 2014).

iii. **% overlap** indicates a percentage of each spot that is covered by neighbouring spots obtained by Equation 2.8.

$$\%\ overlap = 1 - \frac{SS}{\sqrt{Np}} \qquad \textit{Equation 2.8}$$

2.4.4 Effect of LSP on residual stress

The residual stress (RS) profile (Figure 2.10) of a specimen's thickness is defined by size parameters such as surface RS, penetration depth, maximum compressive RS and maximum tensile RS (Ding and Ye, 2006; Busse, 2017). These parameters offer insights into the distribution and characteristics of residual stresses within the material.



g

Figure 2.10. Typical Residual Stress Profile through the thickness and describing its characteristics (Busse, 2017).

Peyre *et al*. (1998) found that the size of the laser spot had an impact on the residual stress profile. They used LSP on medium carbon steel (55C1) at spot diameters of 1 mm and 6 mm. The larger spot size produced a residual stress profile much deeper beneath the treated surface than the smaller one. Ganesh *et al.*, (2012) observed that larger spot sizes result in deeper compressive RS for spring steel. Additionally, larger spot sizes showed better coverage and uniformity due to overlapping of spots, compared to smaller spot sizes (Ganesh *et al*., 2012). In contrast, the work done by Trdan and Grum (2012) on an AA6082-T651 sample found an inverse relationship between spot size and compressive stresses. They observed higher compressive stresses when a spot size of 1.5 mm was used compared to the other two spot sizes of 2.0 mm and 2.5 mm. A constant pulse density of 900 pulses/cm^2 was adopted for all experiments.

2.4.5 Effect of LSP on surface roughness

Understanding a material's surface involves examining its roughness, which refers to the regular or irregular variations from the nominal surface that form its three-dimensional topography. The surface description includes roughness, waviness, lay and flaws (Bhushan, 2001) as illustrated by Figure 2.11.

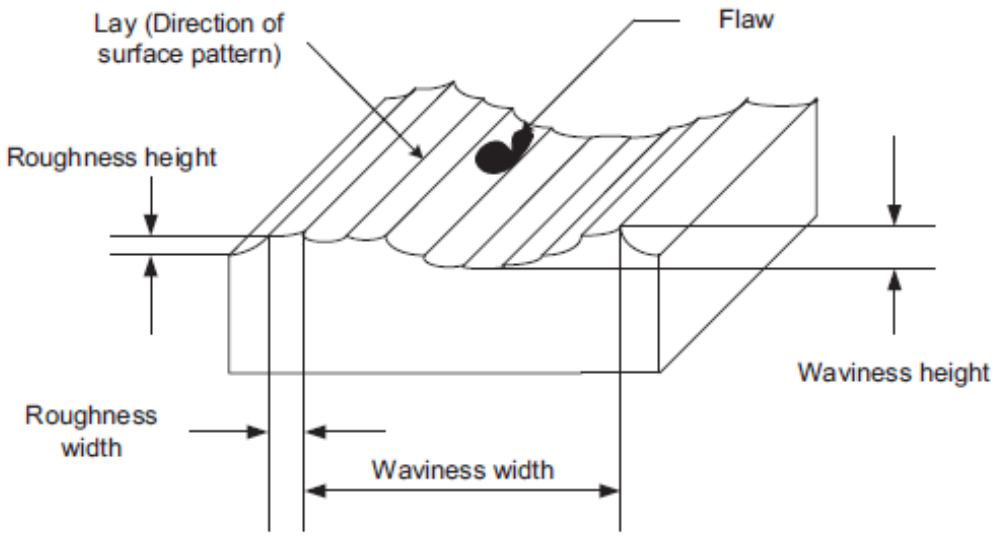


Figure 2.11. Definitions for surface profile (Tseng et al., 2016).

Surface roughness refers to the height variations of a surface relative to a reference plane. It can be quantified by amplitude parameters R_a, R_q, R_t and R_z. R_a is the arithmetic mean of absolute values of vertical deviation from the mean line through the profile (Bhushan, 2001). The method of measurement of R_a is illustrated in Figure 2.12.

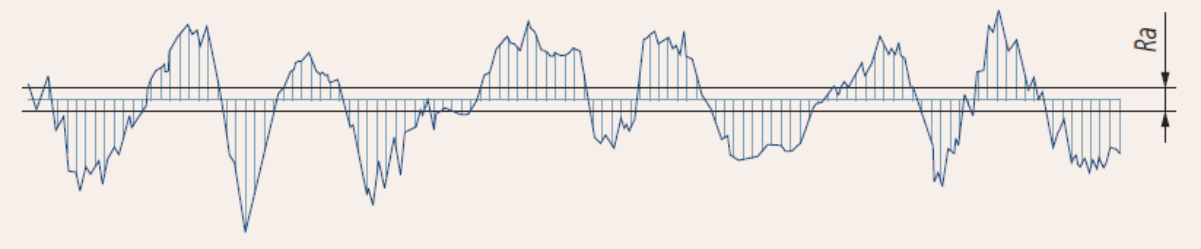


Figure 2.12. Roughness value R_a measurement (Mitutoyo America Corporation, 2016).

The value R_q is the square root of the arithmetic mean of the square of vertical deviation from a reference line (Bhushan, 2001). The R_a and R_q values are calculated by Equations 2.9 and 2.10:

$$R_a = \frac{1}{L}\int_0^L |Y(x)|dx \qquad \textit{Equation 2.9}$$

$$R_q = \sqrt{\left[\frac{1}{L}\right]\int_0^1 (Y(x))^2\,dx} \qquad \textit{Equation 2.10}$$

where L = sampling length and Y = ordinate of the curve of the profile (Lou *et al*., 1998; Tseng *et al*., 2016).

The R_t value is the distance between the highest peak and the lowest valley and R_z is the distance between the averages of the five highest peaks and the five lowest valleys within the sampled length (Bhushan, 2001). The measurement of R_t and R_z is illustrated in Figure 2.13.

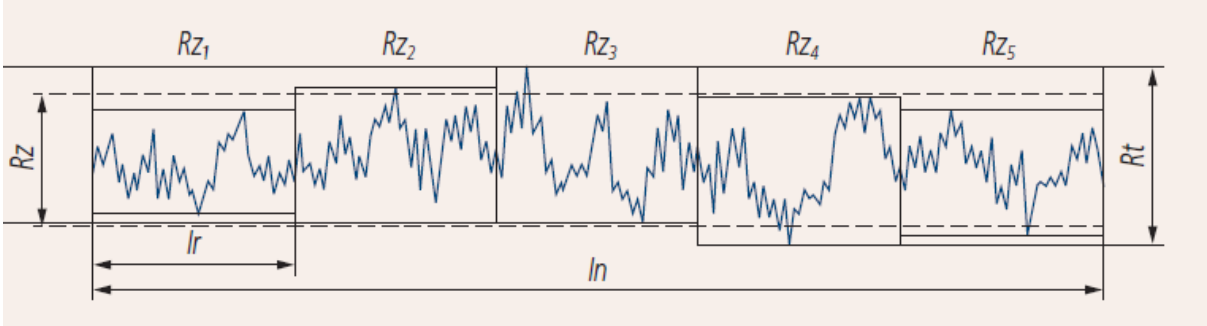


Figure 2.13. Measurement profile for R_t and R_z (Mitutoyo America Corporation, 2016).

Using LSP increases the surface roughness in the treated component (Glaser *et al*., 2014; Becker, 2017; Abeens *et al*., 2019; Sanchez, 2021; Attolico *et al*., 2022; Glaser *et al*., 2022). This results directly from shock waves generated by the component's surface's controlled plasma expansion, which causes local plastic deformation. Plastic deformation results from the plasma pressure rising over the material's dynamic yield strength, changing the near-surface characteristics (Attolico *et al.*, 2022). From LSP carried out on AA6061-T6, Sano *et al.* (2012) observed that the surface lustre changed from metallic to dull greyish upon laser irradiation due to the surface's reaction with nascent-state oxygen from active plasma and the intense electric field of the laser pulse.

Specimens exposed to higher pulse energies of LSP showed an increase in surface roughness (Abeens *et al*., 2019; Attolico *et al*., 2022) because the higher peak pressure-induced increases the depth and the magnitude of deformation (Attolico *et al*., 2022). Becker (2017) found that the surface processed by LSP had lower roughness compared to mechanical shot peening on AA7075-T6 and annealed AA7075. The surface roughness results are shown in Table 2.6. This

agreed with Glaser *et al.* (2022) who made the comparison on AA6056-T4 and found R_a = 1.86 µm after LSPwC and R_a = 7.52 µm after SP. The surface topography is shown in Figure 2.14.

Table 2.6. Surface roughness (R_a) in µm of Shot Peening and Laser Shock Peening (Becker, 2017).

	Pristine sample	**After Shot Peening**	**After Laser Shock Peening**
Annealed AA7075	0.22	11.49	3.29
AA7075-T6	0.22	8.53	2.28

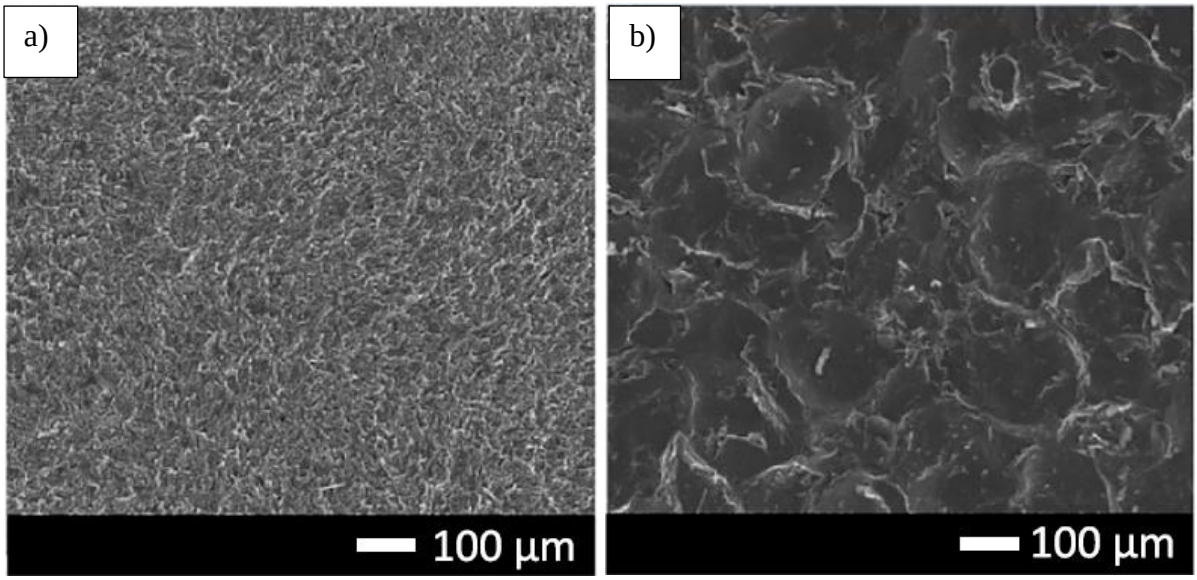


Figure 2.14. SEM-SE images of AA6056-T4 surfaces after a) LPwC and b) SP (*Glaser et al., 2022).*

Beneficial compressive residual stresses are the main cause of the life-enhancement potential of LSP treatment (Ding and Ye, 2006). However, surface degradation may counteract the advantageous compressive residual stress (Ding and Ye, 2006). The combined effects of ablation and deformation led to surface deterioration for LSPwC (Glaser et al., 2022). Both the amount of ablated material from the surface and the local deformation produced by each pulse increase with power intensity. Surface ablation and surface deformation from each pressure pulse work together to increase surface roughness as the number of pulses (N_p) increases. More ablated material results from increasing N_p, and this could produce surface homogeneity at noticeably high coverage (Glaser et al., 2022)

2.4.6 Effect of LSP on microstructure

LSP induces significant effects on grain structure. Firstly, it modifies grain orientation by employing shock waves to cause plastic deformation, resulting in a more uniform distribution of grain orientations (Ivetic *et al*., 2011; Sathyajith and Kalainathan, 2012; Salimianrizi *et al*., 2016; Liu *et al*., 2019; Luo *et al*., 2019). This results in enhanced mechanical properties based on the material's initial texture. Secondly, LSP enhances grain boundary strength by forming dislocation structures and grain boundaries with a higher dislocation density, thereby improving the material's strength near the surface. These alterations collectively contribute to the overall improvement of material characteristics by LSP treatment (Ivetic *et al*., 2011; Sathyajith and Kalainathan, 2012; Salimianrizi *et al*., 2016; Liu *et al*., Luo *et al*., 2019).

The impact of LSP on grain structure can differ based on various factors, including the type of material being treated, laser parameters, energy density, number of laser shots and depth of treatment (Peyre *et al*., 1998; Ding and Ye, 2006; Yadav *et al*., 2017). Although LSP can provide several advantages in terms of enhanced mechanical properties and surface performance, the results will depend on the specific application and the material's reaction to the treatment. The LSP induces grain refinement (Figure 2.15) and increases dislocations, enhancing mechanical properties like hardness and strength. This improved grain structure plays a beneficial role in impeding crack propagation and deterring the occurrence of stress corrosion cracking (Zhang *et al*., 2010). However, Glaser *et al*. (2022) stated there was no grain refinement after LSP, although their micrographs showed a very refined layer down to 150 microns below the surface.

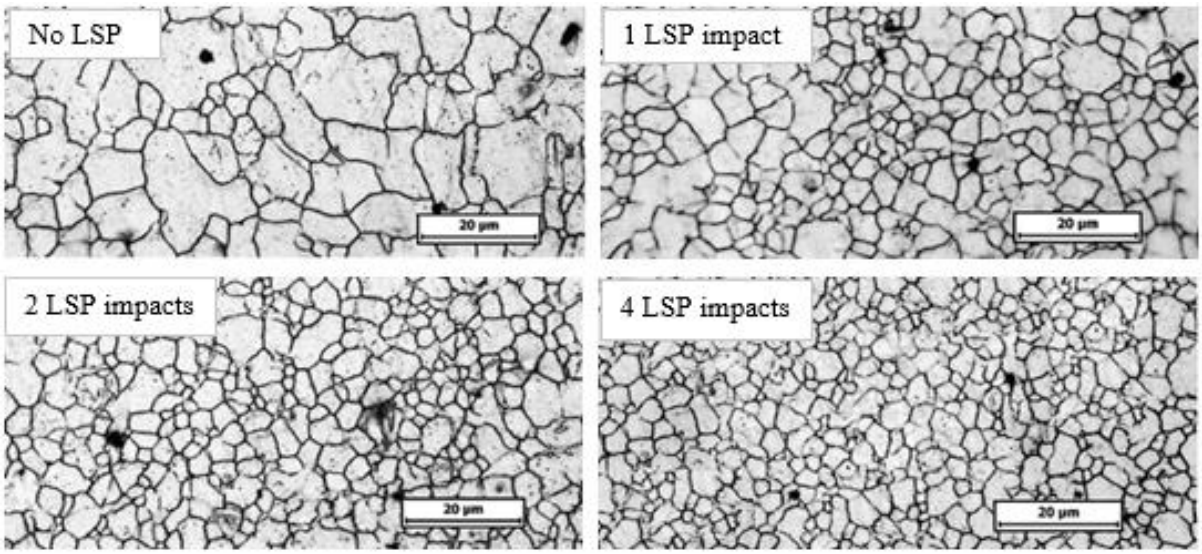


Figure 2.15. Optical micrographs of a cross-section of AZ31B Mg alloy showing grain refinement after different LSP impacts (Zhang et al., 2010).

2.4.7 Effect of LSP on microhardness

Hardness is a measure of a material's resistance to localised plastic deformation, like dents or scratches (Callister, 2007). Quantitative techniques involve controlled application of load by a small indenter, with indentation depth or size determining hardness. The Vickers microhardness test, using a diamond pyramid indenter, is one such technique. The resulting impression is observed and measured under a microscope (Callister, 2007).

Several investigations into the effect of LSP on microhardness showed an increase in the hardness of the material (Sathyajith and Kalainathan, 2012; Salimianrizi *et al*., 2016; Abeens *et al*., 2019; Liu *et al*., 2019; Mostafa *et al*., 2019). The highest microhardness was found near the surface and gradually decreased with depth until it reached a value similar to the unchanged matrix. The increase in hardness of samples treated by LSP is attributed to strain-hardening that occurs during the LSP process. The intense shock waves generated caused significant plastic deformation at the material's surface, introducing dislocations in the crystal lattice (Ding and Ye, 2006). The shock waves that propagate through the sample during LSP apply a load that is above the yield strength which plastically deforms it and causes an increase in the dislocation density. The increased dislocation density acts as a barrier to the movement of

dislocation loops, providing resistance to further plastic deformation and resulting in increased hardness (Zhang *et al*., 2010; Salimianrizi *et al*., 2016; Mostafa *et al*., 2019).

Glaser *et al*. (2022) investigated the effect of LSP on AA6056-T4 by varying laser power intensity from 1 to 7 GW/cm^2 and coverage from 1 to 20 spots/mm^2 and found no significant change in the microhardness. Ding and Ye (2006) explained that for peak-aged aluminium alloys, such as 2024-T851, 7075-T651 and 7075-T73, the precipitation hardening was large enough to mask any shock-induced strain hardening (Ding and Ye, 2006).

2.4.8 Effect of LSP on corrosion

LSP increases surface roughness as discussed in Section 2.4.5. A rough surface has numerous bumps, crevices and irregularities that contribute to an increase in the total surface area (ASM International, 1990). This makes it more convoluted; each bump and crevice adds to the overall surface area of the material. High surface roughness intensifies corrosion by increasing the specific surface area exposed to a corrosive environment. The rough features act as high-stress concentrations and become sources of crack initiation (ASM International, 1990). Studies on laser peened AA6082-T651 (Trdan and Grum, 2012, 2015) and aluminium-silicon alloys (Trdan *et al*., 2011) showed more stable open circuit potentials, less pitting, after peening than untreated material (Trdan and Grum, 2012). This is despite LSPwC increasing surface roughness which in most cases promoted higher corrosion current densities (corrosion rates), with higher power density causing higher surface roughness (Trdan and Grum, 2012, 2015).

Electrochemical processes that occur without any mechanical stimuli, pitting and intergranular corrosion, are affected by residual stresses in a complex manner. Peyre *et al*. (2009) found a decrease in cathodic currents in 10^{-3} M NaCl + 10^{-2} M Na_2SO_4 solution after LSP. Krawiec and Vignal (2011) showed LSP improved the electrochemical impedance (increase in the charge transfer and oxide film resistance) of sites containing the matrix of AA2050-T8 in 0.1 M NaCl solution. Amar *et al*. (2011) used the scanning vibrating electrode technique on laser peened AA2050-T8 and found that LSP prevented intergranular corrosion, increased pitting potential and lowered anodic potential. This was attributed to compressive residual stresses (Amar *et al*., 2011; Krawiec *et al*., 2011). Changes in grain structure induced by LSP can impact corrosion resistance, with finer grain sizes and altered boundaries lowering susceptibility to corrosion (Trdan and Grum, 2012).

Figure 2.16 shows SEM images of specimen surfaces following electrochemical corrosion tests (Wang *et al.*, 2017). Scattered corrosion pits and corrosion cracks were visible on the untreated specimen surfaces (Figure 2.16a) & b)). In contrast, significant improvement was observed after LSP treatment (Figure 2.16c) & d)), suggesting that LSP effectively prevents the formation and growth of corrosion pits and micro-fractures (Wang *et al.*, 2017).

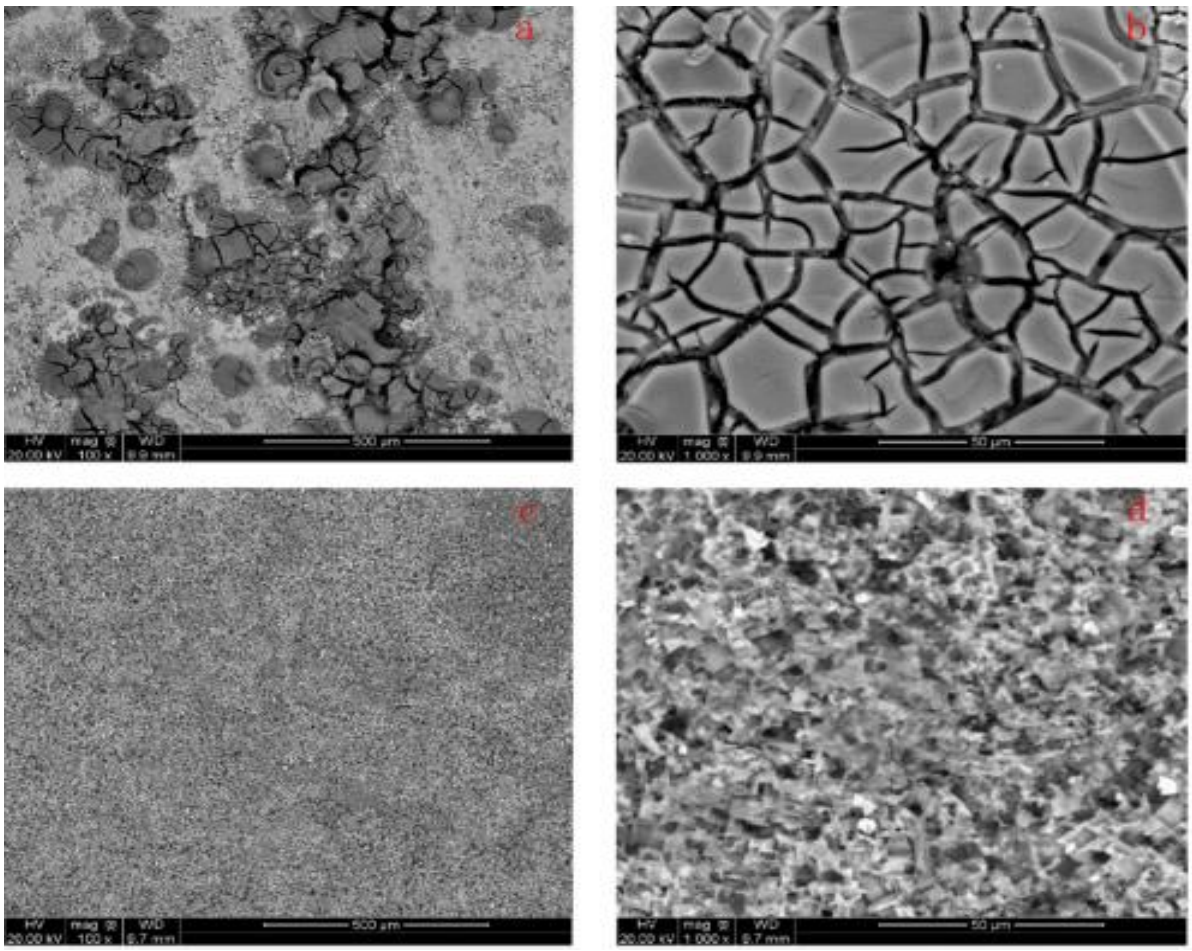


Figure 2.16. Surface morphology of AA7075 specimens' surface after corrosion test: (a) and (b) untreated; and (c) and (d) LSP treated once with 7.17 GW/cm^2 (Wang, 2017).

Wang *et al*. (2017) investigated the abrasion and corrosion resistance of LSP-treated AA7075 in artificial seawater (unspecified concentration), revealing decreased abrasion loss (46%), friction coefficient (0.42 – 0.35) and a 50% reduction in corrosion rate compared to untreated specimens. The positive effects of LSP on SCC resistance are attributed to the introduction of compressive residual stresses and work hardening.

Compressive residual stresses are beneficial for retarding stress corrosion cracking (Lu *et al.*, 2012; Brandenburg *et al.*, 2013; Telang *et al.*, 2015; Wang *et al.*, 2015; Sundar *et al.*, 2016; Yu *et al.*, 2016; Yoo *et al.*, 2023) and corrosion fatigue (Zupanc and Grum, 2010; Brandenburg *et al*., 2013; Abdulstaar *et al*., 2014; Wang *et al*., 2017; Luo *et al*., 2019). The compressive residual stresses created by LSP counteract any applied tensile stresses, reducing the effective tensile stress experienced by the material and making it more resistant to stress corrosion cracking (Lu *et al.*, 2012; Brandenburg *et al.*, 2013; Telang *et al.*, 2015; Wang *et al.*, 2015; Sundar *et al.*, 2016; Yu *et al.*, 2016; Yoo *et al.*, 2023). Work hardening contributes to increased strength and resistance to crack initiation. Sano *et al*. (2006) studied the effect of LSP on SCC, showing the potential to reduce SCC in stainless steel austenite SUS304. Figure 2.17 shows the results of SCC tests performed on 3 mm thick SUS304 samples, with and without LSPwC. The LSP treatment completely prevented the formation and propagation of SCC cracks (Sano *et al.*, 2006). Excessive hardness may lead to brittleness, diminishing ductility and making the material more susceptible to crack initiation and propagation (Raja and Shoji, 2011; Popov, 2015).

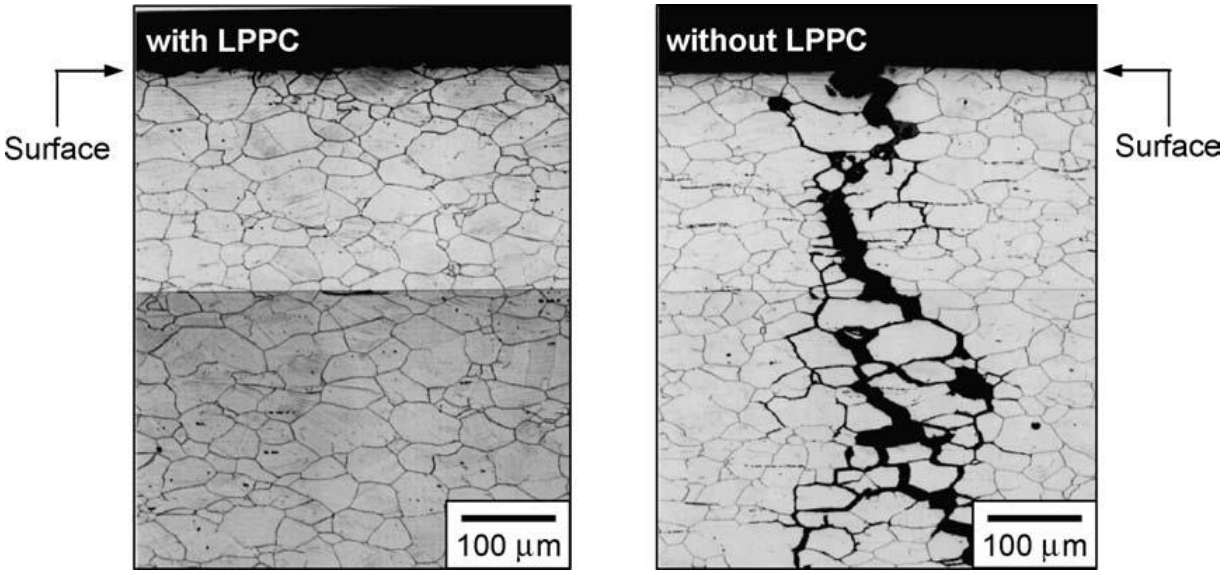


Figure 2.17. Optical images showing SUS304 a) with and b) without peening (Sano et al., 2006).

2.5 Rationale of the project

Aluminium alloys have favourable mechanical properties, although their susceptibility to localised corrosion necessitates effective protection to extend service life. Previous studies have shown LSP's ability to introduce beneficial compressive residual stresses, thereby enhancing mechanical integrity and corrosion resistance. It is difficult to separate the contributions of beneficial compressive residual stresses and the detrimental effects of the induced surface roughness. Hence, it is important to find optimal peening conditions which improve corrosion resistance. Thus, this study was conducted to investigate the corrosion behaviour of aluminium alloy 7075-T651 at different peening parameters.

CHAPTER 3: EXPERIMENTAL PROCEDURE

3.1 Introduction

This project was divided into two phases: surface characterisation and corrosion testing. During the first phase, the goal was to determine the effect of LSP on the surface properties of AA7075-T651 at different peening parameters. In the second phase, the goal was to conduct corrosion tests using different methods on selected samples.

3.2 Sample Preparation

The samples for this study were CNC milled with selected constant machining parameters from a rolled plate of Aluminium Alloy 7075-T651, which was 15 mm thick and purchased from NK Cutting. This batch of samples was part of a previous study in the research group (van Staden, 2018; Chundunsing, 2019). Figure 3.1 displays the sample geometry after milling.

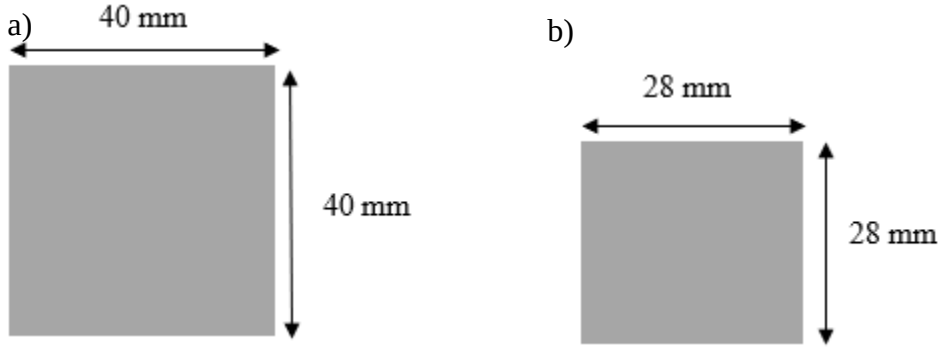


Figure 3.1. Geometry of milled AA7075-T651 samples: a) 14 mm thickness plates and b) 1.6 mm and 10 mm thickness plates.

The Aluminium Association gives a guideline for the chemical composition of AA7075 (The Aluminium Association, 2018) and NK Cutting provided a datasheet (Appendix 1) with bulk compositions within those guidelines, Table 2.3. The material properties are shown in Table 2.4.

3.3 Laser Shock Peening

3.3.1 LSP process

Laser Shock Peening without Coating (LSPwC) experiments were carried out at the Council for Scientific and Industrial Research - National Laser Centre (CSIR NLC) using a Spectra-Physics Quanta-Ray PRO270 Q-switch pulsed Nd:YAG laser of wavelength 1064 nm. Access to the laser was granted through the Rental Pool Programme of the NLC.

The following fixed laser parameters were utilised:

- Pulse length 8.6 ns
- Pulse frequency 20 Hz
- Spot shape circular.

Figure 3.2 is a schematic diagram of an LSP system. To carry out the LSP (with or without coating), a CNC code was programmed to automate the process. The laser energy was regulated by the attenuator, while the sample's positioning was controlled at the CNC XYZ stage. The laser spot size (SS) was adjusted by moving the sample along the z-direction. The laser spot coverage (N_p measured in spots/mm^2) was controlled by modifying the speed at which the sample moved across the laser by setting the speed of the x and y-direction motors in the CNC code (van Staden, 2018). Peening was done in a raster pattern (Figure 2.9b)), where y indicates the scanning direction and x the stepping direction (Figure 3.6), which was aligned with the longitudinal rolling direction of the plate. No ablative coating was applied on the sample surface.

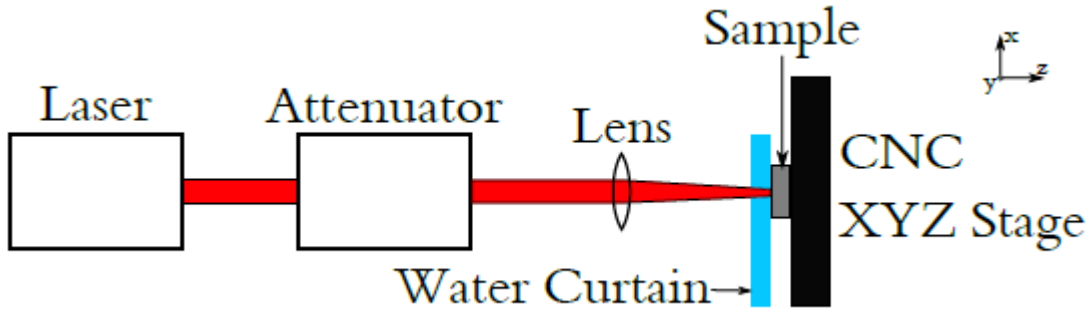


Figure 3.2. Schematic diagram of the experimental LSP configuration (van Staden, 2018).

Figure 3.3a) and b) show the dimensions of the peened samples. The shaded centre represents the area treated by LSPwC.

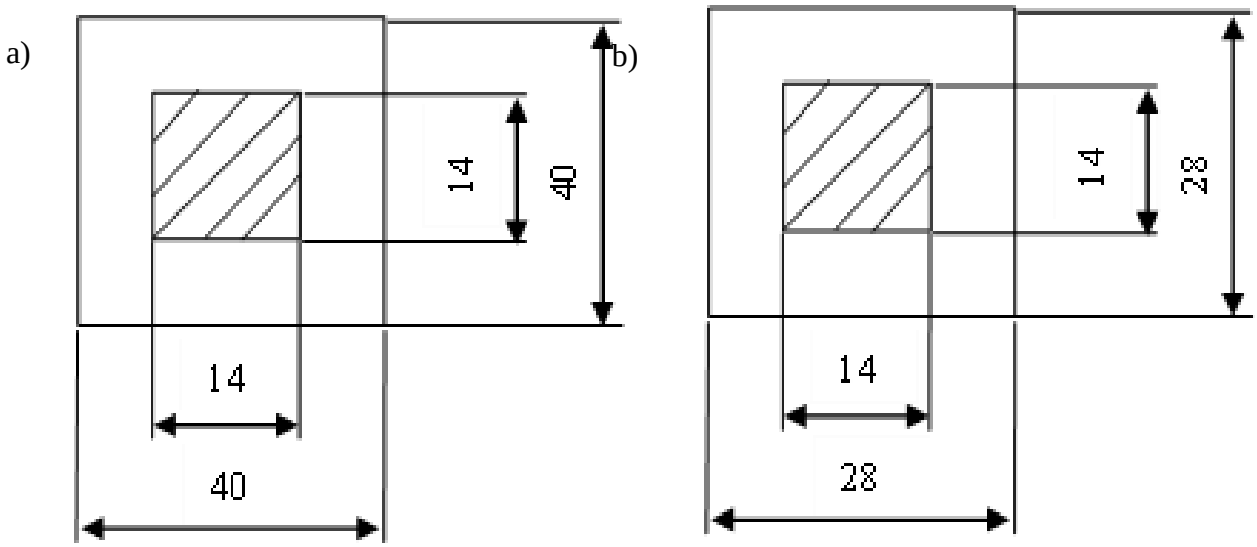


Figure 3.3. Dimensions for a typical AA7075 sample processed by LSPwC with thickness of a) 14 mm and b) 1.6 mm and 10 mm.

3.3.2 Sample identification

Laser shock peening without coating (LSPwC) was carried out at varying power intensities, spot sizes and coverages. The samples were named according to the convention in Figure 3.4 for easier identification of the laser parameters employed.

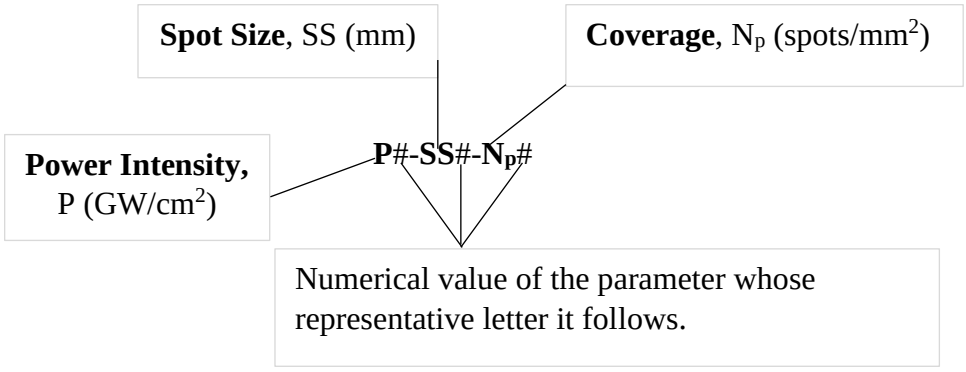


Figure 3.4. Convention for naming samples processed by LSPwC.

Laser parameters used to process AA7075-T651 specimens are listed in Table 3.1.

Table 3.1. Sample information: 14x14 mm LSPwC area.

Sample Name	**Power Intensity (GW/cm^2)**	**Spot Size (mm)**	**Coverage ($Spots/mm^2$)**
40 x 40 mm plate, 14 mm thickness			
P1-SS0.8-N_p40	1	0.8	40
P3-SS0.8-N_p2.5	3	0.8	2.5
P3-SS0.8-N_p5	3	0.8	5
P3-SS0.8-N_p10	3	0.8	10
P3-SS0.8-N_p20	3	0.8	20
P3-SS0.8-N_p40	3	0.8	40
P5-SS0.8-N_p40	5	0.8	40
P3-SS1.5-N_p2.5	3	1.5	2.5
P3-SS1.5-N_p5	3	1.5	5
P3-SS1.5-N_p10	3	1.5	10
28 x 28 mm plate, 10 mm thickness			
P3-SS1.5-N_p5	3	1.5	5
P1.5-SS1-N_p11.25	1.5	1	11.25
P3-SS1-N_p11.25	3	1	11.25
P4.5-SS1-N_p11.25	4.5	1	11.25
P6-SS1-N_p11.25	6	1	11.25
28 x 28 mm plate, 1.6 mm thickness			
P3-SS0.5-N_p45	3	0.5	45
P3-SS0.5-N_p67.1	3	0.5	67.1
P3-SS1-N_p50.38	3	1	50.38
P3-SS1.5-N_p21.88	3	1.5	21.88

3.4 Metallographic Sample Preparation

3.4.1 Sample sectioning

The samples were sectioned by electrical discharge machining using a Gold San CNC wire cutting EDM machine to cut out the LSPwC processed area and produce segments for analysis and

electrochemical corrosion tests. Figure 3.5 a) shows a sample after securing it tightly on the machine, Figure 3.5 b) is the EDM in operation and Figure 3.5 c) shows how three pieces were cut from the peened areas. For electrochemical tests, Segments 1 and 2 were utilised, while Segment 3 was dedicated to surface and cross-sectional analysis. Whenever the need for sectioning arose in other tests, EDM was used.

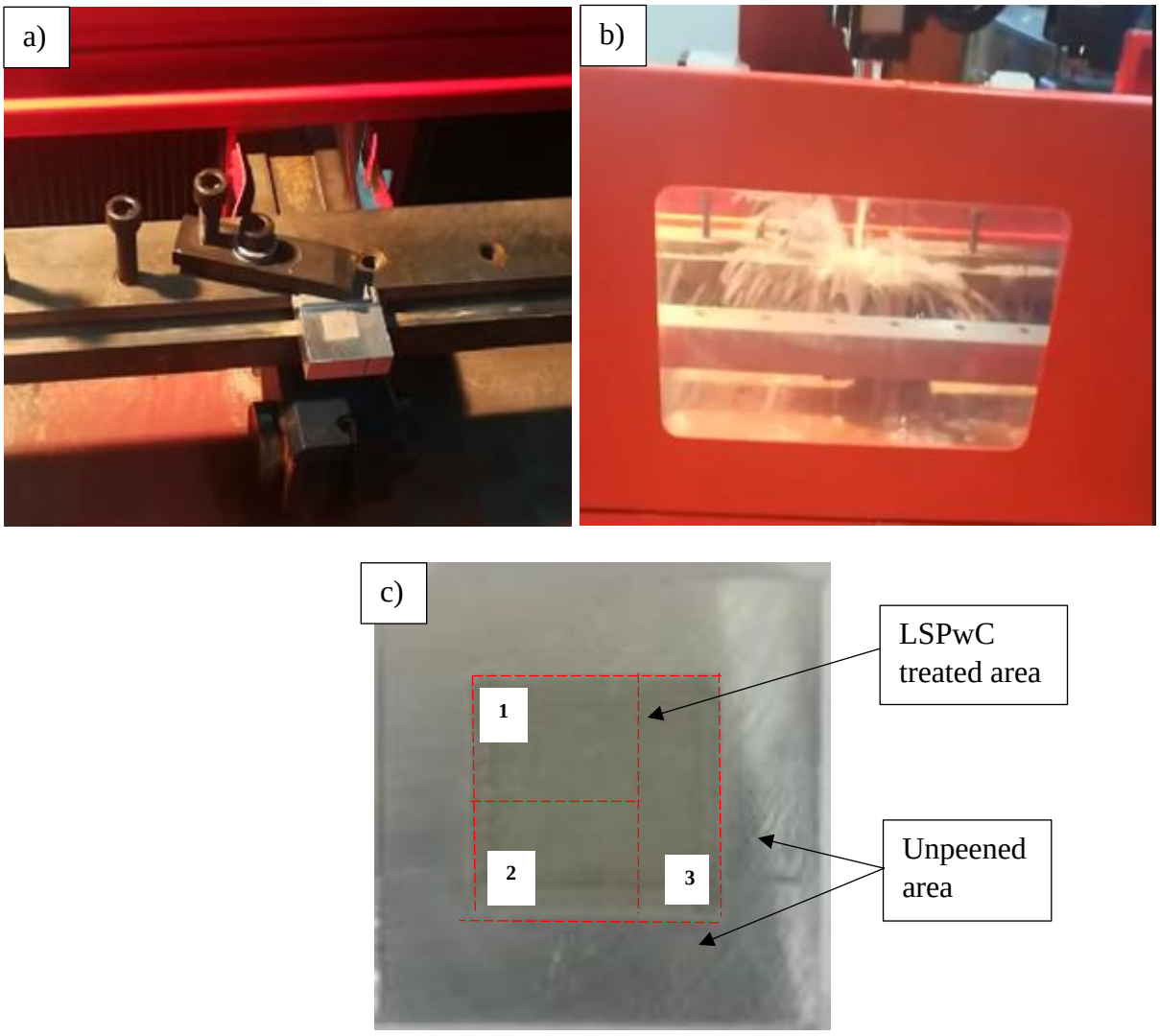


Figure 3.5. Photographs showing: a) sample placement, b) EDM cutting and c) segments obtained from the cutting.

3.4.2 Mounting

The sectioned samples were too small to handle and needed support for grinding and polishing in preparation for microhardness testing and microscopy. Samples for microhardness testing were cold-mounted, while those for scanning electron microscopy (SEM) were hot-mounted.

3.4.2.1 Cold Mounting

Akasel Aka-Clear-2 acrylic powder and liquid were used for cold mounting. The samples were thoroughly cleaned using ethanol before mounting. Vacuum grease was applied inside the mounting cup to allow easy removal when the mount had cured. The mixture was prepared according to the ratio of 2 volumes of powder to 1 volume of liquid and cured for approximately 10 minutes at room temperature.

3.4.2.2 Hot mounting

The samples which were prepared for scanning electron microscopy (SEM) were mounted in Struers PolyFast resin using an Opal 410 hot mounting press. This was done at 180°C for 6 minutes (3 minutes of heating and then water cooled for 3 minutes) under a constant pressure of 250 bar.

3.4.3 Grinding and polishing

Grinding and polishing were done to produce a mirror-like surface finish on the sample cross-sections for microscopy. The specimens were subjected to successive grinding steps with SiC papers of grit sizes 320, 500, 1000 and 1200. Water was used during grinding to cool the surface being ground and remove debris. Once the surface had been ground sufficiently, the samples were polished using the MD-Largo disk and 9 µm LECO diamond suspension. This was followed by MD-mol with 3 µm solution then MD-Chem with LECO Alpha Alumina powder solution. Between each preparation stage, water was used to remove contaminants to avoid cross-contamination from earlier polishing steps. After the samples were rinsed, they were cleaned with ethanol and dried with a hair dryer. The process was repeated where scratches were observed on the surface of the samples.

3.4.4 Etching

Etching was done by swabbing Keller's reagent on a freshly polished specimen. This solution was made by mixing 2 ml HF (48%), 3 ml HCl (concentrated), 5 ml HNO_3 (concentrated) and 190 ml distilled water. Each sample was immersed for 20 seconds and washed in a stream of warm water. The specimen changed colour to dark grey. A blow dryer was used to dry the specimen.

3.5 Microscopy

3.5.1 Optical and stereo microscopy

Images were taken of each etched sample on a Motic BA310Met microscope. Low magnification images of the peened sample surfaces were taken using a Nikon SMZ1500 stereo microscope.

3.5.2 Scanning electron microscopy

A ZEISS Sigma high resolution FE-SEM was used to study the samples' surface and cross-section at high magnifications to observe any surface damage and/or changes that occurred. The samples were examined in secondary electron (SE) mode which captures the topography and backscattered electron (BSE) mode to distinguish the different phases by their different contrasts due to different average atomic numbers. The composition of individual phases and overall analyses of large areas of the samples were analysed by energy dispersive X-ray spectroscopy (EDX). At least five measurements were taken for each composition; the average and standard deviation were reported.

3.6 Surface Roughness

Surface roughness measurements were performed to determine the effect of LSPwC on the surface of the samples. A Huatec SRT-6210 surface roughness tester was used with the variables listed in Table 3.2. The selection of parameters was obtained from the supplied manual and ISO 4288 (ISO 4288, 1996).

Table 3.2. Variables of the SRT-6210 surface roughness tester.

Property	**Specification**
Measuring range	R_a, R_q: 0.005-16.00 µm R_z, R_t: 0.020-160.0 µm
Material of probe pin	Diamond
Cut-off length	0.25 mm, 0.8 mm, 2.5 mm

The experiments were conducted in accordance with the ISO 4287 standard (ISO 4287, 1997). Measurements were done in both the laser scanning and stepping directions as shown in Figure 3.6 a). Each specimen was divided into five equidistant segments along the length and measurements were taken per parameter (Figure 3.6 b)) and the average of these was presented.

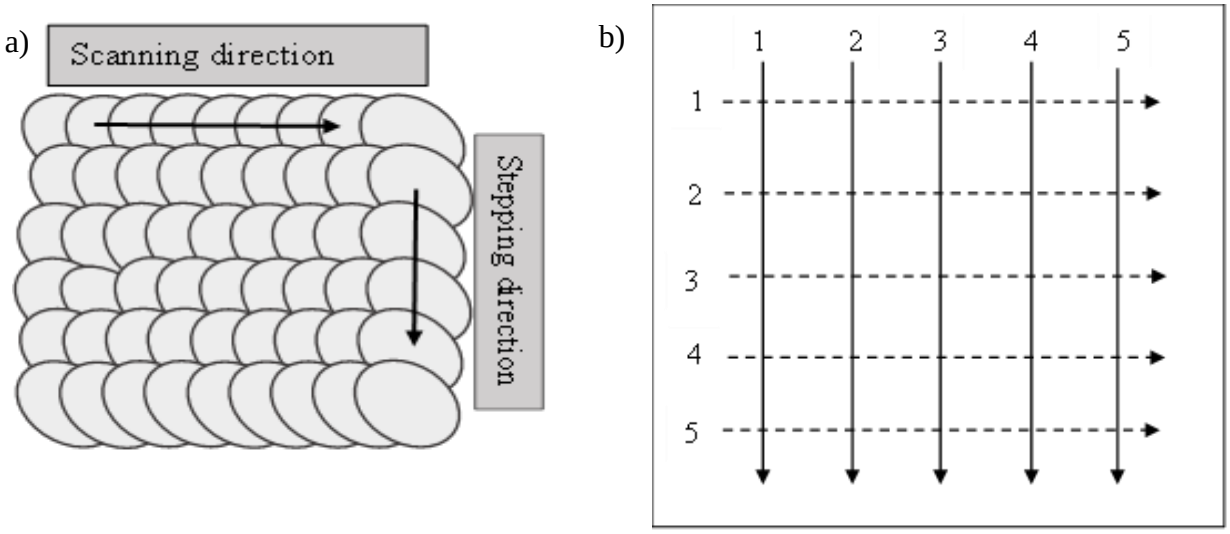


Figure 3.6. Method for surface roughness measurements: a) Peened area showing directions in which surface roughness profile was taken and b) pattern followed to obtain five measurements in each direction.

3.7 Microhardness Tests

Cross-sections of the specimen were prepared by cold mounting then grinding and polishing according to Section 3.4. The microhardness measurements were taken according to ASTM E92 (ASTM E92, 2017) using an Innovatest Falcon 500 hardness testing machine. This machine had a Vickers hardness indenter and two optical microscope objective lenses of magnifications 10x and 50x. The objective lenses were used for sample positioning and viewing the indentation so that its size could be measured. A load of 100 gf was applied to each sample for 10 s dwelling time. The resulting square indentation was measured to determine the hardness of the material. The spacing between each indention was guided by the minimum recommended spacing for Vickers tests as given by ASTM 384 (ASTM E384, 2022), at least 2.5 times the indentation diagonal between indentations and the edge of the specimen, Figure 3.7 a). Adhering to these standards, indentations were made at different depths (0.05, 0.15, 0.25, 0.35, 0.45, 0.60, 0.80, 1.00, 1.50, 2.00, 2.50, 3.00, 3.50 mm) from the peened surface, the pattern followed is given in Figure 3.7 b). At each depth, five indentations were made 0.5 mm apart along the cross-section and the average microhardness measurement (at each depth) and standard deviation were recorded.

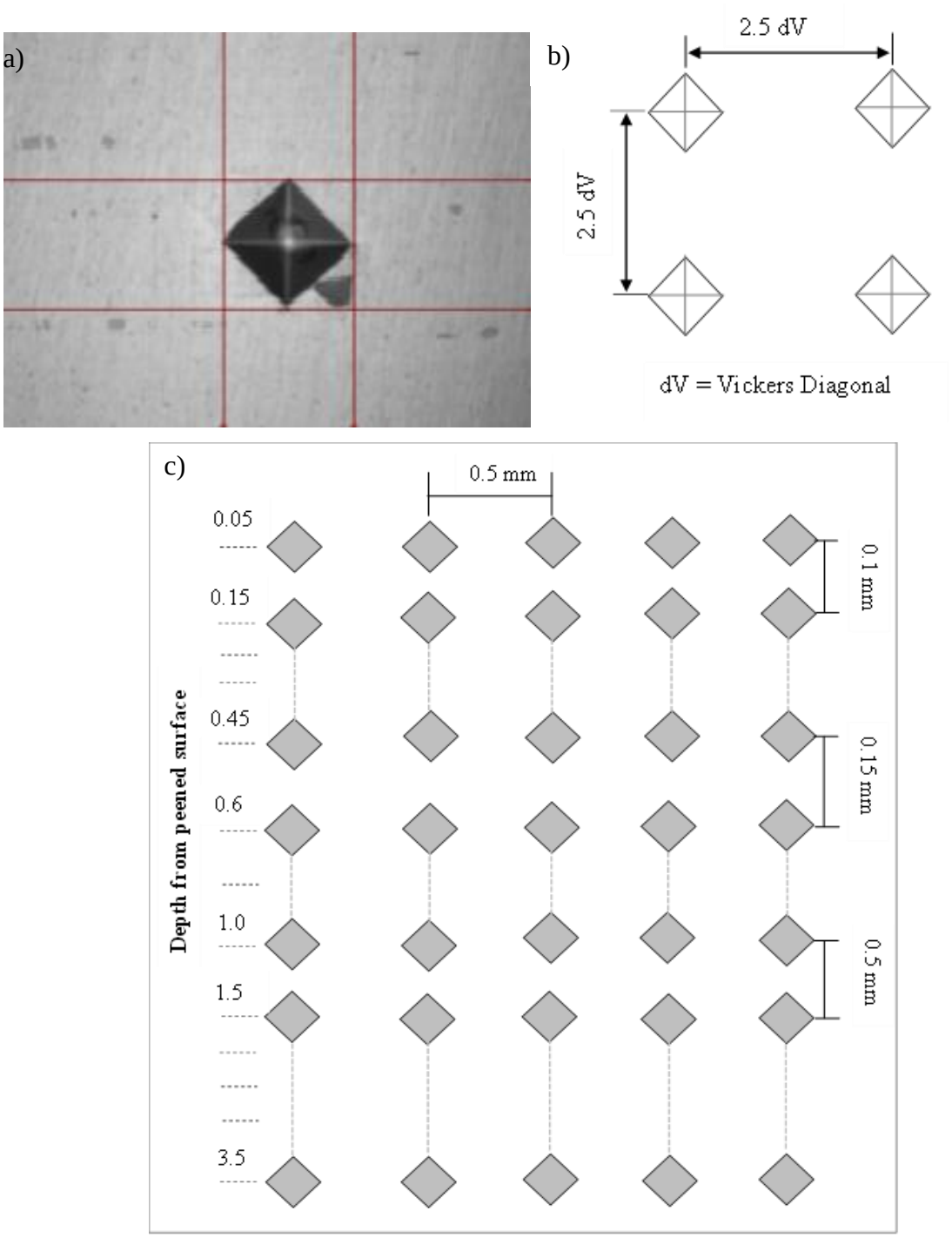


Figure 3.7. Vickers hardness measurements: a) micrograph of typical indentation b) minimum recommended spacing for Vickers indentations (ASTM E384, 2022) and b) indentation pattern adopted for the sample cross-section.

3.8 Corrosion Testing

Corrosion tests were carried out in chloride solutions due to the susceptibility of aluminium to corrosion in the presence of chloride ions. To simulate marine environments, 3.5 wt% NaCl solutions were used. Various salt concentrations discovered in different oceans are listed in Appendix 2. A fresh NaCl solution was prepared for each experiment.

3.8.1 Potentiodynamic polarisation tests

The samples were sectioned using EDM to present the peened surface for corrosion testing. The area exposed to corrosion was 28.3 mm^2 and rubber was used for masking the unexposed surface. A conventional three-electrode electrochemical cell connected to an AutoLab® potentiostat/galvanostat was used for the electrochemical test. A graphite rod was the counter electrode, Ag/AgCl saturated in 3 M KCl was the reference electrode and the test sample was the working electrode as shown in Figure 3.8a). The cross-section of the cell is shown in Figure 3.8b). All tests were carried out in 3.5 wt% NaCl solution at room temperature.

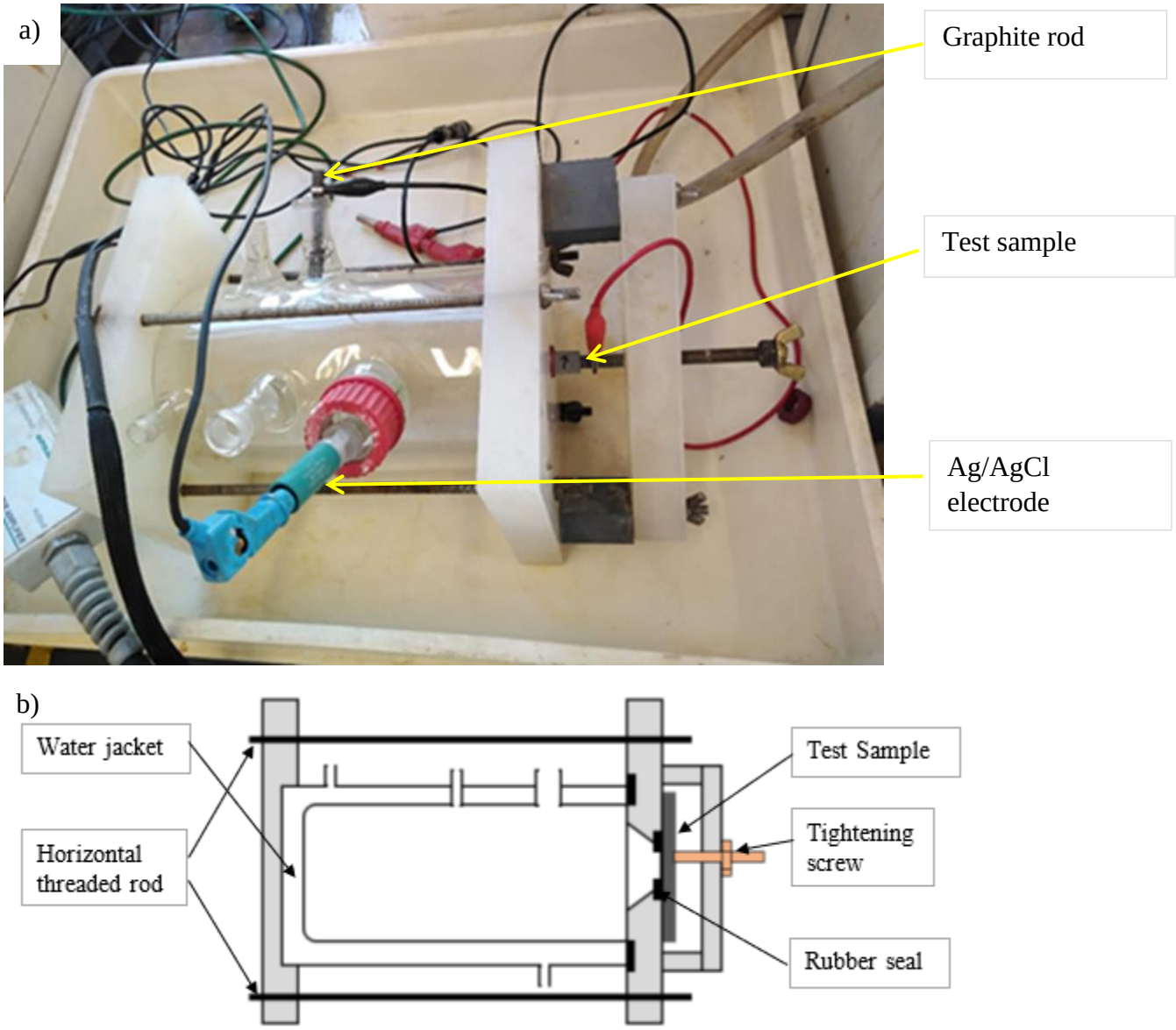


Figure 3.8. Corrosion cell a) photograph b) cross-section.

The samples were exposed to the corrosive environment and open circuit potential (OCP) was measured for one hour to determine the reactivity of the alloys in solution at zero applied current. Potentiodynamic polarisation scans were done after the OCP measurements at 1 mV/s scan rate from -0.5 V to 1 V. The tests were performed in duplicate by testing two identical samples. After each polarisation scan, the solution was replaced with a freshly prepared one.

The corrosion potential and current were obtained from the polarisation experimental data. The corrosion current density and corrosion rates were determined using Equations 3.1-3.3 by ASTM standards G59-97 and G102-89 (ASTM G59, 2014; ASTM G102, 2015).

$$i_{corr} = \frac{I_{corr}}{A} \qquad \textit{Equation 3.1}$$

$$i_{corr} = 10^{6} \frac{B}{R_p} \qquad \textit{Equation 3.2}$$

$$CR = k \frac{i_{corr}}{\rho} EW \qquad \textit{Equation 3.3}$$

where:

i_{corr} = Corrosion current density ($\mu A/cm^2$)

I_{corr} = Corrosion current (μA)

A = Exposed sample area (cm^2)

R_p = Polarisation resistance (ohms)

E_{corr} = Corrosion potential (V)

B = Stern-Geary constant (V)

CR = Corrosion rate (mm/y)

K = 3.27×10^{-3} (mm g/μA cm y)

ρ = Density (g/cm^3)

EW = Equivalent weight (g).

After the electrochemical tests, the samples were removed, rinsed with deionised water and dried. Thereafter, SEM-EDX was used to determine the corrosion products and surface morphology.

3.8.2 Full immersion corrosion tests

Immersion corrosion tests were carried out on 28x28 mm samples that were 10 mm thick. The unpeened Sample 0 and Sample P3-SS1.5-N_p5, which was peened at a laser power intensity of 3 GW/cm^2, spot size of 1.5 mm and coverage of 5 spots/mm^2, were corroded using ASTM G31 in 3.5 wt% NaCl solutions. These samples were available in sufficient numbers to allow for tests in duplicates. The samples were weighed and suspended in a plexiglass container holding the solution. The total exposure time was 30 days with samples removed from the testing environment at 3, 7, 14, 21 and 30 days for analysis. After immersion, the specimens were cleaned with a nylon brush, rinsed with deionised water and blow-dried. Upon inspection under a microscope, it was noted that there was still some corrosion product, so the samples were immersed in nitric acid for 10 minutes (Kerrer & Kelly, 2001) for further cleaning then blow-dried and reweighed. The tests were performed in duplicate and the standard deviation was calculated (ASTM G31-72, 1999). The average corrosion rate, in millimetres per year (mm/y), was calculated using Equation 3.4.

$$Corrosion\ rate = \frac{K \times W}{A \times T \times D} \qquad \textit{Equation 3.4}$$

where:

K = 8.76 x 10^4

W = mass loss in g to the nearest 1mg

A = area in cm^2 to the nearest 0.01

T = time of exposure in hours to the nearest 0.01 h

D = density in g/cm^3.

The surfaces were studied using optical microscopy and SEM-EDX.

3.8.3 Stress corrosion cracking tests

Samples of four different LSPwC parameter combinations were chosen for stress corrosion cracking (SCC) testing. The dimensions of the samples were 28x28 mm and 1.6 mm thickness, with a peened area of 14x14 mm using a laser power intensity of 3 GW/cm^2. Laser spot size and coverage were varied as shown in Table 3.3. An unpeened Sample 0 of the same size was included for comparison.

Table 3.3. Samples used for SCC testing.

Sample Name	**Spot Size (mm)**	**Coverage (spots/mm^2)**
P3-SS0.5-N_p67.1	0.5	67.1
P3-SS0.5-N_p45	0.5	45
P3-SS1-N_p50.38	1	50.38
P3-SS1.5-N_p21.88	1.5	21.88

The three-point bending method was chosen because it allows for easy identification of the point of the highest level of stress and enables the movement of samples while still under stress. This technique also allows for visual inspection at low magnification and can accommodate testing many samples simultaneously and for extended periods (Al-Haidary *et al*., 2020). In three-point loaded specimens, the sample is subjected to both tensile and compression stresses where the tensile stress is on the upper surface and the compression stress is on the lower surface. The maximum bending stress occurs at the centre of the specimen and decreases linearly to zero at the outer supports and the expected results should be at the tensile surface at the maximum stress (Al-Haidary *et al*., 2020).

The samples were prepared following the ASTM G39 (G39 - 99, 2016) standard. The sample holder was designed to hold five samples simultaneously and the specifications used for making it are shown in Figure 3.9a) (more detail is given in Appendix 3). A diagram of a typical sample under stress is shown in Figure 3.9b) and all five samples are shown in Figure 3.9 c). Samples were isolated at the points of contact using layers of PTFE tape to prevent any metallic contact, which can cause cathodic or crevice corrosion. The samples under static load were immersed in 3.5 wt% NaCl solution kept at 25°C and were removed from the solution after 40 days.

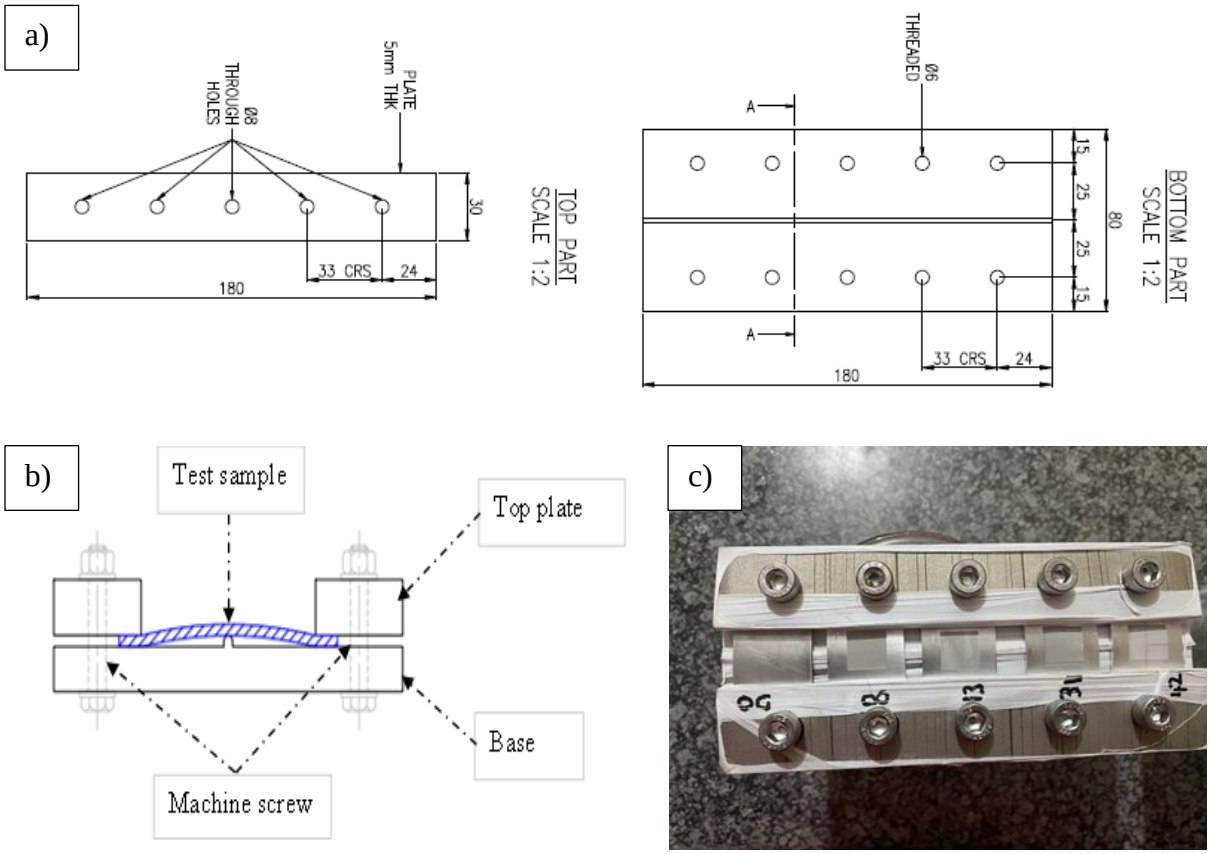


Figure 3.9. Sample holder for SCC: a) design specifications, b) schematic diagram of typical test sample under three-point bending and c) photograph of loaded samples.

Determination of the magnitude of stress subjected to each sample was done using Equation 3.5.

$$\sigma = {}^{6Ety}/_{H^2} \qquad \textit{Equation 3.5}$$

where:

σ = maximum tensile stress

E = Young's modulus of elasticity of AA7075 (Table 2.4)

t = thickness of specimen

y = maximum deflection

H = distance between outer supports.

CHAPTER 4: RESULTS

4.1 Introduction

This chapter contains the findings from experiments on Laser Shock Peening without Coating (LSPwC) of AA7075-T651, focusing on surface characteristics and corrosion behaviour. Analytical techniques used included scanning electron microscopy (SEM), contact profilometry, Vickers microhardness testing and electrochemical investigations. The SEM results revealed topographical changes, while surface roughness tests showed the alterations induced by LSPwC. Vickers microhardness results indicated depth-dependent hardness. Potentiodynamic polarisation gave the metal's E_{corr}, i_{corr} and corrosion rate. Longer-term corrosion performance was evaluated by tests, showing surface alterations, weight loss and corrosion rate after 30 days. Stress corrosion tests in a 3.5 wt% NaCl solution for 40 days assessed resistance to environmentally assisted cracking.

4.2 Analysis of AA7075-T651 as the Control Sample

The control sample (Sample 0) was the unpeened AA7075-T651 which was analysed to compare with the samples modified with LSPwC. The SEM-SE image (Figure 4.1a) shows the topography of the surface which was smooth (from the polishing) apart from a few particles indicated by the red arrows. Figure 4.1b) indicates the composition difference of the surface. Across the bulk of the metal, there were different precipitates of varying sizes and shapes. The white particles were elongated and aligned in the rolling direction. There were also some dark spots distributed over the whole sample.

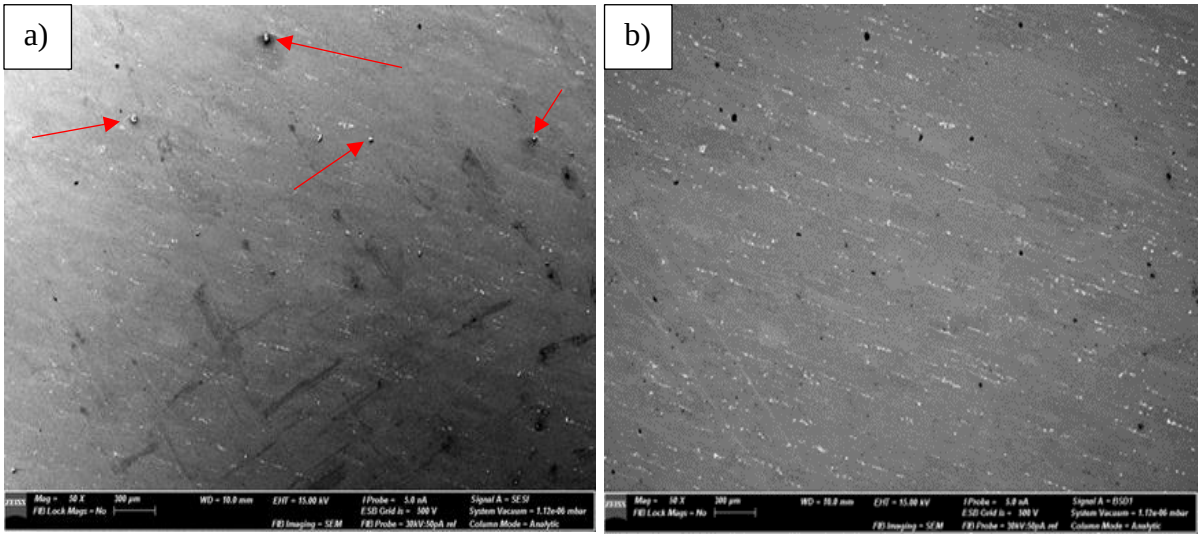


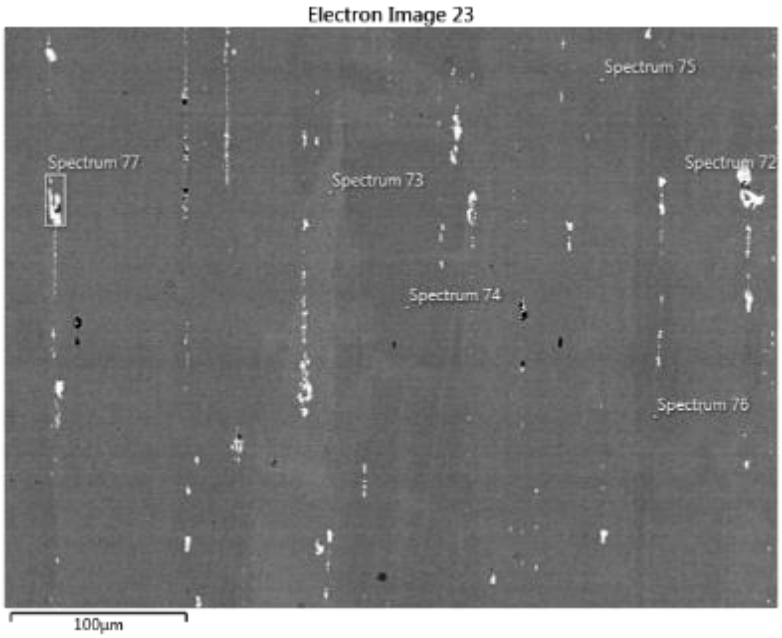
Figure 4.1. SEM images of the unpeened Sample 0: a) SEM-SE showing topography and b) SEM-BSE showing composition with red arrows indicating particles on the surface.

The composition of AA7075-T651 was obtained from the EDX analyses of the surface, Table 4.1. These results matched the specifications provided by the manufacturer 'NK Cutting' (Chapter 3) and agreed with the specifications given by the Aluminium Association (The Aluminium Association, 2018). The light precipitates comprised Cu and Fe which varied as indicated by the high standard deviation. An EDX spectrum for one of the light precipitates is shown in Figure 4.2.

Table 4.1. EDX results of the unpeened Sample 0.

		Al	**Zn**	**Mg**	**Cu**	**Cr**	**O**	**Fe**
Overall surface	wt%	89.1 ± 1.2	6.3 ± 0.3	2.6 ± 0.1	1.4 ± 0.1	0.2 ± 0.0	0.4 ± 0.1	-
	at.%	93.4 ± 0.9	2.8 ± 0.2	2.7 ± 0.1	0.6 ± 0.1	0.2 ± 0.0	0.3 ± 0.1	-
White precipitates	wt%	68.4 ± 3.5	4.2 ± 0.4	1.2 ± 0.5	7.0 ± 1.1	-	-	19.2 ± 4.1
	at.%	79.6 ± 2.6	3.9 ± 0.3	1.7 ± 0.7	5.3 ± 0.7	-	-	9.5 ± 4.2

a)



b)

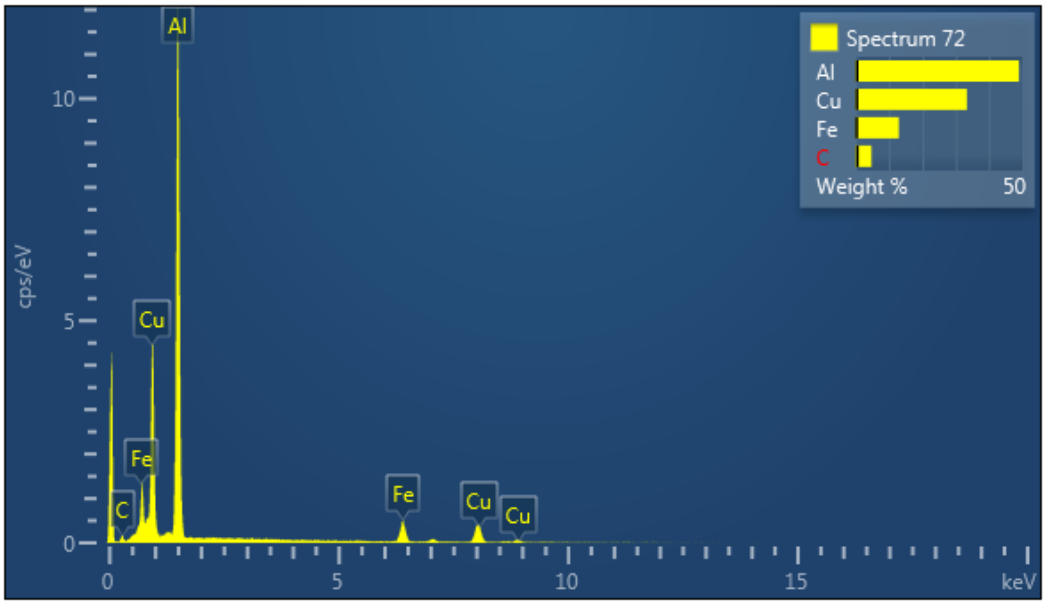


Figure 4.2. a) SEM-BSE image of Sample 0 cross-section showing light precipitates and b) EDX spectrum of the precipitates.

The microstructure of Sample 0 is shown in Figure 4.3 showing pancake-shaped grains elongated in the rolling direction.

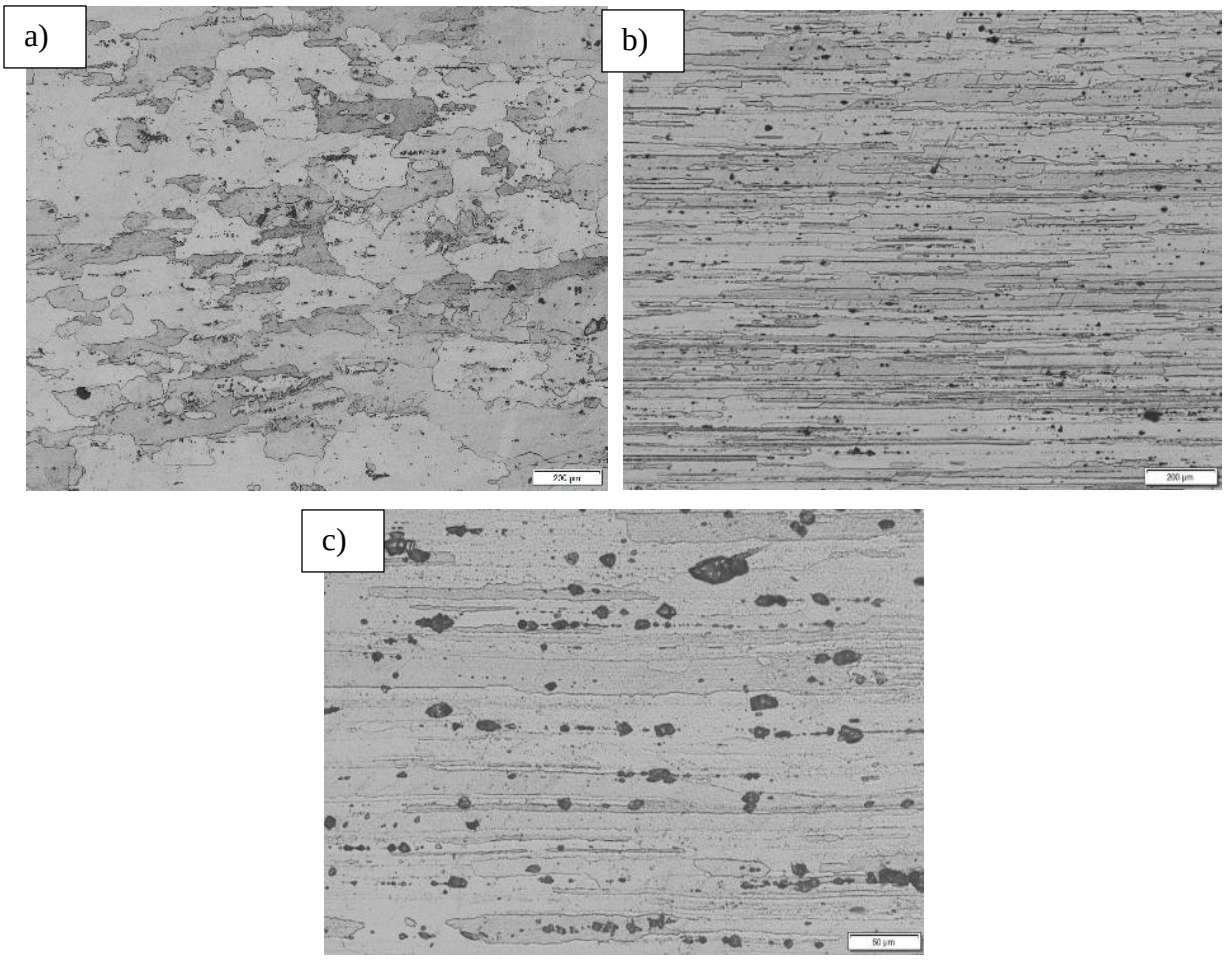


Figure 4.3. Optical images showing the microstructure of AA7075-T651 at different orientations: a) top surface in the transverse direction (to original rolling), b) cross-section in the longitudinal direction at lower and c) higher magnification.

4.3 Surface Morphology After LSPwC

The surface lustre changed from shiny metallic to dull light grey after LSPwC as shown in Figure 4.4 for the surface of sample P3-SS1.5-N_p21.88. The peened surface had many irregularities compared with the smooth unpeened surface.

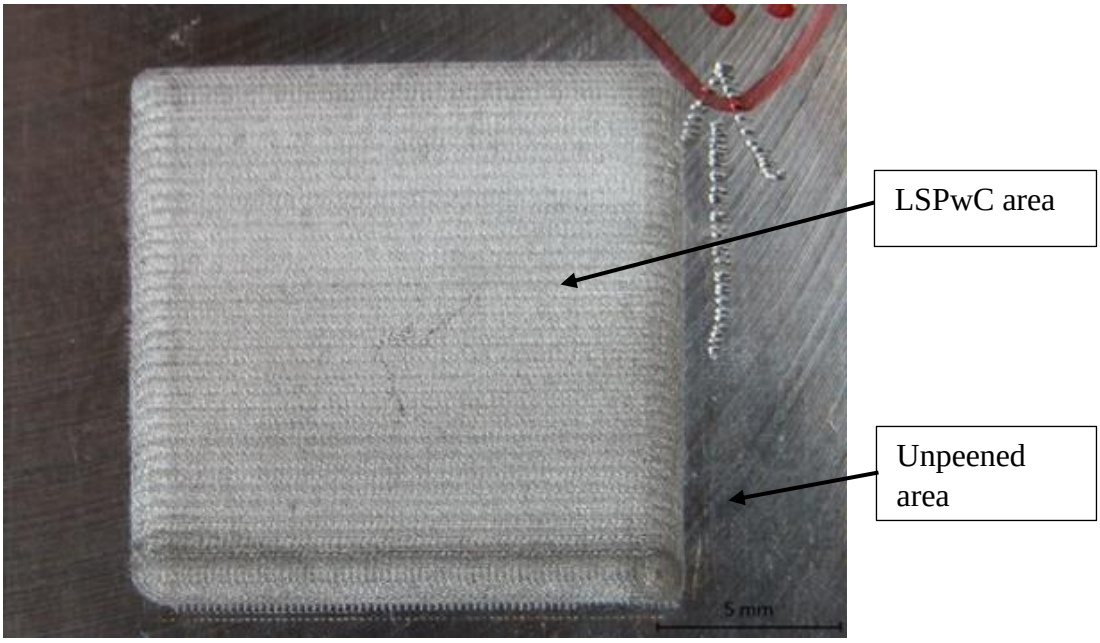


Figure 4.4. Stereo microscope image of the surface of P3-SS1.5-N_p20 after LSPwC.

The SEM-BSE image in Figure 4.5 shows the surface of P1.5-SS1-N_p11.25 treated with PI = 1.5 GW/cm^2, SS = 1 mm and N_p= 11.25 spots/mm^2 which had signs of melting and solidification.

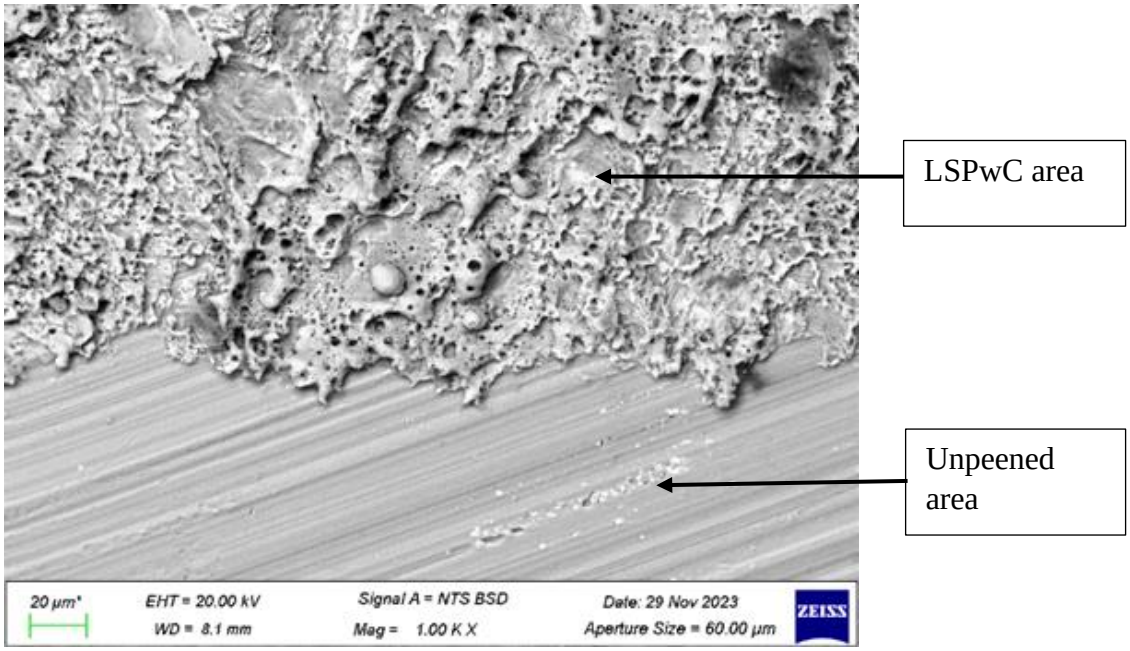


Figure 4.5. SEM-BSE image of the surface of P1.5-SS1-N_p11.25 showing the peened-unpeened interface after LSPwC, with some solidified droplets.

4.3.1 Varying N_p at constant PI and SS

The surface of the low coverage of 2.5 spots per mm^2 showed sequential laser spots, Figure 4.6a). There was little overlap of the laser spots which can be seen almost in full as indicated by the dotted red circles. There were some areas which retained a smooth finish which were left out in the peening pattern indicated by the dotted red arrows. At higher magnification (Figure 4.6b), the splash-like pattern of molten metal was more visible with a centre and splatter on the outer regions. The centre exhibited minimal metal flow, although the metal did ablate. In Figure 4.6c) and d), the solidified droplets are clearer with a high density of pores.

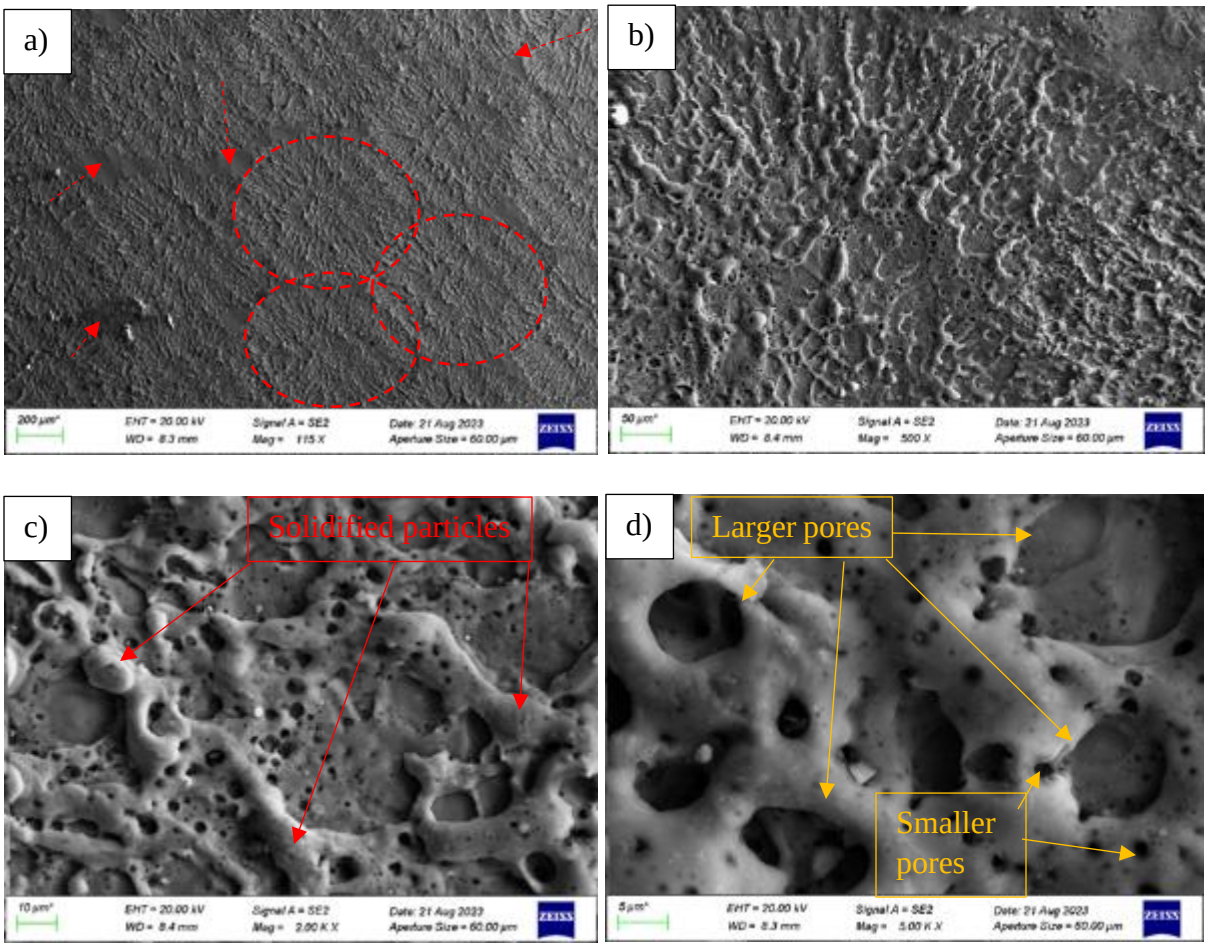


Figure 4.6. SEM-SE images of P3-SS0.8-N_p2.5 surface at different magnifications, showing laser spots (dotted red circle and arrows), solidified ablated particles (red arrows) and pores (orange arrows).

For a higher N_p of 20 spots per mm^2, the surface morphology is shown in Figure 4.7. The laser scanning path formed ridges as indicated in Figure 4.7a) (one such scanning path is indicated by the two parallel red dotted lines) and are due to the edges of laser spots. There were greater spot overlaps, hence individual laser spots were not distinguishable, even at higher magnification as shown in Figure 4.7b). At higher magnification (Figure 4.7c) and Figure 4.7d), pores and voids were indistinguishable on the roughened surface. The higher coverage induced more damage and a greater modification from melting and solidification.

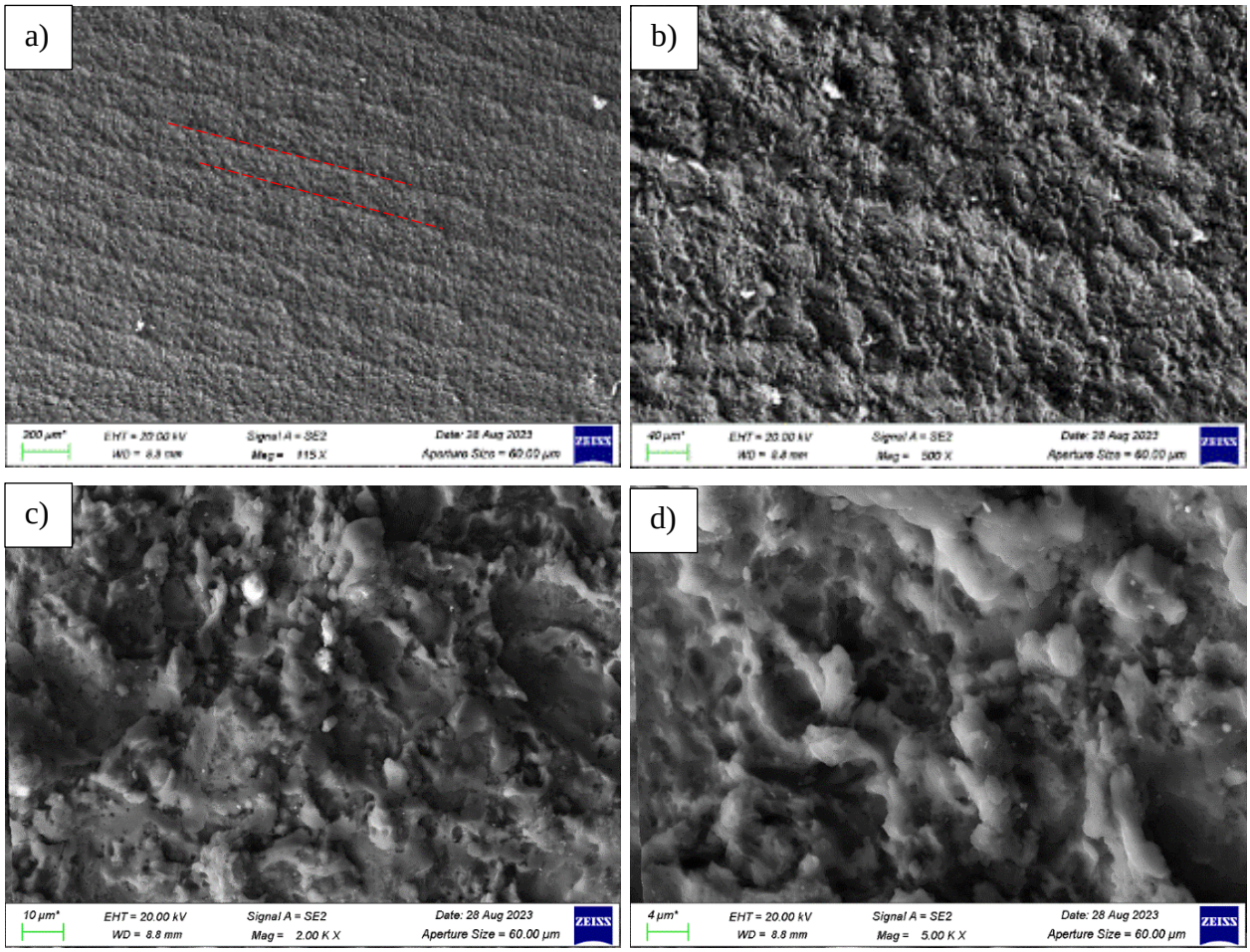


Figure 4.7. SEM-SE images of P3-SS0.8-N_p20 surface at increasing magnifications a) – d), showing peening paths (red lines), ablated products and few pores.

4.3.2 Varying PI at constant SS and N_p

The SEM-SE images for the surfaces of samples peened with PI values of 1, 3 and 5 GW/cm^2, an SS of 0.8 mm and N_p of 40 spots/mm^2 are shown in Figure 4.8 (which are images of the non-corroded areas of the corroded samples). As PI increased, the spots appeared more defined and this effect was more pronounced as PI changed from 1 GW/cm^2 (Figure 4.8a) to 3 GW/cm^2 (Figure 4.8b) to 5 GW/cm^2 (Figure 4.8c).

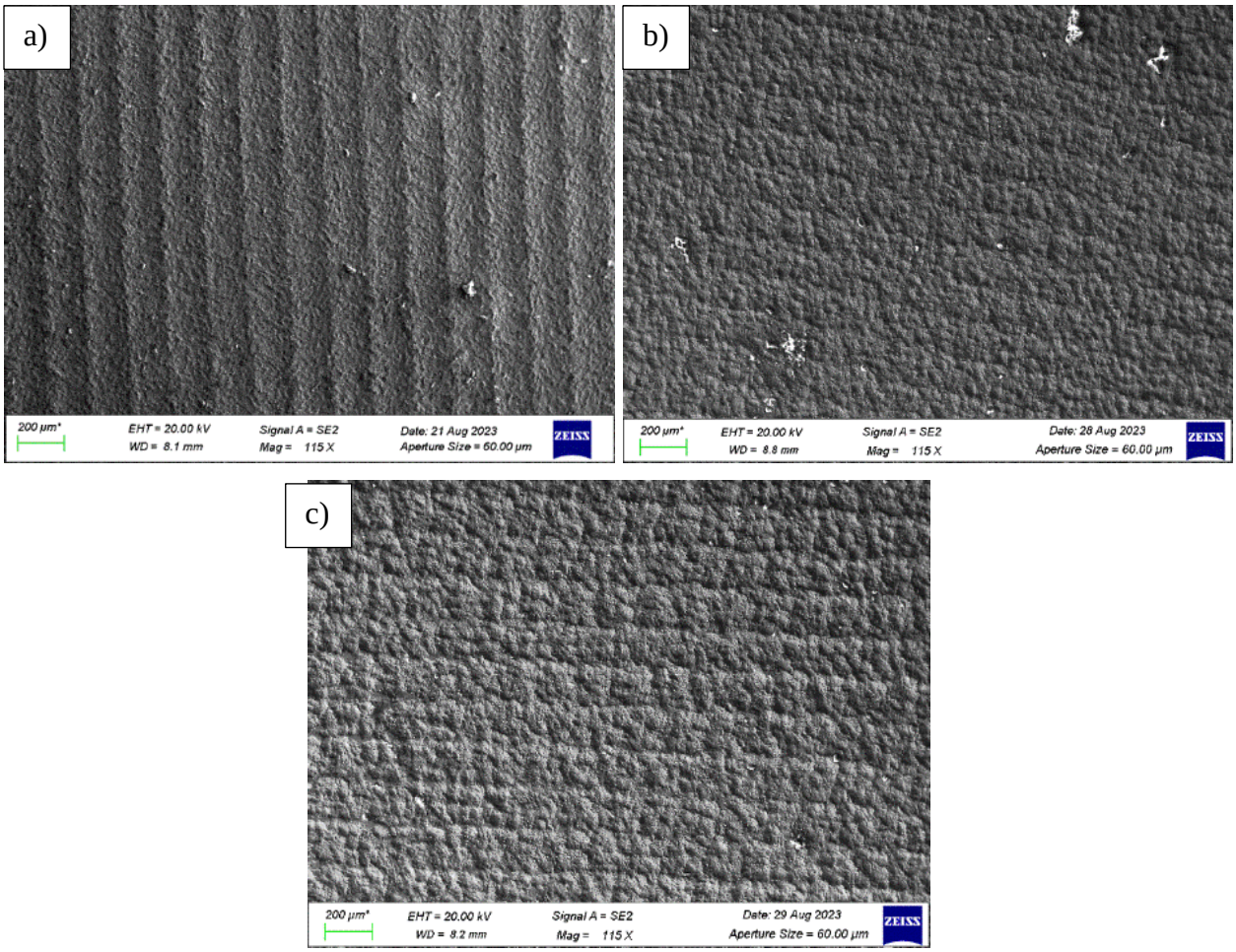


Figure 4.8. SEM-SE images of peened surfaces showing topographic differences at varying PI (GW/cm^2): a) PI=1 b) PI=3 c) PI=5 and constant SS=0.8 mm and N_p=40 spots/mm^2 (white particles in a) and b) are corrosion products).

The SEM-BSE images for the samples peened with PI values of 1.5, 3, 4.5 and 6 GW/cm^2, an SS of 1 mm and N_p of 11.25 spots/mm^2 are shown in Figure 4.9. At the lowest PI (Figure 4.9a)), there were many irregular features and as PI increased, the solidified "mounts" became the most prominent feature and larger.

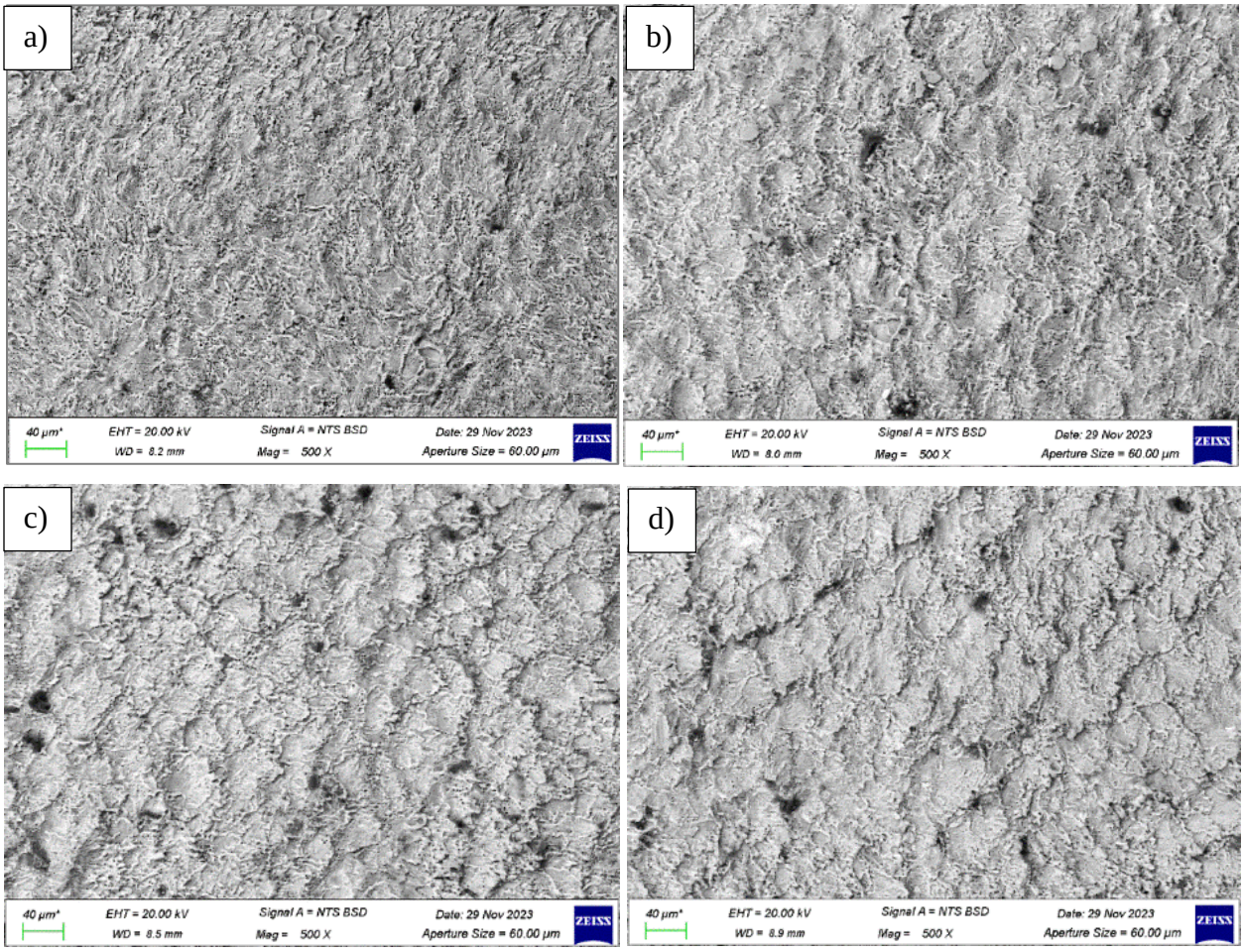


Figure 4.9. SEM-BSE images of PI of a) 1.5 b) 3 c) 4.5 d) 6 GW/cm^2 surfaces showing surface irregularities at varying PI.

4.3.3 Varying SS at constant PI and N_p

At constant PI of 3 GW/cm^2 and N_p of 2.5 spots/mm^2, two spot sizes (SS), 0.8 mm and 1.5 mm were used. At the lower SS (Figure 4.10a) there was a smaller overlap of the spots compared to the surface of 1.5 mm shown in Figure 4.11a). At higher magnification, there were multiple pores and solidified droplets at SS = 0.8 mm which are indicated by red arrows in Figure 4.10b). At SS = 1.5 mm there were fewer pores which were not as pronounced (Figure 4.11b).

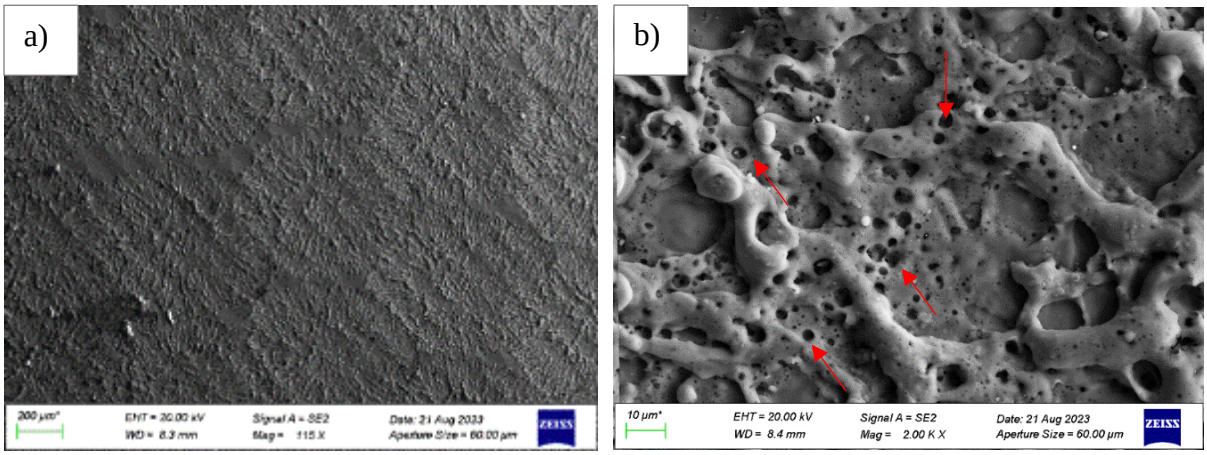


Figure 4.10. SEM-SE images of P3-SS0.8-N_p2.5 surface at: a) lower and b) higher magnification showing pores (red arrows).

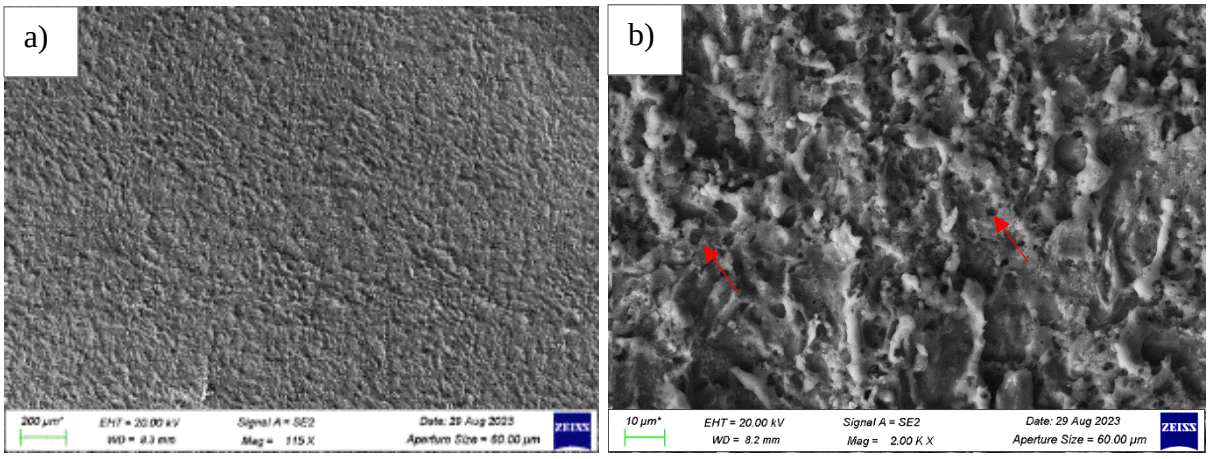


Figure 4.11. SEM-SE images of P3-SS1.5-N_p2.5 surface at: a) lower and b) higher magnification, showing pores (red arrows).

The SEM-SE image in Figure 4.12 shows the surface topography of P3-SS0.8-N_p10 which was rougher than the unpeened sample (Figure 4.1). In Figure 4.12b, the roughened surface showed evidence of melting and subsequent solidification by the solidified "mounts" and pores. Figure 4.13 shows the SEM-BSE image of P3-SS1.5-N_p10's surface after peening showing solidified droplets.

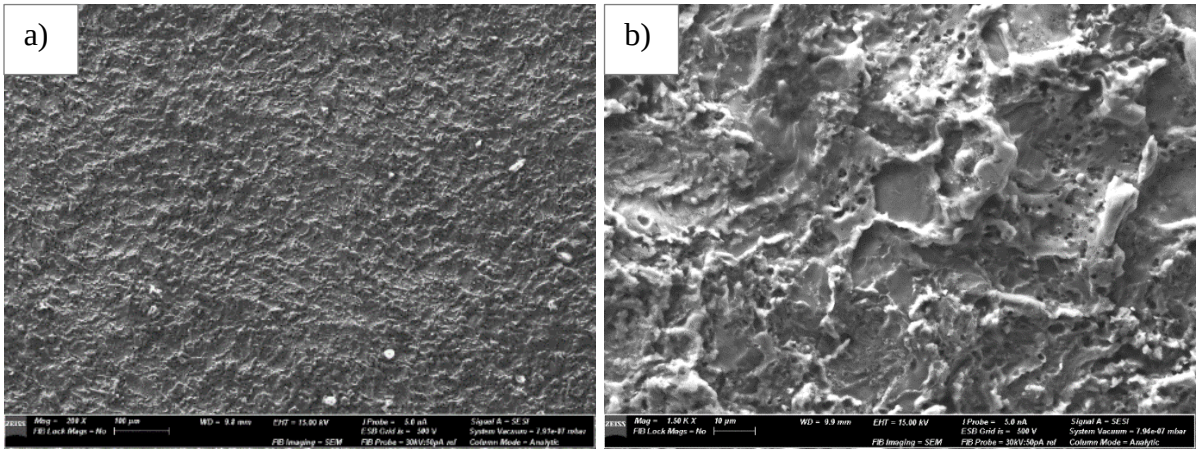


Figure 4.12. SEM-SE micrographs of P3-SS0.8-N_p10 *surface at: a) lower and b) higher magnification showing "mounts" and flatter areas from LSPwC.*

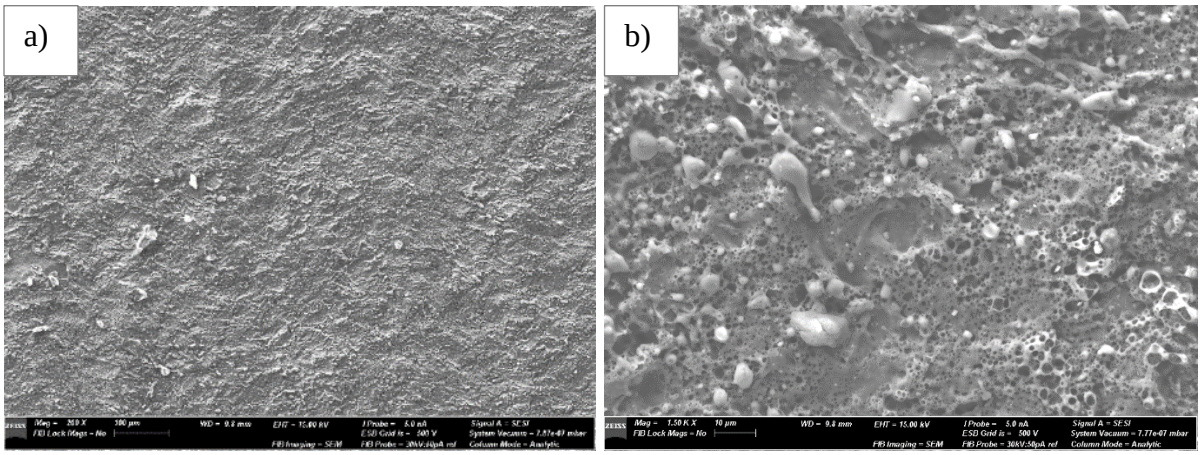


Figure 4.13. SEM-SE micrographs of P3-SS1.5-N_p10 *surface at: a) lower and b) higher magnification showing solidified droplets from LSPwC.*

4.4 Cross-sections after LSPwC

4.4.1 Cross-section of P3-SS0.8-N_p10

This sample underwent LSPwC at a power intensity of 3 GW/cm^2, a spot size of 0.8 mm and a coverage of 10 spots/mm^2. Figure 4.14 shows a cross-section of the melted surface of the LSPwC treated metal, which was uneven. In Figure 4.14b) the pores in the melted parts are more visible, especially in the protrusion circled in red. There were also micro-cracks within 30 µm from the surface than within the substrate.

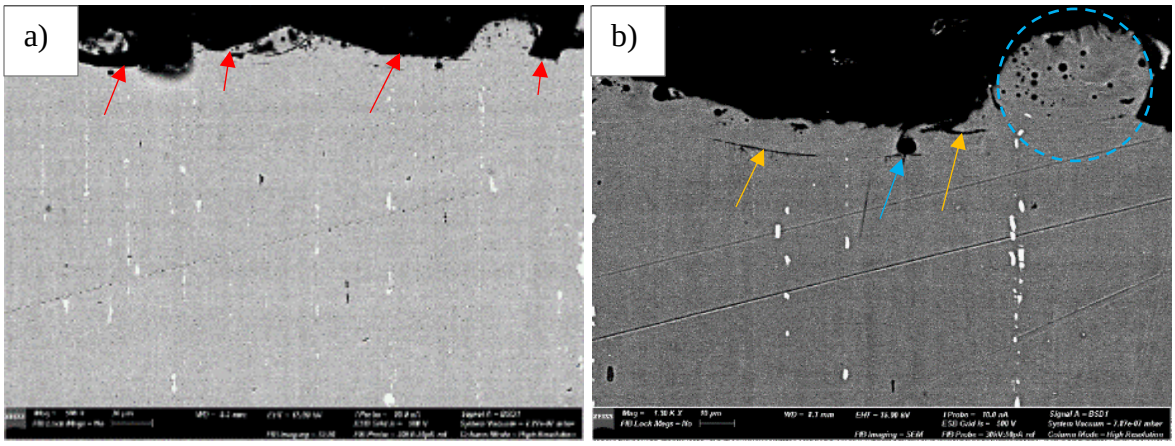


Figure 4.14. SEM-BSE images of P3-SS0.8-N_p10 cross-section at: a) lower and b) higher magnification, showing depressions (red arrows), pores (blue arrow and circle) and cracks (yellow arrows).

The EDX results for P3-SS0.8-N_p10 are listed in Table 4.2. The LSPwC area had high O content and the standard deviation of Al and O indicated the variation of compositions at the various points. At ~30 µm depth, analysis was done on the dark spot, likely a hole (blue arrow in Figure 4.14b)) and high O was detected. Further down the cross-section, there was no correlation between depth and O content, although there was a small amount of oxygen at 61 µm depth.

Table 4.2. EDX results of P3-SS0.8-N_p10.

		Al	**Zn**	**Mg**	**Cu**	**Si**	**O**
LSPwC region	wt%	80.1 ± 2.7	5.7 ± 0.6	2.4 ± 0.2	0.5 ± 0.1	2.0 ± 1.0	9.3 ± 2.6
	at.%	77.4 ± 4.1	2.4 ± 0.3	2.6 ± 0.2	0.2 ± 0.1	1.8 ± 0.9	15.6 ± 3.9
Cross-section							
Depth (µm)		**Al**	**Zn**	**Mg**	**Cu**	**Si**	**O**
30	wt%	38.9	1.6	18.3	3.3	-	38.0
	at.%	37.7	0.5	14.4	2.1	-	45.4
44	wt%	91.5	6.0	2.5	0.0	-	0.0
	at.%	94.8	2.4	2.7	0.0	-	0.0
61	wt%	89.0	6.7	2.4	1.7	-	0.2
	at.%	93.2	2.9	2.8	0.7	-	0.4
74	wt%	89.5	6.5	2.5	1.5	-	0.0
	at.%	93.8	2.7	2.8	0.7	-	0.0

4.4.2 Cross-section of P3-SS1.5-N_p10

The melted surface of the LSPwC treated metal is shown in the cross-section in Figure 4.15. There were “mounts” and micro-cracks within 30 µm below the “hollows”.

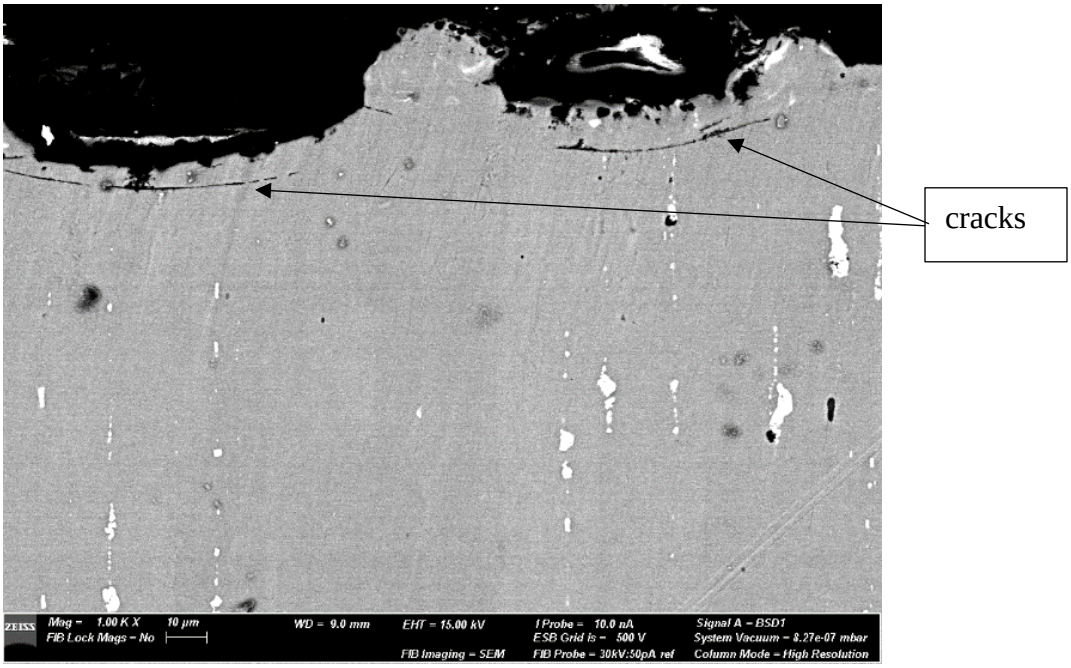


Figure 4.15. SEM-BSE image of P3-SS1.5-N_p10 cross-section, showing hollows and mounts from LSPwC.

The EDX results for P3-SS1.5-N_p10 are listed in Table 4.3. The LSPwC area had high O content. Analysis of the cross-section found higher O content closest to the surface, ~25 µm depth, and not below.

Table 4.3. EDX results of P3-SS1.5-N_p10 cross-section.

Description		**Al**	**Zn**	**Mg**	**Cu**	**O**
LSPwC region	wt%	80.5±0.8	5.7±0.1	2.6± 0.3	2.7±0.1	8.5±0.1
	at.%	84.0±1.3	3.6±0.0	3.0±0.2	0.6±0.0	8.8±0.2
Cross-section						
Depth (µm)		**Al**	**Zn**	**Mg**	**Cu**	**O**
25	wt%	89.4	5.7	1.8	1.6	1.5
	at.%	93.1	3.3	1.8	0.8	1.1
56	wt%	89.7	6.2	2.3	1.8	0.0
	at.%	94.8	2.3	2.3	0.7	0.0
65	wt%	92.7	5.2	2.2	0.0	0.0
	at.%	96.2	1.8	2.0	0.0	0.0

4.5 Surface Roughness

Higher roughness was observed for all samples after LSPwC (Figure 4.17). Most samples showed higher surface roughness in the stepping direction than in the scanning direction. The largest difference in roughness was found in P1-SS0.8-N_p40 and the smallest was in P3-SS0.8-N_p40. The roughness was lower in the stepping direction than in the scanning direction (stepping and scanning directions illustrated in Figure 3.6) for P3-SS0.8-N_p2.5 and P3-SS1.5-N_p2.5. Sample P5-SS0.8-N_p40 had the roughest surface.

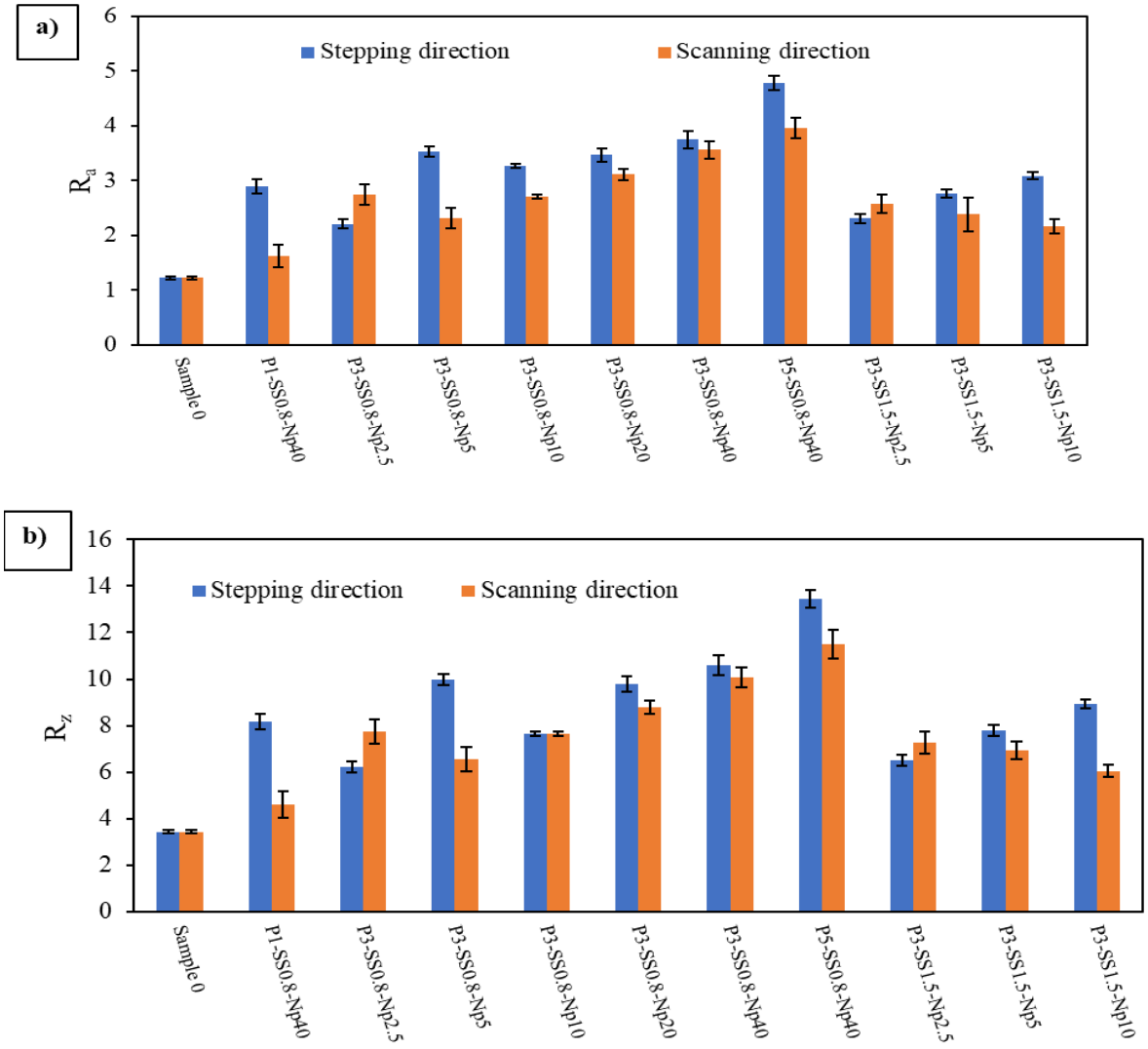


Figure 4.16. Surface roughness a) R_a (mean vertical deviation) b) R_z (distance between the averages of the five highest peaks and lowest valleys) for unpeened and peened samples in the scanning and stepping directions.

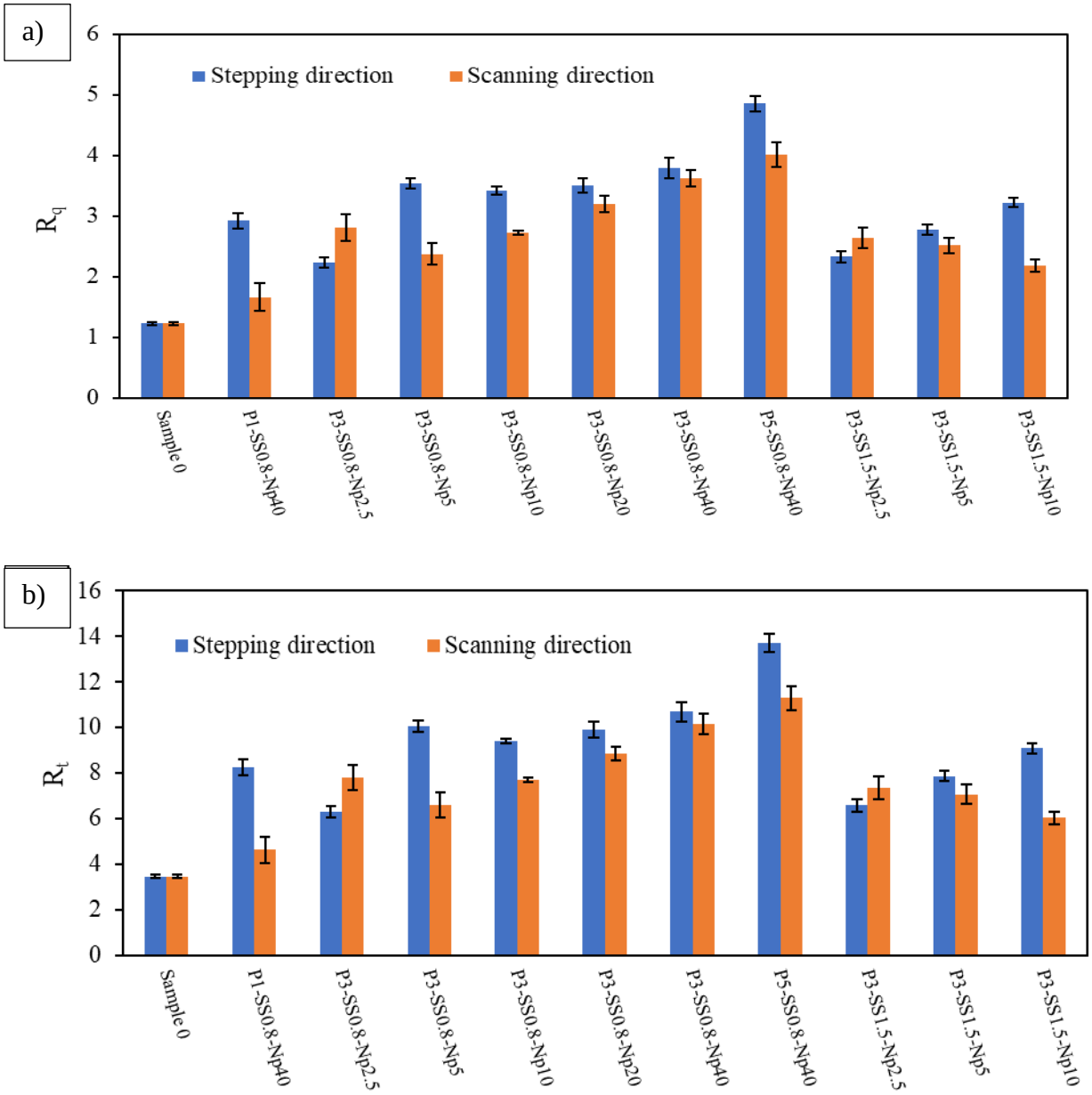


Figure 4.17. Surface roughness a) R_q (square root of the mean of the square of vertical deviation), b) R_t (distance between the highest peak and lowest valley) for unpeened and peened samples in the scanning and stepping directions.

4.6 Microhardness

Most indentations looked like Figure 3.7a) but occasionally there was barrelling Figure 4.18a) and a combination of pin cushioning and barrelling Figure 4.18b).

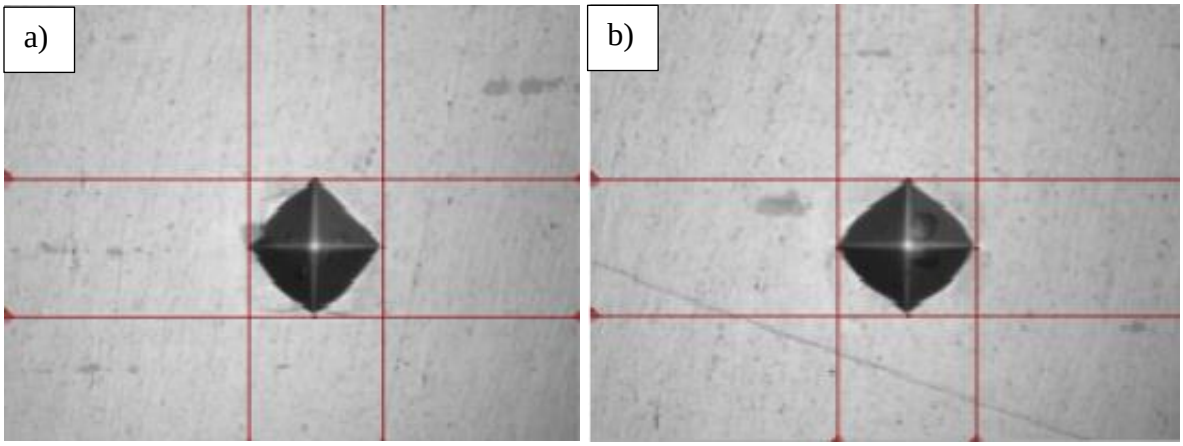


Figure 4.18. Optical microscope image showing Vickers indentation with a) barrelling and b) a combination of barrelling and pin cushioning.

The Vickers microhardness results are shown in Figure 4.19 of peened and unpeened samples as a function of surface depth. Peened samples had higher microhardness than the unpeened ones. The highest microhardness was closest to the peened surface and decreased with increasing depth. Down to 1.5 mm, the results fell into two groups of higher and lower microhardness. Beyond a depth of 1.5 mm, the microhardness was similar to that of the unpeened sample with overlapping standard deviations.

Variation of microhardness with power intensity is shown in Figure 4.20 down to 1.5 mm depth since this is where the values were above the unpeened sample. The greatest effect of LSPwC was down to 0.25 mm from the peened surface where the highest microhardness was recorded. The highest microhardness was at 3 GW/cm^2 followed by 1 GW/cm^2 and 5 GW/cm^2 which were very similar.

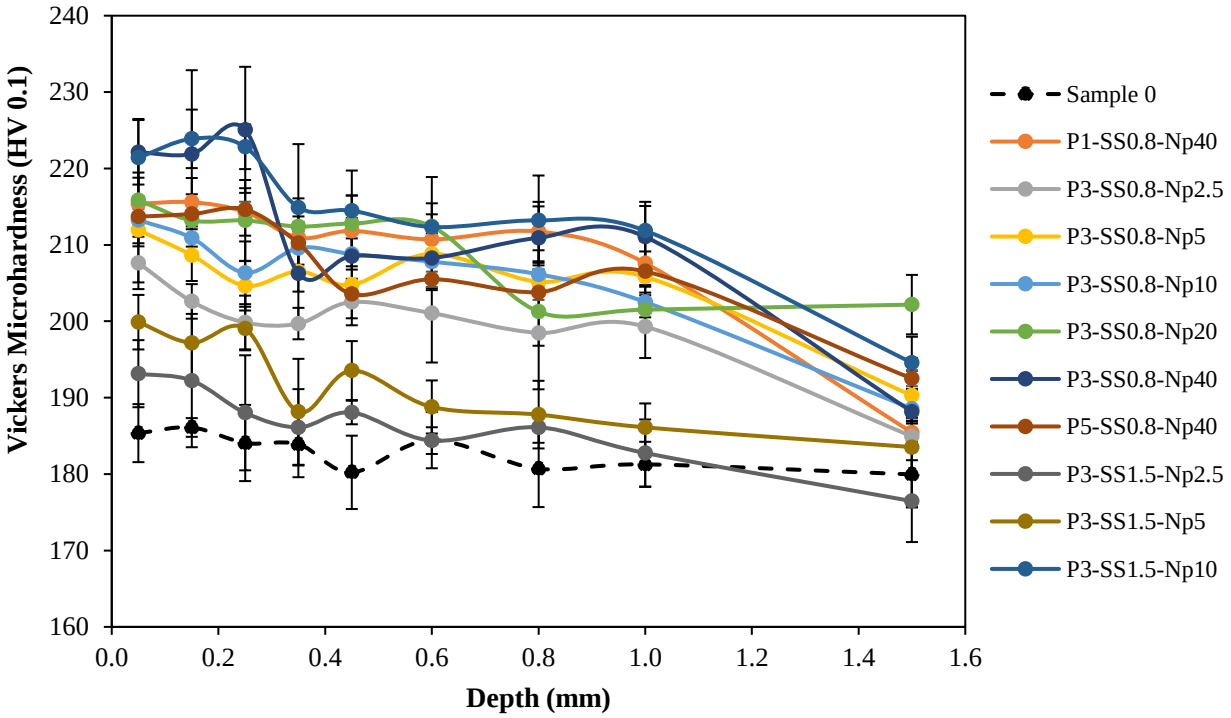


Figure 4.19. Microhardness results of samples at different depths from the peened surface.

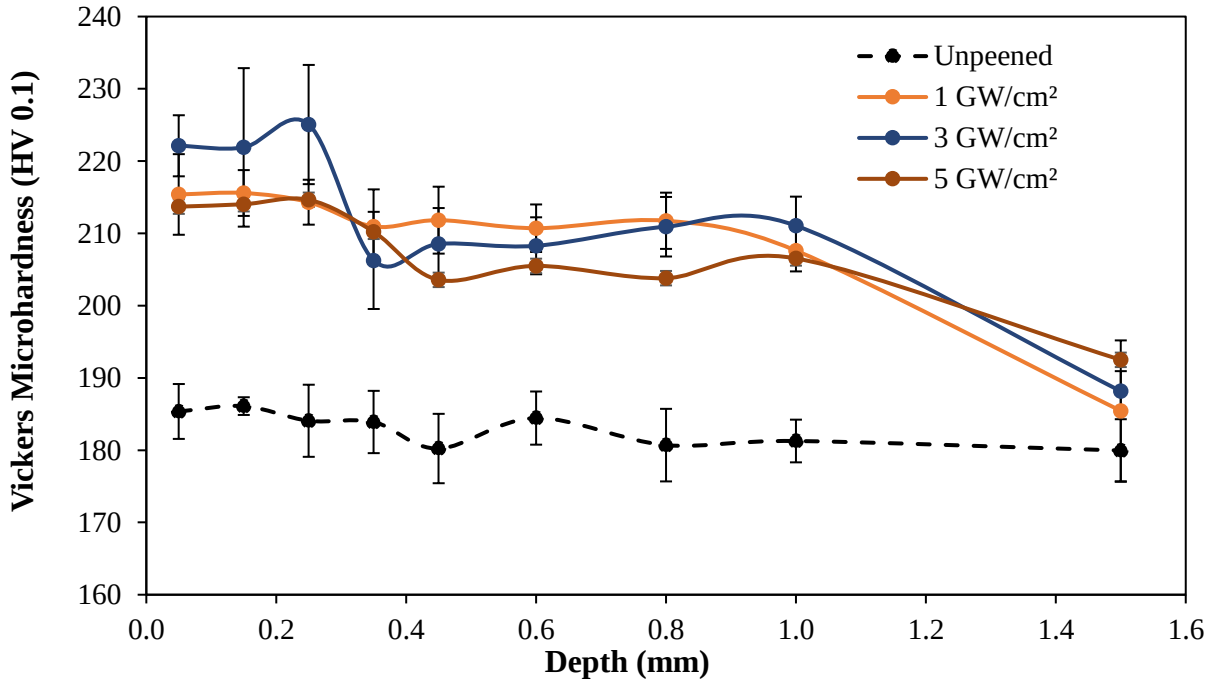


Figure 4.20. Variation of microhardness with laser power intensity.

The variation of microhardness with spot coverage at 3 GW/cm^2 is shown in Figure 4.21 for a spot size of 0.8 mm and Figure 4.22 for 1.5 mm. Higher microhardness occurred for higher spot coverage. In Figure 4.21, the specimen with N_p40 was the hardest followed by N_p20 then N_p10 and N_p5; the lowest hardness was found in N_p2.5. Although the hardness decreased with depth, for N_p20 the decline was steadiest. In Figure 4.22, the sample with N_p10 had significantly higher microhardness than N_p5 and N_p2.5 and the standard deviations of the other samples overlapped.

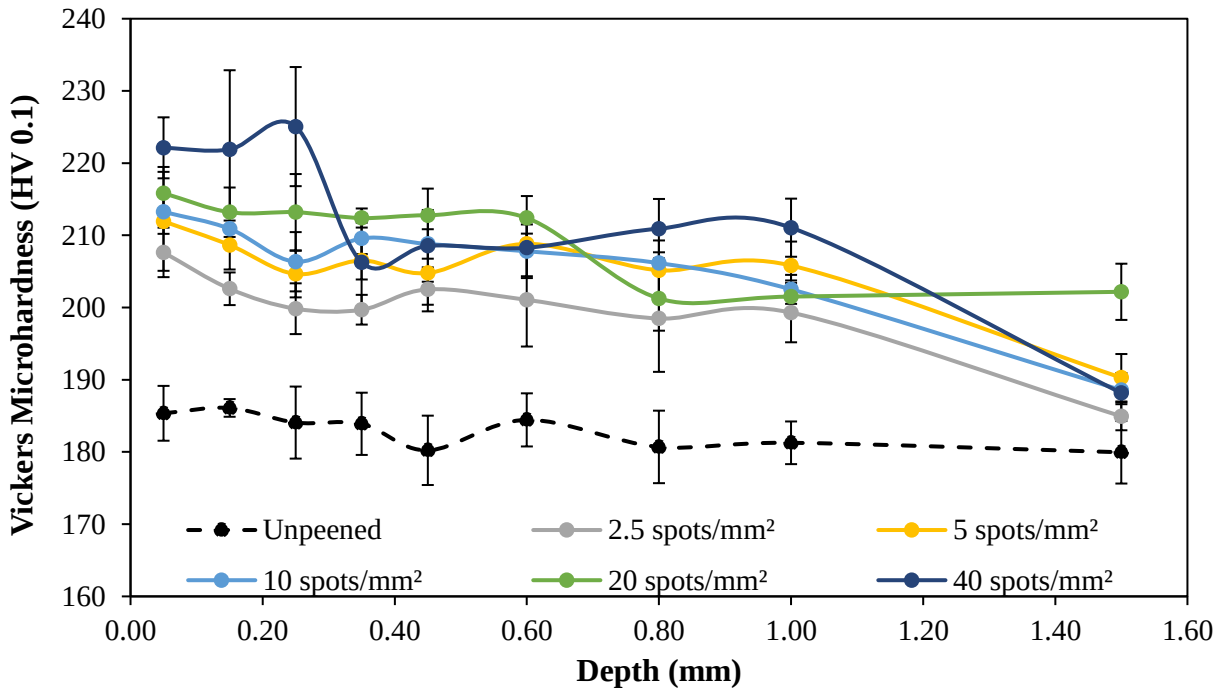


Figure 4.21. Variation of microhardness with spot coverage (N_p) at PI = 3 GW/cm^2, SS = 0.8 mm.

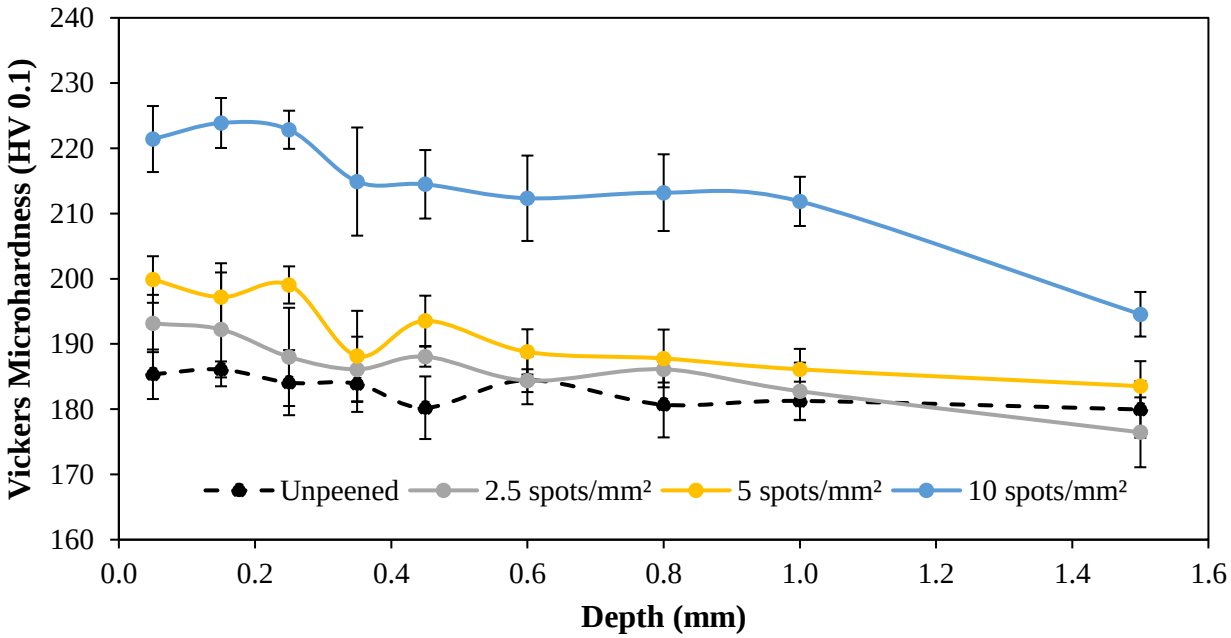


Figure 4.22. Variation of microhardness with spot coverage (N_p) at PI = 3 GW/cm^2, SS = 1.5 mm.

4.7 Electrochemical Corrosion

4.7.1 Open circuit potential (OCP)

The variation of OCP with time for the peened and unpeened samples in 3.5 wt% NaCl is shown in Figure 4.23. All peened samples stabilised at higher OCP values (more positive) than the unpeened sample, Sample 0. The Sample 0 OCP graph was generally stable at the lowest OCP values from -0.80 to -0.82. The P3-SS0.8-N_p20 sample stabilised at the highest OCP value and started at a low OCP of -0.771 V and gradually increased to -0.739 V in the first 850 s. There was a sharp disturbance at 864 s which immediately stabilised to -0.730 V and remained stable to the end of the experiment.

The P3-SS0.8-N_p5 sample had the most stable OCP throughout the exposure period with its highest values similar to P3-SS0.8-N_p20 after 1000 s. The P3-SS1.5-N_p2.5 plot was stable, with the third highest OCP. The P3-SS1.5-N_p5 sample was fourth in magnitude and was stable throughout. The P3-SS1.5-N_p10 sample had a steady increase in the first 350 s and remained stable, with OCP values similar to P1-SS0.8-N_p40 which had stable OCP throughout. The P3-SS0.8-N_p2.5 OCP

steadily increased in the first 552 s and stabilised. The P3-SS0.8- N_p10 plot was erratic in the first 1400 s and then became stable. The P3-SS0.8-N_p40 OCP was stable from -0.80 to -0.81 V in the first 900 s then sharply shifted to -0.772 V and stabilised in that range. The OCP of P5-SS0.8-N_p2.5 increased with a gentle slope in 600 s originally lower than Sample 0, then stabilised above it.

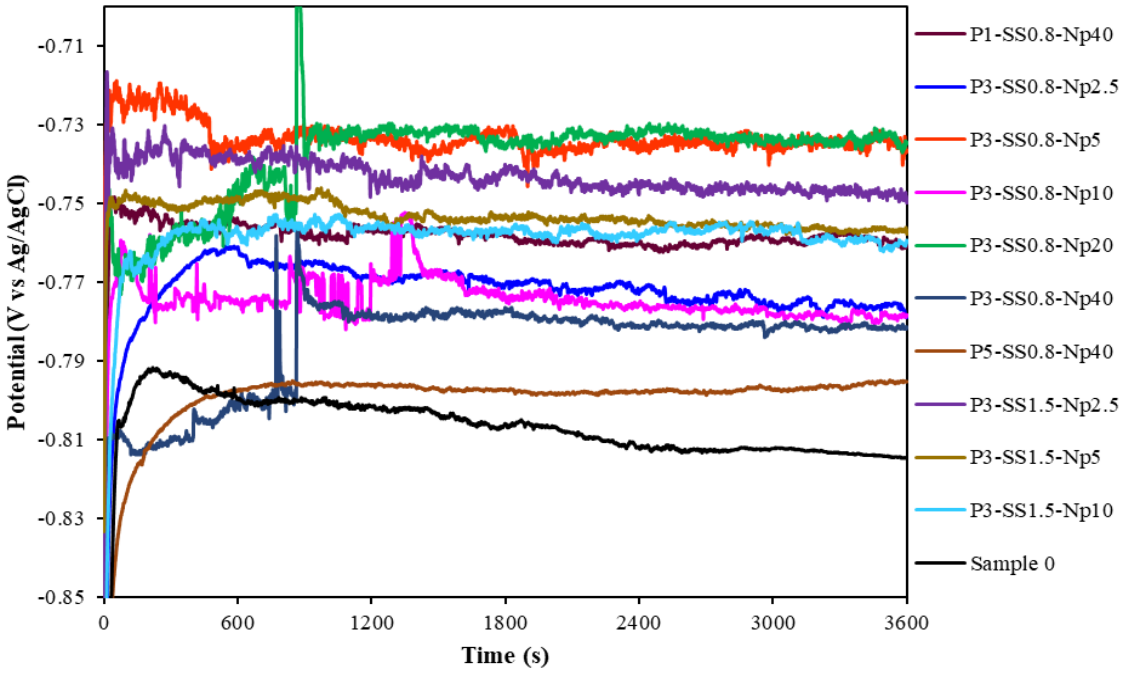


Figure 4.23. Variation of OCP measurements with time in 3.5 wt% NaCl.

4.7.2 Potentiodynamic polarisation

The duplicate potentiodynamic polarisation tests gave similar polarisation curves, Appendix 4. For clarity, a single graph is provided for each sample in Figure 4.24 to Figure 4.28. These figures show the potentiodynamic polarisation curves for peened specimens at various parameters compared to unpeened Sample 0. The polarisation curves showed a similar trend where the current decreased with increasing potential in the cathodic branch until it reached the corrosion current density (corresponding to corrosion potential E_{corr}). With the increase of the applied potential in the anodic branch, the current rapidly increased just after the corrosion potential. The current then stayed almost unchanged, with a large increase in the applied potential in the passive region. At

elevated potential values, Sample 0 and some peened samples; P1-SS0.8-N_p40, P3-SS0.8-N_p2.5, P3-SS0.8-N_p10, P5-SS0.8-N_p40, P3-SS1.5-N_p5 (Figure 4.24, Figure 4.25b), Figure 4.27a), Figure 4.28a)) exhibited a distinctive transition from a passive to transpassive region, marked by a surge in current density. Subsequently, these samples returned to a lower current density, forming additional passive regions.

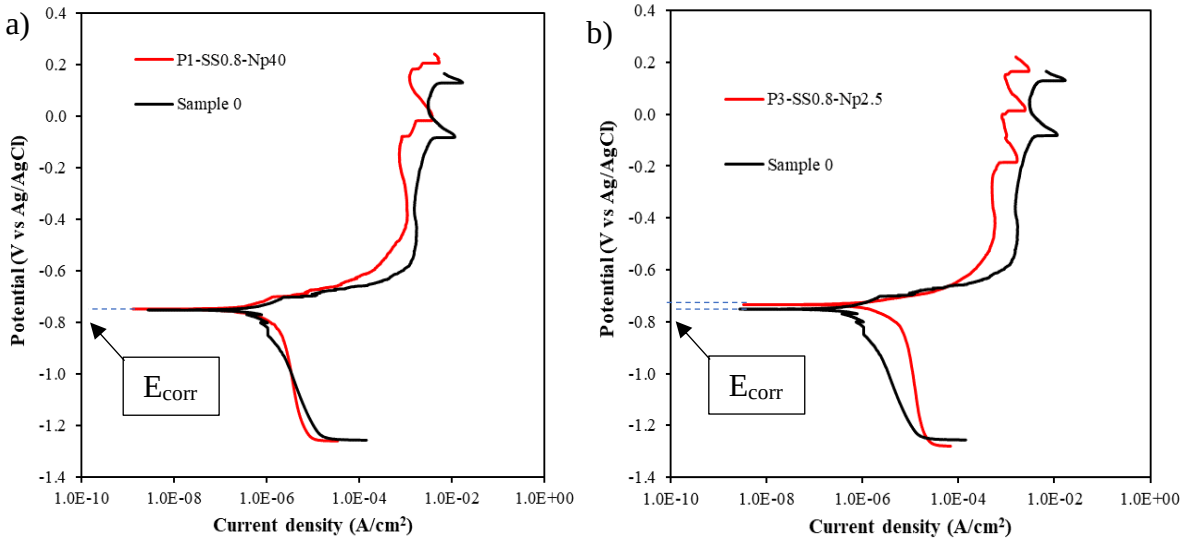


Figure 4.24. Potentiodynamic polarisation curves of a) P1-SS0.8-N_p40 and b) P3-SS0.8-N_p2.5 compared to Sample 0.

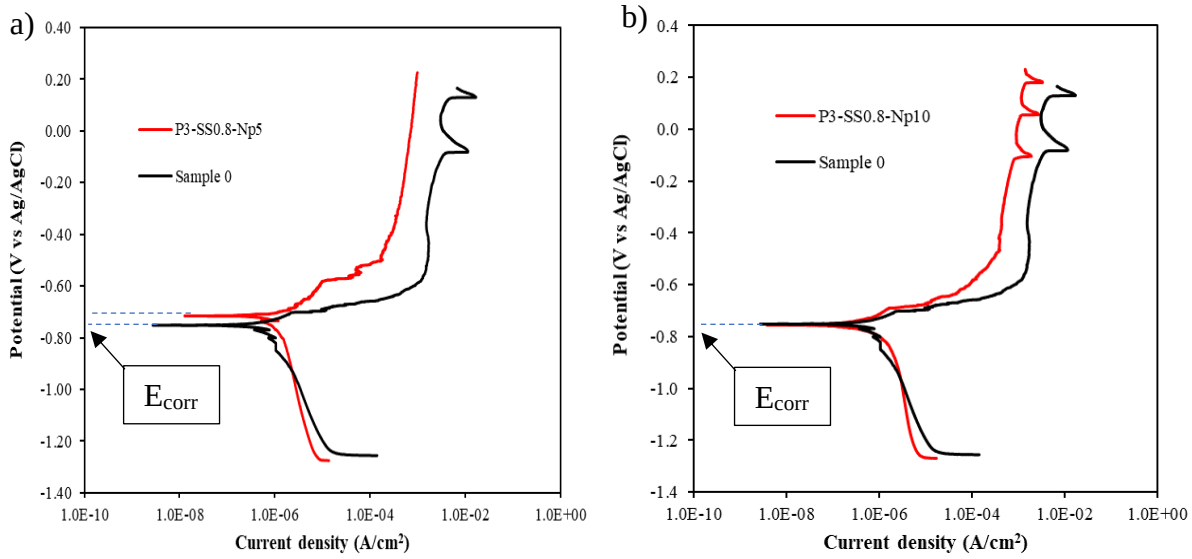


Figure 4.25. Potentiodynamic polarisation curves of a) P3-SS0.8-N_p5 and b) P3-SS0.8-N_p10 compared to Sample 0.

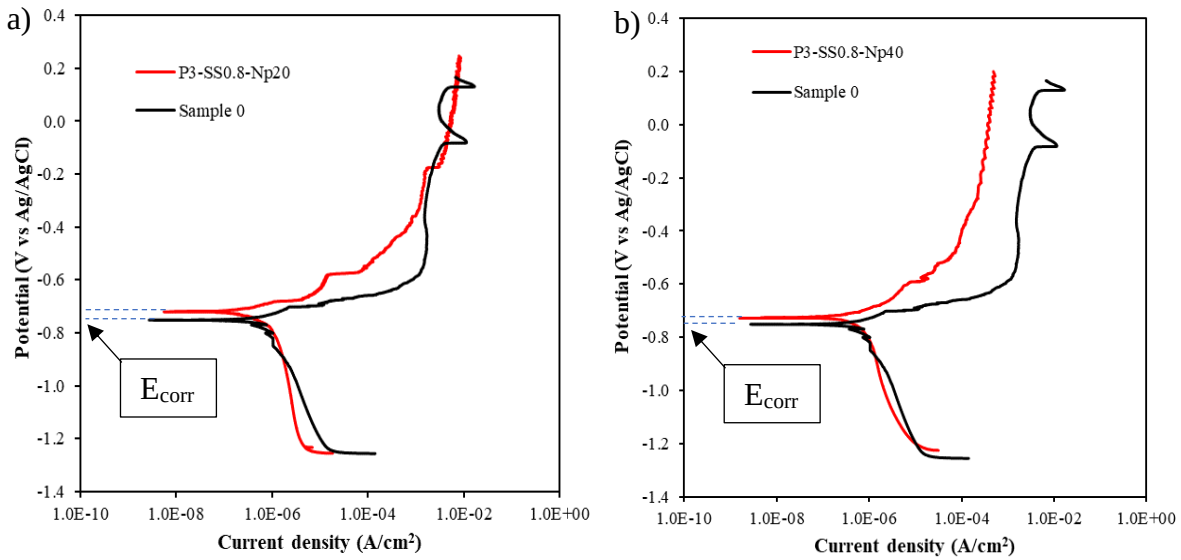


Figure 4.26. Potentiodynamic polarisation curves of a) P3-SS0.8-N_p20 and b) P3-SS0.8-N_p40 compared to Sample 0.

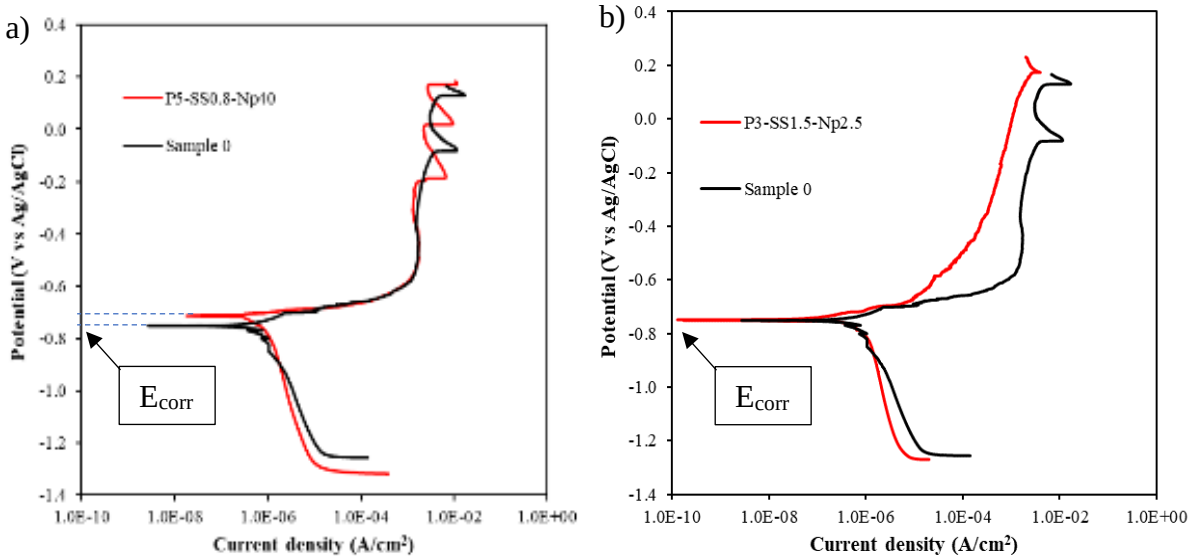


Figure 4.27. Potentiodynamic polarisation curves of a) P5-SS0.8-N_p40 and b) P3-SS1.5-N_p2.5 compared to Sample 0.

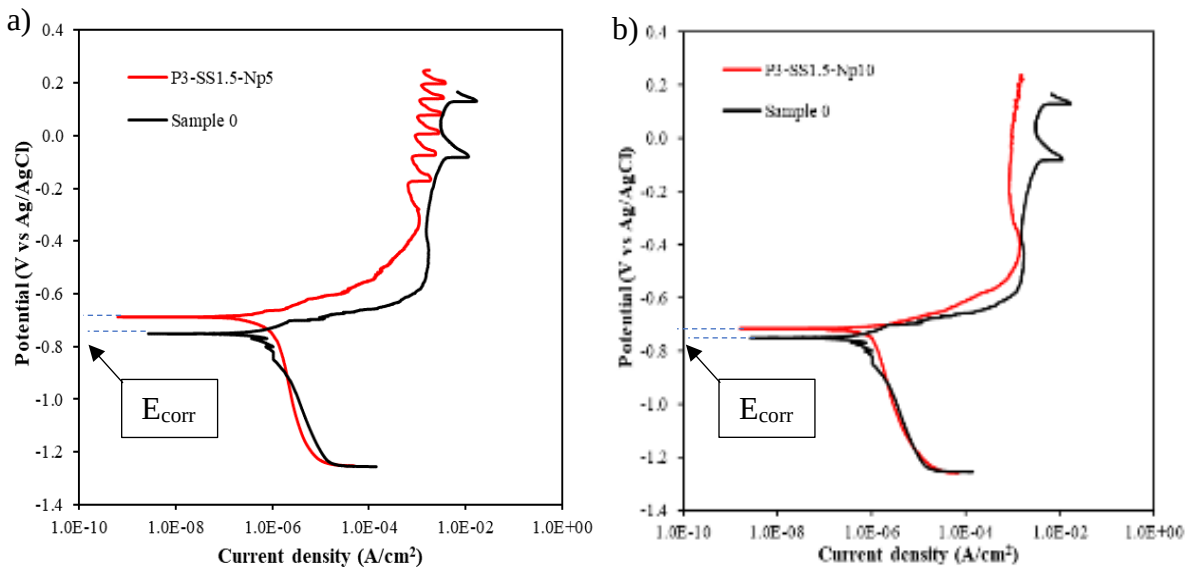


Figure 4.28. Potentiodynamic polarisation curves of a) P3-SS1.5-N_p5 and b) P3-SS1.5-N_p10 compared to Sample 0.

Table 4.4 lists the corrosion parameters obtained from OCP and the potentiodynamic polarisation curves. The OCP values recorded after 1 h for all samples were in the range of -0.735 V to -0.815 V. The E_{corr} values were similar within a narrow range of -0.682 V to –0.760 V. Most peened samples had higher i_{corr} and corrosion rates than the unpeened sample. However, four samples: P1-SS0.8-N_p40, P3-SS0.8-N_p10, P3-SS1.5-N_p2.5 and P3-SS1.5-N_p5 had lower corrosion rates than Sample 0. The lowest corrosion rate was found in P3-SS1.5-N_p2.5 which was four times lower than Sample 0. The corrosion rates calculated in Table 4.4 are also presented in a bar graph, Figure 4.29.

Table 4.4. Corrosion parameters were obtained for each pair of samples.

Sample	**OCP $_{3600s}$ (V)**	**E_{corr} (V)**	**i_{corr} (µA/cm^2)**	**Corrosion Rate x10^{-2} (mm/y)**
Sample 0	-0.815 ± 0.005	-0.747 ± 0.005	1.80 ± 0.13	2.01 ± 0.14
P1-SS0.8-N$_p$40	-0.761 ± 0.002	-0.746 ± 0.002	0.78 ± 0.04	0.87 ± 0.04
P3-SS0.8-N$_p$2.5	-0.779 ± 0.011	-0.739 ± 0.005	3.23 ± 0.05	3.60 ± 0.05
P3-SS0.8-N$_p$5	-0.737 ± 0.007	-0.712 ± 0.003	3.69 ± 0.15	4.28 ± 0.17
P3-SS0.8-N$_p$10	-0.778 ± 0.010	-0.760 ± 0.005	1.12 ± 0.33	1.25 ± 0.37
P3-SS0.8-N$_p$20	-0.735 ± 0.019	-0.718 ± 0.002	2.28 ± 0.06	2.54 ± 0.06
P3-SS0.8-N$_p$40	-0.782 ± 0.008	-0.722 ± 0.007	3.57 ± 0.20	3.98 ± 0.22
P5-SS0.8-N$_p$40	-0.795 ± 0.021	-0.705 ± 0.010	4.88 ± 0.11	5.44 ± 0.13
P3-SS1.5-N$_p$2.5	-0.750 ± 0.019	-0.733 ± 0.014	0.43 ± 0.04	0.48 ± 0.04
P3-SS1.5-N$_p$5	-0.758 ± 0.006	-0.682 ± 0.006	1.15 ± 0.06	1.28 ± 0.07
P3-SS1.5-N$_p$10	-0.759 ± 0.000	-0.720 ± 0.004	1.89 ± 0.06	2.10 ± 0.07

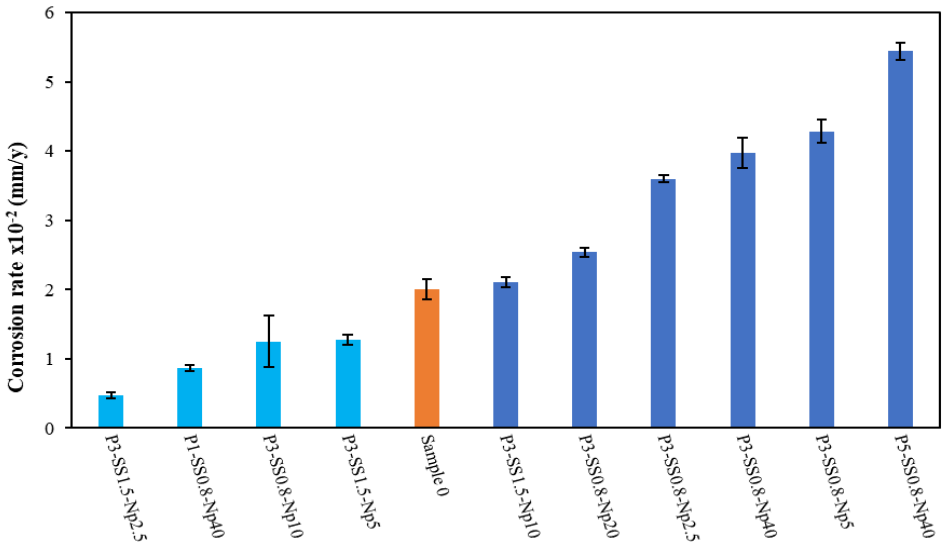


Figure 4.29. Corrosion rates of specimens after potentiodynamic polarisation tests in 3.5 wt% NaCl.

4.7.3 Corrosion products after potentiodynamic polarisation tests

4.7.3.1 Sample 0

The surface of Sample 0 after potentiodynamic polarisation is shown in Figure 4.30 showing clusters of corrosion products. The EDX results listed in Table 4.5 show high O content, indicating the formation of oxides. The Al and O in the corrosion products varied (light and dark) with high standard deviations.

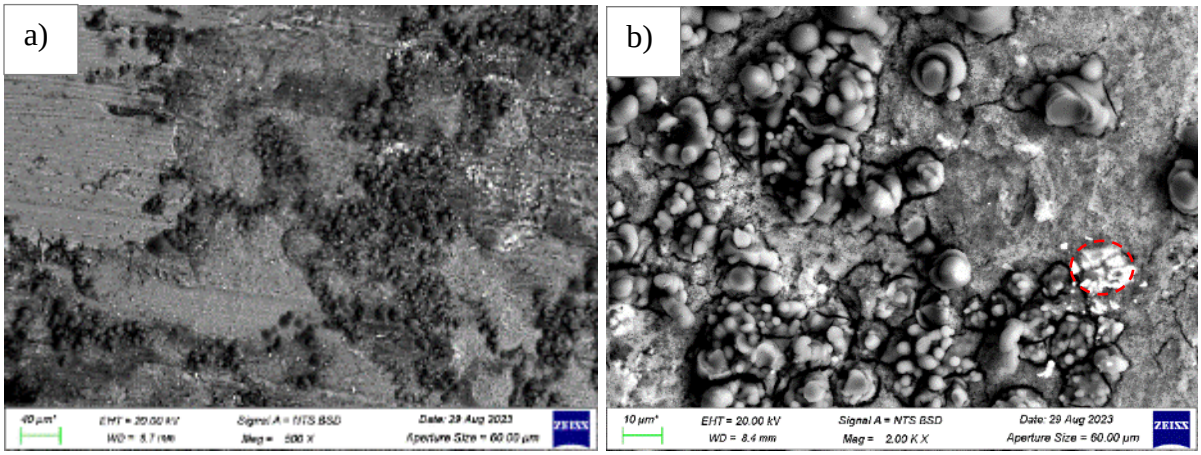


Figure 4.30. SEM-BSE images of Sample 0 surface after potentiodynamic polarisation corrosion test showing corrosion products at: a) lower and b) higher magnification with lighter parts circled.

Table 4.5. EDX results of corrosion products on Sample 0.

		O	Na	Mg	Al	Si	Cl	Cr	Fe	Cu	Zn
Overall area	wt%	23.7 ± 1.7	0.7 ± 0.3	1.9 ± 0.1	66.6 ± 1.5	0.3 ± 0.3	0.1 ± 0.1	0.1 ± 0.1	0.2 ± 0.1	1.2 ± 0.1	5.2 ± 0.3
	at.%	35.2 ± 2.1	0.7 ± 0.4	1.9 ± 0.1	59.2 ± 2.0	0.3 ± 0.3	0.1 ± 0.1	0.1 ± 0.1	0.1 ± 0.1	0.5 ± 0.1	1.9 ± 0.1
Clear area	wt%	9.0 ± 1.2	0.8 ± 0.1	2.4 ± 0.0	80.4 ± 1.3	0.3 ± 0.4	-	-	0.1 ± 0.1	1.3 ± 0.1	5.7 ± 0.0
	at.%	14.2 ± 1.8	0.9 ± 0.1	2.6 ± 0.0	79.1 ± 1.9	0.3 ± 0.4	-	-	0.1 ± 0.1	0.5 ± 0.0	2.3 ± 0.0
Corrosion products	wt%	54.8 ± 10.2	0.4 ± 0.3	0.8 ± 0.4	37.1 ± 7.7	0.7 ± 0.6	0.9 ± 0.7	-	0.2 ± 0.2	1.2 ± 0.8	3.9 ± 1.7
	at.%	67.9 ± 8.6	0.4 ± 0.3	0.7 ± 0.3	28.3 ± 7.3	0.5 ± 0.4	0.5 ± 0.4	-	0.1 ± 0.1	0.4 ± 0.3	1.2 ± 0.6
Lighter area (circled in Figure 4.30b))	wt%	31.3 ± 4.1	0.5 ± 0.1	0.7 ± 0.7	50.1 ± 1.7	1.5 ± 0.7	0.3 ± 0.0	0.4 ± 0.0	7.3 ± 7.3	3.9 ± 1.2	4.0 ± 1.2
	at.%	46.5 ± 3.4	0.5 ± 0.1	0.6 ± 0.6	44.6 ± 1.1	1.2 ± 0.5	0.2 ± 0.0	0.2 ± 0.0	3.3 ± 3.3	1.5 ± 0.5	1.4 ± 0.4

4.7.3.2 P1-SS0.8-N_p40

Corrosion products on the surface of P1-SS0.8-N_p40 are shown in Figure 4.31. The EDX results listed in Table 4.6 show high O content, indicating the formation of oxides. High standard deviations were obtained for both Al and O. Low amounts of C were detected likely due to the rubber used for masking the sample.

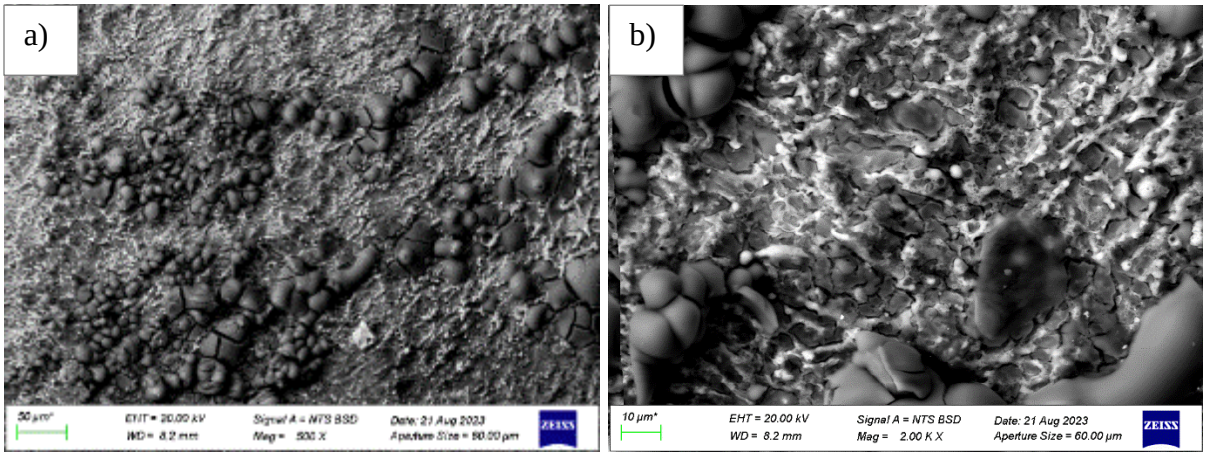


Figure 4.31. SEM-BSE images of P1-SS0.8-N_p40 surface after potentiodynamic polarisation corrosion showing corrosion products at: a) lower and b) higher magnification.

Table 4.6. EDX results of corrosion products on P1-SS0.8-N_p40.

		O	C	Na	Mg	Al	Si	Cl	Cr	Fe	Cu	Zn
Overall area	wt%	33.2 ± 5.7	2.1 ± 0.3	1.0 ± 0.2	1.6 ± 0.2	55.0 ± 5.7	0.9 ± 0.1	0.6 ± 0.4	0.1 ± 0.1	0.2 ± 0.1	1.2 ± 0.2	4.1 ± 0.4
	at.%	46.5 ± 6.5	1.8 ± 0.2	1.0 ± 0.2	1.5 ± 0.2	46.1 ± 6.4	0.7 ± 0.1	0.4 ± 0.3	0.1 ± 0.0	0.1 ± 0.1	0.4 ± 0.1	1.4 ± 0.2
Clear area	wt%	33.1 ± 13.0	0.6 ± 0.5	0.9 ± 1.0	1.6 ± 0.3	56.2 ± 13.3	1.1 ± 1.1	0.4 ± 0.4	0.1 ± 0.1	0.2 ± 0.2	1.5 ± 0.4	4.3 ± 0.9
	at.%	44.9 ± 14.4	0.4 ± 0.4	0.8 ± 0.9	1.5 ± 0.4	49.0 ± 14.7	0.9 ± 0.9	0.3 ± 0.2	0.1 ± 0.0	0.1 ± 0.1	0.5 ± 0.1	1.5 ± 0.4
Corrosion products	wt%	54.7 ± 8.2	2.7 ± 0.4	0.9 ± 1.0	1.0 ± 0.3	33.8 ± 7.2	1.5 ± 1.1	1.6 ± 0.8	0.1 ± 0.1	-	1.0 ± 0.6	2.7 ± 0.4
	at.%	67.9 ± 7.4	2.5 ± 0.6	0.8 ± 0.9	0.8 ± 0.3	24.8 ± 6.6	1.1 ± 0.8	0.9 ± 0.5	0.1 ± 0.0	-	0.3 ± 0.2	0.8 ± 0.2

4.7.3.3 P3-SS0.8-N_p2.5

Corrosion products on the surface of P3-SS0.8-N_p2.5 are shown in Figure 4.32. The EDX results listed in Table 4.7 show high O content indicating the formation of oxides. High standard deviations were obtained for Al and O.

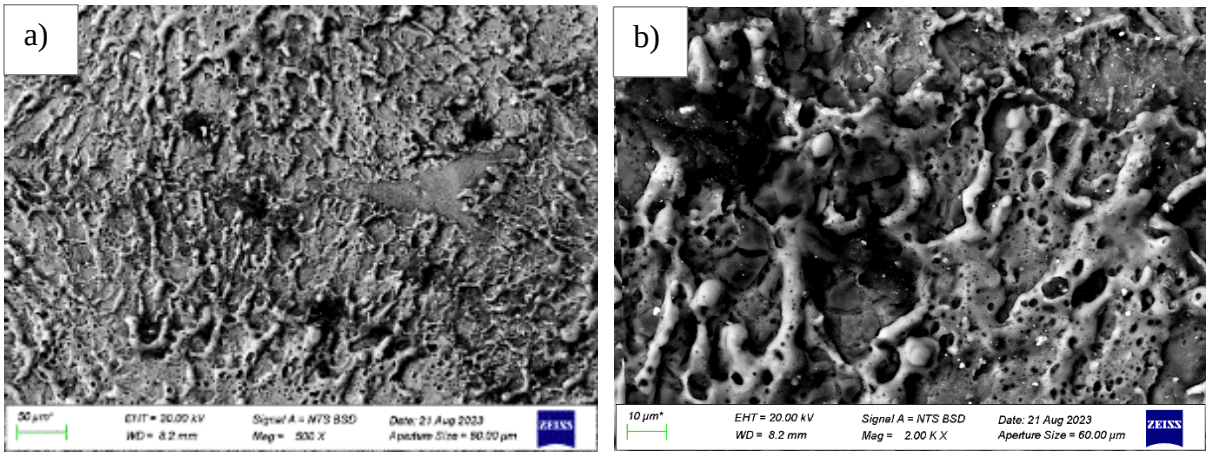


Figure 4.32. SEM-BSE images of P3-SS0.8-N_p2.5 surface after potentiodynamic polarisation corrosion showing corrosion products at: a) lower and b) higher magnification.

Table 4.7. EDX results of corrosion products on P3-SS0.8-N_p2.5.

		O	Na	Mg	Al	Si	Cl	Fe	Cu	Zn
Overall area	wt%	21.6 ± 1.7	0.8 ± 0.1	2.0 ± 0.1	68.3 ± 1.7	0.2 ± 0.1	0.2 ± 0.1	0.4 ± 0.1	1.2 ± 0.1	5.3 ± 0.3
	at.%	32.8 ± 2.3	0.9 ± 0.1	2.0 ± 0.1	61.4 ± 2.2	0.1 ± 0.1	0.1 ± 0.1	0.2 ± 0.0	0.5 ± 0.0	2.0 ± 0.1
Clear area	wt%	9.6 ± 2.2	0.4 ± 0.3	2.3 ± 0.2	81.1 ± 1.6	-	-	-	1.2 ± 0.1	5.4 ± 0.6
	at.%	15.3 ± 3.3	0.5 ± 0.4	2.5 ± 0.2	79.0 ± 2.9	-	-	-	0.5 ± 0.0	2.2 ± 0.3
Corrosion products	wt%	48.5 ± 13.7	0.3 ± 0.2	1.3 ± 0.1	43.3 ± 11.0	0.4 ± 0.3	0.7 ± 0.1	0.4 ± 0.1	1.9 ± 0.8	3.2 ± 1.6
	at.%	61.7 ± 13.1	0.3 ± 0.2	1.1 ± 0.2	34.4 ± 11.7	0.3 ± 0.3	0.4 ± 0.1	0.1 ± 0.1	0.6 ± 0.3	1.1 ± 0.6

4.7.3.4 P3-SS0.8-N_p5

Corrosion products on the surface of P3-SS0.8-N_p5 are shown in Figure 4.33. The EDX results listed in Table 4.8 show high O content, indicating the formation of oxides. High standard deviations were obtained for both Al and O.

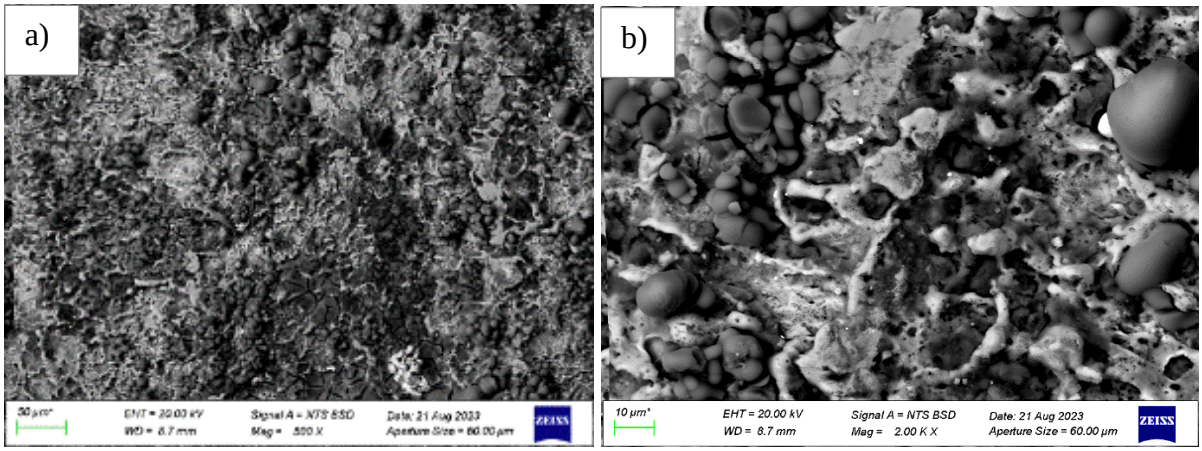


Figure 4.33. SEM-BSE images of P3-SS0.8-N_p5 surface after potentiodynamic polarisation corrosion showing corrosion products at: a) lower and b) higher magnification.

Table 4.8. EDX results of corrosion products on P3-SS0.8-N_p5.

		O	Na	Mg	Al	Si	Cl	Fe	Cu	Zn
Overall area	wt%	26.8 ± 3.8	1.3 ± 0.2	1.6 ± 0.1	61.3 ± 3.6	0.2 ± 0.1	0.7 ± 0.2	0.7 ± 0.4	1.7 ± 0.1	5.7 ± 0.3
	at.%	39.6 ± 4.6	1.3 ± 0.2	1.6 ± 0.2	52.2 ± 4.4	0.2 ± 0.1	0.4 ± 0.1	0.5 ± 0.0	2.1 ± 0.1	5.1 ± 0.1
Clear area	wt%	12.9 ± 7.2	1.3 ± 0.3	1.6 ± 0.2	70.9 ± 5.4	-	-	1.9 ± 0.3	2.8 ± 2.2	8.6 ± 4.6
	at.%	14.7 ± 9.9	1.2 ± 0.2	1.8 ± 0.1	70.3 ± 8.3	-	-	1.2 ± 1.0	3.7 ± 2.2	7.1 ± 0.1
Corrosion products	wt%	64.6 ± 3.7	2.5 ± 0.5	0.8 ± 0.3	25.7 ± 4.7	1.0 ± 0.5	1.2 ± 0.9	2.2 ± 3.6	0.2 ± 0.2	1.8 ± 0.8
	at.%	76.9 ± 2.8	2.2 ± 0.4	0.6 ± 0.2	17.5 ± 3.3	0.7 ± 0.3	0.7 ± 0.5	0.8 ± 1.3	0.1 ± 0.1	0.5 ± 0.3

4.7.3.5 P3-SS0.8-N_p10

Corrosion products on the surface of P3-SS0.8-N_p10 are shown in Figure 4.34. The EDX results listed in Table 4.9 show high O content, indicating the formation of oxides. High standard deviations were obtained for both Al and O.

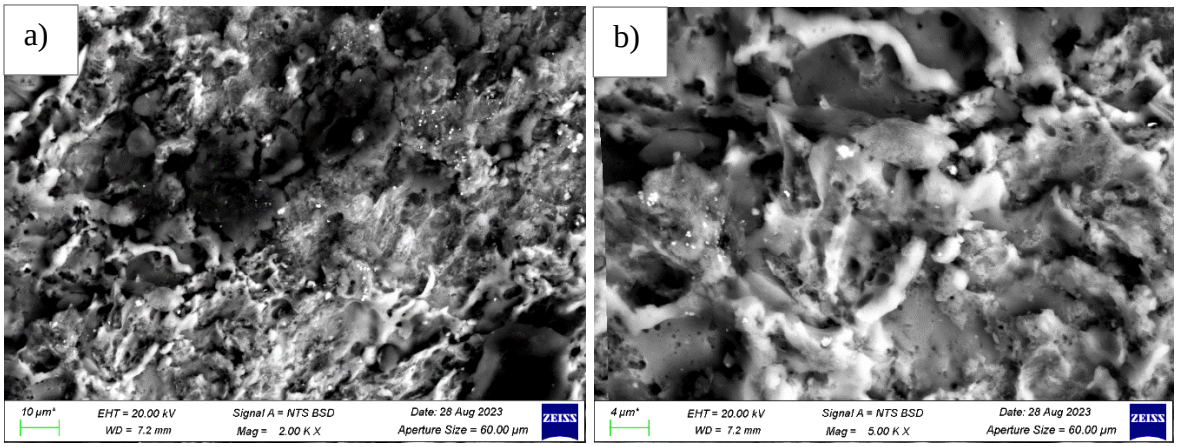


Figure 4.34. SEM-BSE images of P3-SS0.8-N_p10 surface after potentiodynamic polarisation corrosion showing corrosion products at: a) lower and b) higher magnification.

Table 4.9 EDX results of corrosion products on P3-SS0.8-N_p10.

		O	Na	Mg	Al	Si	Cl	Cr	Fe	Cu	Zn
Overall area	wt%	30.3 ± 3.2	0.8 ± 0.2	1.6 ± 0.1	59.7 ± 2.7	0.4 ± 0.1	0.4 ± 0.2	0.2 ± 0.1	0.5 ± 0.1	1.4 ± 0.2	4.7 ± 0.4
	at.%	43.5 ± 3.8	0.8 ± 0.2	1.6 ± 0.1	51.1 ± 3.4	0.3 ± 0.1	0.3 ± 0.1	0.1 ± 0.0	0.2 ± 0.0	0.5 ± 0.1	1.6 ± 0.2
Clear area	wt%	25.3 ± 4.7	0.7 ± 0.0	1.9 ± 0.1	65.8 ± 3.1	-	0.1 ± 0.0	0.2 ± 0.1	-	1.1 ± 0.3	4.9 ± 1.4
	at.%	37.2 ± 5.5	0.7 ± 0.0	1.8 ± 0.0	57.9 ± 4.9	-	0.1 ± 0.0	0.1 ± 0.0	-	0.4 ± 0.1	1.8 ± 0.6
Corrosion products	wt%	53.7 ± 3.4	0.9 ± 0.1	1.0 ± 0.3	38.2 ± 2.8	1.2 ± 0.2	0.7 ± 0.1	-	-	0.6 ± 0.2	3.7 ± 0.3
	at.%	67.2 ± 2.9	0.8 ± 0.1	0.8 ± 0.2	28.6 ± 2.5	0.9 ± 0.2	0.4 ± 0.0	-	-	0.2 ± 0.1	1.1 ± 0.1

4.7.3.6 P3-SS0.8-N_p20

Corrosion products on the surface of P3-SS0.8-N_p20 are shown in Figure 4.35. The EDX results listed in Table 4.10 show high O content, attributed to the formation of oxides. High standard deviations were obtained for Al and O.

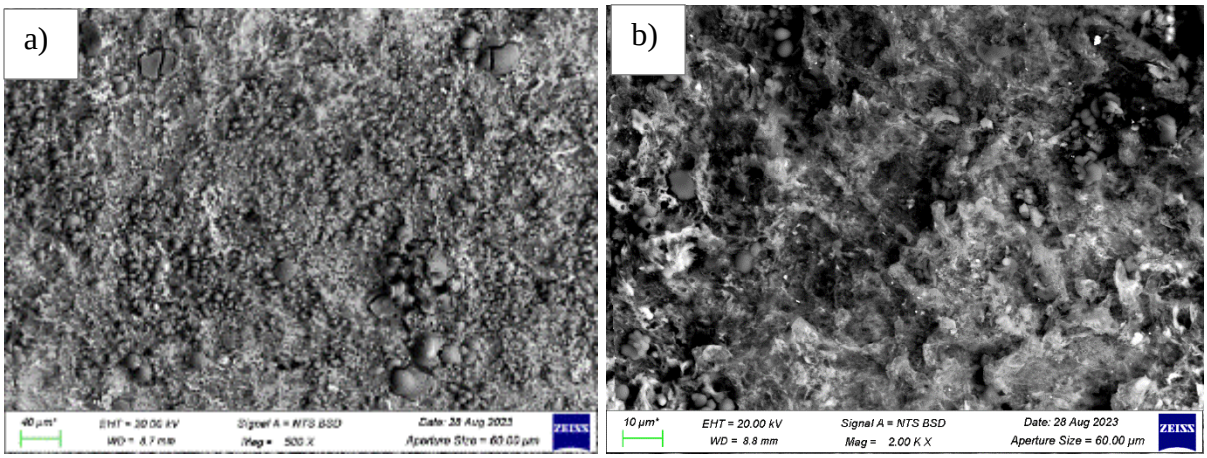


Figure 4.35. SEM-BSE images of P3-SS0.8-N_p20 surface after potentiodynamic polarisation corrosion showing corrosion products at: a) lower and b) higher magnification.

Table 4.10. EDX results of corrosion products on P3-SS0.8-N_p20.

		O	Na	Mg	Al	Si	Cl	Ca	Cr	Cu	Zn
Overall area	wt%	24.3 ± 3.2	0.6 ± 0.4	1.9 ± 0.1	65.9 ± 3.3	0.2 ± 0.2	0.3 ± 0.1	0.1 ± 0.2	0.1 ± 0.1	1.4 ± 0.1	5.2 ± 0.3
	at.%	35.9 ± 4.1	0.7 ± 0.4	1.8 ± 0.1	58.7 ± 4.1	0.2 ± 0.2	0.1 ± 0.1	0.1 ± 0.1	0.1 ± 0.0	0.5 ± 0.0	1.9 ± 0.1
Clear area	wt%	11.4 ± 0.3	0.4 ± 0.4	1.8 ± 0.3	81.8 ± 4.8	-	0.2 ± 0.2	0.3 ± 0.3	0.1 ± 0.1	0.8 ± 0.8	3.2 ± 3.2
	at.%	18.9 ± 0.1	0.5 ± 0.5	2.0 ± 0.3	76.6 ± 2.3	-	0.1 ± 0.1	0.2 ± 0.2	0.1 ± 0.1	0.3 ± 0.3	1.3 ± 1.3
Corrosion products	wt%	61.2 ± 5.2	1.6 ± 0.3	0.9 ± 0.1	30.6 ± 12.7	1.6 ± 0.7	0.9 ± 0.2	0.1 ± 0.1	-	0.5 ± 0.5	2.6 ± 0.6
	at.%	65.7 ± 6.2	1.5 ± 0.2	0.7 ± 0.1	29.0 ± 10.8	1.2 ± 0.5	0.6 ± 0.1	0.3 ± 0.2	-	0.2 ± 0.2	0.8 ± 0.2

4.7.3.7 P3-SS0.8-N_p40

Corrosion products on the surface of P3-SS0.8-N_p40 are shown in Figure 4.36. The EDX results listed in Table 4.11 show high O content, indicating oxide formation, with high standard deviations obtained for Al and O.

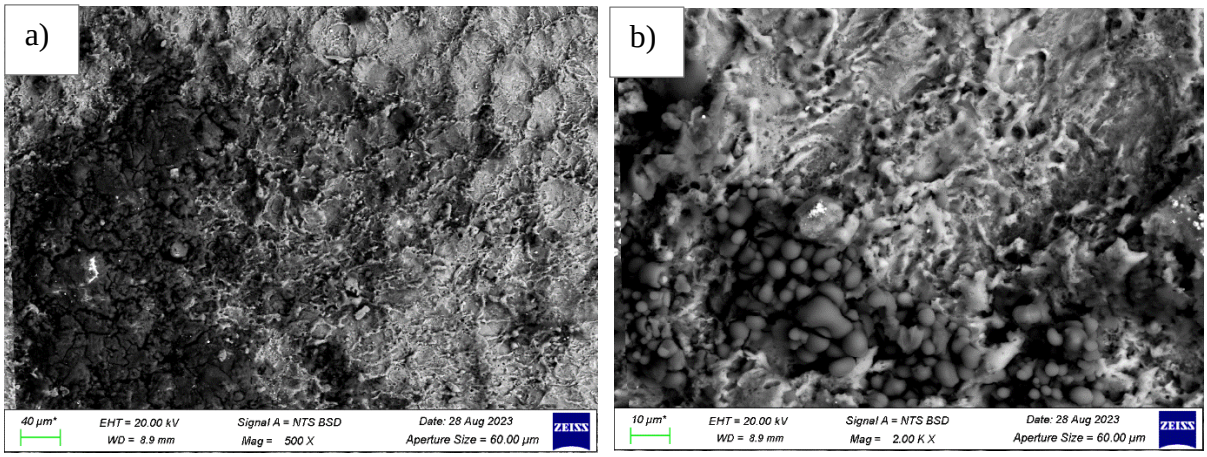


Figure 4.36. SEM-BSE images of P3-SS0.8-N_p40 surface after potentiodynamic polarisation corrosion showing corrosion products at: a) lower and b) higher magnification.

Table 4.11. EDX results of corrosion products on P3-SS0.8-N_p40.

		O	Na	Mg	Al	S	Cl	Cr	Fe	Cu	Zn
Overall area	wt%	21.8 ± 1.1	0.5 ± 0.4	1.9 ± 0.1	68.7 ± 0.1	-	-	0.1 ± 0.1	0.3 ± 0.1	1.2 ± 0.1	5.5 ± 0.2
	at.%	33.1 ± 1.4	0.3 ± 0.4	1.9 ± 0.1	61.9 ± 1.5	-	-	0.1 ± 0.0	0.1 ± 0.1	0.5 ± 0.0	2.1 ± 0.1
Clear area	wt%	15.0 ± 2.5	0.1 ± 0.2	2.0 ± 0.2	73.8 ± 2.0	0.1 ± 0.2	0.1 ± 0.2	0.1 ± 0.2	0.3 ± 0.5	1.5 ± 0.3	7.0 ± 1.4
	at.%	23.6 ± 3.6	0.1 ± 0.3	2.1 ± 0.2	70.4 ± 3.1	0.1 ± 0.2	0.1 ± 0.1	0.1 ± 0.1	0.1 ± 0.2	0.6 ± 0.2	2.8 ± 0.6
Corrosion products	wt%	40.0 ± 11.0	0.6 ± 0.5	1.6 ± 0.3	51.5 ± 10.1	0.3 ± 0.3	0.3 ± 0.2	0.1 ± 0.1	0.2 ± 0.4	1.1 ± 0.8	4.3 ± 2.3
	at.%	51.0 ± 10.9	0.5 ± 0.5	1.5 ± 0.3	44.5 ± 10.3	0.2 ± 0.2	0.2 ± 0.1	0.1 ± 0.0	0.1 ± 0.2	0.4 ± 0.3	1.5 ± 0.8

4.7.3.8 P5-SS0.8-N_p40

Corrosion products on the surface of P5-SS0.8-N_p40 are shown in Figure 4.37. The EDX results listed in Table 4.12 show high O content, indicating the formation of oxides. The standard deviations of Al and O were very high, showing variable composition of the oxides. The light feature circled in Figure 4.37b) had high C content which could be from the rubber used for masking the sample (only one example was found, so there are no standard deviations).

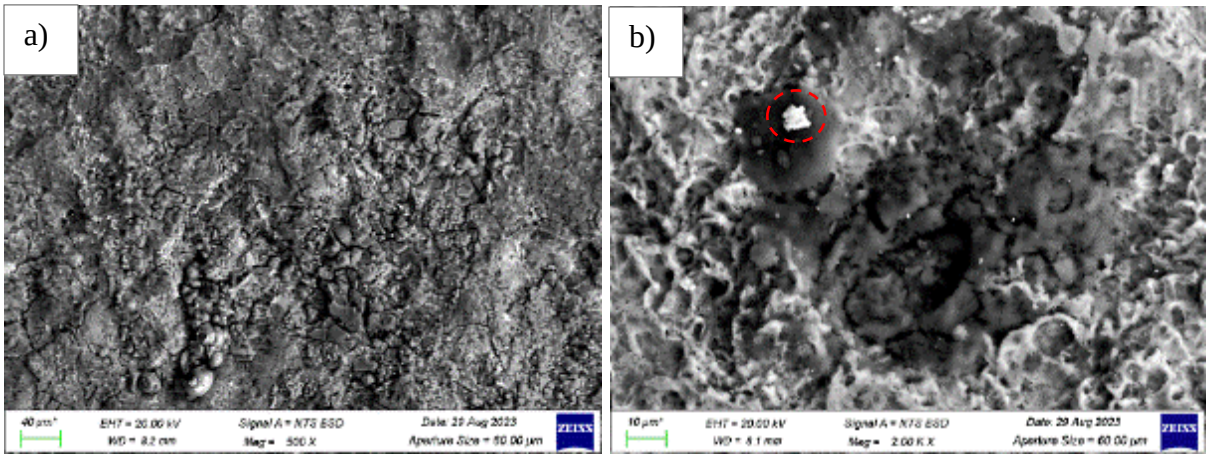


Figure 4.37. SEM-BSE images of P5-SS0.8-N_p40 surface after potentiodynamic polarisation corrosion at: a) lower and b) higher magnification showing corrosion products and light contrast feature (circled).

Table 4.12. EDX results of corrosion products on P5-SS0.8-N_p40.

		O	Na	Mg	Al	Si	Cl	Cr	Fe	Cu	Zn
Overall area	wt%	33.5 ± 8.5	0.9 ± 0.2	1.6 ± 0.3	56.7 ± 8.1	0.2 ± 0.2	0.2 ± 0.1	0.1 ± 0.1	0.3 ± 0.2	1.5 ± 0.1	5.0 ± 0.5
	at.%	46.7 ± 9.7	0.9 ± 0.2	1.5 ± 0.3	48.2 ± 9.3	0.2 ± 0.2	0.1 ± 0.1	0.1 ± 0.0	0.1 ± 0.1	0.5 ± 0.0	1.7 ± 0.3
Corrosion products	wt%	49.0 ± 8.2	0.6 ± 0.2	0.9 ± 0.4	43.2 ± 7.5	0.7 ± 0.4	0.7 ± 0.4	0.2 ± 0.4	0.7 ± 1.6	0.5 ± 0.4	3.5 ± 1.5
	at.%	62.7 ± 7.7	0.5 ± 0.2	0.8 ± 0.3	33.4 ± 7.2	0.5 ± 0.3	0.4 ± 0.2	0.1 ± 0.2	0.3 ± 0.6	0.2 ± 0.1	1.1 ± 0.5
Clear area	wt%	23.8 ± 4.9	0.7 ± 0.1	1.7 ± 0.2	65.9 ± 5.1	0.1 ± 0.2	0.4 ± 0.6	0.3 ± 0.1	0.5 ± 0.6	1.3 ± 0.3	5.3 ± 0.6
	at.%	35.5 ± 6.3	0.7 ± 0.1	1.7 ± 0.2	58.9 ± 6.2	0.1 ± 0.1	0.3 ± 0.4	0.1 ± 0.0	0.2 ± 0.3	0.5 ± 0.1	2.0 ± 0.2
		O	**Na**	**Mg**	**Al**	**Si**	**Cl**	**S**	**C**		**Zn**
Light feature (Figure 4.37)	wt%	18.4	0.3	0.5	20.0	0.2	0.3	0.4	58.5		1.4
	at.%	16.8	0.2	0.3	10.8	0.1	0.2	0.2	71.1		0.3

4.7.3.9 P3-SS1.5-N_p2.5

Corrosion products on the surface of P3-SS1.5-N_p2.5 are shown in Figure 4.38. The EDX results listed in Table 4.13 show high O content, indicating oxide formation, with high standard deviations for Al and O.

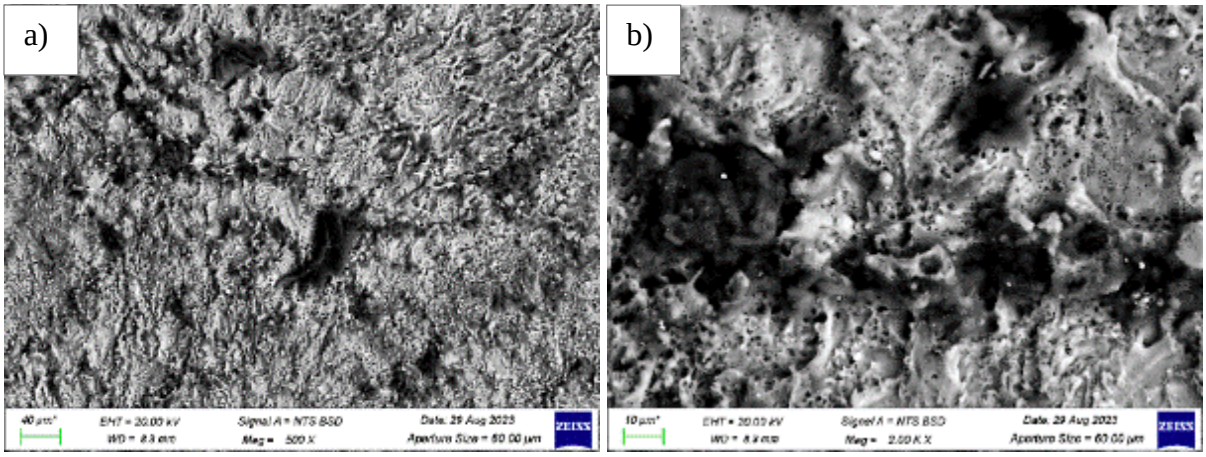


Figure 4.38. SEM-BSE images of P3-SS1.5-N_p2.5 surface after potentiodynamic polarisation corrosion showing corrosion products at: a) lower and b) higher magnification.

Table 4.13. EDX results of corrosion products on P3-SS1.5-N_p2.5.

		O	Na	Mg	Al	Cl	Cr	Fe	Cu	Zn
Overall area	wt%	26.7 ± 1.5	0.7 ± 0.1	1.8 ± 0.1	64.3 ± 1.4	0.3 ± 0.1	0.2 ± 0.1	-	1.2 ± 0.1	4.8 ± 0.2
	at.%	39.1 ± 1.8	0.7 ± 0.1	1.7 ± 0.1	56.0 ± 1.7	0.2 ± 0.1	0.1 ± 0.1	-	0.5 ± 0.0	1.7 ± 0.1
Clear area	wt%	5.7 ± 1.9	0.7 ± 0.1	1.7 ± 0.2	78.8 ± 1.8	0.6 ± 0.0	0.2 ± 0.2	0.5 ± 0.0	2.0 ± 0.4	9.8 ± 2.4
	at.%	9.5 ± 2.3	0.9 ± 0.2	2.1 ± 0.3	81.4 ± 6.6	0.5 ± 0.0	0.1 ± 0.1	0.2 ± 0.0	0.9 ± 0.2	4.4 ± 1.3
Corrosion products	wt%	65.8 ± 2.6	0.7 ± 0.6	0.5 ± 0.3	27.2 ± 7.6	2.5 ± 2.5	0.2 ± 0.3	0.9 ± 1.1	1.2 ± 2.5	1.0 ± 0.8
	at.%	78.1 ± 2.6	0.6 ± 0.5	0.4 ± 0.2	18.5 ± 5.4	1.3 ± 1.4	0.1 ± 0.1	0.3 ± 0.4	0.4 ± 0.7	0.3 ± 0.2

4.7.3.10 P3-SS1.5-N_p5

Corrosion products on the surface of P3-SS1.5-N_p5 are shown in Figure 4.39. The EDX results listed in Table 4.14 show high O content, indicating the formation of oxides. High standard deviations were obtained for Al and O.

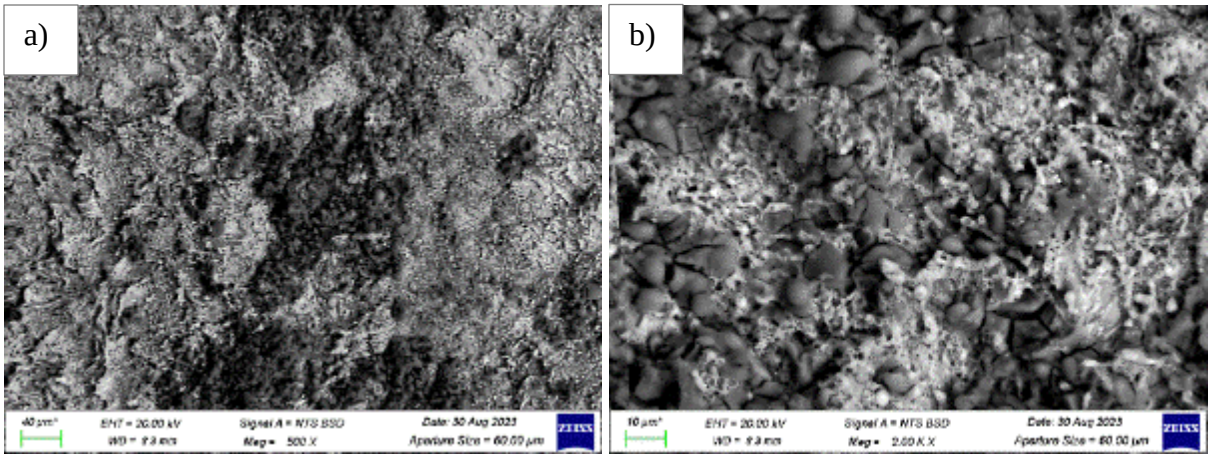


Figure 4.39. SEM-BSE images of P3-SS1.5-N_p5 surface after potentiodynamic polarisation corrosion test showing corrosion products at: a) lower and b) higher magnification.

Table 4.14. EDX results of corrosion products on P3-SS1.5-N_p5.

		O	Na	Mg	Al	Si	S	Cl	Cu	Zn
Overall area	wt%	29.4 ± 3.6	0.6 ± 0.1	1.7 ± 0.1	61.3 ± 3.7	0.6 ± 0.1	0.3 ± 0.0	0.4 ± 0.0	1.2 ± 0.1	4.5 ± 0.2
	at.%	41.9 ± 4.2	0.6 ± 0.1	1.6 ± 0.1	53.0 ± 4.3	0.5 ± 0.1	0.2 ± 0.0	0.2 ± 0.0	0.4 ± 0.0	1.6 ± 0.1
Clear area	wt%	8.9 ± 2.0	0.9 ± 0.0	2.3 ± 0.0	75.1 ± 0.6	0.3 ± 0.0	0.4 ± 0.0	0.3 ± 0.0	2.2 ± 0.0	9.6 ± 0.2
	at.%	17.8 ± 3.3	1.1 ± 0.0	2.2 ± 0.0	72.9 ± 2.5	0.4 ± 0.0	0.3 ± 0.0	0.2 ± 0.0	1.0 ± 0.0	4.1 ± 0.0
Corrosion products	wt%	47.8 ± 7.7	0.7 ± 0.3	1.2 ± 0.3	40.9 ± 6.6	1.3 ± 0.4	1.1 ± 0.5	1.0 ± 0.6	1.0 ± 0.6	5.0 ± 2.4
	at.%	61.8 ± 7.3	0.6 ± 0.3	1.0 ± 0.3	32.6 ± 6.8	0.8 ± 0.3	0.7 ± 0.3	0.6 ± 0.4	0.3 ± 0.2	1.6 ± 0.9

4.7.3.11 P3-SS1.5-N_p10

Corrosion products on the surface of P3-SS1.5-N_p10 are shown in Figure 4.40. The EDX results listed in Table 4.15 show high O content, indicating the formation of oxides. High standard deviations were obtained for Al and O. The light feature (Figure 4.40b)) circled in red had high Fe which was undetected in the other circled in orange.

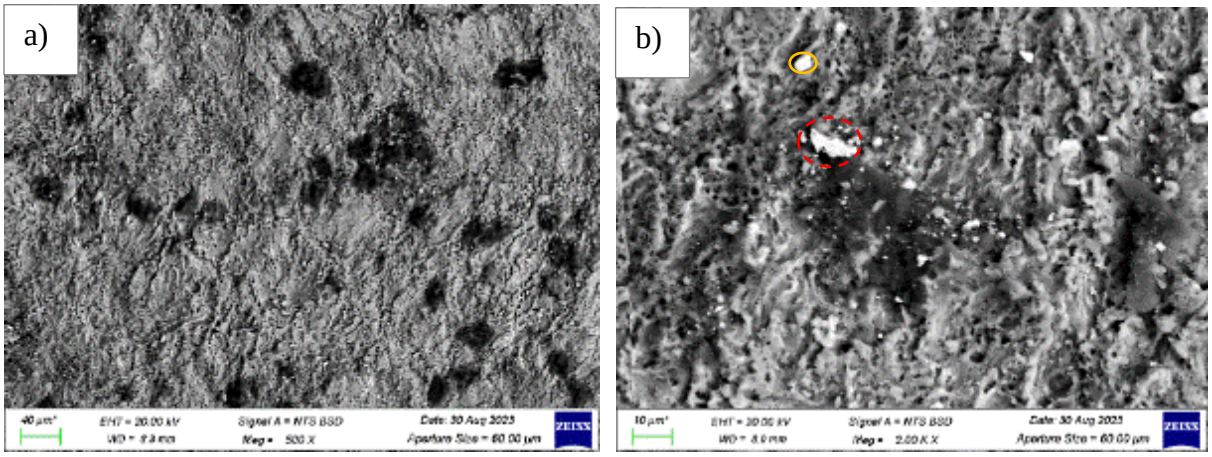


Figure 4.40. SEM-BSE images of P3-SS1.5-N_p10 surface after potentiodynamic polarisation corrosion at: a) lower and b) higher magnification showing corrosion products, including lighter particles (circles).

Table 4.15. EDX results of corrosion products on P3-SS1.5-N_p10.

		O	Na	Mg	Al	Si	Cl	K	Fe	Cu	Zn
Overall area	wt%	25.7 ± 0.4	1.0 ± 0.3	1.8 ± 0.0	63.2 ± 1.2	0.4 ± 0.0	0.8 ± 0.3	0.4 ± 0.0	1.1 ± 0.5	1.0 ± 0.1	4.6 ± 0.1
	at.%	37.3 ± 0.4	1.0 ± 0.3	1.7 ± 0.1	56.3 ± 0.8	0.4 ± 0.0	0.5 ± 0.2	0.2 ± 0.0	0.5 ± 0.2	0.4 ± 0.0	1.7 ± 0.0
Clear area	wt%	6.8 ± 0.3	0.7 ± 0.1	1.8 ± 0.4	79.3 ± 0.5	0.7 ± 0.3	0.1 ± 0.0	-	-	1.7 ± 0.1	8.9 ± 0.2
	at.%	11.6 ± 0.2	0.8 ± 0.3	2.0 ± 0.4	80.6 ± 0.6	0.5 ± 0.2	0.1 ± 0.1	-	-	0.7 ± 0.2	3.7 ± 0.3
Corrosion products	wt%	42.6 ± 6.3	2.1 ± 0.1	0.9 ± 0.0	41.8 ± 1.8	1.9 ± 0.0	2.8 ± 0.1	1.2 ± 0.4	3.2 ± 0.0	0.8 ± 0.0	2.7 ± 1.0
	at.%	56.0 ± 5.7	1.9 ± 0.2	0.8 ± 0.0	35.0 ± 3.2	1.4 ± 0.0	1.7 ± 0.0	0.7 ± 0.2	1.3 ± 0.0	0.3 ± 0.0	0.9 ± 0.4

		O	Na	Mg	Al	Si	Cl	K	Fe	Ca	Zn	Mn
Light feature 1 (circled in Figure 4.40b))	wt%	20.5	7.4	0.6	18.4	-	29.8	22.4	-	-	0.9	-
	at.%	34.2	8.6	0.7	18.2		22.5	15.4	-	-	0.4	-
Light feature 2 (circled in Figure 4.40b))	wt%	14.9	-	-	2.6	0.5	-	0.3	79.3	0.3	1.1	1.0
	at.%	36.8	-	-	3.8	0.7	-	0.3	56.7	0.3	0.7	0.7

4.7.4 Corroded surface morphology after cleaning

The SEM images of corroded unpeened and peened specimens after cleaning with HNO_3 are shown in Figure 4.41 to Figure 4.51. The unpeened specimen (Sample 0, Figure 4.41) had severe pitting, with areas where the pits combined and increased the extent of corrosion and there were also cracks. In some peened specimens, the size of pits was small with fewer cracks. The lowest pitting was observed on P1-SS0.8-N_p40 (Figure 4.42), P3-SS1.5-N_p2.5 (Figure 4.49) and P3-SS1.5-N_p5 (Figure 4.50). There was more pitting on the surfaces of P3-SS0.8-N_p20 (Figure 4.46), P5-SS0.8-N_p40 (Figure 4.48) and P3-SS1.5-N_p10 (Figure 4.51), which had more square shaped pits.

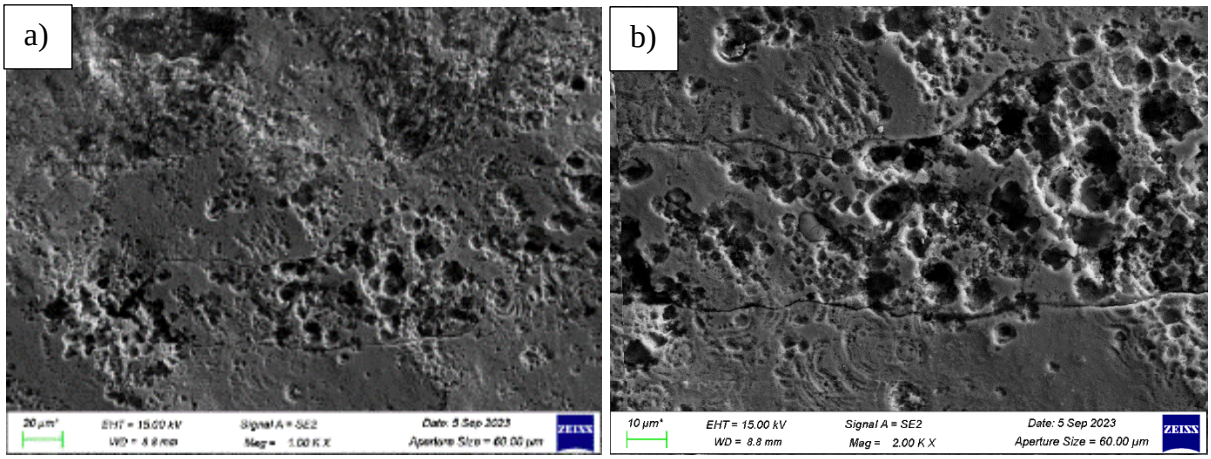


Figure 4.41. SEM-SE images of Sample 0 surface after potentiodynamic polarisation corrosion at: a) lower and b) higher magnification showing pits and cracks.

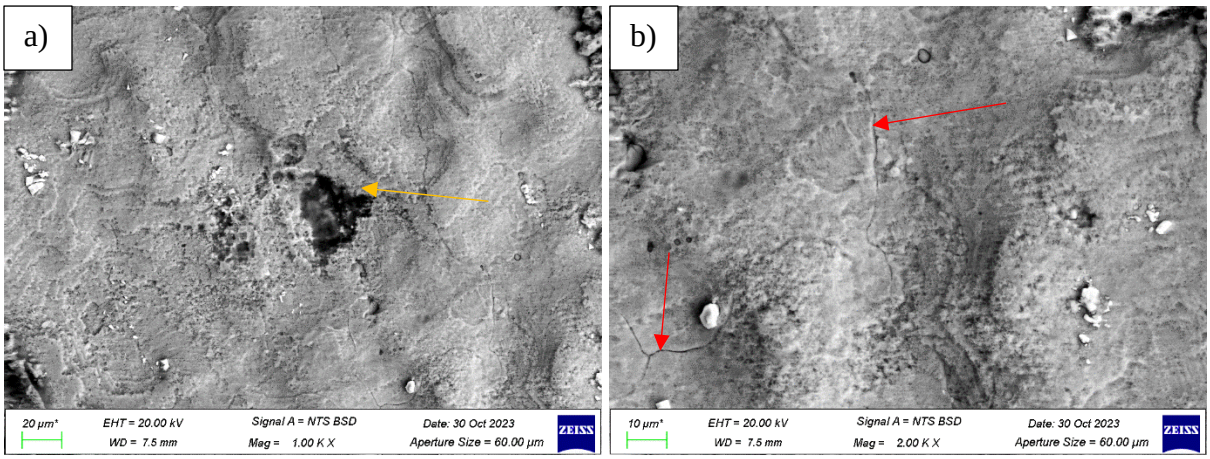


Figure 4.42. SEM-BSE images of P1-SS0.8-N_p40 surface after potentiodynamic polarisation corrosion at: a) lower and b) higher magnification showing pits, larger hole (orange arrow), cracks (red arrows) and lighter particles.

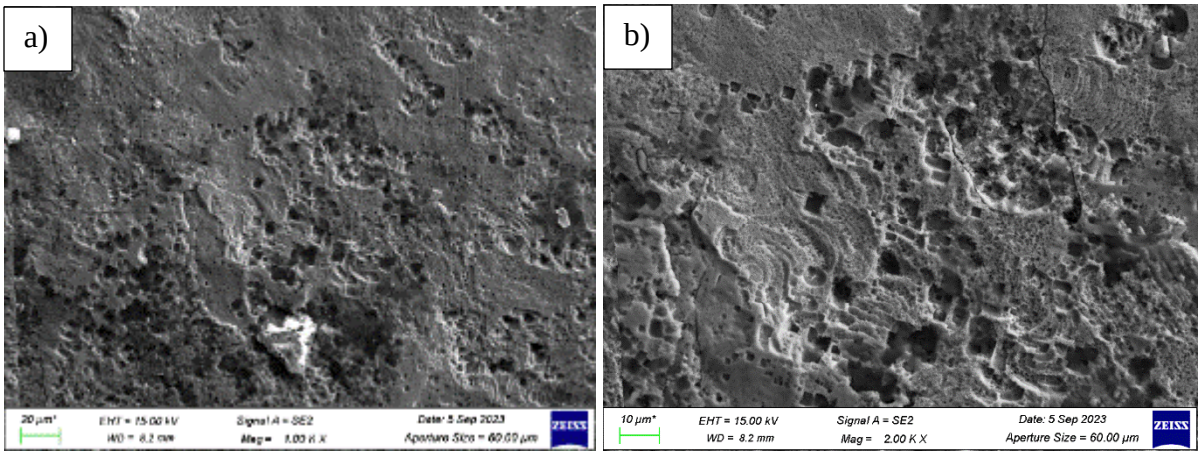


Figure 4.43. SEM-SE images of P3-SS0.8-N_p2.5 surface after potentiodynamic polarisation corrosion at: a) lower magnification showing pits and light features and b) higher magnification showing square pits.

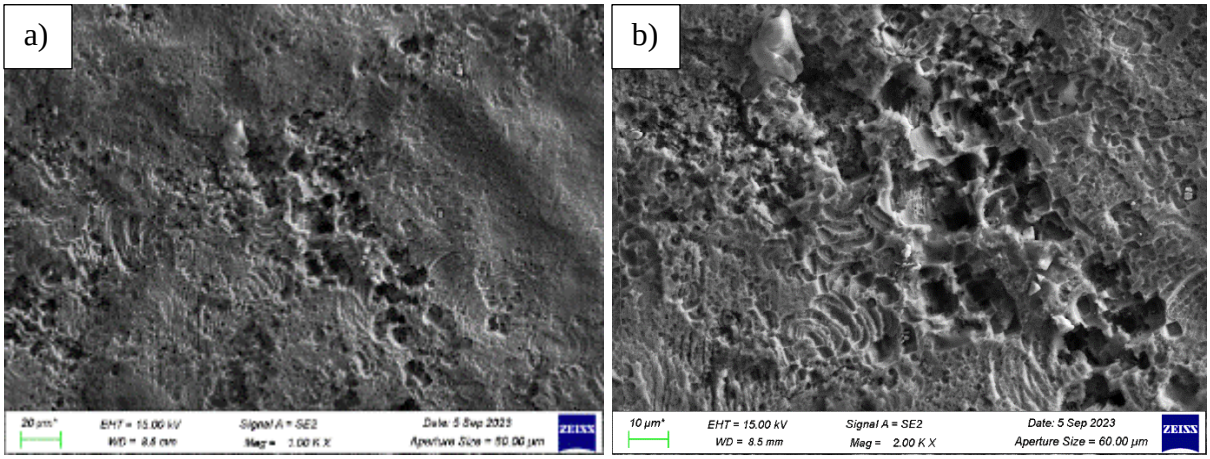


Figure 4.44. SEM-SE images of P3-SS0.8-N_p5 surface after potentiodynamic polarisation corrosion at: a) lower and b) higher magnification showing some square pits.

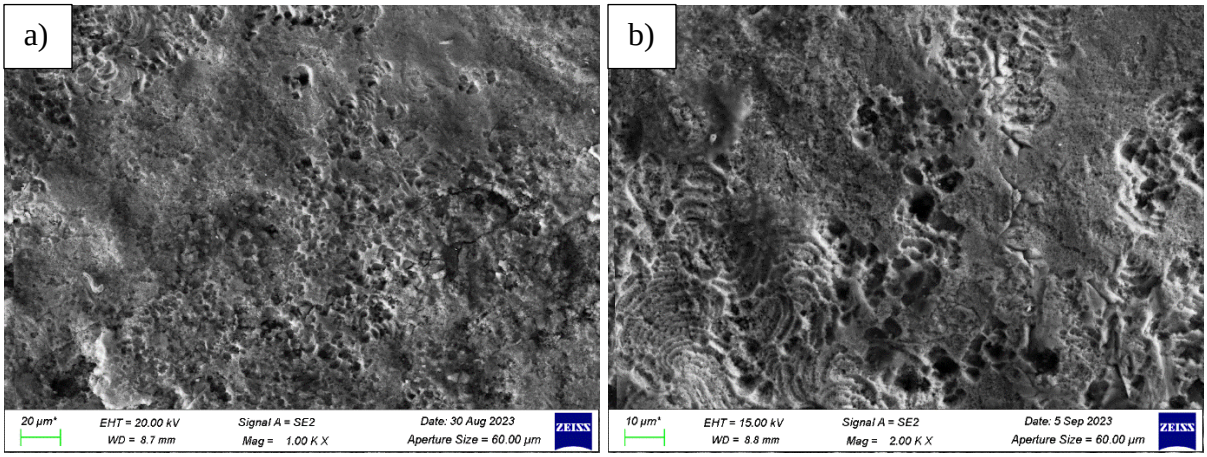


Figure 4.45. SEM-SE images of P3-SS0.8-N_p10 surface after potentiodynamic polarisation corrosion at: a) lower and b) higher magnification showing pits.

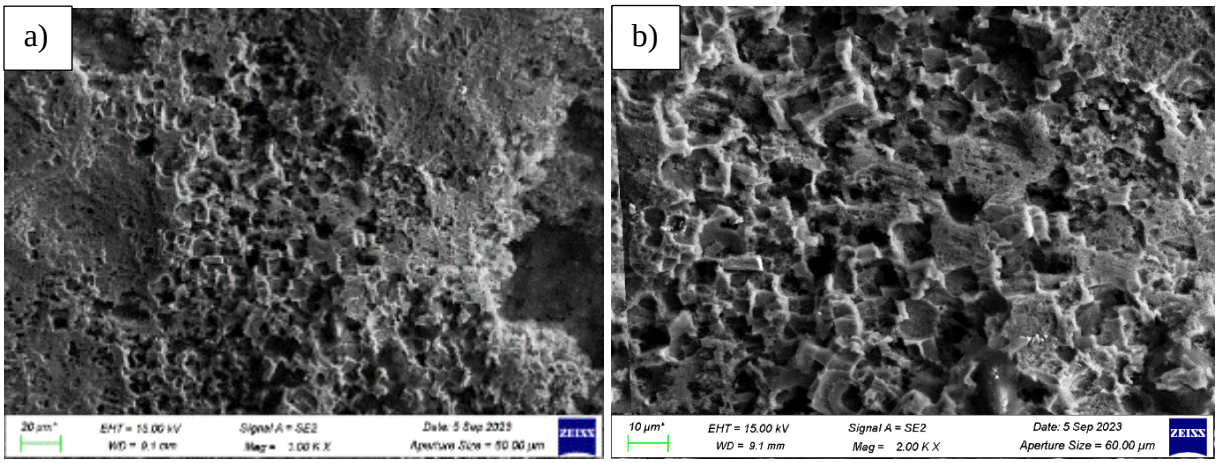


Figure 4.46. SEM-SE images of P3-SS0.8-N_p20 surface after potentiodynamic polarisation corrosion at: a) lower and b) higher magnification showing many square pits.

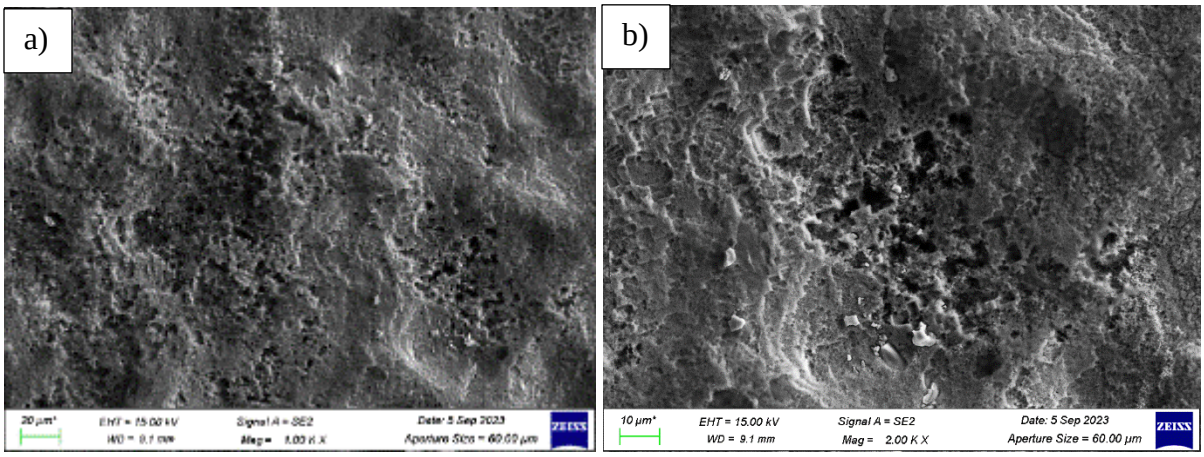


Figure 4.47. SEM-SE images of P3-SS0.8-N_p40 surface after potentiodynamic polarisation corrosion at: a) lower and b) higher magnification showing square pits and light particles.

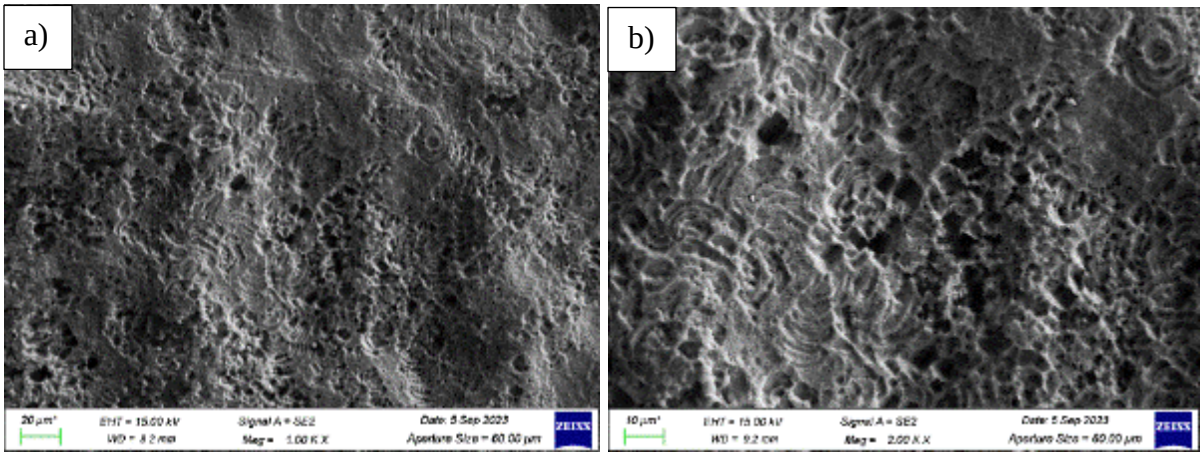


Figure 4.48. SEM-SE images of P5-SS0.8-N_p40 surface after potentiodynamic polarisation corrosion test at: a) lower and b) higher magnification showing irregular pits.

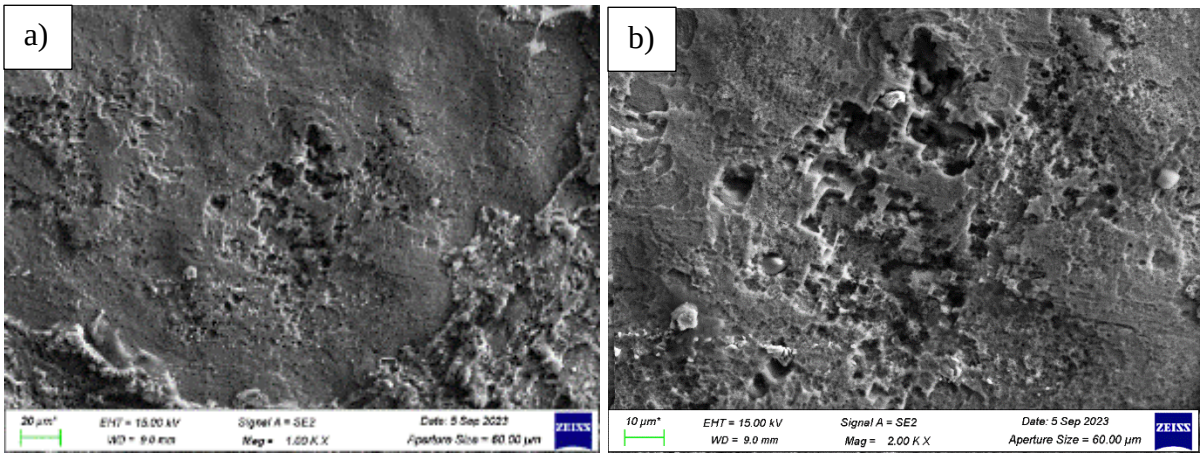


Figure 4.49. SEM-SE images of P3-SS1.5-N_p2.5 surface after potentiodynamic polarisation corrosion test at: a) lower and b) higher magnification showing few pits and unaffected area with light particles.

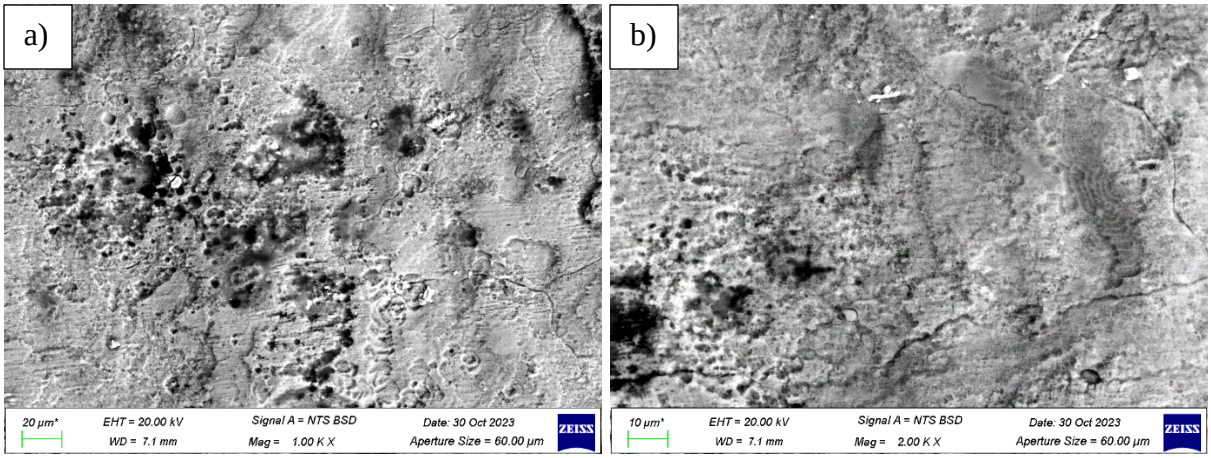


Figure 4.50. SEM-BSE images of P3-SS1.5-N_p5 surface after potentiodynamic polarisation corrosion test at: a) lower and b) higher magnification showing few pits.

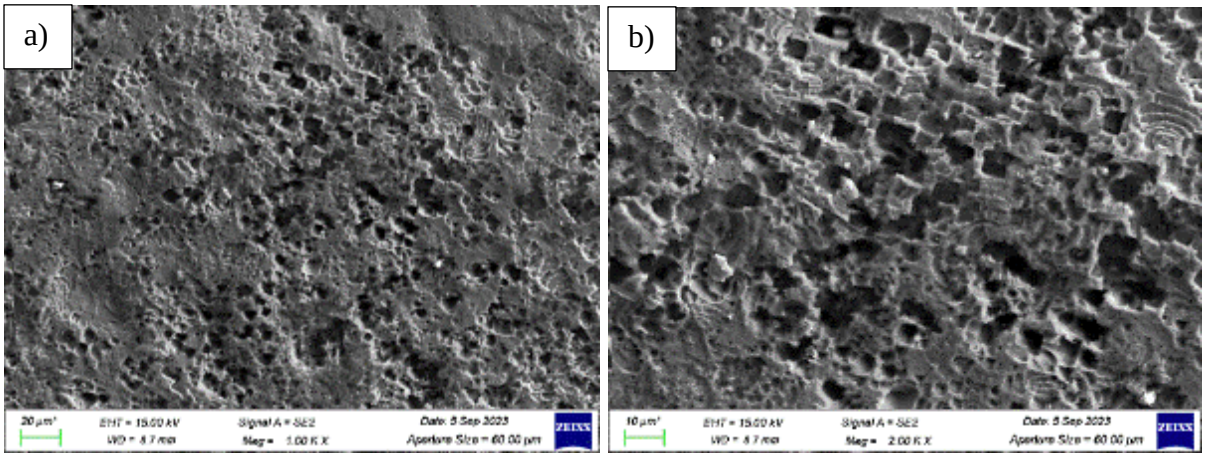


Figure 4.51. SEM-SE images of P3-SS1.5-N_p10 surface after potentiodynamic polarisation corrosion test at: a) lower and b) higher magnification showing many square pits.

4.8 Full Immersion Corrosion Tests - Weight loss for Sample 0 and P3-SS1.5-N_p5

After 30-day immersion in 3.5 wt% NaCl solution, Sample 0 had a layer of corrosion products on the surface with a few areas relatively free of the product (circled in red) shown in Figure 4.52a). There were several cracks in the product layer which were more visible in Figure 4.52b). The EDX

results of Sample 0 surface after immersion are listed in Table 4.16. Corrosion products included aluminium oxide as indicated by the high content of O. Low Cl and Na amounts were also detected.

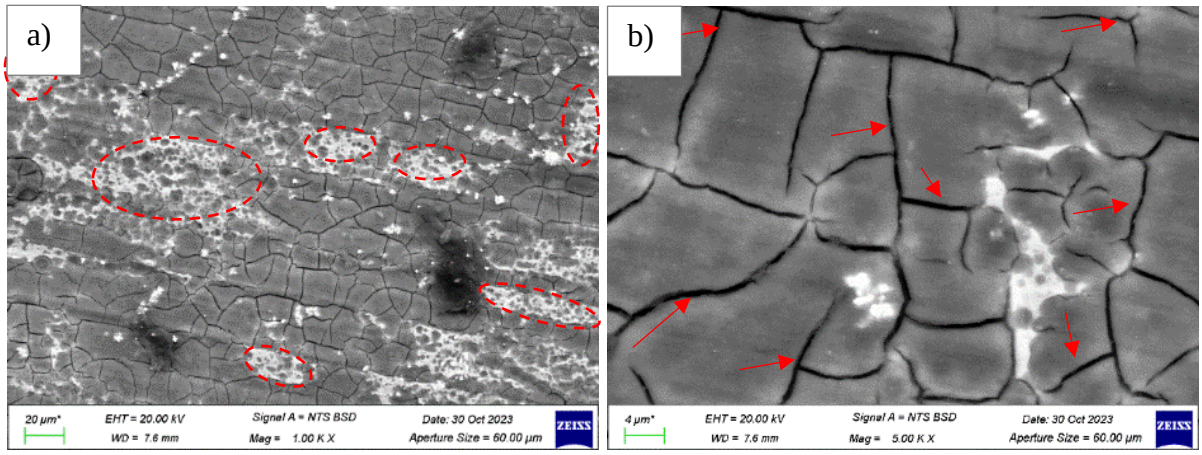


Figure 4.52. SEM-BSE images of Sample 0 surface after 30-day immersion at: a) lower and b) higher magnification, showing areas with less corrosion product (red ovals) and cracks on the corrosion product (red arrows).

Table 4.16. EDX results of corroded Sample 0 after 30 days in 3.5 wt% NaCl solution.

	O	**Na**	**Mg**	**Al**	**Si**	**Cl**	**Ca**	**Cr**	**Cu**	**Zn**
wt%	33.4 ± 2.6	1.1 ± 0.1	1.4 ± 0.2	52.7 ± 3.7	2.9 ± 0.4	0.2 ± 0.1	0.5 ± 0.1	0.4 ± 0.0	2.9 ± 0.6	4.5 ± 0.1
at.%	47.4 ± 3.2	1.1 ± 0.1	1.3 ± 0.2	44.6 ± 3.7	2.4 ± 0.3	0.1 ± 0.1	0.3 ± 0.1	0.2 ± 0.0	1.0 ± 0.2	1.6 ± 0.1

The surface of P3-SS1.5-N_p5 had corrosion products settled on the "hollows" caused by LSPwC (Figure 4.53). There were several cracks on the product layer which were more visible in Figure 4.53b) with lighter particles. The EDX results of the P3-SS1.5-N_p5 surface post-immersion (Table

4.17) revealed the presence of aluminium oxide as signified by elevated O levels, alongside minimal Cl and Na.

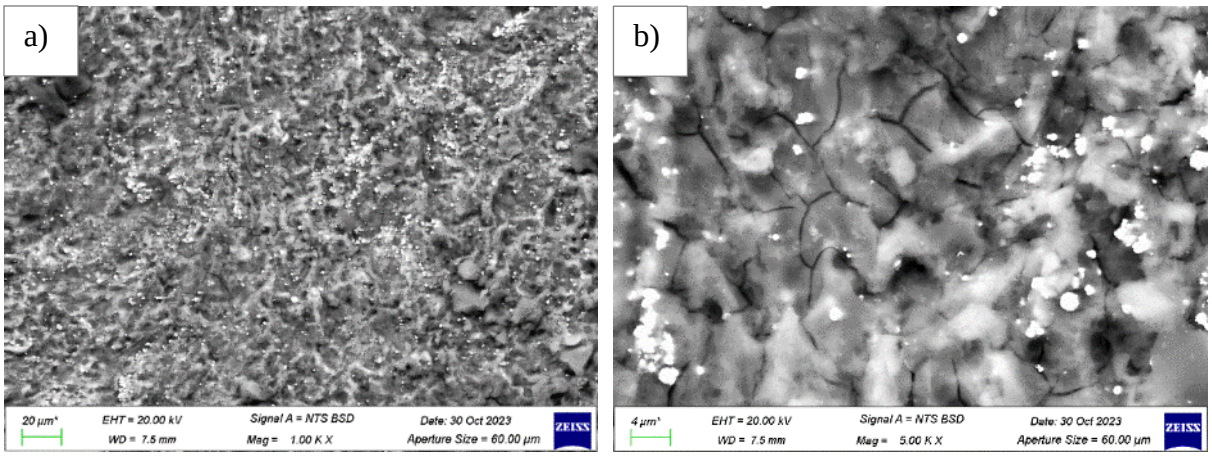


Figure 4.53. SEM-BSE images of the corroded surface of P3-SS1.5-N_p5 after 30-day immersion at: a) lower and b) higher magnification, showing corrosion products and light particles.

Table 4.17. EDX results of corroded P3-SS1.5-N_p5 after 30 days in 3.5 wt% NaCl solution.

	O	**Na**	**Mg**	**Al**	**Si**	**S**	**Cl**	**Ca**	**Cr**	**Fe**	**Cu**	**Zn**
wt%	40.1 ± 3.8	0.5 ± 0.2	1.0 ± 0.2	45.0 ± 3.3	2.6 ± 0.2	0.5 ± 0.1	0.9 ± 0.5	0.2 ± 0.1	0.4 ± 0.0	0.7 ± 0.1	4.1 ± 0.2	4.0 ± 0.7
at.%	55.2 ± 3.7	0.5 ± 0.2	0.9 ± 0.2	37.3 ± 3.5	2.0 ± 0.2	0.3 ± 0.1	0.5 ± 0.3	0.1 ± 0.1	0.2 ± 0.0	0.3 ± 0.0	1.4 ± 0.1	1.3 ± 0.3

The weight losses (ΔW = difference between initial and final weights) of Sample 0 and P3-SS1.5-N_p5 were calculated using Equation 3.4 and are presented in Figure 4.54 as a function of immersion time in 3.5 wt% NaCl solution. The value of ΔW for the test specimens increased with increasing immersion time. Sample 0 had more weight loss than P3-SS1.5-N_p5 throughout. The difference in ΔW for the peened and unpeened samples widened as time progressed.

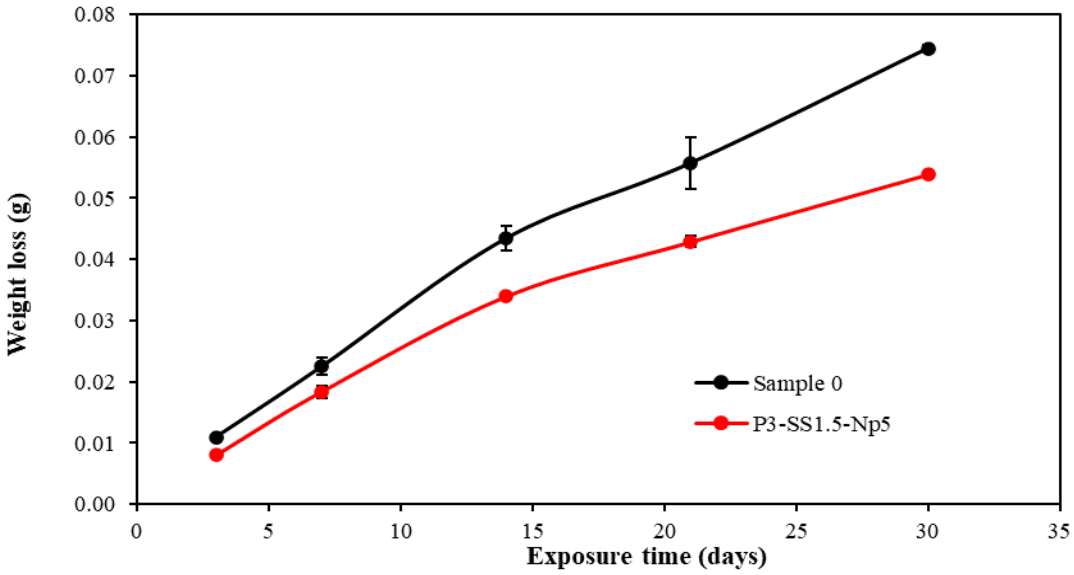


Figure 4.54. Variation of weight loss as a function of immersion time for Sample 0 and P3-SS1.5-N_p5 immersed in 3.5 wt% NaCl solution (standard deviations for the LSPwC samples were too small to show).

The corrosion rates for unpeened Sample 0 and P3-SS1.5-N_p5 are plotted against time as shown in Figure 4.55. For both specimens, the corrosion rate was highest in the beginning (especially in Sample 0) and gradually decreased as immersion time increased.

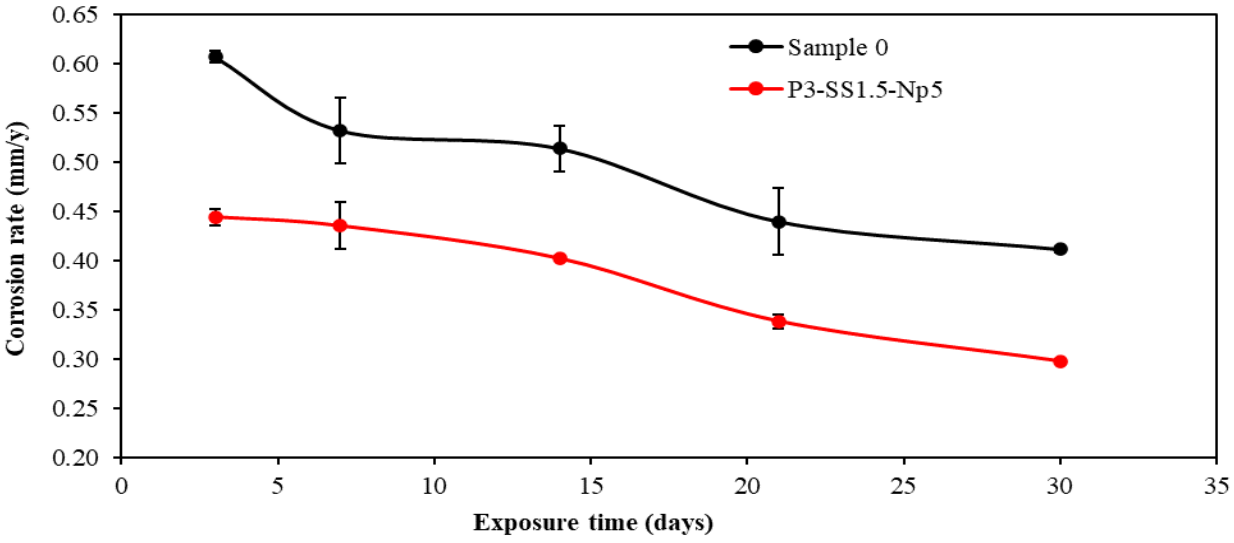


Figure 4.55. Variation of the corrosion rate as a function of immersion time for Sample 0 and P3-SS1.5-N_p5 immersed in 3.5 wt% NaCl solution.

Figure 4.56 to Figure 4.64 show surface morphologies of Sample 0 and P3-SS1.5-N_p5 after different immersion times and after cleaning. After three days, there were more small and shallow pits on Sample 0 (Figure 4.56) than on the peened sample (Figure 4.57). For P3-SS1.5-N_p5, smooth patches were observed on the corroded areas but much of the area still had the rough LSPwC layer. Hemispherical pits were observed and with increased time, the pits became wider and apparently deeper.

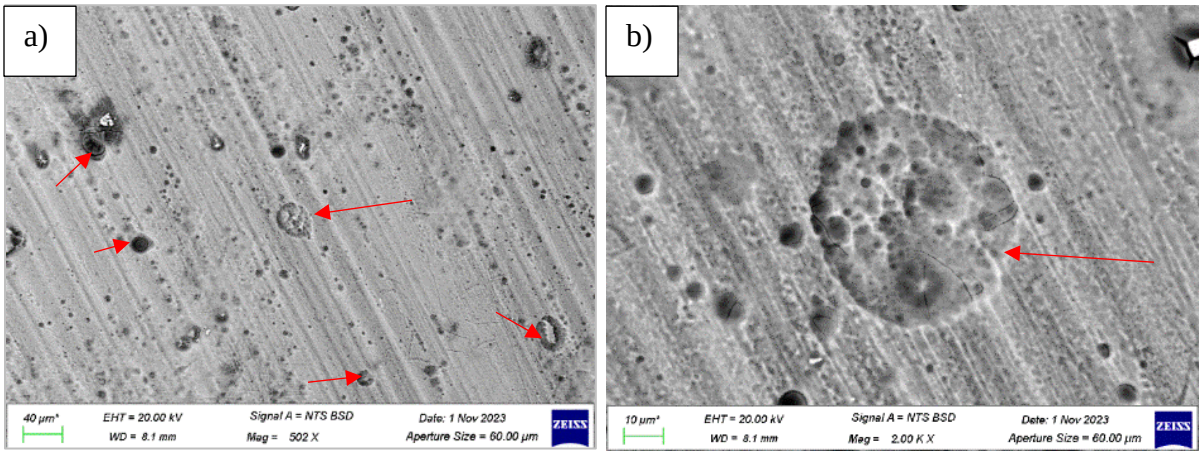


Figure 4.56. SEM-BSE images of Sample 0 surface after 3-day immersion at: (a) lower and (b) higher magnification showing corrosion pits (red arrows) and rolling lines.

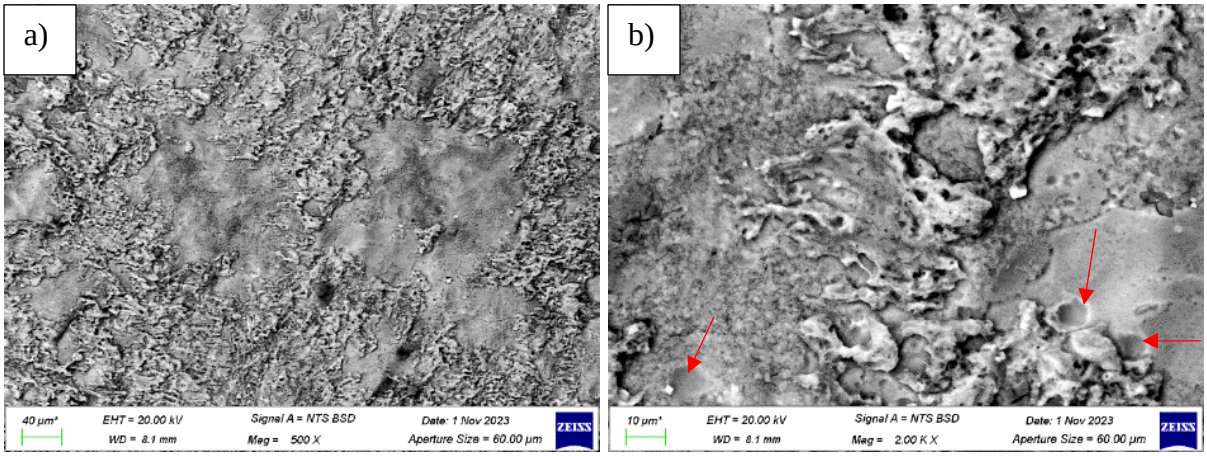


Figure 4.57. SEM-BSE images of P3-SS1.5-N_p5 surface at: (a) lower and (b) higher magnification showing corrosion pits (red arrows) after 3-day immersion.

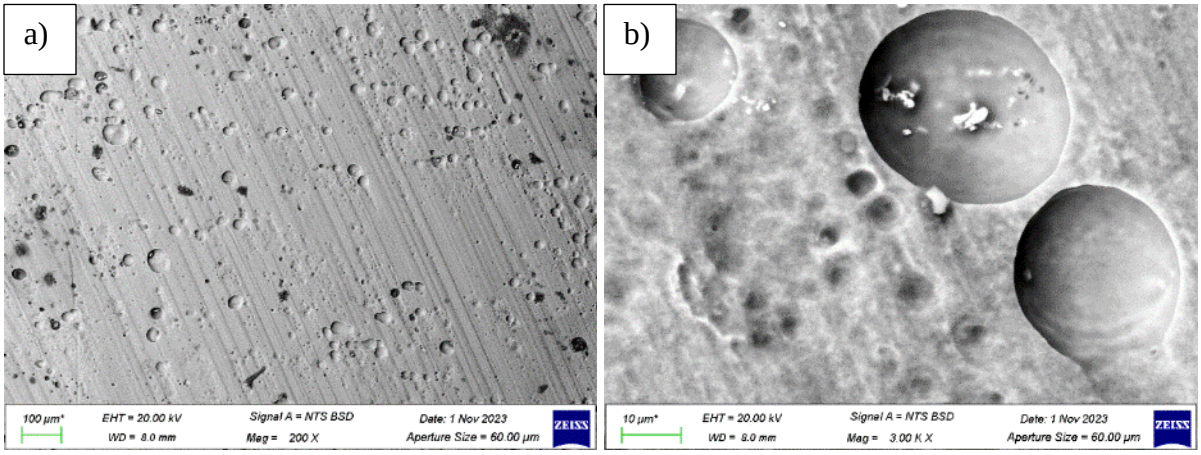


Figure 4.58. SEM-BSE images of Sample 0 surface at: (a) lower and (b) higher magnification showing hemispherical corrosion pits with white particles after 7-day immersion.

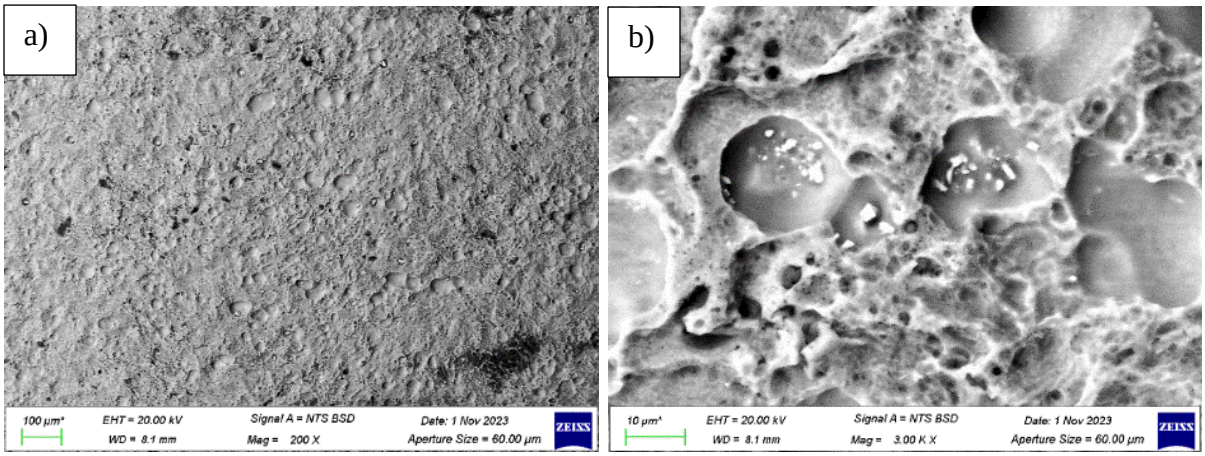


Figure 4.59. SEM-BSE images of P3-SS1.5-N_p5 surface at: (a) lower and (b) higher magnification showing hemispherical corrosion pits with white particles after 7-day immersion.

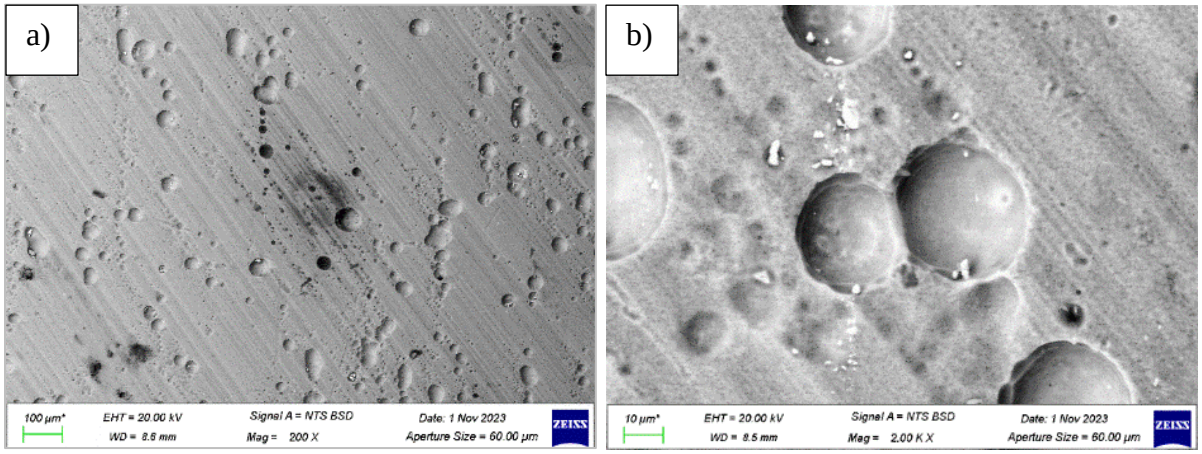


Figure 4.60. SEM-BSE images of Sample 0 surface at: (a) lower and (b) higher magnification showing hemispherical corrosion pits merging after 14-day immersion.

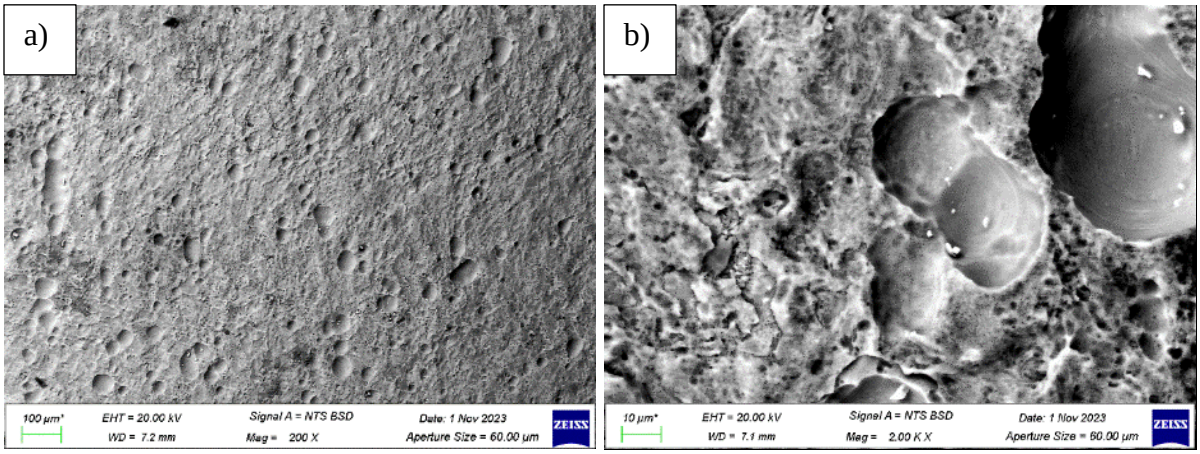


Figure 4.61. SEM-BSE images of P3-SS1.5-N_p5 surface at: (a) lower and (b) higher magnification showing hemispherical corrosion pits merging after 14-day immersion.

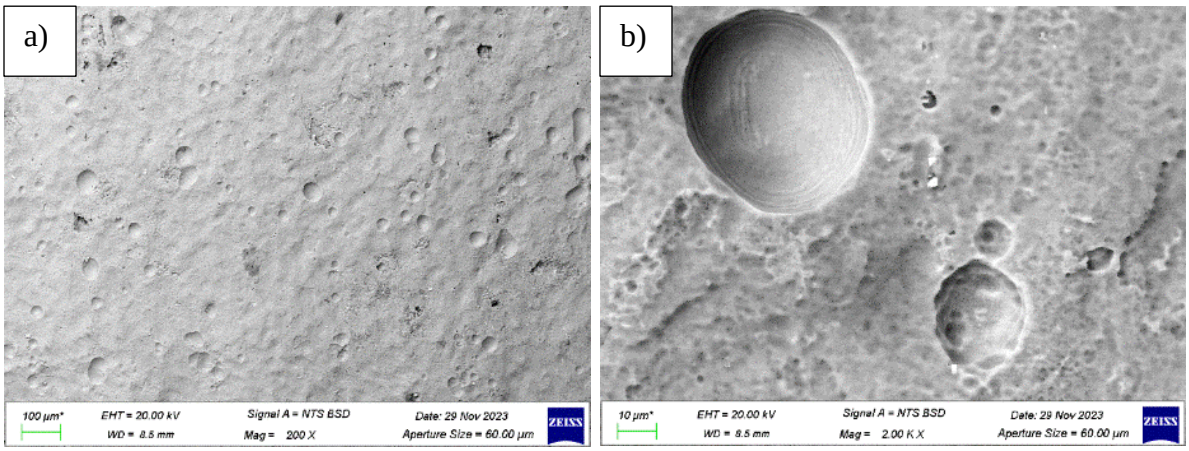


Figure 4.62. SEM-BSE images of P3-SS1.5-N_p5 surface at: (a) lower and (b) higher magnification showing hemispherical corrosion pits after 21-day immersion.

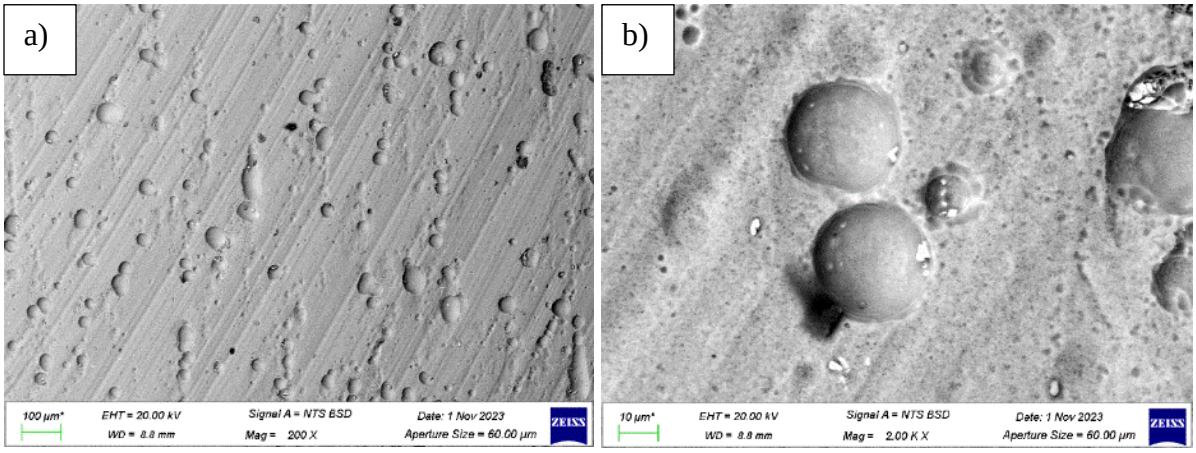


Figure 4.63. SEM-BSE images of Sample 0 surface at: (a) lower and (b) higher magnification showing corrosion pits after 30-day immersion.

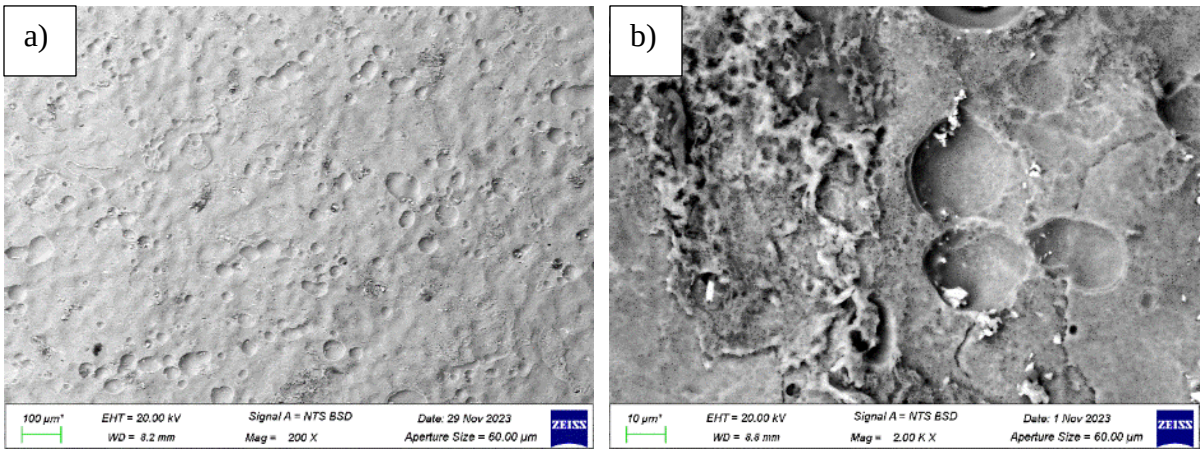


Figure 4.64. SEM-BSE images of P3-SS1.5-N_p5 surface at: (a) lower and (b) higher magnification showing hemispherical corrosion pits after 30-day immersion.

4.9 Stress Corrosion Cracking (SCC)

Within the first day of testing, small white crystals started appearing on the surface of the specimens tested under three-point bending in 3.5wt% NaCl solution for 40 days. Further observations on each specimen are given below.

4.9.1 Sample 0

SEM images in Figure 4.65 show the surface of Sample 0 after SCC testing, revealing multiple cracks of varying lengths with branching. The cracks in Figure 4.65a) were initiated at different places, with some starting at pits (circled in Figure 4.65b)) and others branching from pre-existing cracks. Corrosion products were detected within the crack, indicated by arrows in Figure 4.65c) and some areas had significant corrosion (Figure 4.65d)).

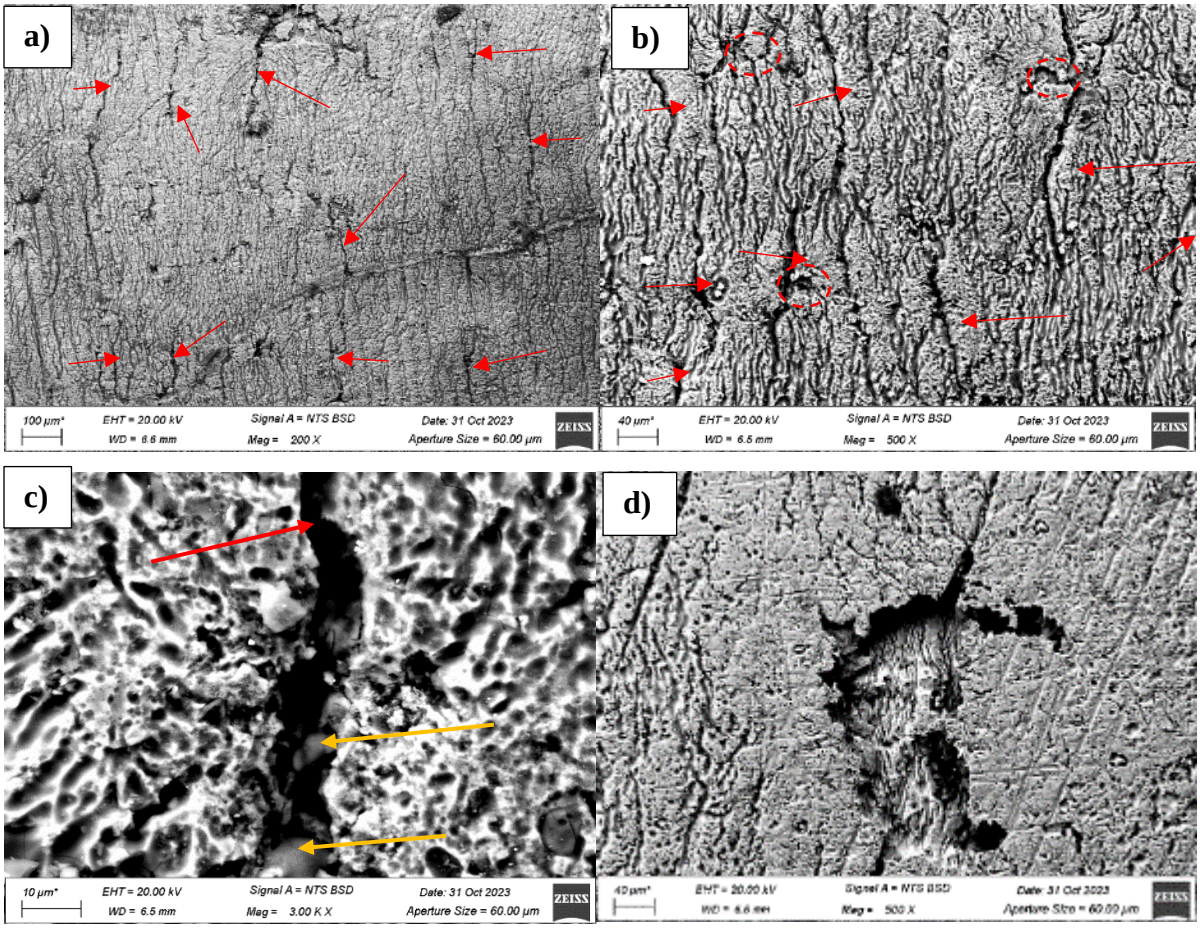


Figure 4.65. SEM-BSE images of Sample 0 after 40 days of SCC, showing surface cracks indicated by red arrows, pits circled in red and corrosion products inside the crack (orange arrows).

Figure 4.66 shows a cross-section of Sample 0 after SCC testing. The crack started off as a single crack and branched into two at ~23 µm depth, with one branch extending to a maximum depth of 50 µm and ended in several near-horizontal cracks.

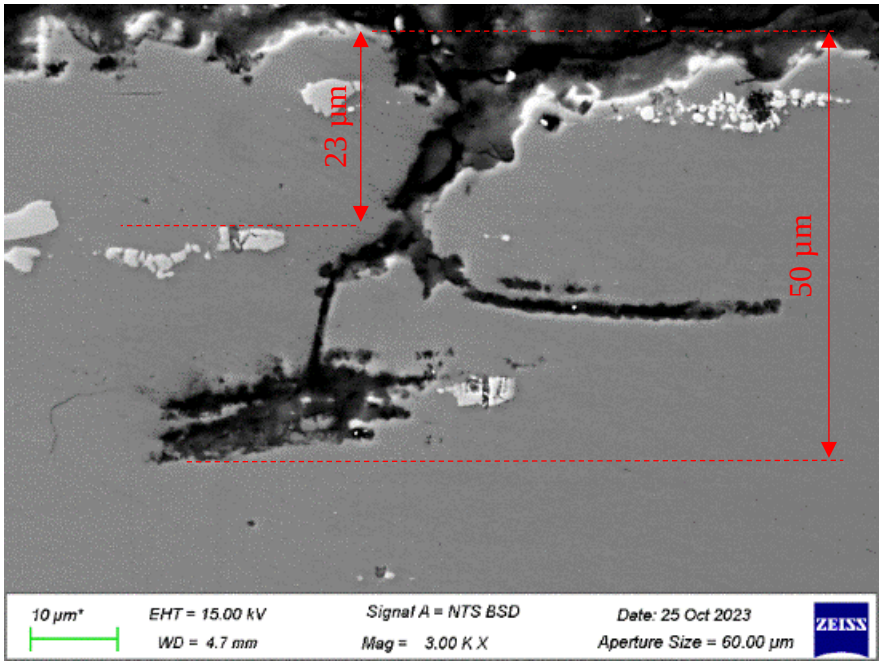


Figure 4.66. SEM-BSE image of a cross-section of Sample 0 showing cracks after SCC.

4.9.2 P3-SS0.5-N_p45

The surface of P3-SS0.5-N_p45 after the SCC test (Figure 4.67) had cracks that propagated in the rolling direction and were parallel to each other (Figure 4.67a)). In Figure 4.67b), the major cracks, indicated by the red arrows, are surrounded by shallow clusters of cracks (example circled in red).

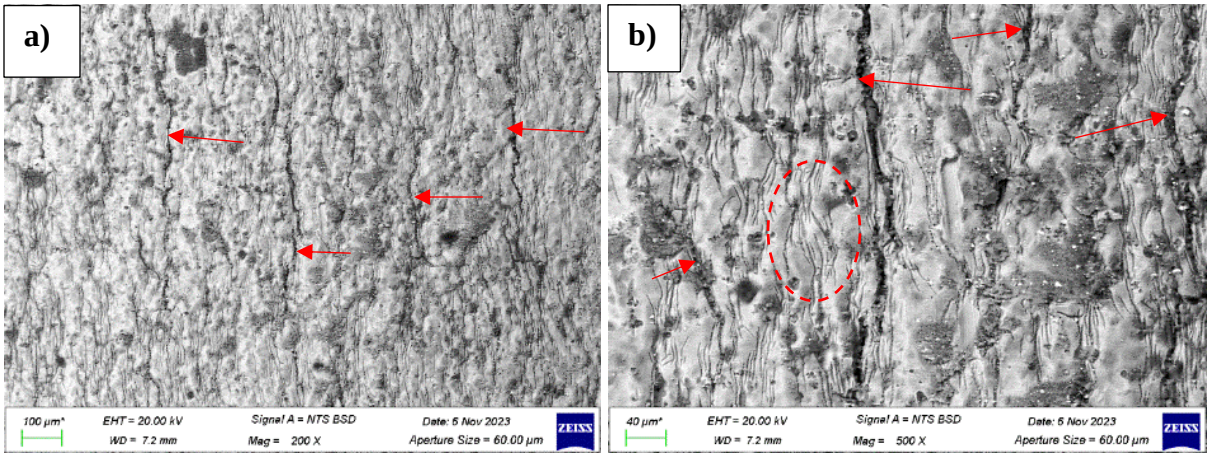


Figure 4.67. SEM-BSE images of P3-SS0.5-N_p45 surface after 40 days of SCC, at: a) lower and b) higher magnifications, showing arrows pointing to cracks and crack clusters circled in red.

The cross-section of P3-SS0.5-N_p45 (Figure 4.68) shows that the major crack initiated from a pit and propagated into the substrate at an angle. At a depth of ~40 µm, a minor horizontal crack branched from the initial crack. At ~52 µm, the crack deviated to the left and continued to ~68 µm before branching into two narrower cracks which were ~17 µm long. A shallower crack was present and is indicated by the orange arrow.

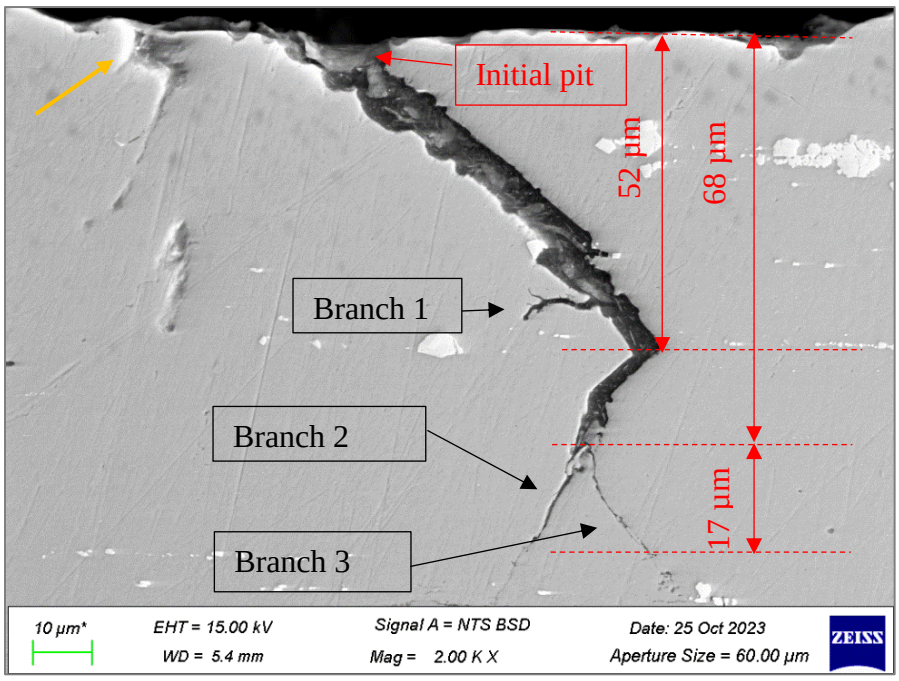


Figure 4.68. SEM-BSE image of a cross-section of P3-SS0.5-N_p45 showing the depth of the major crack caused by SCC and orange arrows indicating the shallow one.

4.9.3 P3-SS1-N_p50.38

The surface of P3-SS1-N_p50.38 showed few major cracks, Figure 4.69a), together with clusters of minor pits. At higher magnification, some corrosion product was found lodged inside the crack even after cleaning. There was also some pitting indicated by the blue arrows and minor cracks branching into clusters in Figure 4.69b).

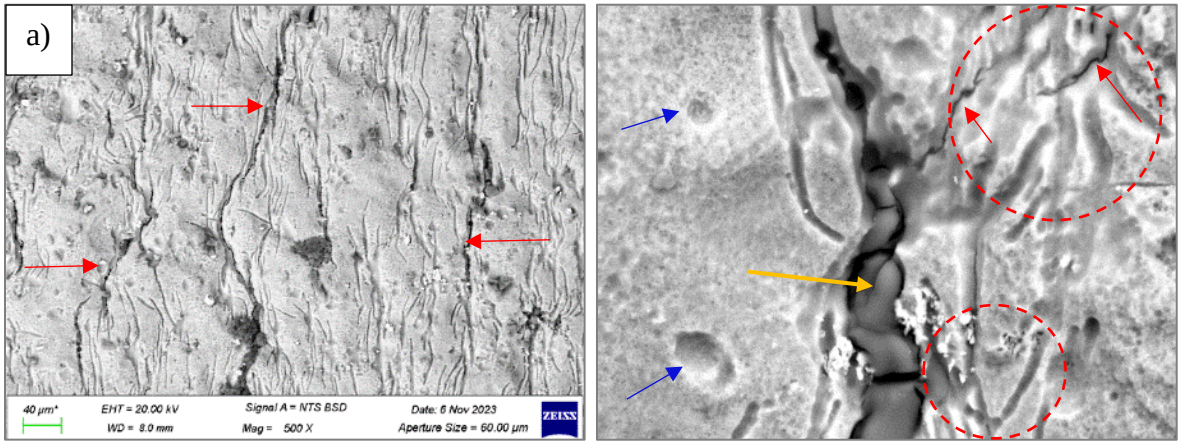


Figure 4.69. SEM-BSE images of P3-SS1-N_p50.38 surface after SCC, at: a) lower and b) higher magnification, showing major cracks (red arrows), minor cracks circled in red, corrosion product (orange arrow) and pits (blue arrows).

The cross-section of P3-SS1-N_p50.38 (Figure 4.70) showed pits ~7 µm deep similar to those caused by LSPwC. There were horizontal cracks similar to those observed after LSPwC in Figure 4.14 and Figure 4.15.

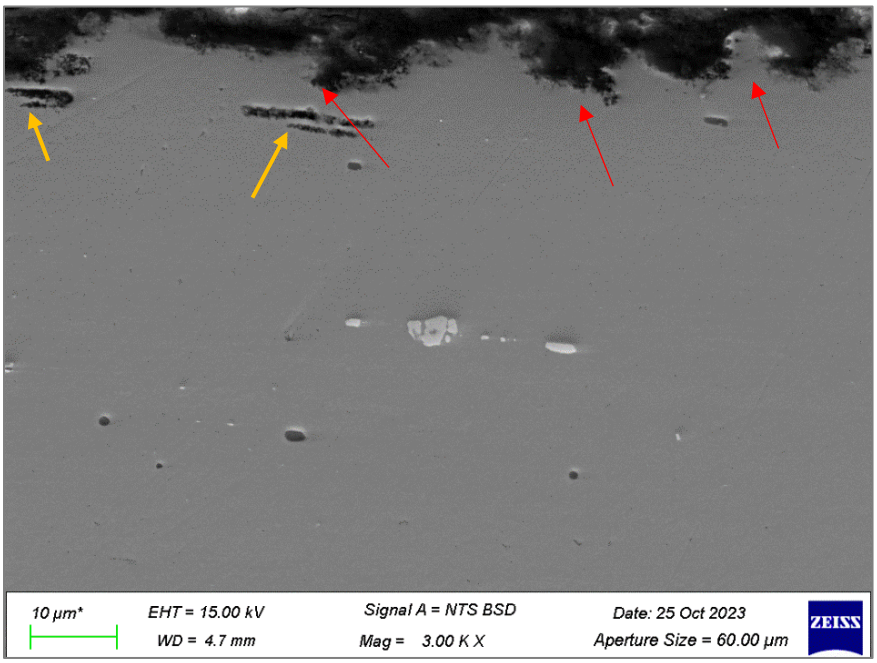


Figure 4.70. SEM-BSE image of a cross-section of P3-SS1-N_p50.38 showing shallow pits (red arrows) and horizontal cracks (orange arrows).

4.9.4 P3-SS0.5-N_p67.1

The surface of P3-SS0.5-N_p67.1 had few cracks as shown in Figure 4.71a). Figure 4.71b shows a prominent crack surrounded by clusters of shallow cracks which appeared to branch from corrosion pits.

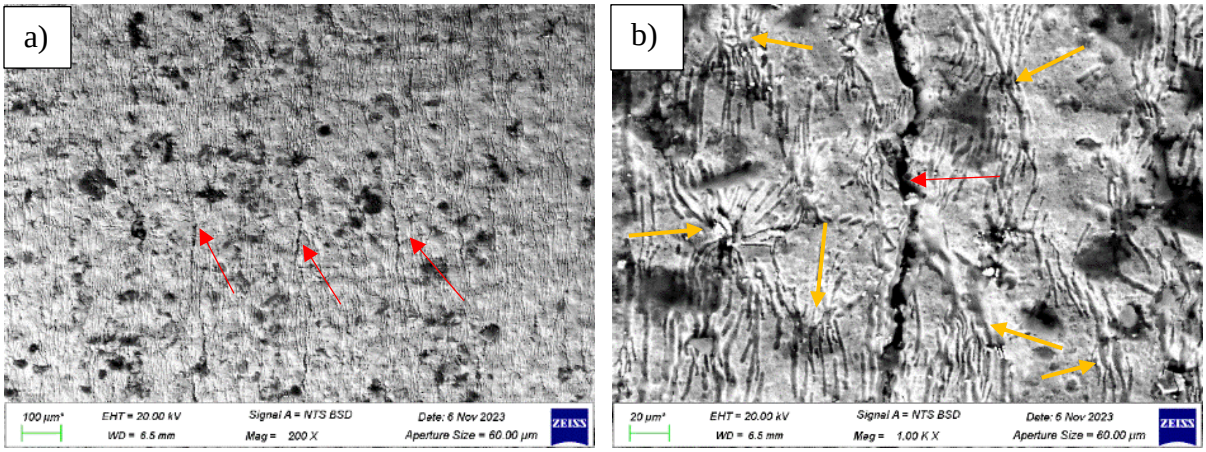


Figure 4.71. SEM-BSE images of P3-SS0.5-N_p67.1 surface after 40 days of SCC at: a) lower and b) higher magnifications, showing major (red arrows) and minor cracks (orange arrows).

The cross-section of P3-SS0.5-N_p67.1 shown in Figure 4.72 shows pits (indicated by red arrows) with one which formed a crack (indicated by the orange arrow).

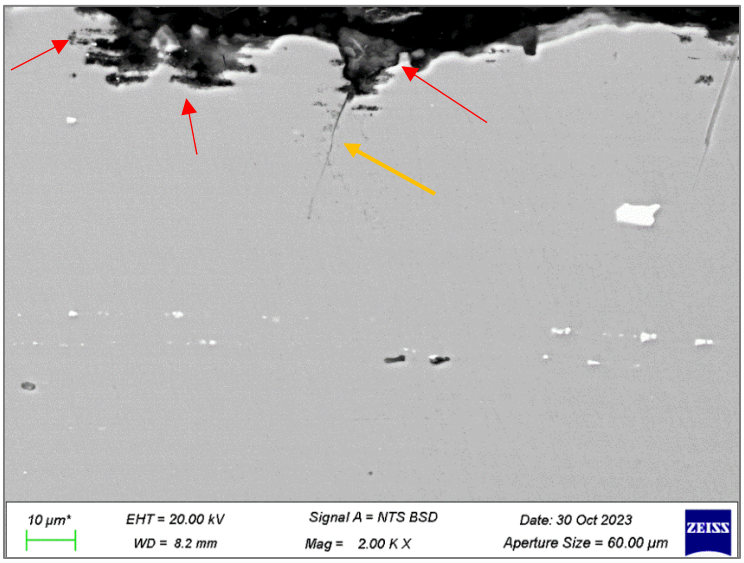


Figure 4.72. SEM-BSE image of a cross-section of P3-SS0.5-N_p67.1 after SCC showing pits indicated by red arrows and a crack (orange arrow).

4.9.5 P3-SS1.5-N_p21.88

The surface of P3-SS1.5-N_p21.88 showed few major cracks, Figure 4.73a). A higher magnification image of a major crack surrounded by shallow cracks is shown in Figure 4.73b).

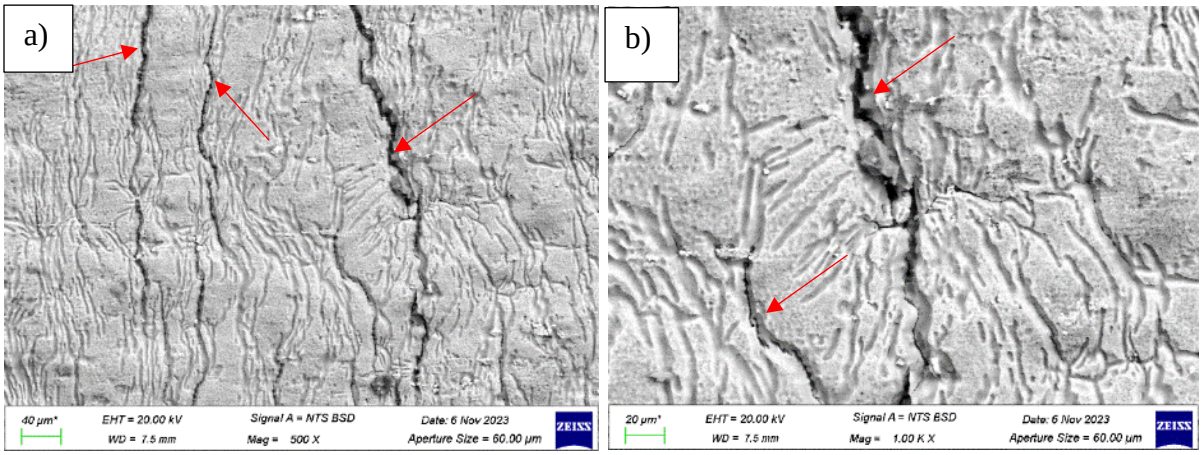


Figure 4.73. SEM-BSE images of P3-SS1.5-N_p21.88 surface after 40 days of SCC at: a) lower and b) higher magnifications showing red arrows pointing to the major crack.

The cross-section, Figure 4.74, showed shallow pits in P3-SS1.5-N_p21.88. One pit which was deeper than the others at ~10 µm depth, had started to develop two cracks and the longer one had propagated to 6.7 µm.

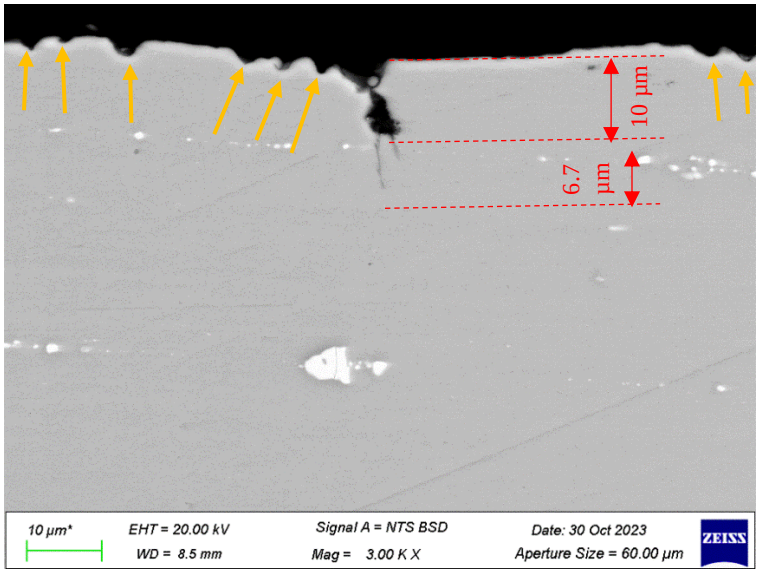


Figure 4.74. SEM-BSE image of a cross-section of P3-SS1.5-N_p21.88 showing the depth of cracks caused by SCC with orange arrows pointing to pits.

CHAPTER 5: DISCUSSION

5.1 Effect of LSPwC on surface morphology

The observed changes in surface morphology following Laser Shock Peening without Coating (LSPwC) were the alteration of the surface lustre from a shiny metallic appearance to a dull light grey, Figure 4.4. The peened surface had irregularities in the form of "mounts and hollows", craters, pores and solidified droplets, in contrast to the smoother unpeened surface. SEM images (Figures 4.5 – 4.13) revealed signs of melting and solidification. Gerland *et al*. (1992); Sano *et al*. (2006); Ding and Ye (2006) observed that the absence of a protective coating on the metal surface during LSPwC can cause severe surface melting and vaporisation, which led to the formation of resolidified droplets and craters, creating a rough surface. The cross-section showed "hollows" caused by the ablative interaction of the surface and laser. Mawaad *et al*. (2012) reported that LSPwC induces melting of the top surface layer, leading to microcrack formation to relieve stress during cooling. This effect was observed in the cracks on the sample cross-sections (Figures 4.14 and 4.15). However, this apparent thermal effect in this work was only observed a few micrometres from the top surface.

5.1.1 Surface features when varying coverage (N_p)

At a lower N_p of 2.5 spots/mm², sequential laser spots with minimal overlap created a surface with smooth parts within the roughened LSPwC area, as shown in Figure 4.6. However, at a higher N_p of 20 spots/mm² (Figure 4.7), the overlapping laser spots formed ridges and individual spots became indistinguishable, resulting in a roughened surface with more pronounced damage due to increased melting and solidification. The repeated melting and cooling at higher spot overlap reduced craters and pores by allowing molten metal to flow into spaces between defects, thus mitigating surface irregularities.

5.1.2 Surface features when varying power intensity (PI)

Power intensity (PI) variations also influenced surface features. Increased PI values (Figure 4.8 and Figure 4.9) led to more defined laser spots, with solidified "mounts" becoming a dominant feature. As PI increased, “hollows” became wider and deeper due to enhanced surface ablation. Mostafa *et al*. (2019) and Glaser *et al*. (2014) found that with increased PI, there was higher ablative interaction and thermal impact which caused the “hollows”/pits to become wider and deeper.

5.1.3 Surface features when varying spot size (SS)

Smaller spot size (SS) of 0.8 mm (Figure 4.10) resulted in lower spot overlap, more pronounced pores and solidified droplets. A larger SS of 1.5 mm (Figure 4.11) showed fewer pores and less pronounced surface irregularities. The topography of the roughened surface showed melting and solidification, with SEM-BSE images (Figures 4.10 & 4.11) showing solidified droplets.

5.1.4 Oxide formation

The LSPwC area showed an increased oxygen content, indicating oxide formation from the reaction with water (used as confinement medium) during peening. This agrees with Sano *et al.* (2006), who attributed oxide layer formation to the reaction of the confinement water layer by active plasma and the intense electric field of the focused laser pulse.

5.2 Effect of LSPwC on surface roughness

All tested samples had increased roughness after Laser Shock Peening without Coating (LSPwC), a result of the induced plastic deformation and surface ablation. The roughness values were higher in the stepping direction where the stylus would pass through the ridges which gave higher peaks. Similarly, Glaser *et al.* (2014) found the surface roughness of AA6056-T4 to be consistently higher in the stepping than scanning direction at different LSP parameters. The relationship between surface roughness and the LSPwC parameters is explored below.

5.2.1 Effect of varying power intensity on surface roughness

Laser power intensity was varied at constant coverage (N_p = 40 spots/mm^2) and spot size (SS 0.8 mm). A strong correlation was observed across all four surface roughness metrics, indicating that as power intensity increased, surface roughness also increased (Figure 5.1 and Figure 5.2.). The unpeened sample roughness is indicated by the first point at zero power intensity. Mostafa *et al*. (2019) found that with increased PI, there was higher ablative interaction and thermal impact which caused the hollows/pits to become wider and deeper. High peaks and low valleys translate to higher roughness values. Other studies (Glaser *et al.*, 2014; Abeens *et al.*, 2019; Attolico *et al.*, 2022; Glaser *et al.*, 2022) also found a positive linear relationship between surface roughness and laser power intensity.

The surface roughness comparison varying PI at constant coverage (N_p = 40 spots/mm^2) and spot size (SS 0.8 mm) in Figure 5.3 revealed a notable similarity between R_a and R_q, as well as between R_z and R_t. This convergence in values can be ascribed to the inherent statistical characteristics of these surface roughness parameters. Specifically, R_a and R_q signify the average roughness, while R_z and R_t correspond to the peak-to-valley height.

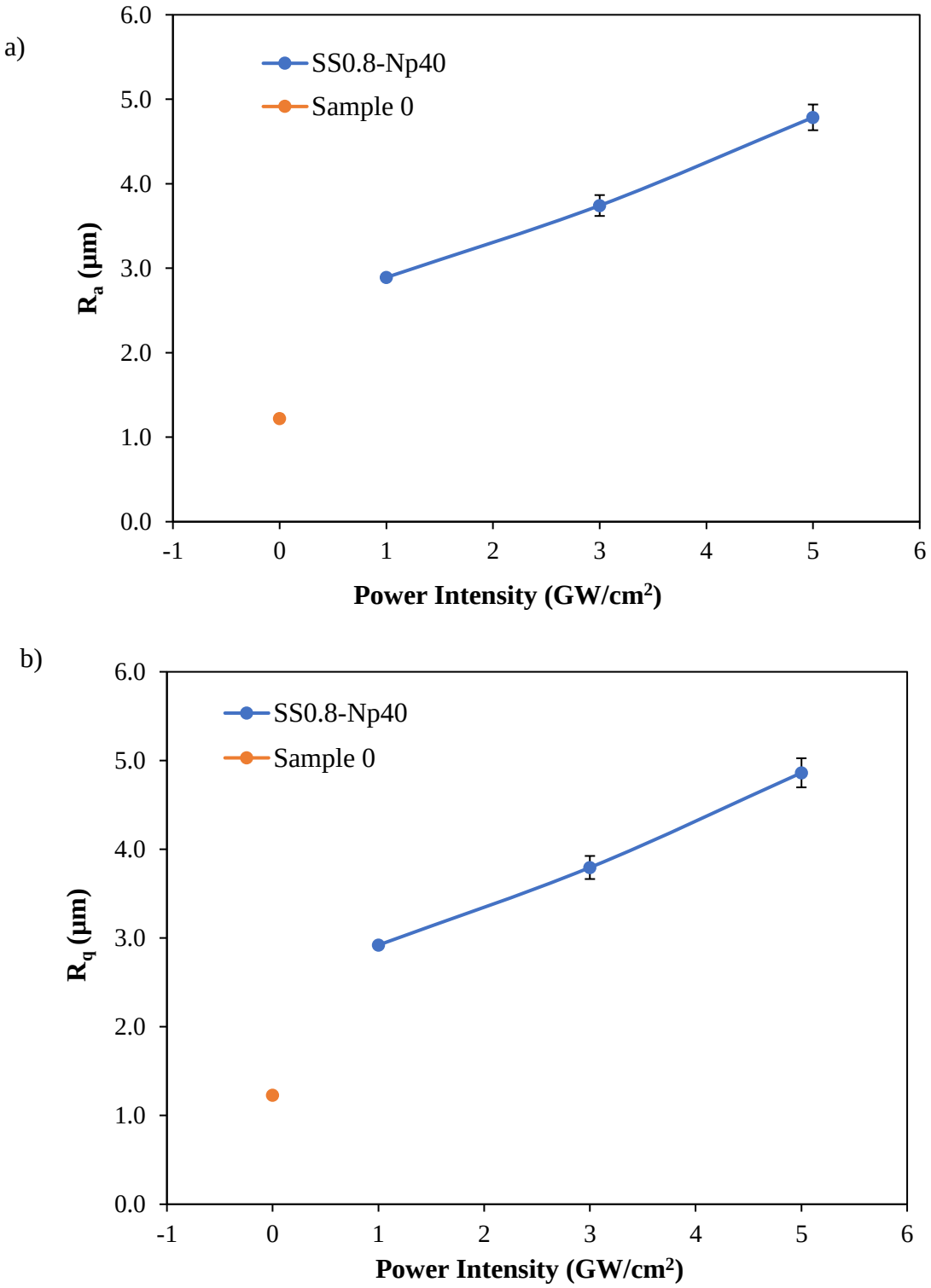


Figure 5.1. Relationship of power intensity (PI) and surface roughness: a) R_a (mean vertical deviation), b) R_q (square root of the mean of the square of vertical deviation).

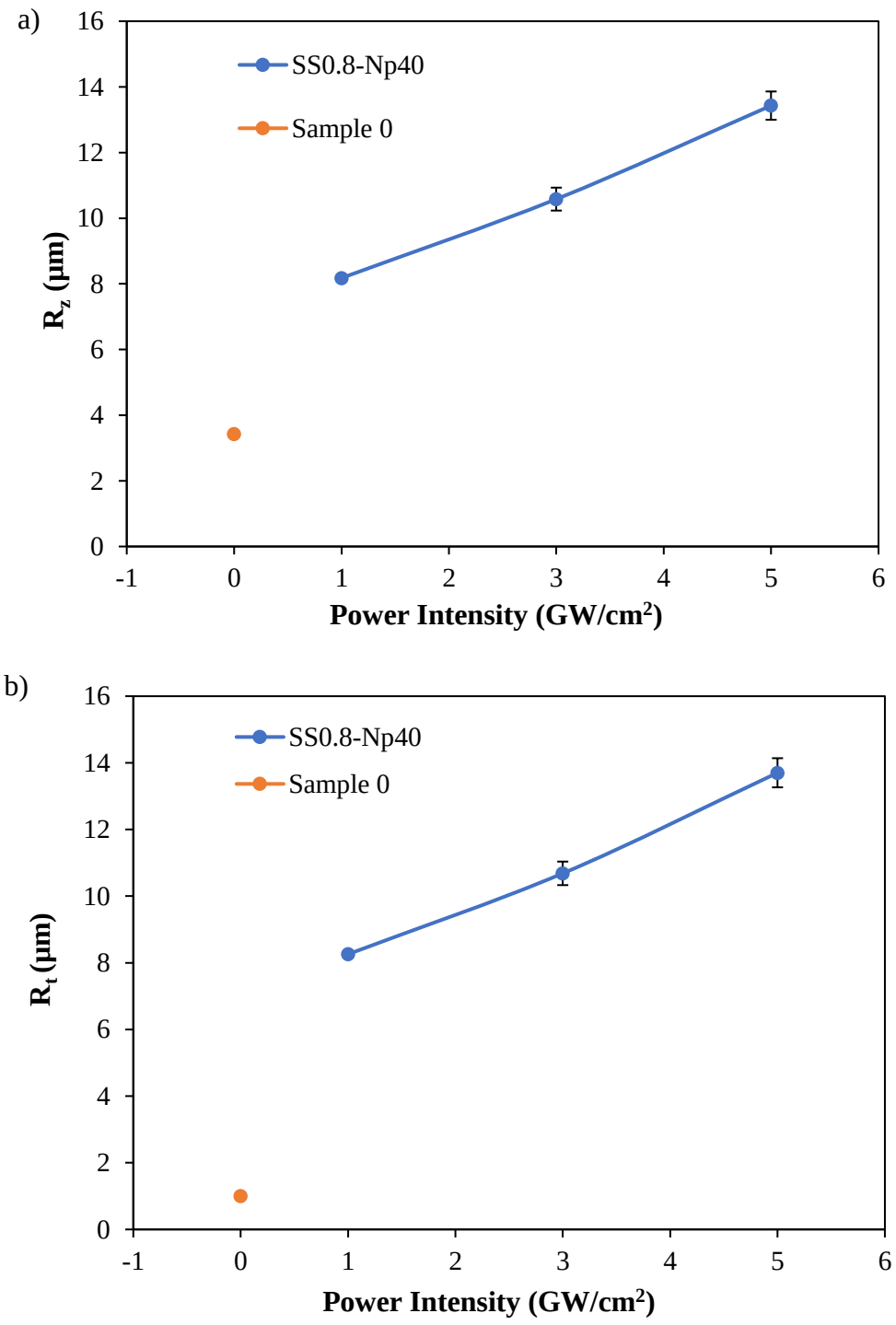


Figure 5.2. Relationship of power intensity (PI) and surface roughness: a) R_z (distance between the averages of the five highest peaks and lowest valleys), b) R_t (distance between the highest peak and lowest valley).

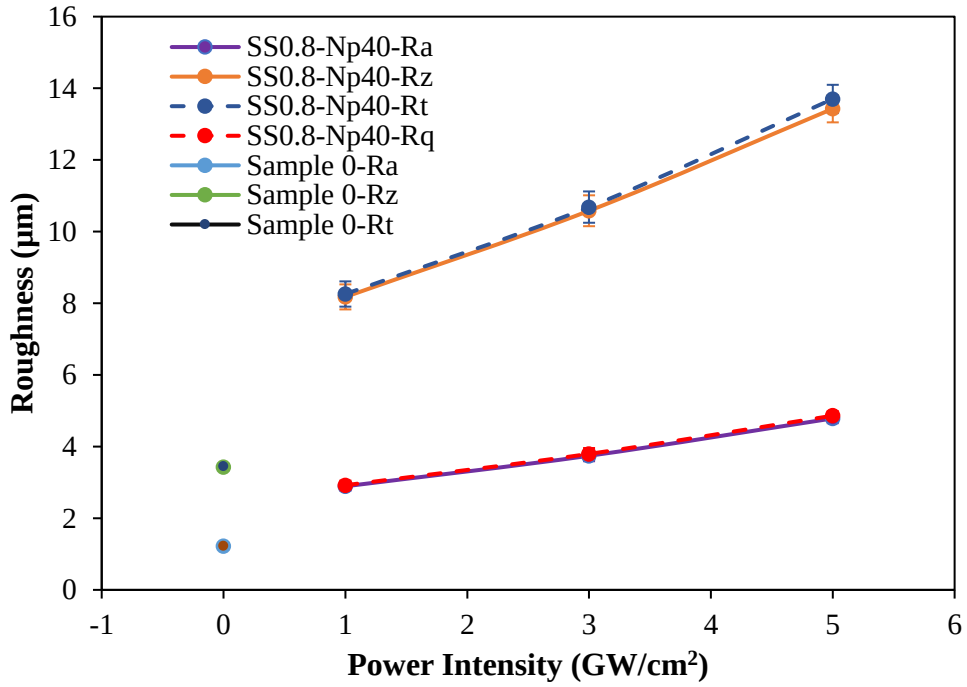


Figure 5.3. Comparison of surface roughness metrics at varying power intensity.

5.2.2 Effect of varying coverage on surface roughness

The variation of surface roughness with coverage (N_p) at power intensity = 3 GW/cm^2, spot size = 0.8 mm is shown in Figure 5.4 and Figure 5.5. The unpeened sample roughness is indicated by the first point at zero coverage. The roughness increased as N_p increased although it was not a strong linear relationship. Figure 5.6 and Figure 5.7 show a stronger relationship between surface roughness and N_p at a constant power intensity of 3 GW/cm^2 and a spot size of 1.5 mm. As N_p increased, the surface roughness increased. Each pressure pulse's surface deformation and surface ablation combine to cause increased surface roughness from the LPwC process. Consequently, an increase in the number of laser pulses per mm^2 leads to a rougher surface (Sathyajith and Kalainathan, 2012; Glaser *et al.*, 2014, 2022). The surface roughness comparison in Figure 5.8 and Figure 5.9 revealed a similarity between R_a and R_q, as well as between R_z and R_t.

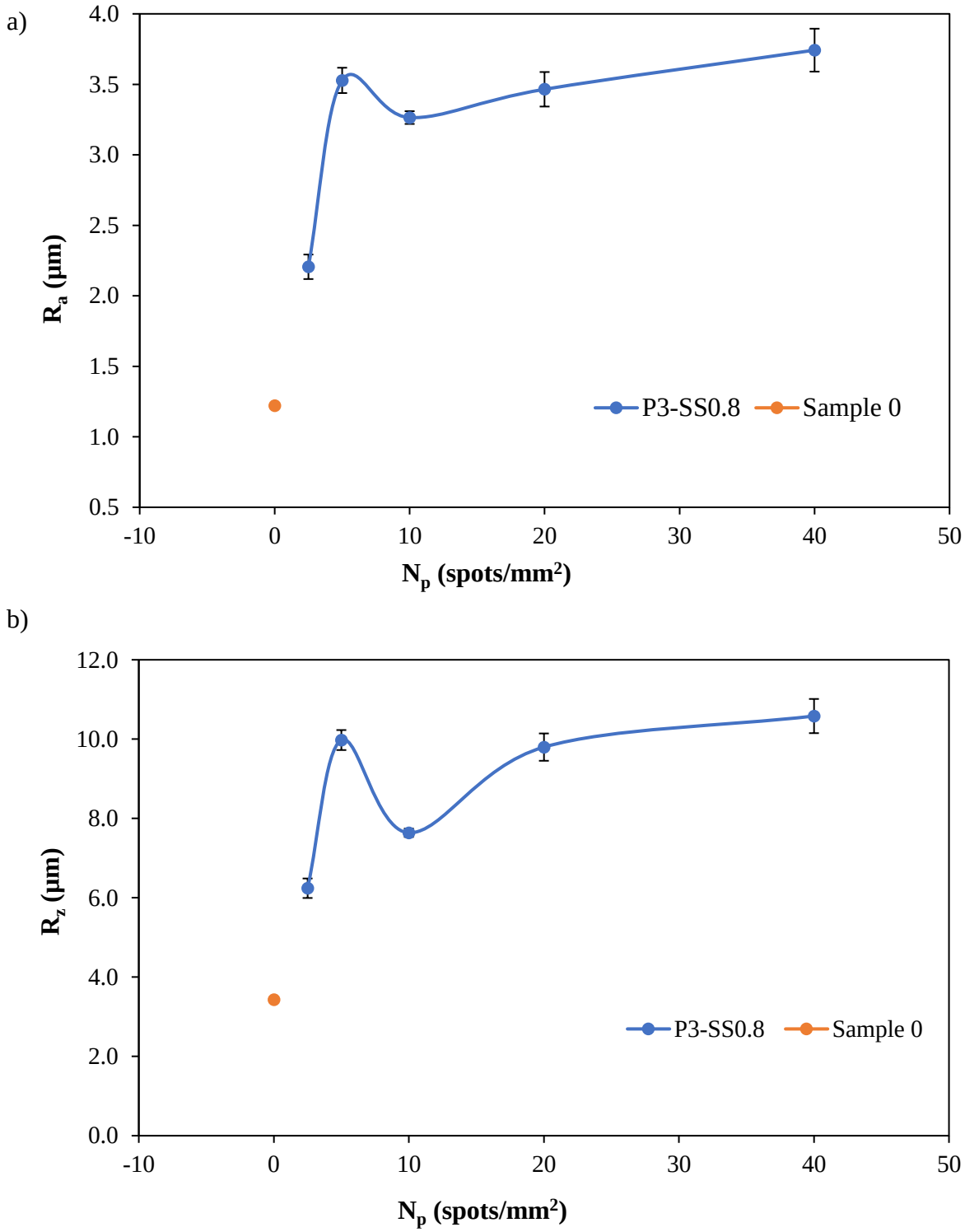


Figure 5.4. Surface roughness: a) R_a (mean vertical deviation), b) R_z (distance between the averages of the five highest peaks and lowest valleys relationship with coverage at PI = 3 GW/cm^2, SS = 0.8 mm.

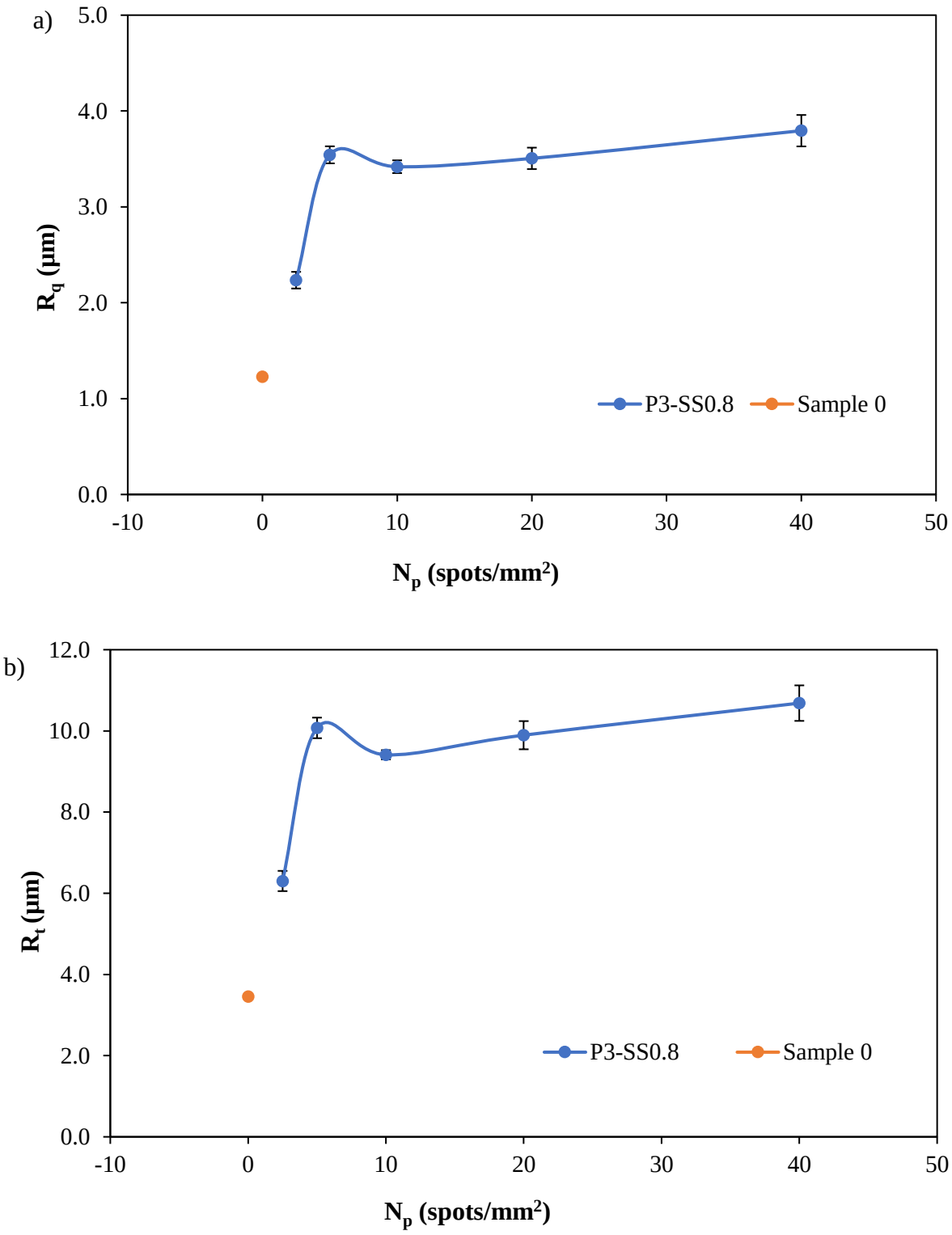
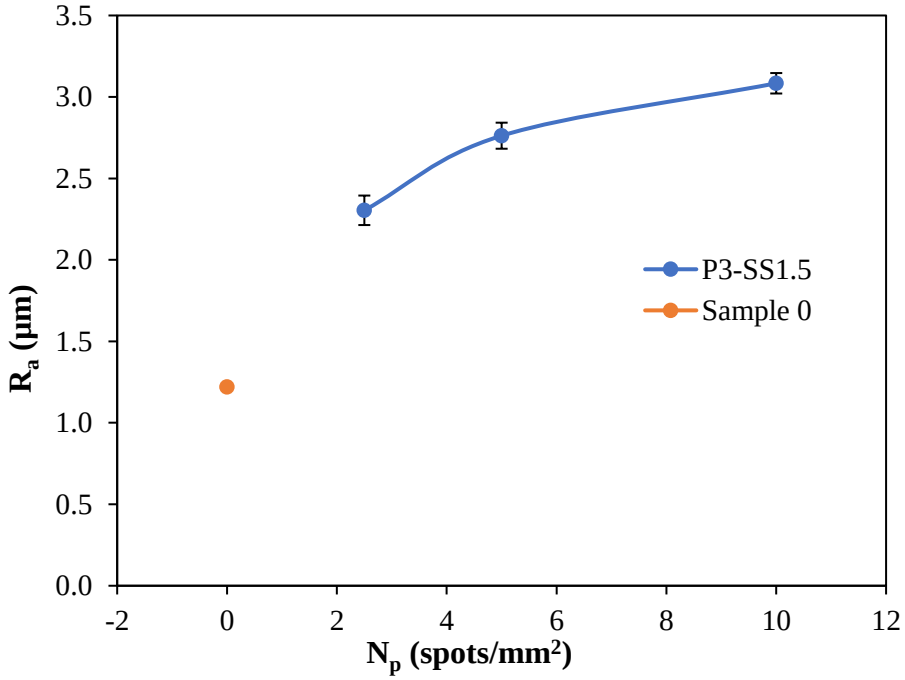


Figure 5.5. Surface roughness: a) R_q (square root of the mean of the square of vertical deviation), b) R_t (distance between the highest peak and lowest valley) relationship with coverage at PI = 3 GW/cm^2, SS = 0.8 mm.

a)



b)

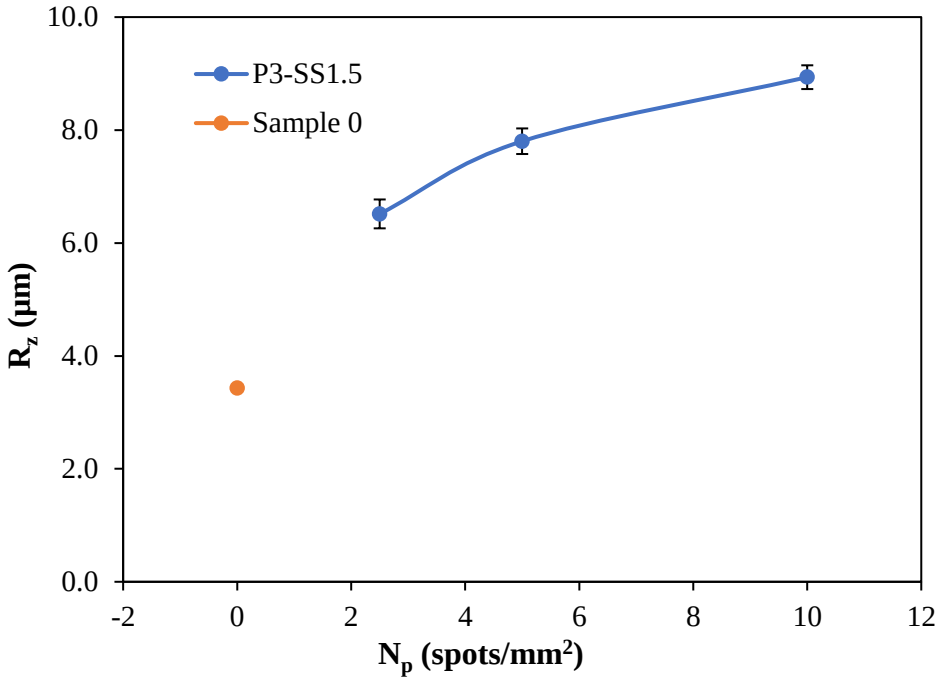
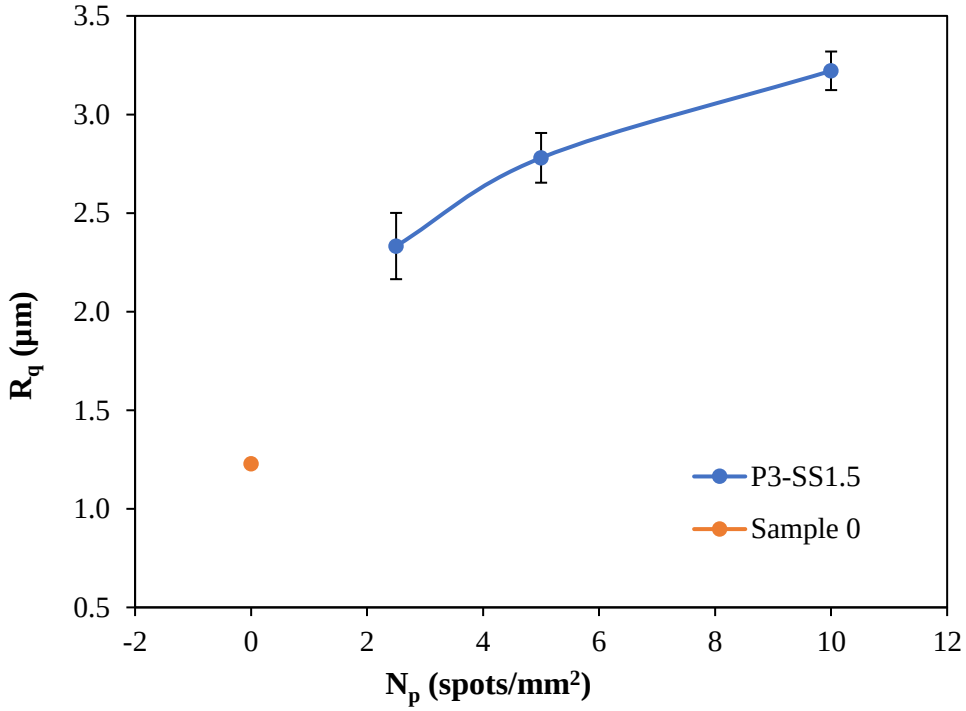


Figure 5.6. Surface roughness: a) R_a (mean vertical deviation), b) R_z (distance between the averages of the five highest peaks and lowest valleys) relationship with coverage at PI = 3 GW/cm^2, SS = 1.5 mm.

a)



b)

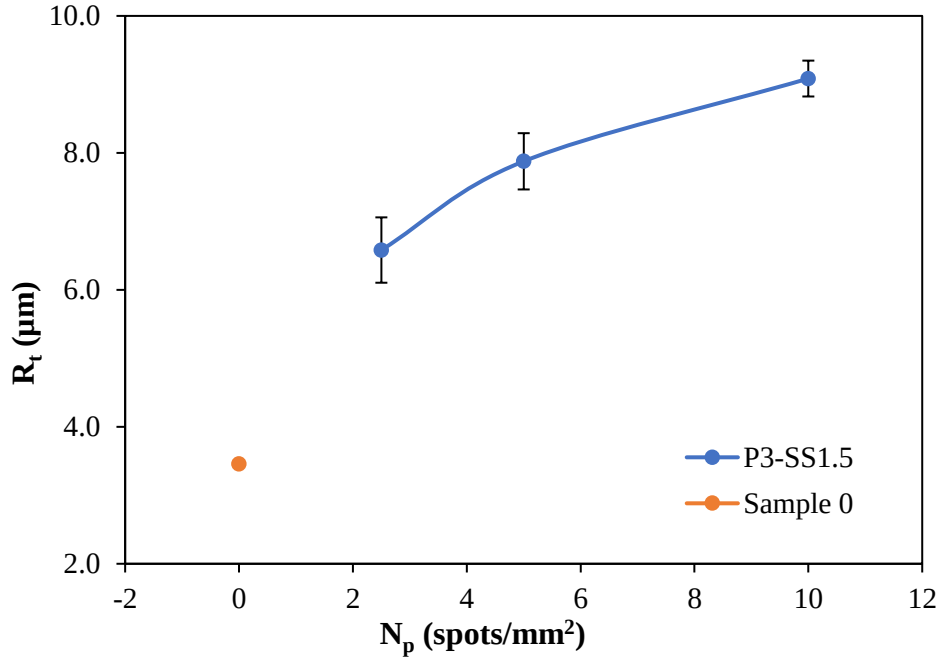


Figure 5.7. Surface roughness: a) R_q (square root of the mean of the square of vertical deviation), b) R_t (distance between the highest peak and lowest valley) relationship with coverage at PI = 3 GW/cm^2, SS = 1.5 mm.

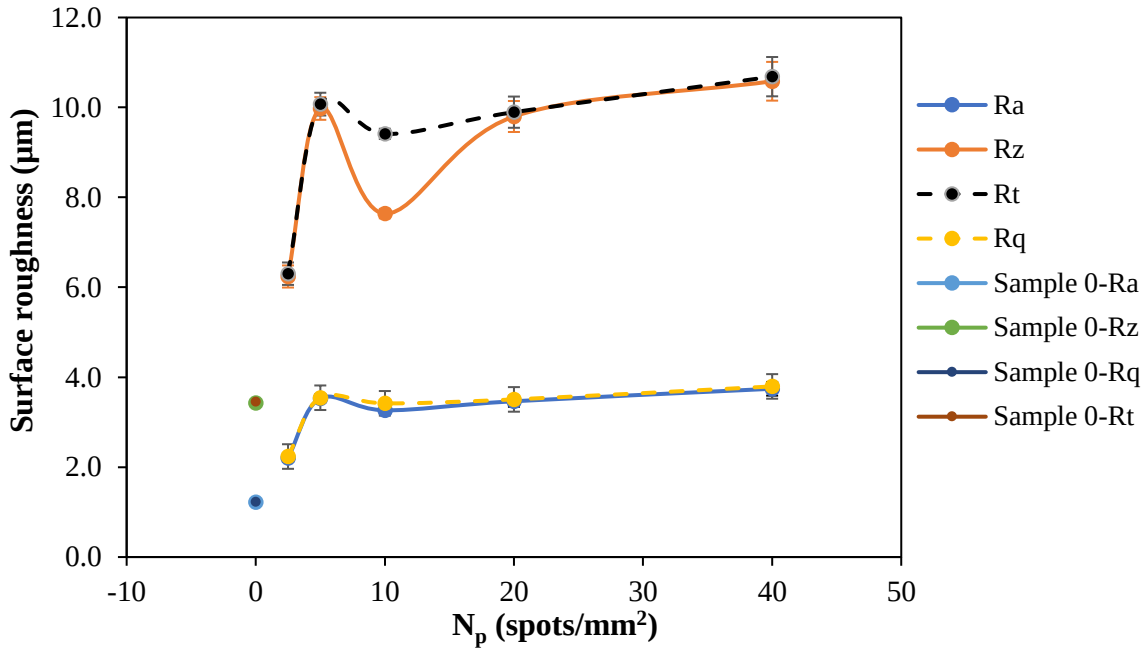


Figure 5.8. Comparison of surface roughness metrics varying coverage at PI = 3 GW/cm^2, SS = 0.8 mm.

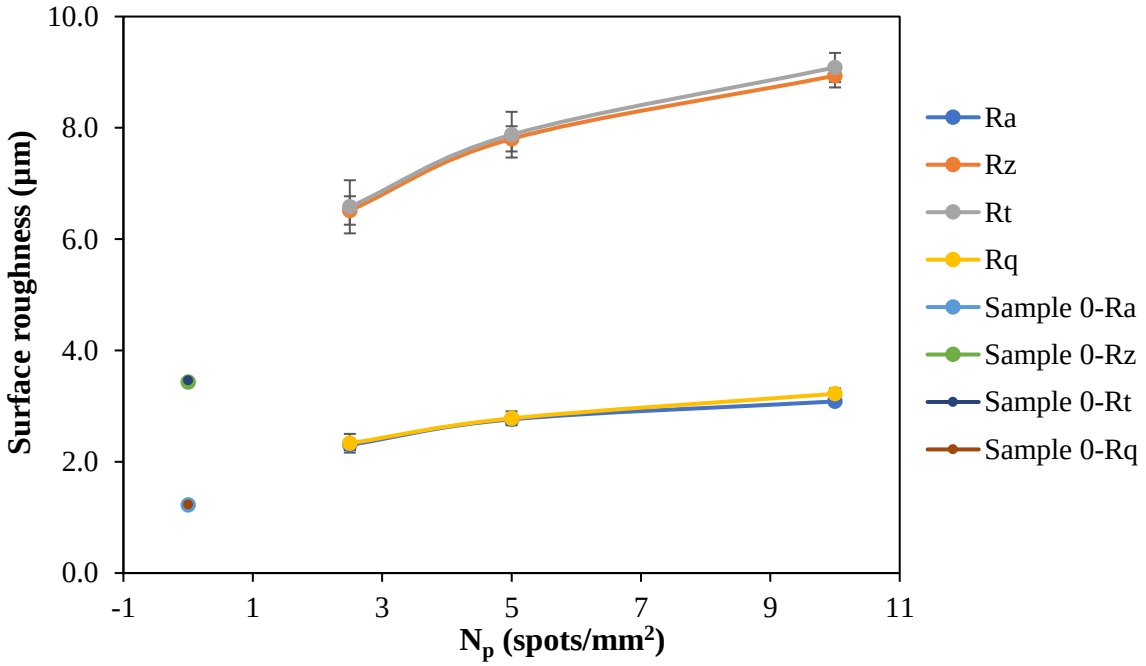


Figure 5.9. Comparison of surface roughness metrics varying coverage at PI = 3 GW/cm^2, SS = 1.5 mm.

5.2.3 Effect of varying spot size (SS) on surface roughness

In Figure 5.10, a comparison between SS0.8 and SS1.5 revealed a similarity in the mean roughness metrics (R_a and R_q) and the peak-to-valley height metrics (R_z and R_t). The relationship between surface roughness and spot size is shown in Figure 5.11 and Figure 5.12 for the different coverages at constant PI = 3 GW/cm^2. For specimens peened at N_p2.5, the larger spot size (1.5 mm) had higher roughness values than SS0.8, even though the error bars were overlapping. At N_p5, the roughness values were significantly higher for SS0.8 than SS1.5. At N_p10, roughness values were slightly higher for SS0.8 than SS1.5.

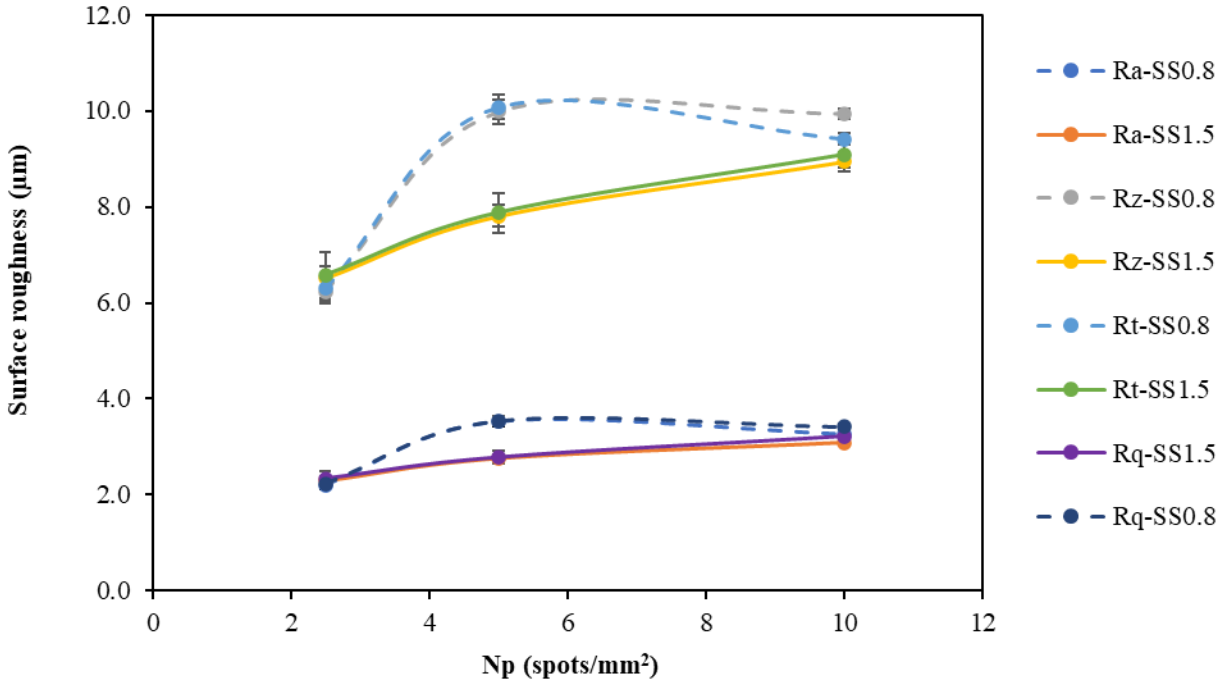


Figure 5.10. Comparison of surface roughness metrics at SS = 0.8 mm & SS = 1.5 mm.

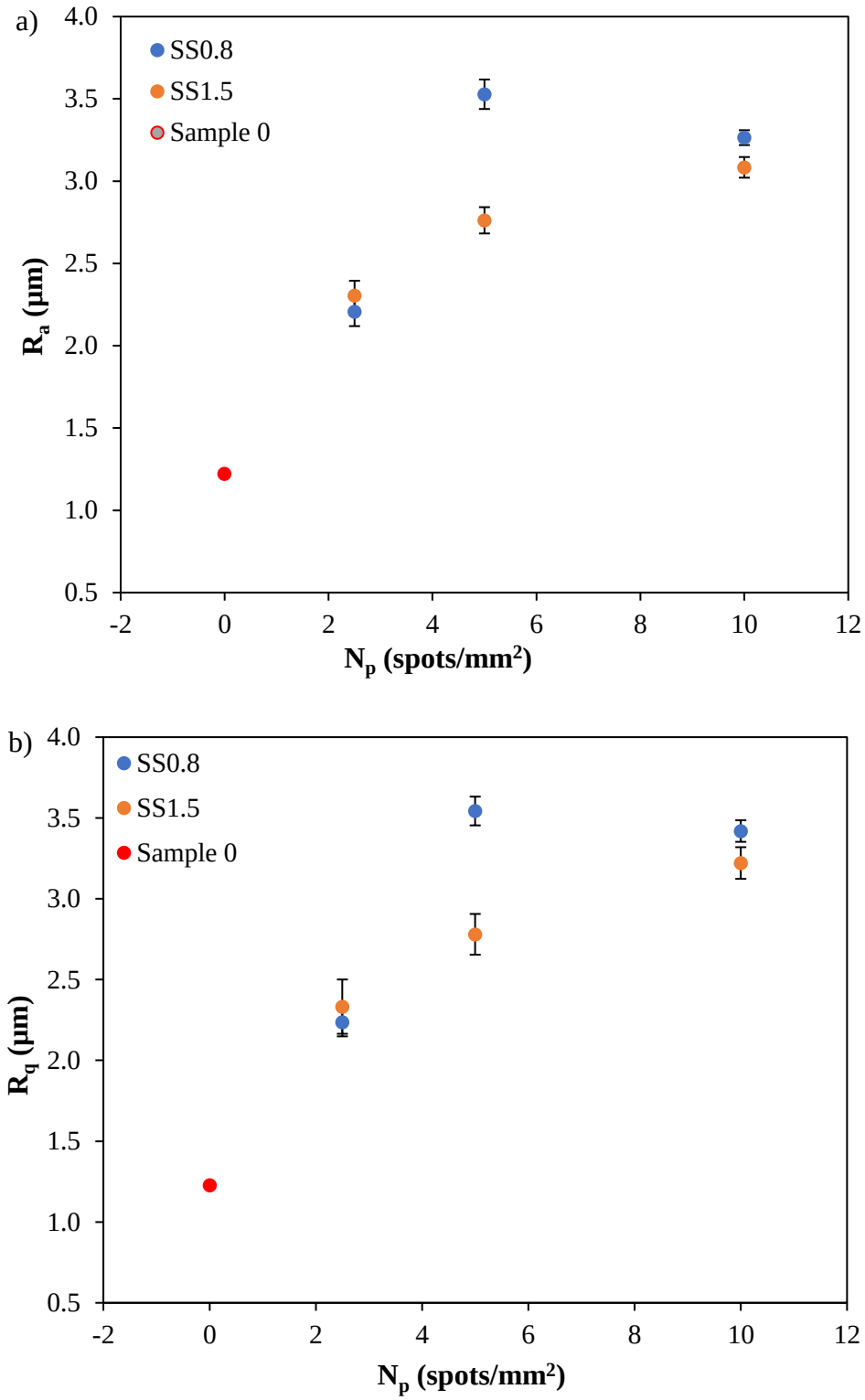


Figure 5.11. Surface roughness: a) R_a (mean vertical deviation), b) R_q (square root of the mean of the square of vertical deviation) comparison at SS = 0.8 mm & SS = 1.5 mm.

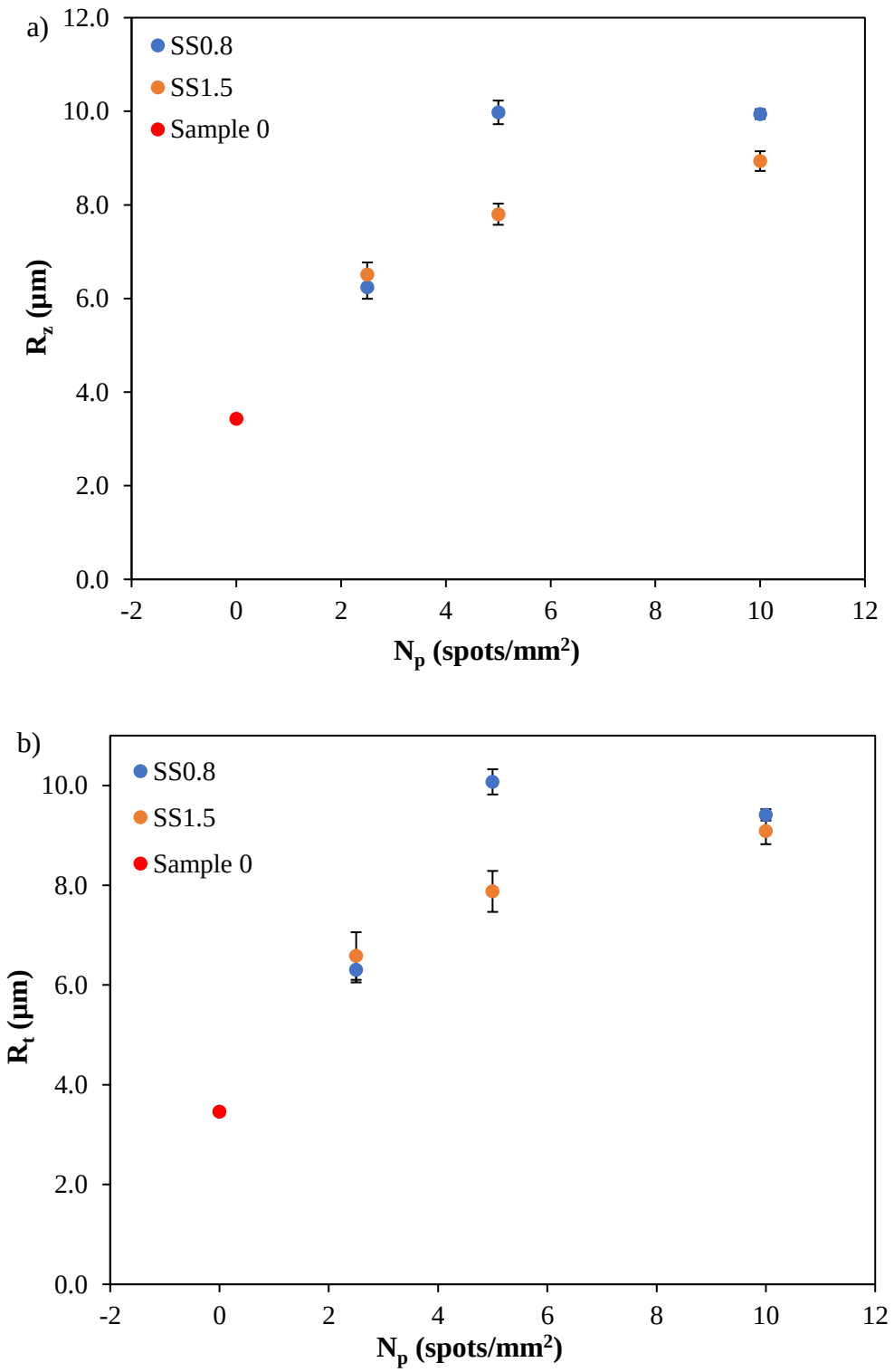


Figure 5.12. Surface roughness: a) R_z (distance between the averages of the five highest peaks and lowest valleys), b) R_t (distance between the highest peak and lowest valley) comparison at SS = 0.8 mm & SS = 1.5 mm.

5.3 Effect of LSPwC on microhardness

All tested samples showed increased hardness after LSPwC (Figure 4.19). This was attributed to strain hardening induced by LSPwC (Zhang *et al*., 2010; Salimianrizi *et al*., 2016; Mostafa *et al*., 2019). The observed decrease in hardness with increasing depth into the material was attributed to diminishing shock wave intensity away from the surface. This led to a reduced level of dislocation density and strain hardening at increased depth (Zhang *et al*., 2010; Salimianrizi *et al*., 2016; Mostafa *et al*., 2019). Consequently, beyond 1.5 mm from the peened surface, microhardness values were similar to those before LSPwC. These results agree with Sathyajith and Kalainathan, 2012; Salimianrizi *et al.*, 2016; Abeens *et al.*, 2019; Liu *et al*., 2019 and Mostafa *et al.*, 2019 where LSP increased hardness, with the greatest values near the surface, gradually decreasing with depth to a value similar to the unchanged matrix.

Figure 5.13 shows how peak hardness varied with the different LSPwC parameters investigated. In Figure 5.13a), hardness showed a positive correlation with increasing N_p for both spot sizes of 0.8 mm and 1.5 mm. With a spot size of 0.8 mm (blue), there was a more gradual increase in hardness, whereas, with a spot size of 1.5 mm (orange), the increase was steeper, particularly noticeable from N_p5 to N_p10, showing a greater effect for the larger spot size. There was no discernible correlation between PI and hardness (Figure 5.13b). The highest hardness was noted in P3, followed by P5 and finally, P1, although some standard deviations overlapped. However, there were only three data points; therefore, it can be suggested that with more data points, a relationship might have been better identified. Mostafa et al. (2019) discovered that laser peening with concurrent increases in the number of laser shots per unit area (N_p) and laser intensity (PI) increased metal hardness.

Unlike Ding and Ye (2006), who thought that precipitation hardening might mask the strain hardening, this was not seen in the current work as positive relationships were seen (Figure 5.13a)). Conversely, Ding and Ye (2006) thought that the beneficial surface compression could be offset by the surface damage, which would give more scatter in the data, and this was observed in Figure 5.13 b).

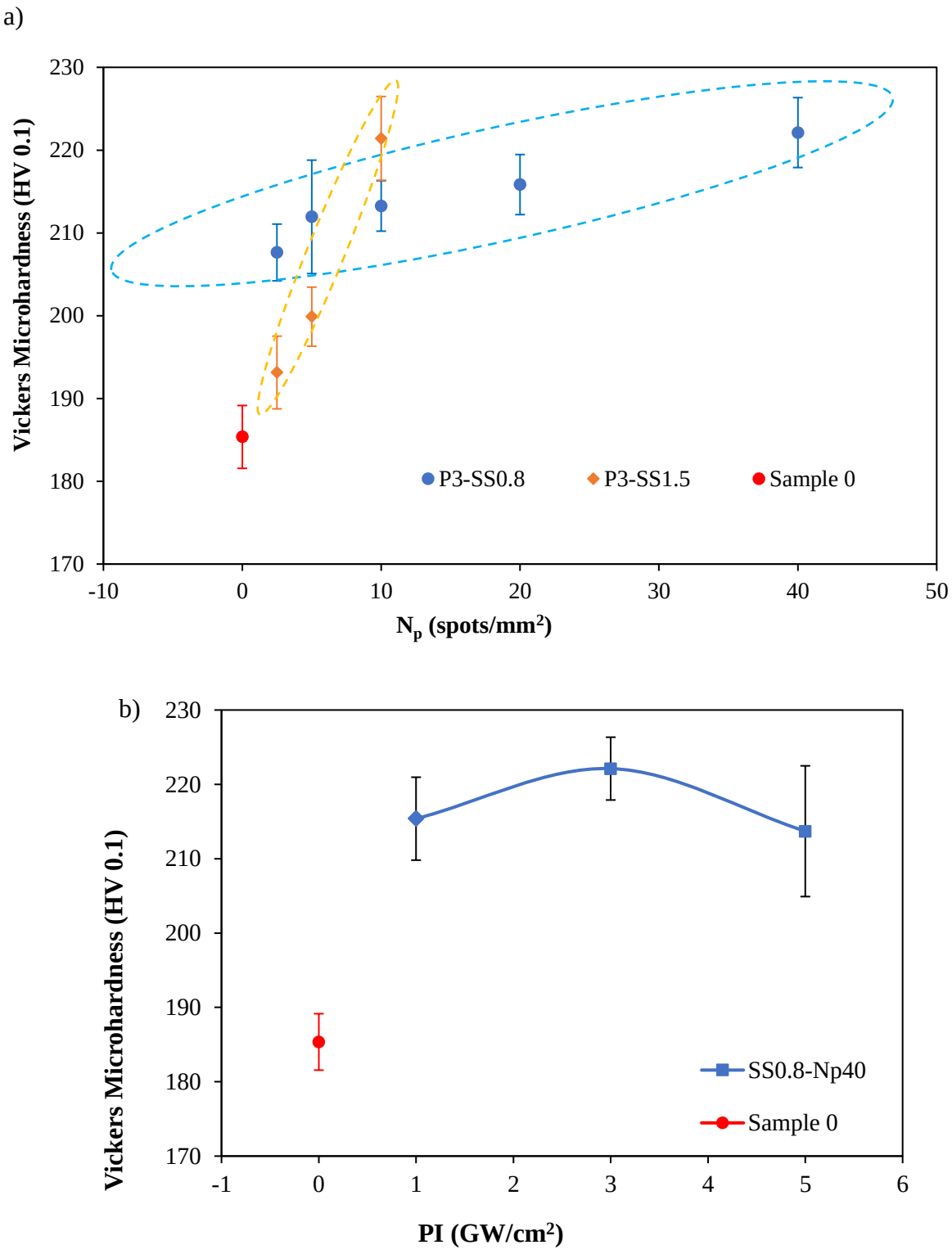


Figure 5.13. Relationship of the peak hardness for: a) N_p at constant P3-SS0.8 (blue), P3-SS1.5 (orange) and b) PI at constant SS0.8-N_p40 with Sample 0 in red.

5.4 Potentiodynamic polarisation behaviour after LSPwC

5.4.1 Open circuit potential (OCP)

The application of LSPwC led to a shift toward less negative OCP values compared to the unpeened sample. These changes were minimal, measuring below 80 mV, in agreement with Trdan and Grum (2012, 2015) on LSPwC of AA6082 and Sanchez (2021) on LSP and LSPwC of AA7075-T651. Lourenco *et al.* (2019) and Yang *et al.* (2019) identified that a shift to higher potential values indicated passive behaviour and oxide layer growth. This does not mean OCP can solely represent corrosion resistance but rather reflects the corrosion tendency of material in an electrolyte (Yang *et al*., 2019). A more negative OCP implies easier electron loss and promoted oxidation reactions (Lameche-Djeghaba *et al*., 2014; Arunachalam *et al*., 2018; Lourenço *et al*., 2019; Yang *et al*., 2019).

5.4.2 Potentiodynamic polarisation curves

Examining the corrosion parameters obtained from polarisation curves (Table 4.4), the E_{corr} values were similar within a narrow range of -0.682 V to -0.760 V. Most laser-peened samples displayed higher i_{corr} and corrosion rates compared to the unpeened sample. This confirms the disadvantage of LSP which induces compressive residual stresses, but inadvertently increases surface roughness, thus deteriorating corrosion resistance (Sanchez *et al*., 2021; Hu *et al*., 2022). The unevenness of rough surfaces undermined the uniformity of the passivation film making it easy to break. Microcracks caused by LSPwC may have also contributed to this worsened corrosion resistance (Hu *et al*., 2022) where the observed "hollows" caused by surface ablation from LSPwC provide sites for the accumulation of corrosive substances, heightening the potential for corrosion.

However, improved corrosion resistance after LSPwC was seen in four samples (P1-SS0.8-N_p40, P3-SS0.8-N_p10, P3-SS1.5-N_p2.5 and P3-SS1.5-N_p5) which showed lower corrosion rates than the unpeened Sample 0. Notably, P3-SS1.5-N_p2.5 had a corrosion rate four times lower than Sample 0. The combination of these LSP parameters yielded the lowest surface roughness values (Figure 4.17) and enhanced hardness (Figure 4.19), despite it being among the samples with the lowest hardness values post-peening. This outcome was attributed to the synergistic effects of introduced compressive stresses, microstructure modification, work hardening and the formation of a

protective oxide layer after LSPwC. Other studies also found improved corrosion after laser shock peening on different alloys and at different LSP conditions (Krawiec *et al.*, 2011; Lu *et al.*, 2012; Trdan and Grum, 2012, 2015; Wang *et al.*, 2017; Yang *et al.*, 2019; Luo *et al.*, 2022).

5.4.3 Effect of LSP parameters on corrosion parameters

5.4.3.1 Varying power intensity (PI)

As power intensity increased from 1 to 3 GW/cm^2, E_{corr} increased as shown in Figure 5.14a), although there were overlapping error bars indicating similar values at PI = 3 and 5 GW/cm^2. In contrast, the OCP values decreased as PI increased. Theoretically, higher E_{corr} values correspond to lower i_{corr} and corrosion rates (ASM International, 1990a). However, this trend was not observed on E_{corr} obtained from the polarisation curves but rather on the one-hour OCP values. There was a strong linear correlation of power intensity with i_{corr} (Figure 5.15a) and corrosion rate (Figure 5.15b) without overlapping error bars. As power intensity increased, i_{corr} increased and corrosion rate also increased. This implies that the higher extent of surface ablation negatively impacted corrosion resistance.

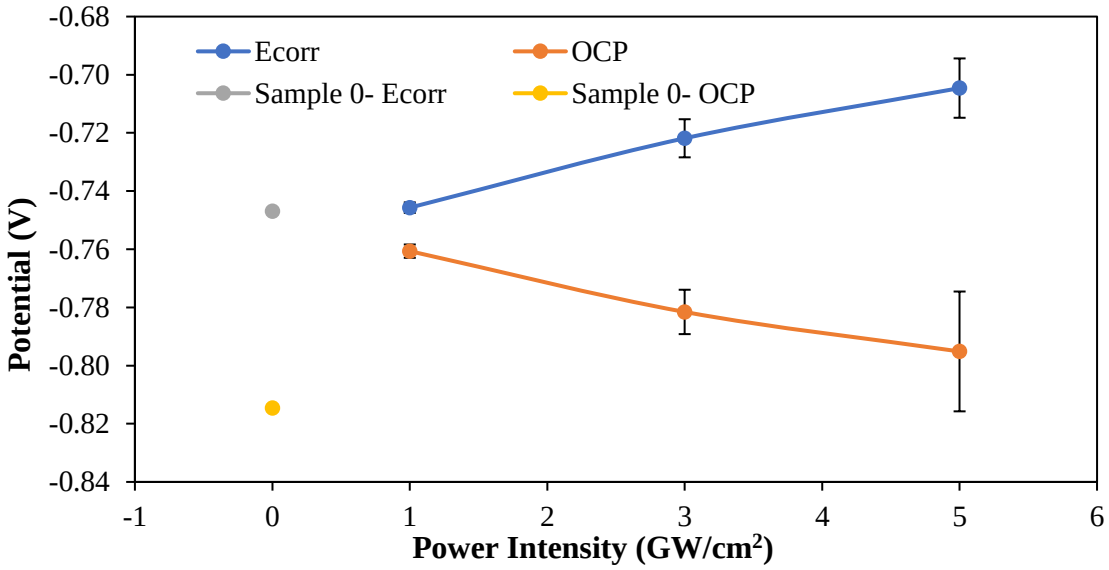


Figure 5.14. Relationships between laser power intensity for: OCP and E_{corr}.

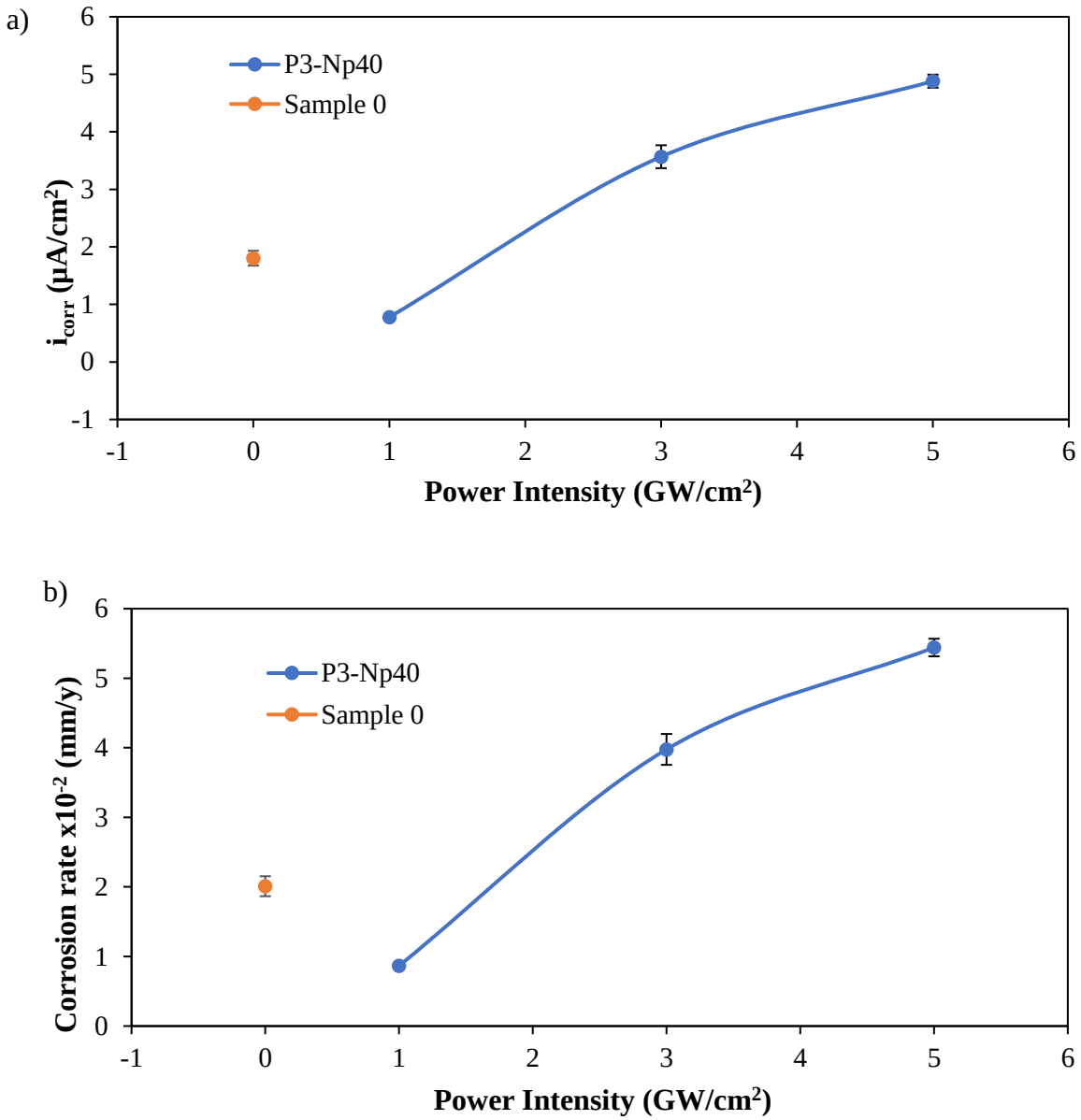


Figure 5.15. Relationships between laser power intensity for: a) i_{corr} and b) corrosion rate.

5.4.3.2 Varying coverage (N_p)

For samples peened at PI = 3 GW/cm^2 and SS = 0.8 mm, E_{corr} and OCP had an unclear relationship with N_p as the error bars mostly overlapped (Figure 5.16a). The i_{corr} and corrosion rate started high at N_p2.5 and N_p5, dropped at N_p10 and then started increasing again as shown in Figure 5.16b) and Figure 5.17. However, there was a more linear relationship at N_p = 10, 20 and 40 for i_{corr} and corrosion rate.

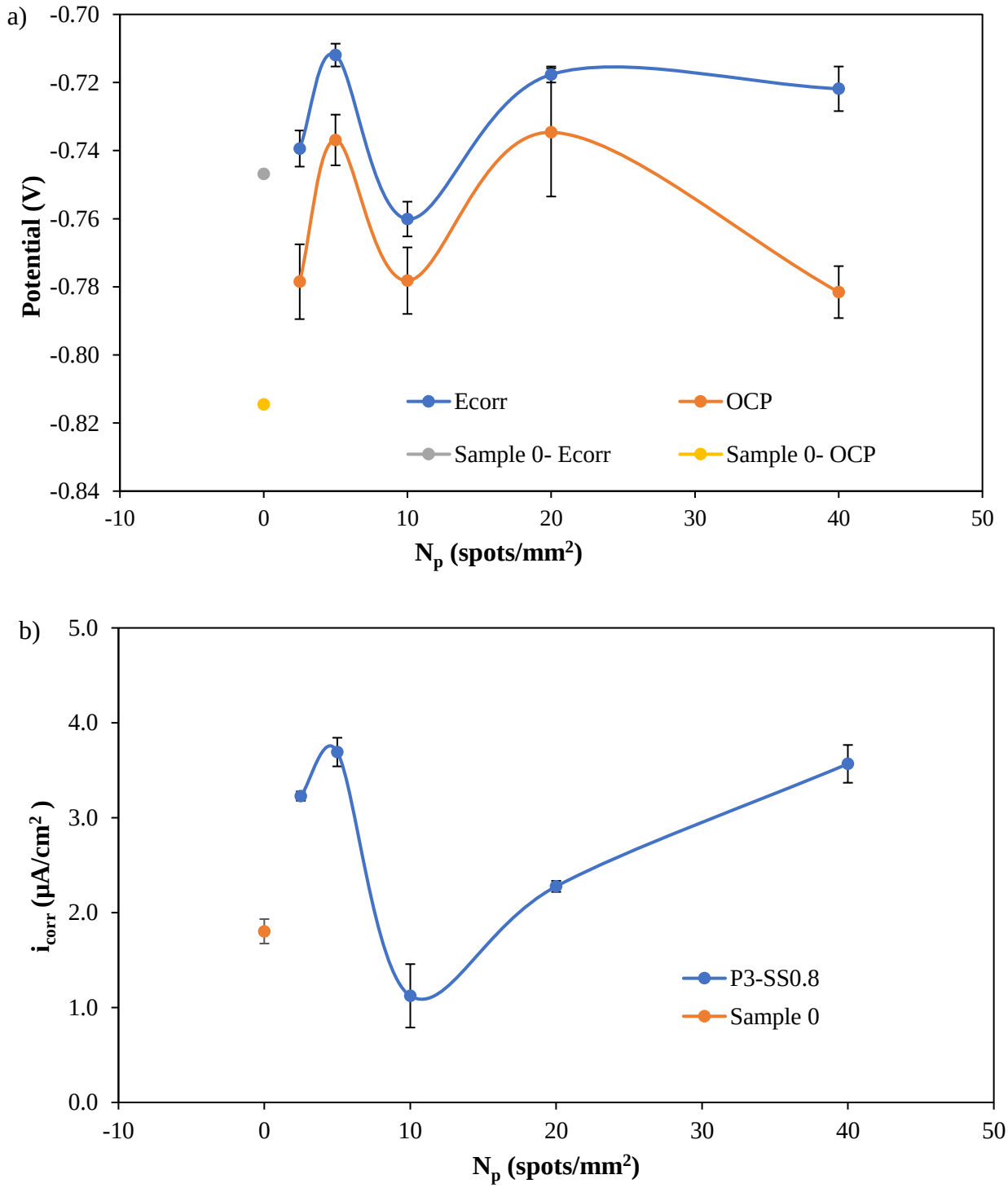


Figure 5.16. Relationship of spot coverage with: a) E_{corr}, OCP and b) i_{corr} at PI = 3 GW/cm^2, SS = 0.8 mm.

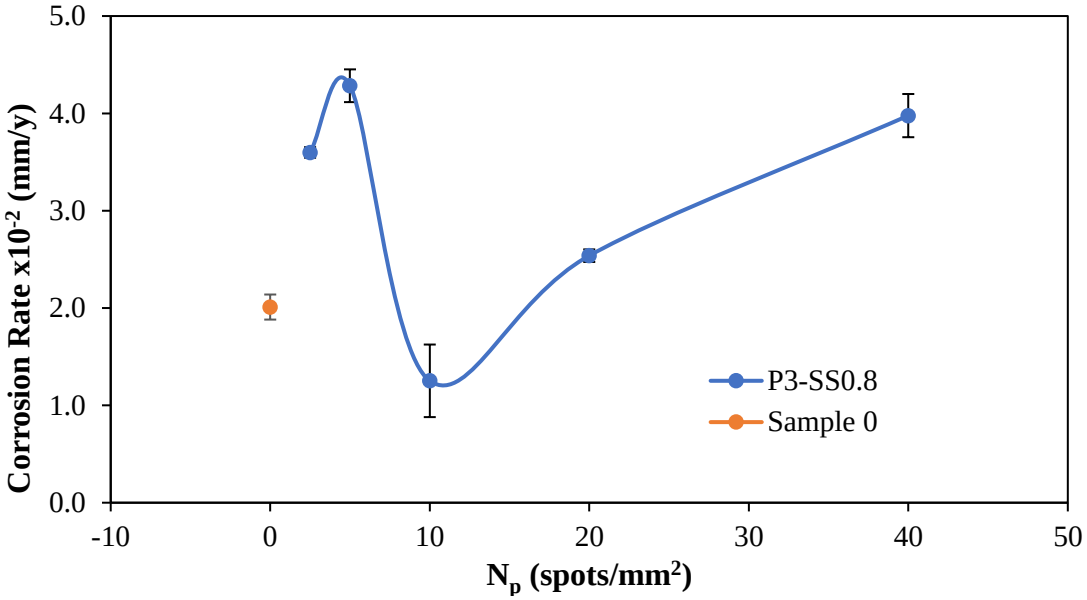


Figure 5.17. Relationship of spot coverage with corrosion rate at PI = 3 GW/cm^2, SS = 0.8 mm.

At PI = 3 GW/cm^2 and SS = 1.5 mm, no correlation could be deduced for OCP and E_{corr} with spot coverage (Figure 5.18). The E_{corr} was initially low at N_p2.5 then increased at N_p5 and decreased at N_p10. The OCP remained constant as N_p increased. There was a strong linear relationship between coverage and i_{corr} and corrosion rate (Figure 5.19). As coverage increased, i_{corr} increased and the corrosion rate increased.

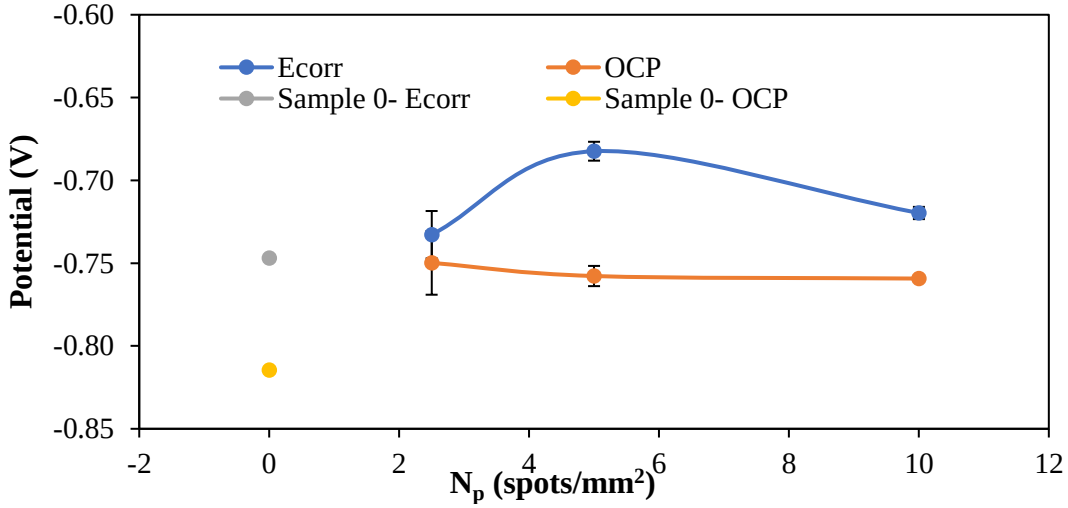


Figure 5.18. Relationship of spot coverage with E_{corr} and OCP at PI = 3 GW/cm^2, SS = 0.8 mm.

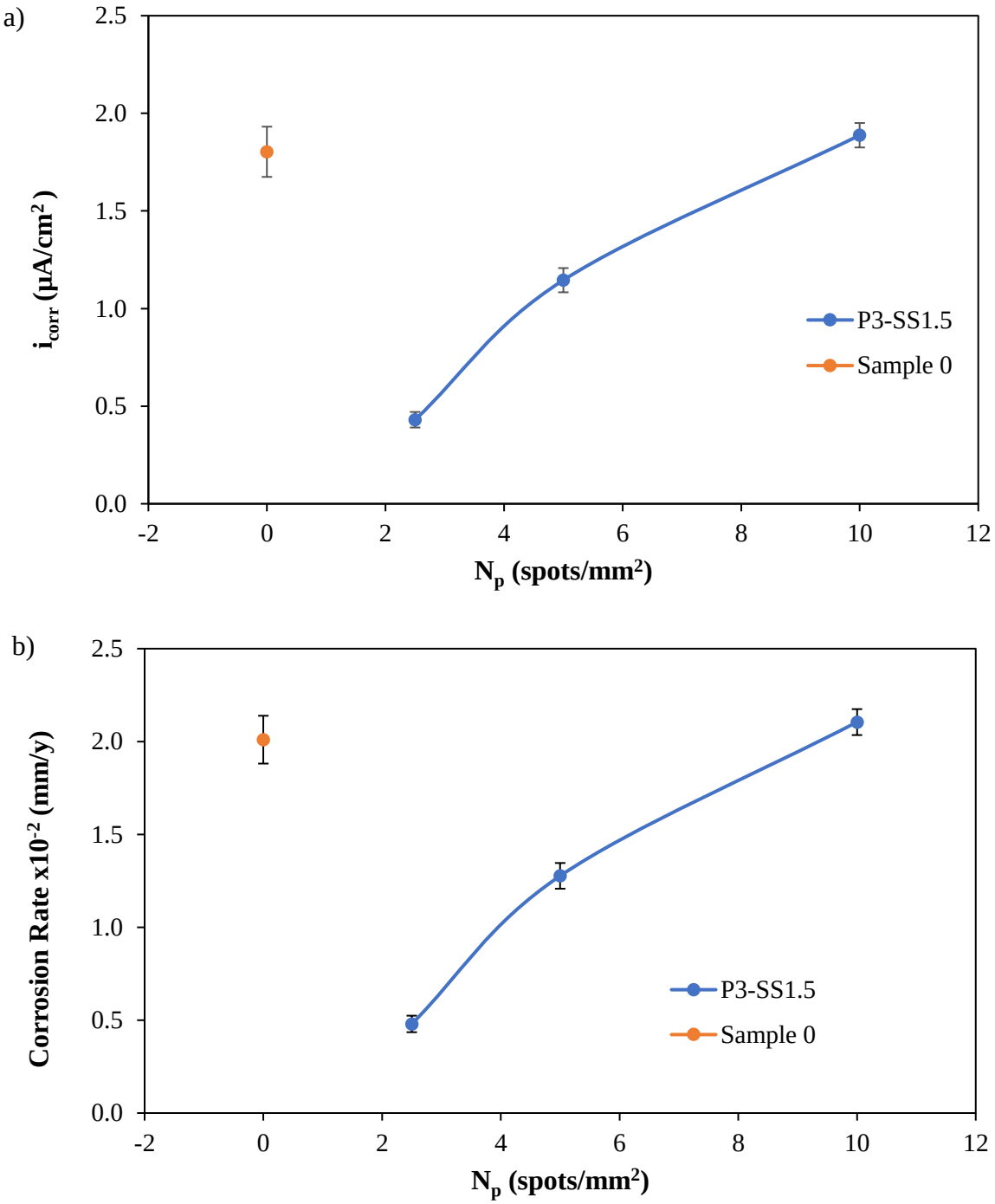


Figure 5.19. Relationship of spot coverage with: a) i_{corr} and b) corrosion rate at PI = 3 GW/cm^2, SS = 0.8 mm.

5.4.3.3 Varying spot size

A comparison was made between two spot sizes, 0.8 mm and 1.5 mm, at a constant power intensity of 3 GW/cm^2. Figure 5.20 shows how E_{corr} and OCP varied with spot size at three different coverages. At N_p = 2.5 spots/mm^2, E_{corr} for both spot sizes were similar, with overlapping error bars. At N_p = 5 and 10 spots/mm^2, the E_{corr} for 0.8 mm was more negative than for 1.5 mm. Figure 5.21a) and Figure 5.21b) show how i_{corr} and corrosion rate varied with spot size. At N_p = 2.5 and 5 spots/mm^2, the i_{corr} and corrosion rate was higher for 0.8 mm than for 1.5 mm spot size. At N_p = 10 spots/mm^2, i_{corr} and corrosion rate were lower for 0.8 mm than for 1.5 mm spot size.

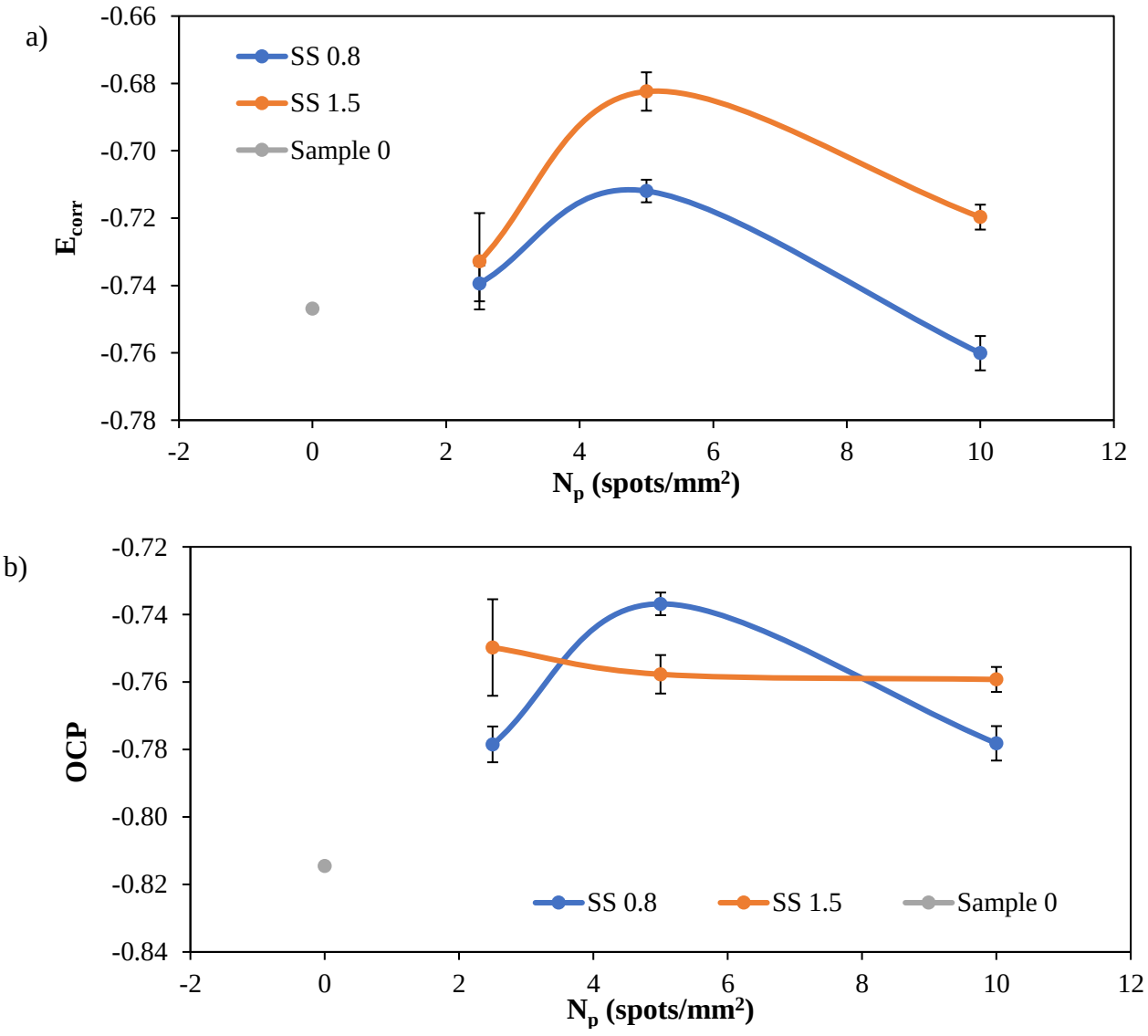


Figure 5.20. Effect of varying spot size on: a) E_{corr}, b) OCP.

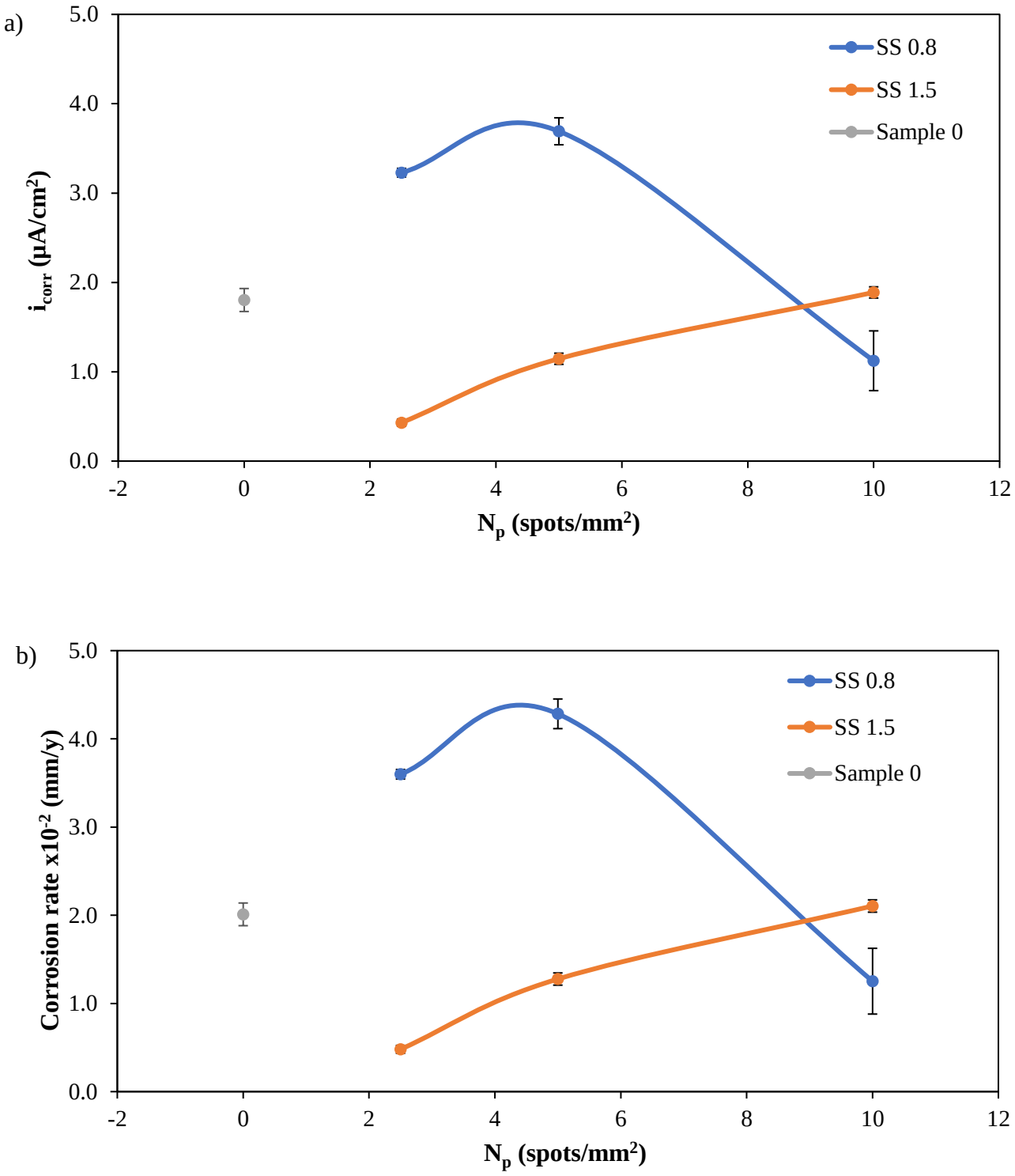


Figure 5.21. Effect of varying spot size on: a) i_{corr}, b) corrosion rate.

5.4.4 Surface analysis after potentiodynamic polarisation

The EDX analysis revealed that the predominant corrosion products were aluminium and oxygen. This agrees with work by other scholars in which the corrosion products were found to be aluminium oxides, mainly Al_2O_3 and $Al(OH)_3$ (Ghali, 2010; Vargel, 2004), despite the absence of hydrogen (H) detection (which being light, would not be identified) in the EDX results. This reaction likely occurred according to Equation 2.4. Little to no Cl and Na were detected, probably because these soluble ions were washed away during cleaning. Following potentiodynamic polarisation, some square-shaped pits were observed on the surfaces indicative of localised corrosion caused by the salt solution (Figure 4.43-Figure 4.51). Specimens with higher i_{corr} and corrosion rates showed more pitting. Corrosion pits develop when chloride ions replace oxygen on the aluminium alloy surface, breaking down the protective film (Vargel, 2004). As corrosion advances, the chlorine complex around the pits increases, causing the pits to grow in both size and depth (Luo *et al*., 2022).

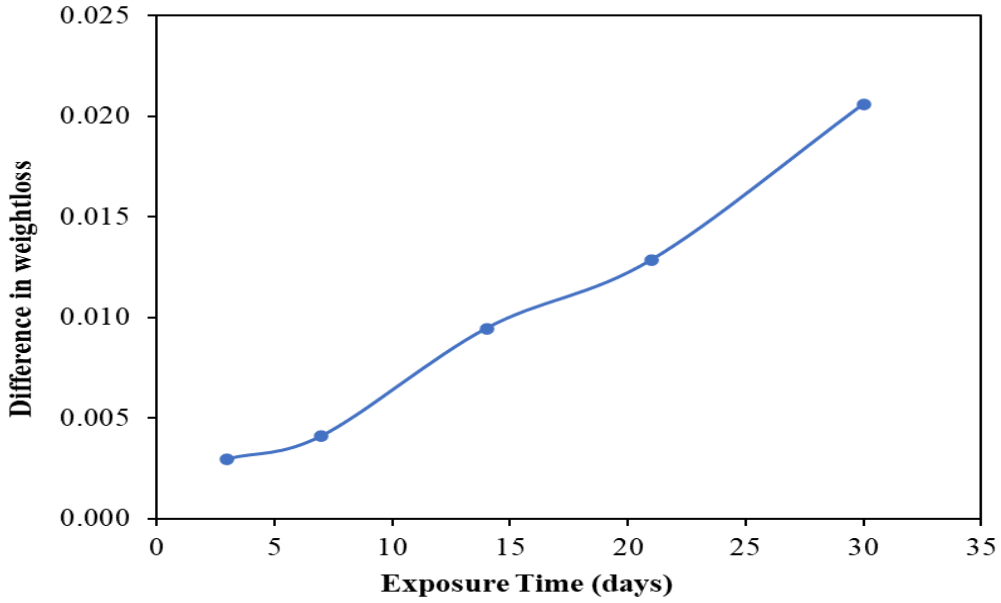
5.5 Immersion weight loss tests

A layer of aluminium oxide was formed on the surfaces with cracks (Figure 4.52) caused by the propagation of Cl^- ions through the passive layer (ASM International, 1990b). The susceptibility of the samples to corrosion was shown by weight loss over time in the NaCl solution. The weight loss (ΔW) (Figure 4.54) for Sample 0 and P3-SS1.5-N_p5 specimens increased with increasing immersion time. This was due to the continuous dissolution under the aggressive action of the chloride ions (ASM International, 1990b). The unpeened Sample 0 had higher weight loss than the P3-SS1.5-N_p5 peened sample throughout the exposure period (30 days). The difference between ΔW of Sample 0 and P3-SS1.5-N_p5 widened as exposure time increased as shown in Figure 5.22a).

The peened sample demonstrated superior corrosion resistance compared to Sample 0, affirming the positive impact of LSPwC over an extended period. Improved corrosion resistance had been observed on P3-SS1.5-N_p5 using potentiodynamic polarisation tests which were more accelerated than immersion tests. After immersion of both Sample 0 and P3-SS1.5-N_p5 specimens, the corrosion rate was highest after three days (Figure 4.55) and gradually decreased as immersion time increased. The difference in corrosion rate was highest (0.16 mm/y) after three days in NaCl

then decreased and remained fairly constant (between 0.11 mm/y and 0.10 mm/y) up to 30 days (Figure 5.22b). Figures 4.56-4.64 show the surface morphologies of Sample 0 and P3-SS1.5-N_p5 after removing the corrosion products. Hemispherical pits were observed in both samples and they became apparently deeper and wider as time progressed. LSPwC samples had smaller pits than the unpeened sample.

a)



b)

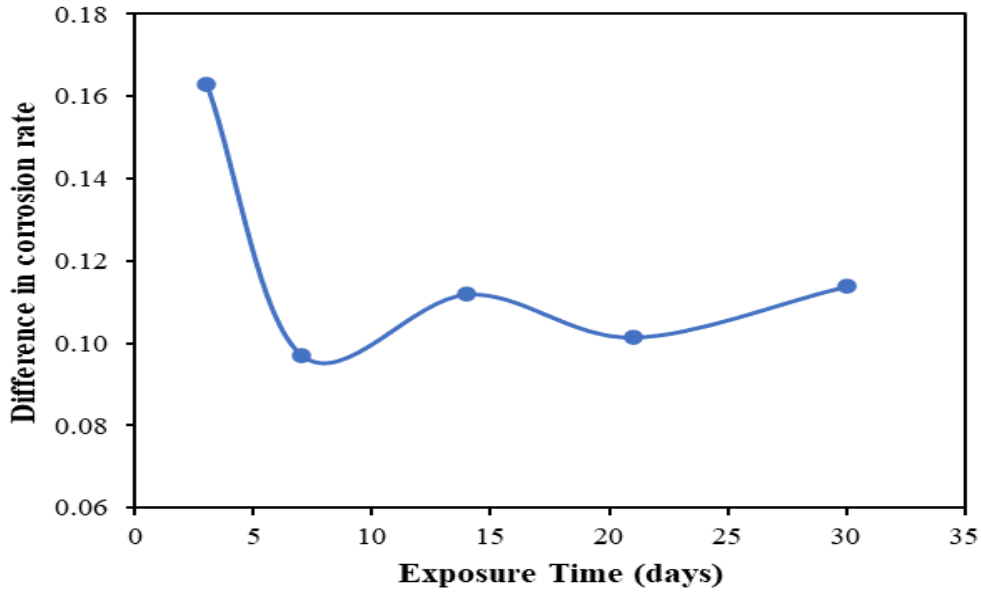


Figure 5.22. Difference of: a) weight loss and b) corrosion rate between Sample 0 and P3-SS1.5-N_p5 over time immersed in NaCl.

5.6 Stress corrosion cracking (SCC)

Multiple cracks were observed in the top surface with some branching out from other cracks. In three-point bending tests, the specimen experiences a combination of tensile and bending stresses (Raja and Shoji, 2011; Al-Haidary *et al.*, 2020), which leads to deviations in a crack's central line which forms multiple tangled cracks (Raja and Shoji, 2011). The SEM images of the top surface also showed cracks that originated from pits (Figure 4.65, Figure 4.67, Figure 4.69, Figure 4.71 and Figure 4.73). Cartner *et al*. (2008) observed a similar phenomenon where salt crystals accumulated on the stressed specimen and probably disrupted the protective anodised surface layer and then formed pits. Corrosion products were observed inside some cracks (Figure 4.65c) and Figure 4.69b)). Hu *et al*. (2022) found that deep pits can accumulate corrosive substances, which exacerbate corrosion.

The extent of susceptibility to SCC was easier to compare on the specimens' cross-sections. Where cracks were visible in the cross-section, the deepest crack was observed at the centre where the highest stress was applied. The sample P3-SS0.5-N_p45 exhibited the highest susceptibility to SCC, having the largest observed crack in the cross-section (Figure 5.23). In contrast, the other three peened samples, P3-SS1.5-N_p21.88, P3-SS0.5-N_p67.1 and P3-SS1-N_p50.38, demonstrated improved performance compared to Sample 0. Sample P3-SS1-N_p50.38 did not have any visible cracks in the cross-section (only pits and horizontal cracks caused by LSPwC were found (Figure 4.70)). This improvement in SCC resistance was attributed to the compressive residual stresses which counteracted the tensile stress. LSP improved grain structure which plays a beneficial role in impeding crack propagation and deterring the occurrence of stress corrosion cracking (Zhang *et al.*, 2010). The work hardening effect of LSPwC also helped to strengthen the specimens.

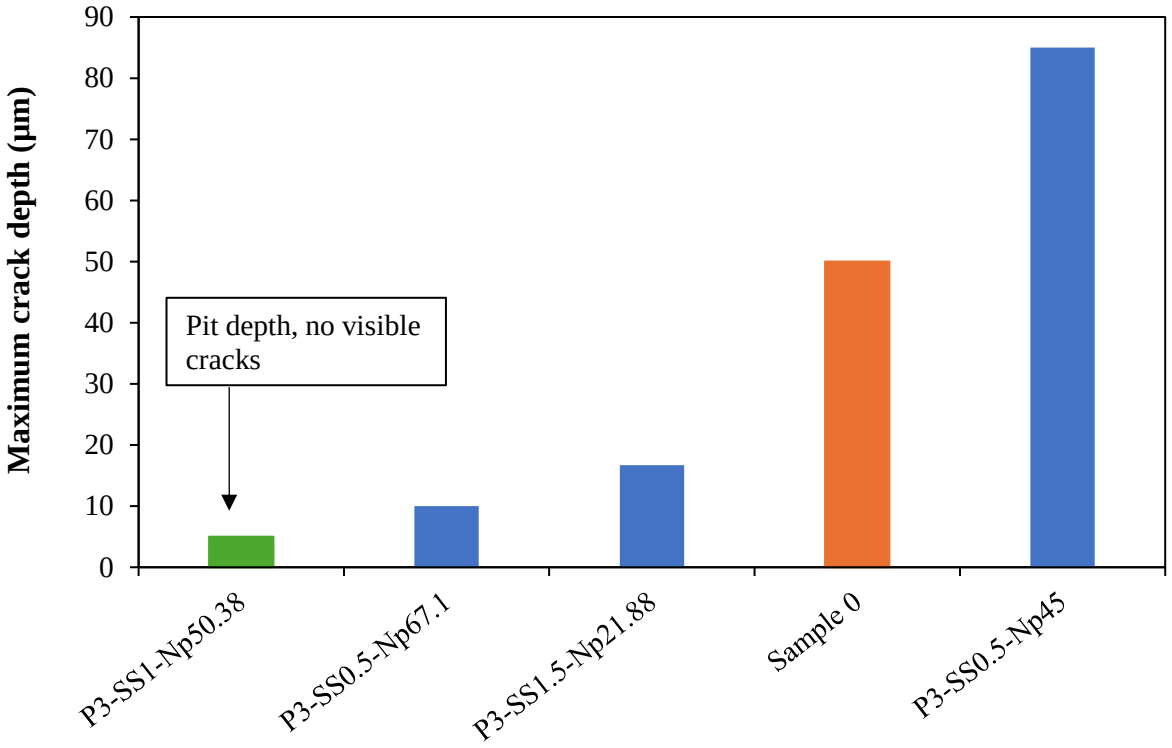


Figure 5.23. Maximum crack depth of specimens after SCC tests.

5.7 Summary

The LSPwC caused an increase in surface roughness and microhardness. Most peened samples had higher corrosion rates than the unpeened sample. This was likely due to the increased surface roughness which decreased corrosion resistance. Improved corrosion resistance after LSPwC was seen in P1-SS0.8-N_p40, P3-SS0.8-N_p10, P3-SS1.5-N_p2.5 and P3-SS1.5-N_p5 which had lower corrosion rates than the unpeened Sample 0. The best corrosion resistance was found in P3-SS1.5-N_p2.5 which had a corrosion rate four times lower than Sample 0. The LSPwC samples were less susceptible to SCC due to the work hardening effect of the peening process with the best sample being Sample P3-SS1-N_p50.38 which had no visible cracks in the sample cross-section. Further research should be conducted with a wider range of spot sizes to better understand the impact on surface roughness, microhardness and corrosion. Moreover, optimisation of LSPwC parameters is needed to enhance compressive residual stresses and work hardening at lower power intensity

while minimising negative effects on surface roughness. Electrochemical Impedance Spectroscopy could be done to provide a more comprehensive understanding of electrochemical characterisation. Lastly, exploring the effects of LSPwC on different materials can determine if the benefits observed in this study can be extended to other metals and alloys.

CHAPTER 6: CONCLUSIONS AND RECOMMENDATIONS

6.1 Conclusions

Aluminium alloy 7075-T651 underwent surface treatment by Laser Shock Peening without Coating (LSPwC). The LSPwC parameters varied power intensity (1-5 GW/cm^2), coverage (2.5-67 spots/mm^2) and spot size (0.5-1.5 mm). Surface modifications were evaluated by stereo microscopy, scanning electron microscopy (SEM) and contact profilometry. Surface roughness was quantified using four metrics: R_a, R_q, R_z and R_t. Vickers microhardness tests were conducted at different depths to determine the hardness variation with depth. Potentiodynamic polarisation analysis provided insights into the metal's corrosion behaviour, yielding E_{corr}, i_{corr} and corrosion rate. Longer-term corrosion performance was evaluated by tests monitoring surface alterations, weight loss and corrosion rate over 30 days immersed in NaCl solution. Stress corrosion tests were performed by three-point bending in 3.5 wt% NaCl solution for 40 days to assess the metal's resistance to environmentally assisted cracking. Corrosion products were analysed by SEM-EDX.

6.1.1 Effect of LSPwC on surface roughness

All tested samples had increased roughness after Laser Shock Peening without Coating (LSPwC), due to the induced plastic deformation and surface ablation. The roughness was higher in the stepping direction where the stylus would pass through the ridges which gave higher peaks.

It was concluded that:

a) Increasing laser power intensity (PI) increased surface roughness (R_a, R_z, R_t, R_q), at constant coverage (N_p = 40 spots/mm^2) and spot size (SS = 0.8 mm). This was because higher PI increased ablative interaction and thermal impact which caused the “hollows”/pits to become wider and deeper.
b) As coverage (N_p) increased, the surface roughness increased. A stronger linear relationship between surface roughness and N_p was observed at a constant power intensity of 3 GW/cm^2 and spot size of 1.5 mm.
c) No clear relationship between surface roughness and laser spot size was found in this study.

6.1.2 Effect of LSPwC on hardness

All peened samples showed increased hardness due to strain hardening induced by LSPwC.

The following conclusions were made:

a) There was a positive correlation between hardness and coverage (N_p) for both spot sizes of 0.8 mm and 1.5 mm. With a spot size of 0.8 mm, there was a more gradual increase in hardness, whereas with a spot size of 1.5 mm, the increase was higher.
b) There was no correlation between laser power intensity (PI) and hardness. The highest hardness was for P3, followed by P5 and finally, P1 at constant coverage (N_p = 40 spots/mm^2) and spot size (SS 0.8 mm).

The LSPwC increased metal hardness until 1.5 mm. Beyond that, microhardness values were similar to pre-LSPwC due to diminished shockwave intensity away from the surface.

6.1.3 Effect of LSPwC on corrosion

6.1.3.1 Potentiodynamic polarisation

The LSPwC both improved and worsened AA7075-T651's corrosion resistance depending on the peening parameters. Most laser-peened parameters used in this study had higher i_{corr} and corrosion rates than the unpeened sample. This was likely due to the increased surface roughness which decreased corrosion resistance. However, improved corrosion resistance after LSPwC was seen in four samples (P1-SS0.8-N_p40, P3-SS0.8-N_p10, P3-SS1.5-N_p2.5 and P3-SS1.5-N_p5 (power intensity-spot size-coverage) which had lower corrosion rates than the unpeened Sample 0. Notably, P3-SS1.5-N_p2.5 had a corrosion rate four times lower than Sample 0. The combination of these LSP parameters yielded the lowest surface roughness values and enhanced hardness post-peening. This was attributed to the synergistic effects of introduced compressive stresses, microstructure modification, work hardening and the formation of a protective oxide layer after LSPwC. Thus:

a) As power intensity increased, i_{corr} increased and corrosion rate also increased. Thus, a higher extent of surface ablation negatively impacted corrosion resistance.
b) There was a strong, direct linear relationship between coverage and i_{corr} and corrosion rate.

The EDX analysis revealed that the main predominant corrosion products were aluminium oxides. Pitting was the dominant corrosion mechanism. Specimens with higher i_{corr} and corrosion rates showed more pitting.

6.1.3.2 Immersion weight loss tests

The P3-SS1.5-N_p5 peened sample demonstrated superior corrosion resistance than the unpeened Sample 0, demonstrating the positive impact of LSPwC over an extended period. Additionally, the difference in corrosion rates between Sample 0 and P3-SS1.5-N_p5 was highest after three days (0.16) in NaCl and gradually decreased (until 0.10) as immersion time increased.

6.1.3.3 Stress corrosion cracking (SCC)

The three-point bending induced tensile and bending stresses, which led to the formation of multiple tangled cracks on the top surface of all specimens. Salt crystals which accumulated on the stressed specimen disrupted the protective anodised surface layer. LSPwC samples were less susceptible to SCC due to the work hardening effect of the peening process. The best SCC resistance was observed for Sample P3-SS1-N_p50.38 which had no visible cracks in the sample cross-section.

6.1.4 Overall Findings

Laser Shock Peening without Coating increased the surface roughness of AA7075. All peened specimens showed increased hardness due to strain hardening. Most peened samples had higher corrosion rates than the unpeened sample, likely because of the increased surface roughness which decreased corrosion resistance. LSPwC samples were less susceptible to SCC due to the work hardening effect of the peening process. Improved corrosion resistance after LSPwC was observed in specific samples which had lower corrosion rates than the unpeened Sample 0. The best corrosion resistance was found in P3-SS1.5-N_p2.5 which had a corrosion rate four times lower than Sample 0. The LSPwC samples were less susceptible to SCC due to the work hardening effect of the peening process with the best sample being Sample P3-SS1-N_p50.38 which had no visible cracks in the sample cross-section.

6.2 Recommendations For Future Work

Suggestions for future work based on the conclusions of this study are:

1. Conduct further research with a wider range of spot sizes to understand the effect of spot size on surface roughness, microhardness and corrosion.
2. Optimise LSPwC parameters to enhance compressive residual stresses and work hardening at lower power intensity (<3 GW/cm^2) and minimise the negative effects of surface roughness.
3. Electrochemical Impedance Spectroscopy (EIS) is recommended after potentiodynamic polarisation for more comprehensive electrochemical characterisation, to give information on impedance changes, surface film integrity post-peening, real-time monitoring of LSP-induced modifications and verification of corrosion mechanisms affected by the peening process.
4. Explore the effects of LSPwC on different types of materials to determine if the observed benefits can be extended to other metals and alloys.

REFERENCES

Abdulstaar, M., Mhaede, M., Wollmann, M., Wagner, L., 2014. Investigating the effects of bulk and surface severe plastic deformation on the fatigue, corrosion behaviour and corrosion fatigue of AA5083. Surf. Coat. Technol. 254, 244–251. https://doi.org/10.1016/j.surfcoat.2014.06.026

Abeens, M., Muruganandhan, R., Thirumavalavan, K., Kalainathan, S., 2019. Surface modification of AA7075-T651 by laser shock peening to improve the wear characteristics. Mater. Res. Express 6, 066519. https://doi.org/10.1088/2053-1591/ab0b0e

Adachi, T., Takehisa, H., Nakajima, M., Sano, Y., 2008. Effect of laser peening on fatigue properties for aircraft structure parts. Presented at the International Conference on Shot Peening.

Al-Haidary, J.T., Haddad, J.S., Alfaqs, F.A., Zayadin, F.F., 2020. Susceptibility of Aluminum Alloy 7075 T6 to stress corrosion cracking. SAE Int. J. Mater. Manuf. 14, 05-14-02–0013. https://doi.org/10.4271/05-14-02-0013

AlHazaa, A.N., Sherif, E.-S.M., 2015. Corrosion behavior of Al7075, Ti-6Al-4Vand Sn-3.6Ag-1Cu alloys in 3.0 wt.% sodium chloride solutions using potentiodynamic polarization measurements. Int. J. Electrochem. Sci. 10, 4193–4207. https://doi.org/10.1016/S1452-3981(23)06615-4

Aliyah, A.N., Anawati, A., 2019. Effect of heat treatment on microstructure and mechanical hardness of aluminum alloy AA7075. IOP Conf. Ser. Mater. Sci. Eng. 541, 012007. https://doi.org/10.1088/1757-899X/541/1/012007

Amar, H., Vignal, V., Krawiec, H., Josse, C., Peyre, P., Da Silva, S.N., Dick, L.F., 2011. Influence of the microstructure and laser shock processing (LSP) on the corrosion behaviour of the AA2050-T8 aluminium alloy. Corros. Sci. 53, 3215–3221. https://doi.org/10.1016/j.corsci.2011.05.066

Andreatta, F., Terryn, H., De Wit, J.H.W., 2004. Corrosion behaviour of different tempers of AA7075 aluminium alloy. Electrochimica Acta 49, 2851–2862. https://doi.org/10.1016/j.electacta.2004.01.046

Arriscorreta, C.A., Hoeppner, D.W., 2012. Effects of prior corrosion and stress in corrosion fatigue of Aluminum Alloy 7075-T6. Corrosion 68, 950–960. https://doi.org/10.5006/0512

Arunachalam, S.R., Galyon Dorman, S.E., Buckley, R.T., Conrad, N.A., Fawaz, S.A., 2018. Effect of electrical discharge machining on corrosion and corrosion fatigue behavior of aluminum alloys. Int. J. Fatigue 111, 44–53. https://doi.org/10.1016/j.ijfatigue.2018.02.005

ASM Aerospace Specification Metals INC, 2023. Aluminum 7075-T6; 7075-T651. ASM.

ASM International, 1990a. ASM handbook, Volume 13A Corrosion: Fundamentals, Testing and Protection, 10th edition. ed. ASM International, Materials Park, Ohio.

ASM International, 1990b. ASM handbook, Volume 13B Corrosion: Materials, 10th edition. ed. ASM International, Materials Park, Ohio.

ASTM E92, 2017. Test Methods for Vickers Hardness and Knoop Hardness of Metallic Materials. https://doi.org/10.1520/E0092-17

ASTM E384, 2022. Test Method for Microindentation Hardness of Materials. ASTM International. https://doi.org/10.1520/E0384-22

ASTM G39, 2016. Practice for Preparation and Use of Bent-Beam Stress-Corrosion Test Specimens. ASTM International, 100 Barr Harbor Drive, PO Box C700, West Conshohocken, PA 19428-2959. United States. https://doi.org/10.1520/G0039-99R16

ASTM G59, 2014. Standard Test Method for Conducting Potentiodynamic Polarization Resistance Measurements, in: Annual Book of ASTM Standards. ASTM International, West Conshohocken, PA.

ASTM G102, 2015. Standard Practice for Calculation of Corrosion Rates and Related Information from Electrochemical Measurements, in: Annual Book of ASTM Standards. ASTM International, West Conshohocken, PA.

Attolico, M.A., Barile, C., Casavola, C., Moramarco, V., Furfari, D., Busse, D.O., 2022. Effects of Laser Shock Peening on Surface Roughness and Residual Stress of AA 7050-T7451. J. Mater. Eng. Perform. 31, 7973–7988. https://doi.org/10.1007/s11665-022-06857-7

Becker, A., 2017. The effect of laser shock peening and shot peening on the fatigue performance of aluminium alloy 7075, MSc Dissertation, University of Cape Town. http://hdl.handle.net/11427/25161

Bhushan, B. (Ed.), 2001. Surface Roughness Analysis and Measurement Techniques, in: Modern Tribology Handbook, Mechanics and Materials Science Series. CRC Press, Boca Raton, FL.

Birbilis, N., Hinton, B., 2011. Corrosion and corrosion protection of aluminium, in: Fundamentals of Aluminium Metallurgy. Elsevier, pp. 574–604. https://doi.org/10.1533/9780857090256.2.574

Brandenburg, K., Hornbach, D., Mason, P., 2013. Use of Engineered Compressive Residual Stresses to Mitigate Stress Corrosion Cracking and Corrosion Fatigue in Sensitized 5XXX Series Aluminum Alloys. Proceedings of Department of Defense Virtual Corrosion Conference, Cincinnati, Ohio.

Busse, D., 2017. Extending Fatigue Life of Aircraft Fuselage Structures Using Laser Peening, PhD thesis, Cranfield University. http://dspace.lib.cranfield.ac.uk/handle/1826/14651

Callister, W.D., 2007. Materials science and engineering: an introduction, 7th edn. John Wiley & Sons, New York.

Cao, Z., Che, Z., Zou, S., Fei, Q., 2011. Numerical simulation of residual stress field induced by laser shock processing with square spot. J. Shanghai Univ. Engl. Ed. 15, 553–556. https://doi.org/10.1007/s11741-011-0785-1

Cartner, J.L., Haggard, W.O., Ong, J.L., Bumgardner, J.D., 2008. Stress corrosion cracking of an aluminum alloy used in external fixation devices. J. Biomed. Mater. Res. B Appl. Biomater. 86B, 430–437. https://doi.org/10.1002/jbm.b.31038

Chan, C.P., Yue, T.M., Man, H.C., 2003. The effect of excimer laser surface treatment on the pitting corrosion fatigue behaviour of aluminium alloy 7075. J. Mater. Sci. 38, 2689–2702. https://doi.org/10.1023/A:1024498922104

Chundunsing, A.N.N., 2019. Surface Integrity and Corrosion Resistance of Aluminium 7075 Alloy processed by Laser Shock Peening Without Coating, BSc dissertation, University of Mauritius, Mauritius. https://library.uom.ac.mu/libero/WebOpac.cls?VERSION=2&ACTION=DISPLAY&RSN=10215404&DATA=UOM&TOKEN=mb2P6AD2UN9288&Z=1

Correa, C., Peral, D., Porro, J.A., Díaz, M., Ruiz De Lara, L., García-Beltrán, A., Ocaña, J.L., 2015. Random-type scanning patterns in laser shock peening without absorbing coating in 2024-T351 Al alloy: A solution to reduce residual stress anisotropy. Opt. Laser Technol. 73, 179–187. https://doi.org/10.1016/j.optlastec.2015.04.027

Cramer, S.D., Covino Jr, B.S., Moosbrugger, C., Sanders, B.R., Anton, G.J., Hrivnak, N., Kinson, J., Polakowski, C., Muldoon, K., Henry, S.D., 2003. ASM handbook. ASM International Materials Park, Ohio.

Davis, J.R., 2000. Corrosion: Understanding the basics. ASM International, Materials Park, Ohio.

Dietzel, W., Srinivasan, P.B., Atrens, A., 2011. Testing and evaluation methods for stress corrosion cracking (SCC) in metals, in: Stress Corrosion Cracking: Theory and Practice, pp. 133–166, Woodhead Pub, Oxford Philadelphia. DOI:10.1533/9780857093769.2.133

Ding, K., Ye, L., 2006. Laser shock peening: performance and process simulation, Woodhead Publishing in materials. CRC Press; Woodhead Pub, Boca Raton: Cambridge, England.

Dollah, M., Robinson, M.J., 2011. Stress corrosion cracking of aluminium alloy 7075(w) under tensile and compressive loading. Corros. Eng. Sci. Technol. 46, 42–48. https://doi.org/10.1179/147842208X386340

Fontana, M.G., 1986. Corrosion engineering, 3rd edn, McGraw-Hill series in Materials Science and Engineering. McGraw-Hill, New York.

Ganesh, P., Sundar, R., Kumar, H., Kaul, R., Ranganathan, K., Hedaoo, P., Tiwari, P., Kukreja, L.M., Oak, S.M., Dasari, S., Raghavendra, G., 2012. Studies on laser peening of spring steel for automotive applications. Opt. Lasers Eng. 50, 678–686. https://doi.org/10.1016/j.optlaseng.2011.11.013

Gao, M., Feng, C.R., Wei, R.P., 1998. An analytical electron microscopy study of constituent particles in commercial 7075-T6 and 2024-T3 alloys. Metall. Mater. Trans. A 29, 1145–1151. https://doi.org/10.1007/s11661-998-0240-9

Gerland, M., Hallouin, M., Presles, H.N., 1992. Comparison of two new surface treatment processes, laser-induced shock waves and primary explosive: application to fatigue behaviour. Mater. Sci. Eng. A 156, 175–182. https://doi.org/10.1016/0921-5093(92)90149-U

Ghali, E., 2010. Corrosion resistance of aluminum and magnesium alloys: understanding, performance and testing, Wiley series in corrosion. John Wiley, Hoboken, N.J.

Glaser, D., Polese, C., Bedekar, R.D., Plaisier, J., Pityana, S., Masina, B., Mathebula, T., Troiani, E., 2014. Laser Shock Peening on a 6056-T4 aluminium alloy for airframe applications.

Adv. Mater. Res. 891–892, 974–979. https://doi.org/10.4028/www.scientific.net/AMR.891-892.974

Glaser, D., Polese, C., Venter, A.M., Marais, D., Plaisier, J.R., 2022. Evaluation of laser shock peening process parameters incorporating Almen strip deflections. Surf. Coat. Technol. 434, 128158. https://doi.org/10.1016/j.surfcoat.2022.128158

Gujba, A., Medraj, M., 2014. Laser peening process and its impact on materials properties in comparison with shot peening and ultrasonic impact peening. Materials 7, 7925–7974. https://doi.org/10.3390/ma7127925

Gustafsson, S., 2011. Corrosion properties of aluminium alloys and surface treated alloys in tap water, MSc dissertation, UPTEC K 11028, Examensarbete30hp, Uppsala university.

Hoeppner, D.W., Chandrasekaran, V., Taylor, A.M.H., 2000. Review of pitting corrosion fatigue models, in: Structural integrity for the next millennium. Presented at the 20th ICAF Symposium, Electronic Printing Services, Dayton, OH, pp. 253–276.

Hombergsmeier, E., Holzinger, V., Heckenberger, U.C., 2014. Fatigue crack retardation in LSP and SP treated aluminium specimens. Adv. Mater. Res. 891–892, 986–991. https://doi.org/10.4028/www.scientific.net/AMR.891-892.986

Hu, W., Peng, X., Ding, Y., Zhu, Z., Ma, G., Wang, J., Ye, Z., Li, D., 2022. The effect of laser shock processing on the microstructures and properties of 2060 Al Li alloys. Surf. Coat. Technol. 434, 128208. https://doi.org/10.1016/j.surfcoat.2022.128208

Imran, M., Khan, A.R.A., 2019. Characterization of Al-7075 metal matrix composites: a review. J. Mater. Res. Technol. 8, 3347–3356. https://doi.org/10.1016/j.jmrt.2017.10.012

ISO 4287, 1997. Geometrical Product Specifications (GPS)- Surface texture: Profile method- terms, definitions and surface texture parameters.

ISO 4288, 1996. Geometrical Product Specifications (GPS)-Surface texture: Profile method- Rules and procedures for the assessment of surface texture.

Ivetic, G., Meneghin, I., Troiani, E., Molinari, G., Lanciotti, A., Ristori, V., Ocaña, J., Morales, M., Porro, J., Polese, C., 2011. Characterisation of fatigue and crack propagation in laser shock peened open hole 7075-T73 aluminium specimens, in: ICAF 2011 Structural Integrity: Influence of Efficiency and Green Imperatives. Springer, pp. 855–866.

Jin, Y., Cai, P., Wen, W., Nagaumi, H., Xu, B., Zhang, Y., Zhai, T., 2015. The anisotropy of fatigue crack nucleation in an AA7075-T651 Al alloy plate. Mater. Sci. Eng. A 622, 7–15. https://doi.org/10.1016/j.msea.2014.11.007

Jones, R., 2003. Stress-Corrosion Cracking, in: ASM Handbook Corrosion: Fundamentals, Testing and Protection. ASM international Materials Park, Ohio, pp. 346–366.

Kalyon, A., Özyürek, D., 2017. Investigation of the effect of different heat treatments on wear behavior of AA7075 alloy. Acta Phys. Pol. A 131, 150–152. https://doi.org/10.12693/APhysPolA.131.150

Khalid, M.Y., Umer, R., Khan, K.A., 2023. Review of recent trends and developments in aluminium 7075 alloy and its metal matrix composites (MMCs) for aircraft applications. Results Eng. 20, 101372. https://doi.org/10.1016/j.rineng.2023.101372

Kim, J., Kim, Y.-J., Kim, J.-S., 2012. Effects of laser source geometry on laser shock peening residual stress. Trans. Korean Soc. Mech. Eng. A 36, 609–615. https://doi.org/10.3795/KSME-A.2012.36.6.609

Krawiec, H., Vignal, V., Amar, H., Peyre, P., 2011. Local electrochemical impedance spectroscopy study of the influence of ageing in air and laser shock processing on the micro-electrochemical behaviour of AA2050-T8 aluminium alloy. Electrochimica Acta 56, 9581–9587. https://doi.org/10.1016/j.electacta.2011.01.091

Lameche-Djeghaba, S., Benchettara, A., Kellou, F., Ji, V., 2014. Electrochemical behaviour of pure aluminium and Al–5%Zn alloy in 3% NaCl solution. Arab. J. Sci. Eng. 39, 113–122. https://doi.org/10.1007/s13369-013-0876-7

Liu, P., Sun, S., Hu, J., 2019. Effect of laser shock peening on the microstructure and corrosion resistance in the surface of weld nugget zone and heat-affected zone of FSW joints of 7050 Al alloy. Opt. Laser Technol. 112, 1–7. https://doi.org/10.1016/j.optlastec.2018.10.054

Lou, S.M., Chen, C.J., Li, M.C., 1998. Surface roughness prediction technique for CNC end-milling. J. Ind. Technol. 15, 1-6.

Lourenço, J.C., Robin, A.L.M., Faria, M.I.S.T., Prisco, L.P., Puccini, M.C., Oliveira, L.D.D., 2019. Corrosion Behavior of AA7075-T73 Aluminum Alloy During Machining of Aeronautical Components. Mater. Res. 22, e20180218. https://doi.org/10.1590/1980-5373-mr-2018-0218

Lu, J.Z., Luo, K.Y., Yang, D.K., Cheng, X.N., Hu, J.L., Dai, F.Z., Qi, H., Zhang, L., Zhong, J.S., Wang, Q.W., Zhang, Y.K., 2012. Effects of laser peening on stress corrosion cracking (SCC) of ANSI 304 austenitic stainless steel. Corros. Sci. 60, 145–152. https://doi.org/10.1016/j.corsci.2012.03.044

Luo, K.Y., Yin, Y.F., Wang, C.Y., Chai, Q.F., Cai, J., Lu, J.Z., Lu, Y.F., 2019. Effects of laser shock peening with different coverage layers on fatigue behaviour and fractural morphology of Fe-Cr alloy in NaCl solution. J. Alloys Compd. 773, 168–179. https://doi.org/10.1016/j.jallcom.2018.09.147

Luo, D., Li, F., Xing, G., 2022. Corrosion resistance of 6061-T6 aluminium alloy and its feasibility of near-surface reinforcements in concrete structure. Rev. Adv. Mater. Sci. 61, 638–653. https://doi.org/10.1515/rams-2022-0048

Mitutoyo America Corporation, 2016. Quick Guide to surface roughness measurement.

Mostafa, A.M., Hameed, M.F., Obayya, S.S., 2019. Effect of laser shock peening on the hardness of Al7075 alloy. J. King Saud Univ. - Sci. 31, 472–478. https://doi.org/10.1016/j.jksus.2017.07.012

PalmSens, 2023. Polarization curve with Evan's diagram. URL https://www.palmsens.com/knowledgebase-article/tafel-plot-and-evans-diagram/ (accessed 12.4.23).

Pantelakis, S., Tserpes, K. (Eds.), 2020. Revolutionizing aircraft materials and processes. Springer International Publishing, Cham. https://doi.org/10.1007/978-3-030-35346-9

Pedersen, K.O., Børvik, T., Hopperstad, O.S., 2011. Fracture mechanisms of aluminium alloy AA7075-T651 under various loading conditions. Mater. Des. 32, 97–107. https://doi.org/10.1016/j.matdes.2010.06.029

Peyre, P., Berthe, L., Scherpereel, X., Fabbro, R., 1998. Laser-shock processing of aluminium-coated 55C1 steel in water-confinement regime, characterization and application to high-cycle fatigue behaviour. J. Mater. Sci. 33, 1421–1429. https://doi.org/10.1023/A:1004331205389

Peyre, P., Vignal, V., Amar, H., Song, H., Pelletier, H., Ji, V., 2009. Modification of the electrochemical properties of 2050-T8 aluminium alloys by a LSP surface treatment, in: International Congress on Applications of Lasers & Electro-Optics. Presented at the ICALEO® 2009: 28th International Congress on Laser Materials Processing, Laser

Microprocessing and Nanomanufacturing, Laser Institute of America, Orlando, Florida, USA, pp. 116–121. https://doi.org/10.2351/1.5061469

Polmear, I.J., Nie, J.-F., Qian, M., StJohn, D., 2017. Light alloys: metallurgy of the light metals, Fifth edition. ed. Butterworth-Heinemann, an imprint of Elsevier, Oxford.

Popov, B.N., 2015. Stress Corrosion Cracking, in: Corrosion Engineering. Elsevier, pp. 365–450. https://doi.org/10.1016/B978-0-444-62722-3.00009-4

Raja, V.S., Shoji, T. (Eds.), 2011. Stress Corrosion Cracking: Theory and Practice, Woodhead Publishing in materials. Woodhead Pub, Oxford Philadelphia.

Rankin, J.E., Hill, M.R., Hackel, L.A., 2003. The effects of process variations on residual stress in laser peened 7049 T73 aluminum alloy. Mater. Sci. Eng. A 349, 279–291.

Rao, A.C.U., Vasu, V., Govindaraju, M., Srinadh, K.V.S., 2016. Stress corrosion cracking behaviour of 7xxx aluminum alloys: A literature review. Trans. Nonferrous Met. Soc. China 26, 1447–1471. https://doi.org/10.1016/S1003-6326(16)64220-6

Roberge, P.R., 2000. Handbook of Corrosion Engineering, McGraw-Hill handbooks. McGraw-Hill, New York.

Roberge, P.R., 2008. Corrosion Engineering: Principles and Practice. McGraw-Hill, New York.

Rometsch, P.A., Zhang, Y., Knight, S., 2014. Heat treatment of 7xxx series aluminium alloys—Some recent developments. Trans. Nonferrous Met. Soc. China 24, 2003–2017. https://doi.org/10.1016/S1003-6326(14)63306-9

Salimianrizi, A., Foroozmehr, E., Badrossamay, M., Farrokhpour, H., 2016. Effect of Laser Shock Peening on surface properties and residual stress of Al6061-T6. Opt. Lasers Eng. 77, 112–117. https://doi.org/10.1016/j.optlaseng.2015.08.001

Sanchez, A., 2021. Micro-mechanisms of fatigue and corrosion in a laser shock peened aerospace aluminium alloy, PhD Thesis, University of Southampton. https://doi.org/10.5258/SOTON/T0030

Sanchez, A.G., Leering, M., Glaser, D., Furfari, D., Fitzpatrick, M.E., Wharton, J.A., Reed, P.A.S., 2021. Effects of ablative and non-ablative laser shock peening on AA7075-T651 corrosion and fatigue performance. Mater. Sci. Technol. 37, 1015–1034. https://doi.org/10.1080/02670836.2021.1972272

Sano, Y., Akita, K., Masaki, K., Ochi, Y., Altenberger, I., Scholtes, B., 2006. Laser Peening without Coating as a Surface Enhancement Technology. J. Laser Micro Nanoengineering 1, 161–166. https://doi.org/10.2961/jlmn.2006.03.0002

Sano, Y., Obata, M., Kubo, T., Mukai, N., Yoda, M., Masaki, K., Ochi, Y., 2006. Retardation of crack initiation and growth in austenitic stainless steels by laser peening without protective coating. Mater. Sci. Eng. A 417, 334–340. https://doi.org/10.1016/j.msea.2005.11.017

Sano, Y., Masaki, K., Gushi, T., Sano, T., 2012. Improvement in fatigue performance of friction stir welded A6061-T6 aluminum alloy by laser peening without coating. Mater. Des. 1980-2015 36, 809–814. https://doi.org/10.1016/j.matdes.2011.10.053

Sathyajith, S., Kalainathan, S., 2012. Effect of laser shot peening on precipitation hardened aluminum alloy 6061-T6 using low energy laser. Opt. Lasers Eng. 50, 345–348. https://doi.org/10.1016/j.optlaseng.2011.11.002

Singleton, R., 2003. Cabinet Testing. ASM Handbook, 13, 471–477.

Starke, E.A., Staley, J.T., 1996. Application of modern aluminum alloys to aircraft. Prog. Aerosp. Sci. 32, 131–172. https://doi.org/10.1016/0376-0421(95)00004-6

Stiekema, N. J., 2021. Investigation of the cavitation bubble oscillation period during laser shock peening, MSc Dissertation, University of the Witwatersrand, Johannesburg. https://hdl.handle.net/10539/37773

Sundar, R., Ganesh, P., Kumar, B.S., Gupta, R.K., Nagpure, D.C., Kaul, R., Ranganathan, K., Bindra, K.S., Kain, V., Oak, S.M., Singh, B., 2016. Mitigation of stress corrosion cracking susceptibility of machined 304l stainless steel through laser peening. J. Mater. Eng. Perform. 25, 3710–3724. https://doi.org/10.1007/s11665-016-2220-3

Telang, A., Gill, A.S., Teysseyre, S., Mannava, S.R., Qian, D., Vasudevan, V.K., 2015. Effects of laser shock peening on SCC behavior of Alloy 600 in tetrathionate solution. Corros. Sci. 90, 434–444. https://doi.org/10.1016/j.corsci.2014.10.045

The Aluminium Association, 2018. International Alloy Designations and Chemical Composition Limits for Wrought Aluminum and Wrought Aluminum Alloys.

Trdan, U., Ocaña, J.L., Grum, J., 2011. Surface modification of aluminium alloys with laser shock processing. Stroj. Vestn. - J. Mech. Eng. 57, 9-21. https://doi.org/10.5545/sv-jme.2010.119

Trdan, U., Grum, J., 2012. Evaluation of corrosion resistance of AA6082-T651 aluminium alloy after laser shock peening by means of cyclic polarisation and ElS methods. Corros. Sci. 59, 324–333. https://doi.org/10.1016/j.corsci.2012.03.019

Trdan, U., Grum, J., 2015. Investigation of corrosion behaviour of aluminium alloy subjected to laser shock peening without a protective coating. Adv. Mater. Sci. Eng. 2015, 1–9. https://doi.org/10.1155/2015/705306

Tseng, T.-L. (Bill), Konada, U., Kwon, Y. (James), 2016. A novel approach to predict surface roughness in machining operations using fuzzy set theory. J. Comput. Des. Eng. 3, 1–13. https://doi.org/10.1016/j.jcde.2015.04.002

van Staden, S. N., 2018. Residual stress measurement and parametric analysis of laser shock peening of aluminium alloy 7075 with different thicknesses, MSc Dissertation, University of the Witwatersrand, Johannesburg. https://hdl.handle.net/10539/25672

Vargel, C., 2004. Corrosion of Aluminium, 1st edn. Elsevier, Amsterdam; Boston.

Wang, J.T., Zhang, Y.K., Chen, J.F., Zhou, J.Y., Ge, M.Z., Lu, Y.L., Li, X.L., 2015. Effects of laser shock peening on stress corrosion behavior of 7075 aluminum alloy laser welded joints. Mater. Sci. Eng. A 647, 7–14. https://doi.org/10.1016/j.msea.2015.08.084

Wang, H., Ning, C., Huang, Y., Cao, Z., Chen, X., Zhang, W., 2017. Improvement of abrasion resistance in artificial seawater and corrosion resistance in NaCl solution of 7075 aluminum alloy processed by laser shock peening. Opt. Lasers Eng. 90, 179–185. https://doi.org/10.1016/j.optlaseng.2016.10.016

Wu, J., Zhao, J., Qiao, H., Hu, X., Yang, Y., 2020. The new technologies developed from laser shock processing. Materials 13, 6: 1453. https://doi.org/10.3390/ma13061453

Yadav, M.J., Jinoop, A.N., Danduk, C., Subbu, S.K., 2017. Laser Shock Processing: Process Physics, Parameters and Applications. Mater. Today Proc. 4, 7921–7930. https://doi.org/10.1016/j.matpr.2017.07.128

Yang, Y., Zhou, W., Tong, Z., Chen, L., Yang, X., Larson, E.A., Ren, X., 2019. Electrochemical corrosion behavior of 5083 aluminum alloy subjected to laser shock peening. J. Mater. Eng. Perform. 28, 6081–6091. https://doi.org/10.1007/s11665-019-04299-2

Yoo, Y.R., Choi, S.H., Kim, Y.S., 2023. Effect of laser shock peening on the stress corrosion cracking of 304L Stainless Steel. Metals 13, 516. https://doi.org/10.3390/met13030516

Yu, J., Gou, G., Zhang, L., Zhang, W., Chen, H., Yang, Y.P., 2016. Ultrasonic impact treatment to improve stress corrosion cracking resistance of welded joints of aluminum alloy. J. Mater. Eng. Perform. 25, 3046–3056. https://doi.org/10.1007/s11665-016-2087-3

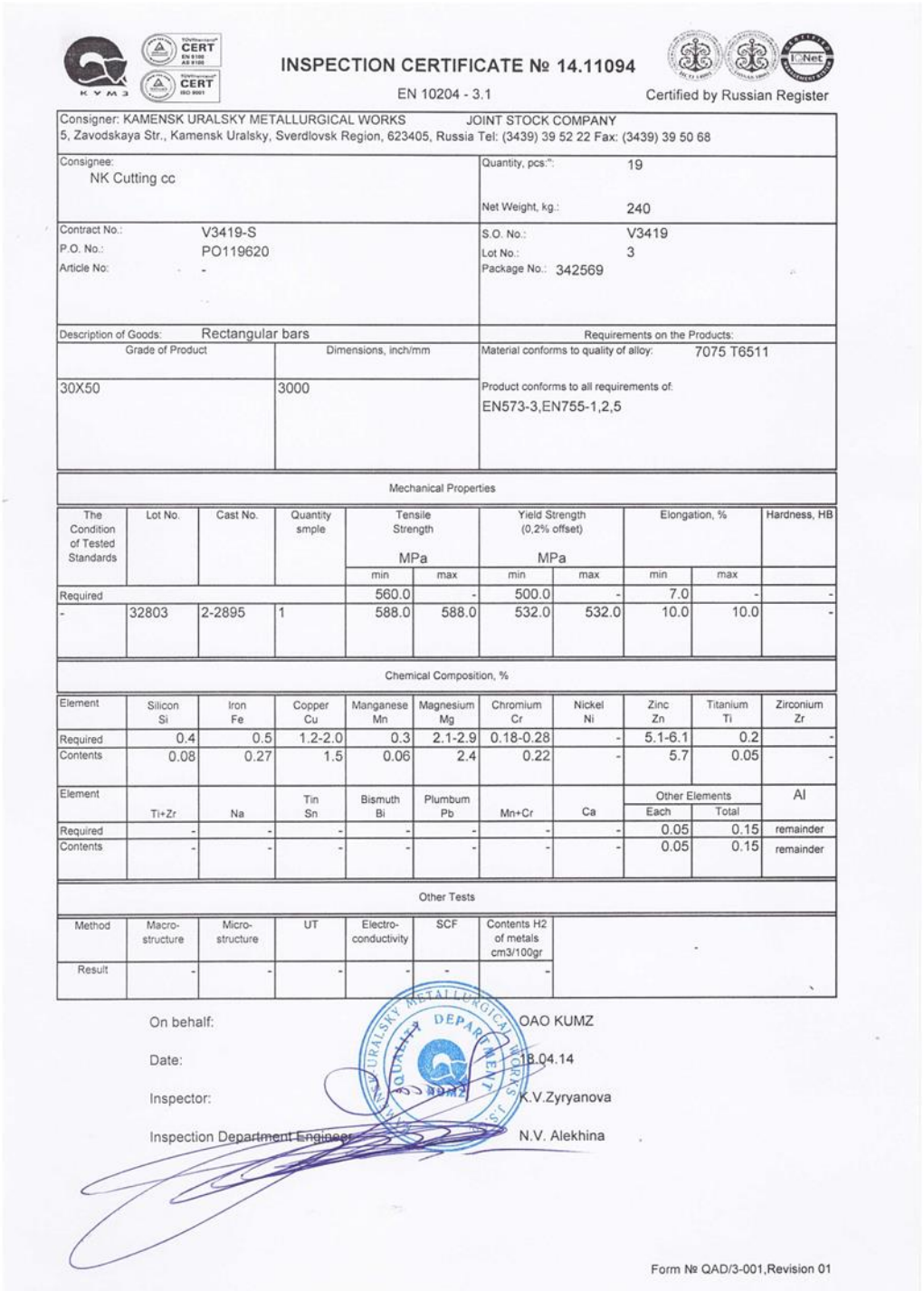
Yue, T.M., Dong, C.F., Yan, L.J., Man, H.C., 2004. The effect of laser surface treatment on stress corrosion cracking behaviour of 7075 aluminium alloy. Mater. Lett. 58, 630–635. https://doi.org/10.1016/S0167-577X(03)00583-4

Zhang, Y., You, J., Lu, J., Cui, C., Jiang, Y., Ren, X., 2010. Effects of laser shock processing on stress corrosion cracking susceptibility of AZ31B magnesium alloy. Surf. Coat. Technol. 204, 3947–3953. https://doi.org/10.1016/j.surfcoat.2010.03.015

Zupanc, U., Grum, J., 2010. Effect of pitting corrosion on fatigue performance of shot-peened aluminium alloy 7075-T651. J. Mater. Process. Technol. 210, 1197–1202. https://doi.org/10.1016/j.jmatprotec.2010.03.004

APPENDICES

Appendix 1: AA7075-T651 Data Sheet



INSPECTION CERTIFICATE № 14.11094

EN 10204 - 3.1

Certified by Russian Register

Consigner: KAMENSK URALSKY METALLURGICAL WORKS JOINT STOCK COMPANY
5, Zavodskaya Str., Kamensk Uralsky, Sverdlovsk Region, 623405, Russia Tel: (3439) 39 52 22 Fax: (3439) 39 50 68

Consignee: NK Cutting cc	Quantity, pcs.": 19
	Net Weight, kg.: 240
Contract No.: V3419-S	S.O. No.: V3419
P.O. No.: PO119620	Lot No.: 3
Article No: -	Package No.: 342569
Description of Goods: Rectangular bars	Requirements on the Products:

Grade of Product	Dimensions, inch/mm	Material conforms to quality of alloy: 7075 T6511
30X50	3000	Product conforms to all requirements of: EN573-3,EN755-1,2,5

Mechanical Properties

The Condition of Tested Standards	Lot No.	Cast No.	Quantity smple	Tensile Strength MPa		Yield Strength (0,2% offset) MPa		Elongation, %		Hardness, HB
				min	max	min	max	min	max	
Required				560.0	-	500.0	-	7.0	-	-
-	32803	2-2895	1	588.0	588.0	532.0	532.0	10.0	10.0	-

Chemical Composition, %

Element	Silicon Si	Iron Fe	Copper Cu	Manganese Mn	Magnesium Mg	Chromium Cr	Nickel Ni	Zinc Zn	Titanium Ti	Zirconium Zr
Required	0.4	0.5	1.2-2.0	0.3	2.1-2.9	0.18-0.28	-	5.1-6.1	0.2	-
Contents	0.08	0.27	1.5	0.06	2.4	0.22	-	5.7	0.05	-

Element	Ti+Zr	Na	Tin Sn	Bismuth Bi	Plumbum Pb	Mn+Cr	Ca	Other Elements Each	Other Elements Total	Al
Required	-	-	-	-	-	-	-	0.05	0.15	remainder
Contents	-	-	-	-	-	-	-	0.05	0.15	remainder

Other Tests

Method	Macro-structure	Micro-structure	UT	Electro-conductivity	SCF	Contents H2 of metals cm3/100gr
Result	-	-	-	-	-	-

On behalf: OAO KUMZ

Date: 18.04.14

Inspector: K.V.Zyryanova

Inspection Department Engineer: N.V. Alekhina

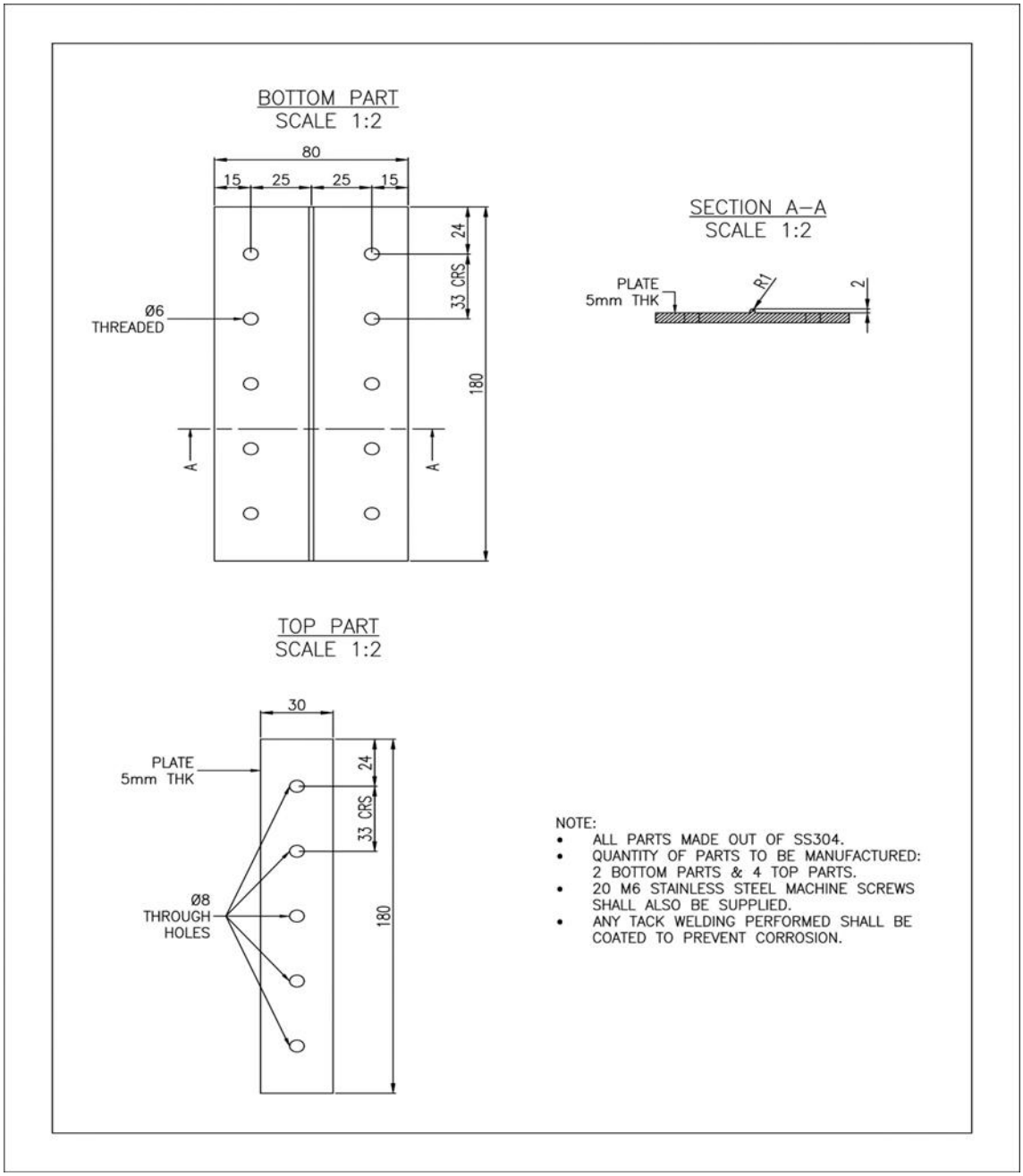
Form № QAD/3-001,Revision 01

Appendix 2: Salt concentrations in selected oceans and seas

Table A2.1. Salt concentrations in selected oceans and seas (Arriscorreta and Hoeppner, 2012).

Ocean	**Salt concentration (%NaCl)**
Atlantic Ocean	3.54
Pacific Ocean	3.49
Mediterranean Sea	3.7 – 3.9
Red Sea	Up to 4.1

Appendix 3: SCC Sample Holder Specifications



Appendix 4: Potentiodynamic Polarisation Curves for the Second Test

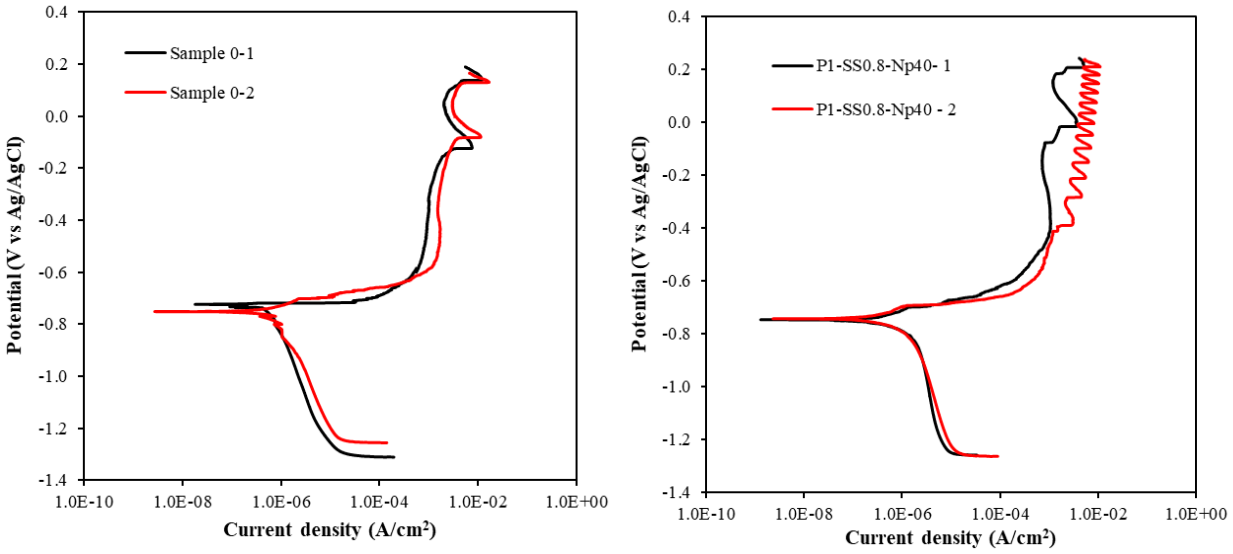


Figure A4.0.1. Potentiodynamic polarisation curves of a) Sample 0 and b) P1-SS0.8-N_p40 after duplicate tests.

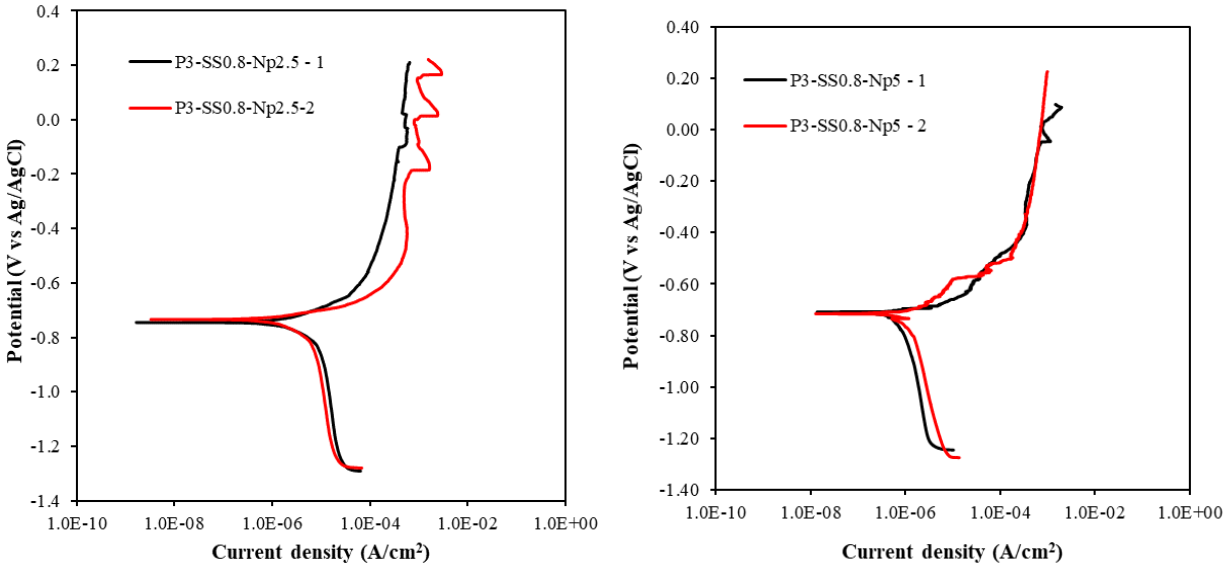


Figure A4.0.2. Potentiodynamic polarisation curves of a) P3-SS0.8-N_p2.5 and b) P3-SS0.8-N_p5 after duplicate tests.

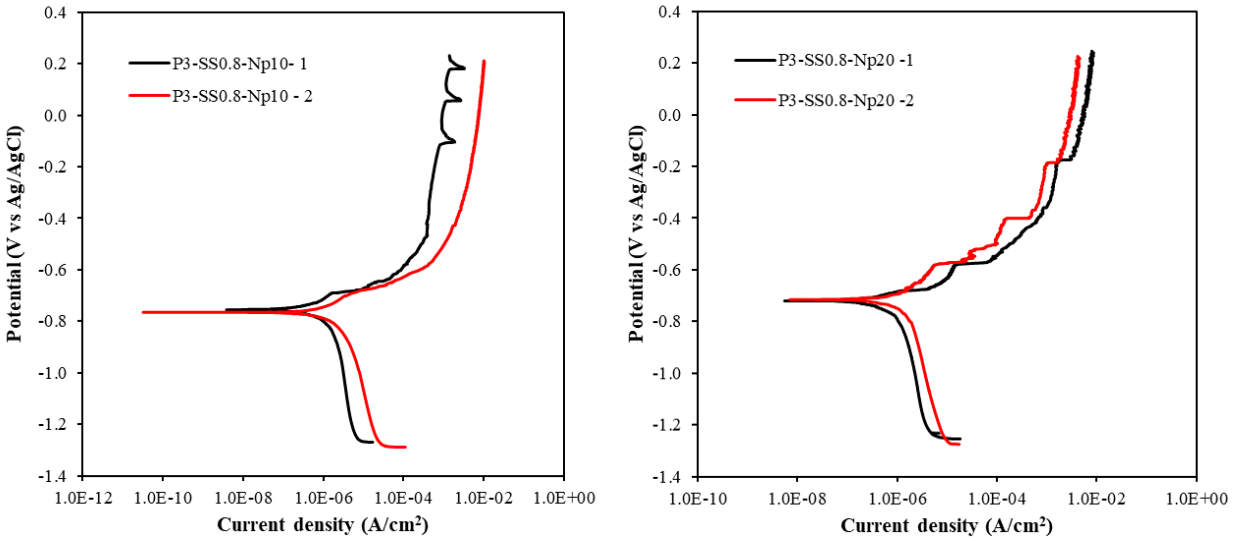


Figure A4.0.3. Potentiodynamic polarisation curves of a) P3-SS0.8-N_p10 and b) P3-SS0.8-N_p20 after duplicate tests.

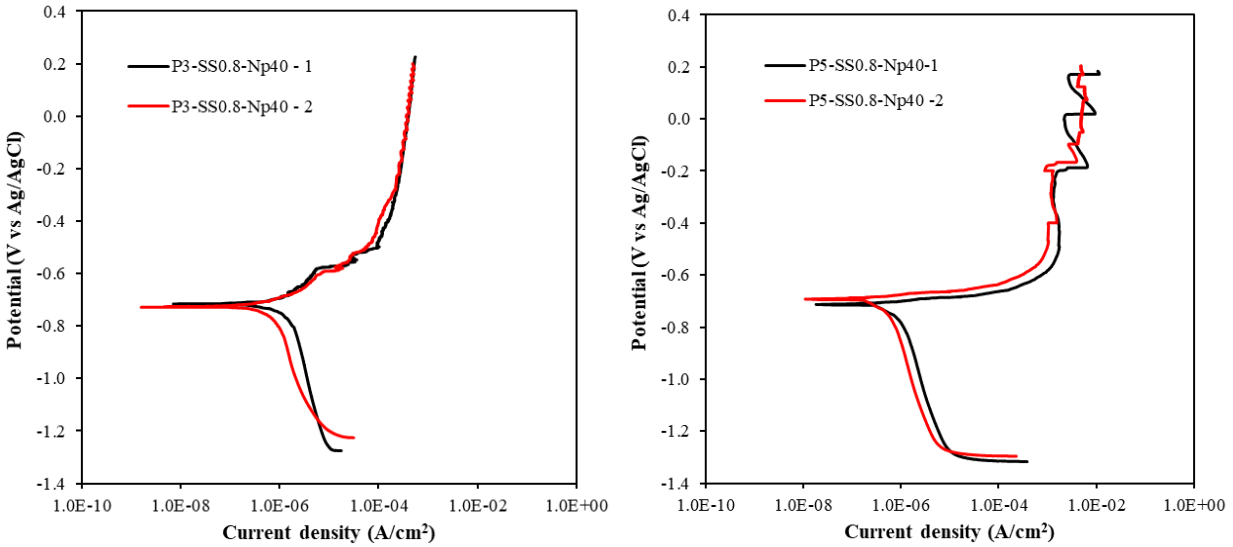


Figure A4.0.4. Potentiodynamic polarisation curves of a) P3-SS0.8-N_p40 and b) P5-SS0.8-N_p40 after duplicate tests.

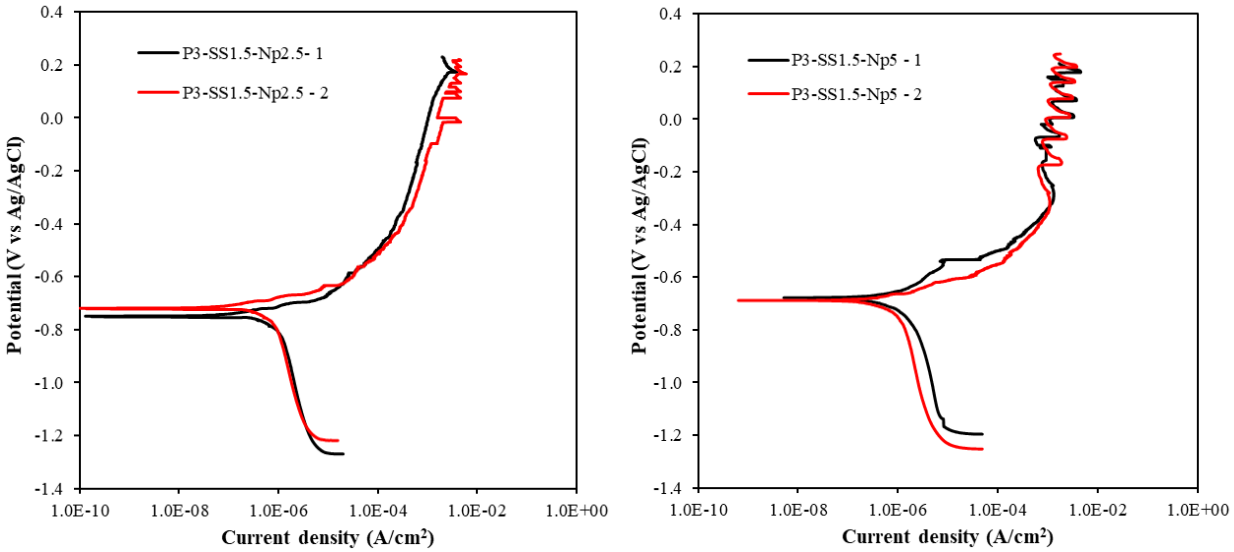


Figure A4.0.5. Potentiodynamic polarisation curves of a) P3-SS1.5-N_p2.5 and b) P3-SS1.5-N_p5 after duplicate tests.

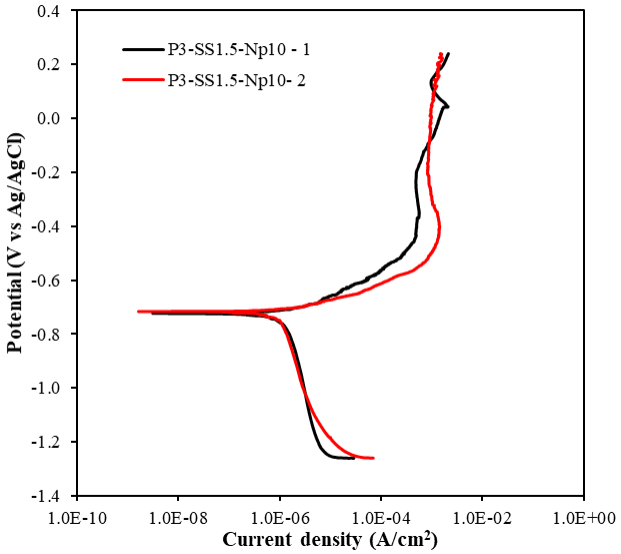


Figure A4.0.6. Potentiodynamic polarisation curves of a) P3-SS1.5-N_p10 after duplicate tests.

Appendix 5: Contributions From This Study

Poster Presentation:

N. Shonhai, A.N.N. Chundunsing, C. Polese, L.A. Cornish, H. Ramasawmy, *Investigation of Corrosion Behaviour of Aeronautical Aluminium Alloy 7075 Processed by Laser Shock Peening without Coating*, 8th International Conference on Laser Peening and Related Phenomena (8th ICLPRP), 22-27 October 2023, Gyeongju, Korea (A097).

DOI: 10.13140/RG.2.2.10874.88000

https://www.iclprp2023.org/

- Winner of the Best Poster Award

Oral Presentations:

N. Shonhai, A.N.N. Chundunsing, C. Polese, L.A. Cornish, H. Ramasawmy, *Corrosion Behaviour of Conventional Aeronautical Aluminium Alloy 7075 Processed by Laser Shock Peening without Coating*, The Annual Aeronautical Society of South Africa (AeSSA) Conference, 27-28 July 2023, Pretoria, South Africa

https://www.aessa.org.za/

N. Shonhai, C. Polese, L.A. Cornish, *A Study of the Effect of Laser Shock Peening without Coating at Different Parameters on AA7075 Surface Integrity*, 14th African Laser Centre Student Workshop, 13–15 November 2023, Stellenbosch, South Africa

DOI: 10.13140/RG.2.2.18005.19688

https://academic.sun.ac.za/physics/websites/alc_workshop_2023_nov/documents/program/ALC_Nov-2023_Student_Workshop_Program.pdf



Figure A5.1. Best poster award from the ICLPRP.



This is to certify that

Ms Natsai Shonhai

made a presentation at the

14th AFRICAN LASER CENTRE
WORKSHOP 2023
STELLENBOSCH

Chairman .....

15 November 2023

Stellenbosch
UNIVERSITY
IYUNIVESITHI
UNIVERSITEIT

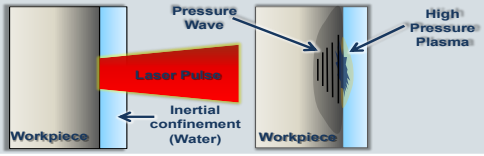
Figure A5.2. Certificate of attendance at the 14th ALC workshop 2023.

Investigation of Corrosion Behaviour of Aeronautical Aluminium Alloy 7075 Processed by Laser Shock Peening without Coating

N. Shonhai, A.N.N. Chundunsing, C. Polese, L.A. Cornish and H. Ramasawmy

Introduction

Aluminium alloys are used in the aeronautical industry because of their good mechanical properties including a high strength-to-weight ratio. However, they are susceptible to localised corrosion attack. Laser Shock Peening (LSP) is a surface treatment aimed at inducing favourable compressive residual stresses in metallic structures, thus improving their mechanical performance.



The introduction of LSP technology during production and maintenance can significantly increase aeronautical components' performance. LSP can be controlled using several parameters, as listed in the table below. Together, they induce modifications in the material which can also influence its corrosion resistance.

Power Intensity (PI)	Spot Size (SS)	Coverage (Np)
$PI = \frac{energy}{pulse\ length\ x\ area}$ (GW/cm²)	Ø (mm)	Number of laser pulses (spots) per mm²

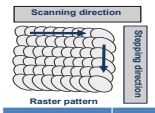
Objectives

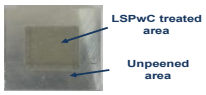
- To analyse surface modifications induced on AA7075 -T651 by LSPwC
- To assess the resistance of LSPwC -treated components to corrosion

Methods

LSP processing was done at the CSIR Photonics Centre:

- Laser: Q-switched Nd:YAG
- Wavelength (λ): 1064 nm
- LSP without protective coating (LSPwC)



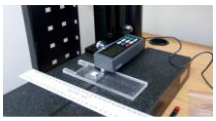


Parameter	Level 1	Level 2	Level 3	Level 4	Level 5
SS	0.8	1.5	-	-	-
PI	1	3	5	-	-
Np	2.5	5	10	20	40

The surface morphology was examined by a Scanning Electron Microscope (SEM) and by measuring the surface roughness using a stylus profilometer. The Vickers microhardness was also measured.



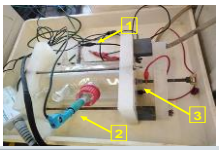
Scanning electron microscope (SEM)



Stylus profilometer



INNOVATEST hardness testing machine



1. Counter electrode – graphite rod
2. Reference electrode – Ag/AgCl saturated in 3 M KCl
3. Working electrode – test sample

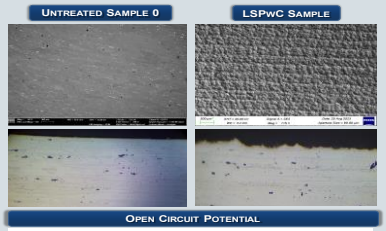
Electrochemical cell

Corrosion Tests

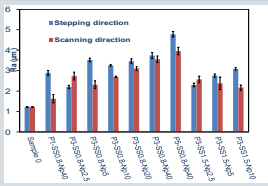
- All tests were carried out in 3.5 wt% NaCl solution at 20 °C
- Open Circuit Potential (OCP) was measured for 1 h to determine the reactivity of the specimens in solution at zero applied current
- Potentiodynamic Polarisation scans at 1 mV/s scan rate from -0.5 V to 1 V.

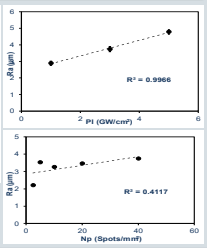
Results

Untreated Sample 0 / LSPwC Sample



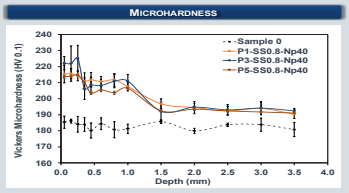
Surface Roughness





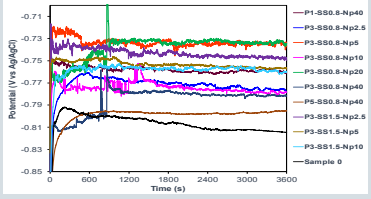
- Surface roughness increased significantly as PI increased
- A medium correlation was observed for Np.

Microhardness



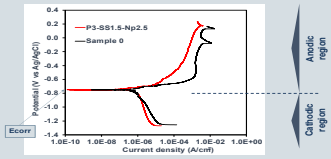
- Microhardness increased after LSPwC. Further, it decreased through the depth and remained constant after 1.5 mm
- There was no correlation between microhardness and PI.

Open Circuit Potential



The OCP of the LSPwC samples were stable and similar, all within an 80mV range and more noble than the baseline Sample 0.

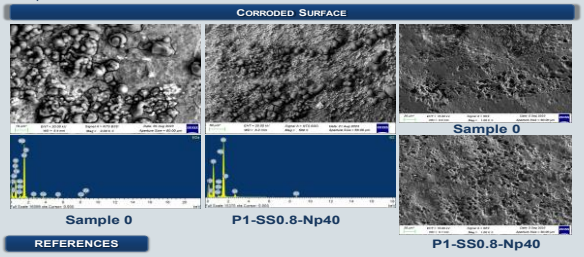
Potentiodynamic Polarisation



Sample ID	E_{corr} (V)	I_{corr} (µA/cm²)	Corrosion Rate x10⁻² (mm/y)
Sample 0	-0.747 ± 0.005	1.80 ± 0.13	2.01 ± 0.14
P1-SS0.8-Np40	-0.746 ± 0.002	0.78 ± 0.04	0.87 ± 0.04
P3-SS0.8-Np2.5	-0.739 ± 0.005	3.23 ± 0.05	3.60 ± 0.05
P3-SS0.8-Np5	-0.712 ± 0.003	3.69 ± 0.15	4.28 ± 0.17
P3-SS0.8-Np10	-0.760 ± 0.005	1.12 ± 0.33	1.25 ± 0.37
P3-SS0.8-Np20	-0.718 ± 0.002	2.28 ± 0.06	2.54 ± 0.06
P3-SS0.8-Np40	-0.722 ± 0.007	3.57 ± 0.20	3.98 ± 0.22
P5-SS0.8-Np40	-0.705 ± 0.010	4.88 ± 0.11	5.44 ± 0.13
P3-SS1.5-Np2.5	-0.733 ± 0.014	0.43 ± 0.04	0.48 ± 0.04
P3-SS1.5-Np5	-0.682 ± 0.006	1.15 ± 0.06	1.28 ± 0.07
P3-SS1.5-Np10	-0.720 ± 0.004	1.89 ± 0.06	2.10 ± 0.07

Similar E_{corr} range within 80 mV

Corroded Surface



Conclusions

- Surface roughness increased with PI and Np
- LSPwC increased the microhardness of AA7075
- There was no notable difference in the microstructure after LSPwC
- Some LSPwC parameter combinations gave better corrosion resistance than the unpeened sample.

Acknowledgements

The authors would like to acknowledge the generous support of:

- DSI-NRF Centre of Excellence in Strong Materials (CoE-SM)
- African Laser Centre (ALC)
- CSIR Photonics Centre Rental Pool Programme (RPP)
- DSI Collaborative Programme in Additive Manufacturing (CPAM)

References

[1] Ding, K., Ye, L., 2006. Laser Shock Peening : Performance and Process Simulation, Woodhead Publishing Limited, Cambridge, England

[2] Sano, Y. et al., 2006. Laser Peening without Coating as a Surface Enhancement Technology. J. Laser Micro/Nanoengineering 1, 161–166. https://doi.org/10.2961/jlmn.2006.03.0002

[3] Pedersen, K.O., Børvik, T., Hopperstad , O.S., 2011. Fracture Mechanisms of Aluminium Alloy AA7075-T651 under Various Loading Conditions . Mater. Des. 32, 97–107. https://doi.org/10.1016/j.matdes.2010.06.029

Figure A5.3. Poster presented at the 8th International Conference on Laser Peening and Related Phenomena.

AESSA Abstract

Corrosion Behaviour of Conventional Aeronautical Aluminium Alloy 7075 Processed by Laser Shock Peening without Coating

Shonhai, N.[1,2], Chundunsing, A.N.N.[3,4], Polese, C.[2,3], Cornish, L.A.[1,2] and Ramasawmy, H.[4]

[1]School of Chemical and Metallurgical Engineering, University of the Witwatersrand, 1 Jan Smuts Avenue, Johannesburg, 2000, South Africa
[2]DSI-NRF Centre of Excellence in Strong Materials, hosted by the University of the Witwatersrand
[3]School of Mechanical, Industrial and Aeronautical Engineering, University of the Witwatersrand, 1 Jan Smuts Avenue, Johannesburg, 2000, South Africa
[4]Mechanical and Production Engineering Department, University of Mauritius, Reduit, 80837, Mauritius

Aluminium alloys are still used in approximately 50-90% of modern airframe structures due to their good mechanical behaviour, ease of design and manufacture. High strength, i.e. peak-aged aluminium alloys are typically selected for conventional primary structures because of their favourable weight/strength ratio and good corrosion resistance. However, these aluminium alloys remain the subject of numerous studies due to their susceptibility to localised corrosion attack in more aggressive environments. Especially in a chloride environment, peak-aged aluminium alloys tend to show increased susceptibility to pitting corrosion and stress corrosion cracking. Therefore, additional surface protection is usually provided by various types of coatings or, in cases in which both mechanical and microstructural enhancements are required, with different surface engineering processing techniques.

In this regard, Laser Shock Peening (LSP) is an innovative surface treatment that has attracted interest because of its ability to increase the performance of aluminium aeronautical components and has already been widely approved as a potential substitute for the standard mechanical Shot Peening (SP) technology, for both manufacturing and maintenance.

In comparison to SP, the LSP process enables several beneficial effects, such as higher fatigue strength with a delay in fatigue crack initiation and retarded fatigue crack growth due to greater depths of higher compressive residual stresses and enhanced surface finish.

Yet, despite several research focused on LSP influence on residual stress fields and fatigue, detailed investigations devoted to a deeper analysis of surface integrity and localised corrosion and stress-corrosion cracking susceptibility is rather limited, especially on heat-treated, peak-aged aluminium alloys.

In this work, the corrosion behaviour of a conventional AA7075-T651 after LSP without protective coating was investigated. The laser processing parameters varied were power intensity (1-5 GW/cm^2), spot size (diameter 0.8-1.5 mm) and coverage (2.5-40 spots/mm^2). For

LSPeened samples, Scanning Electron Microscope images showed rough surfaces with areas of re-melting and solidification and some micro-cracks. Energy Dispersive X-ray microanalysis revealed an increase in oxygen content, indicating the formation of an oxide film. Higher surface roughness values were recorded due to intense surface ablation. Electrochemical corrosion tests (open-circuit potential and potentiodynamic polarisation scans) were carried out in 3.5 wt% NaCl solution, with LSPeened specimens tested and compared with the unpeened (baseline) samples under similar conditions.

The results showed higher corrosion rates for most LSPeened samples. Relationships between the observed results and LSP processing parameters were identified for microstructure, Knoop and Vickers microhardness and residual stress, helping in reaching a better understanding of the potentials and limits of the without coating LSP process for the aeronautical industry.

ALC ABSTRACT

Stellenbosch UNIVERSITY IYUNIVESITHI UNIVERSITEIT SPI Stellenbosch Photonics Institute

alc african laser centre

A study of the effect of laser shock peening without coating at different parameters on AA7075 surface integrity

N. Shonhai[1], C. Polese[2] and L.A. Cornish[1]

[1] School of Chemical and Metallurgical Engineering, WITS, Johannesburg, South Africa.
[2]School of Mechanical, Industrial and Aeronautical Engineering, WITS, Johannesburg, South Africa.

T9
Time 16h10

lesley.cornish@wits.ac.za

Aluminium alloys are the preferred material for modern airframe structures due to their ease of manufacture, light weight and good mechanical properties. However, these alloys are susceptible to localised corrosion, particularly in chloride environments, which can lead to pitting corrosion and stress corrosion cracking. To protect them, various coatings and surface modification techniques are used. Laser shock peening (LSP) is a promising surface treatment that provides deeper compressive residual stresses and improved surface finish, resulting in higher fatigue strength and delayed fatigue crack initiation than conventional Shot Peening (SP). However, research is limited on the influence of LSP on residual stress, fatigue resistance, surface integrity and localised corrosion and stress-corrosion cracking susceptibility, especially on heat treated, peak-aged aluminium alloys. This study investigated the surface modifications and resultant corrosion behaviour of conventional AA7075-T651 after LSP without a protective coating. The LSP process parameters were varied: power intensity (1-5 GW/cm^2), spot size (diameter 0.8-1.5 mm) and laser pulse density (2.5-40 spots/mm^2). For LSP samples, SEM micrographs showed rough surfaces with areas of re-melting and solidification with micro-cracks on some samples. Surface roughness measurements showed higher roughness due to intense surface ablation, with increased roughness as power intensity increased. The EDX analyses revealed increased oxygen on the peened surfaces. Potentiodynamic polarisation showed higher corrosion rates for most LSP samples than unpeened samples, although lower corrosion rates were obtained for some combinations of LSP parameters. The relationships between the LSP processing parameters and the surface roughness, microstructure, Vicker's microhardness and corrosion parameters are being determined to better understand the potential and limitations of the LSP process without coating. Further work is being done to investigate the effect of LSP on stress corrosion cracking using a three-point bending system in a 3.5 wt% NaCl solution.